Optical Vertical Couplers
by
Ion Exchange in Glass

by

Peter C. Noutsios, M.Eng., B.Eng(Hon.)

Department of Electrical Engineering
McGill University, Montreal
July 1996

A thesis submitted to the Faculty of Graduate Studies and Research in partial fulfillment of the requirements for the degree of Doctor of Philosophy

ISBN 0-612-19759-X

Dedicated to my loving wife, Maria,

for her patience and understanding

Abstract

Planar and channel optical waveguides fabricated by field-assisted $K^+ - Na^+$ ion exchange in soda-lime glass are studied. An optical characterization of planar surface guides for a given set of fabrication conditions has been performed to determine the refractive index profile. Parallel to this, the ion-exchange diffusion process has been modelled numerically to predict the concentration profile of these waveguides. Direct measurements of the profiles using electron microprobe analysis has been carried out.

The results of the characterization were used in the design and fabrication of a novel vertically integrated optical directional coupler. This device, composed of single-mode surface and buried ion-exchanged waveguides, allows for the optical fiber coupling to the buried guide and efficient power transfer to the surface guide, where the light can be detected by a modelled $GaAs$ photodetector. An improved version of the device using a sputtered Al_2O_3 surface guide allows for edge coupling to the detector. Calculations of the $GaAs$ absorption coefficient show an optimum behavior for a given thickness of Al_2O_3.

An implicit finite-difference vector beam propagation method (FD-VBPM), that was improved to account for graded-index profiles, has been developed and used in the design of both directional-coupler structures. Finally, a three-dimensional FD-VBPM algorithm was implemented for the channel-guide version of the improved coupler.

Résumé

La fabrication de guides optiques planaires et canales par un échange d'ions potassium-sodium assisté d'un champ électrique dans un substrat de verre soda-calcique est étudiée. On a effectué une caractérisation expérimentale des guides optiques planaires dans une gamme de conditions de fabrication pour déterminer le profile d'indice. Parallèlement, le procès de diffusion par échange d'ions a été résolu numériquement pour prédire le profil de concentration de ces guides d'onde. Des mesures directes des profiles en utilisant un micro-analyseur à sonde électronique ont été faites.

Les resultats de la caractérisation ont été utilisés pour le design et la fabrication d'un nouveau coupleur directionnel integré verticalement dans le substrat. Cet appareil, composé des guides d'onde monomodes en surface et ensevelis par l'échange d'ions, permet le couplage d'un fibre optique au guide enseveli et le transfer d'energie au guide surface, où l'onde est detecté par un photodetecteur modèl de $GaAs$ (arsenide de gallium). Un version amelioré de cet appareil, fabriqué d'un guide surface de Al_2O_3 (oxide d'aluminum) permet le couplage à bord par le detecteur. Des calculs de la coefficient d'absorption de $GaAs$ ont a démontrés une conduite optimale pour une épaisseur specifique de Al_2O_3.

Un version implicite de la méthode FD-VBPM ('Finite Difference Vector Beam Propagation Method'), qui a été amelioreé pour des profiles d'indices rampés, a été développé et utilisé pour le design de deux structures de couplage directionnel. Finalement, un version en trois dimensions de la FD-VBPM a été employé pour la version amelioré de l'appareil composé de guide canal.

ACKNOWLEDGEMENTS

I would like to thank my supervisor, Professor Gar Lam Yip, for his close guidance, encouragement and support during our eight-year collaboration through my Masters' and Ph.D. degrees. His wise, fatherly advice and optimistic attitude have greatly inspired me.

I am very grateful to my former colleague, Dr. Feng Xiang, for his help during my research work and for many interesting discussions. I also acknowledge a former postdoctoral colleague, Prof. K. Kishioka, Osaka Electro-Communication University, for his technical expertise, especially in the design and construction of the field-assisted ion-exchange apparatus. The technical advice of Dr. Jacques Albert of the Communication Research Center is also greatly appreciated for the device aspect of the work. His financial support through a government contract is acknowledged.

I must express my gratitude to Lawrence Chen, an excellent undergraduate student, who worked closely with me for two summers on the experimental and theoretical aspects of the near-field profiling work. In addition, the help of students Thang Pham and Serge Haumont are acknowledged.

Thanks go out to my fellow colleagues for their many stimulating discussions. In particular, the contributions from John Nikolopoulos, Dennis Kan and Phillippe Allard are acknowledged. Finally, I thank my friend and colleague Ziad Shukri of the solid-state lab for his expertise on high vaccuum techniques for evaporation and sputtering. In addition, his sense of humor and companionship throughout our Ph.D. years will always be cherished.

I have also benefited from the technical assistance of Glenn Poirier of the Department of Earth and Planetary Sciences for the EPMA analysis. In addition, the prompt and accurate mechanical work of Don Pavlasek and Bela Disco of the Electrical Engineering Workshop is also acknowledged. Finally, I give thanks to Joseph Mui, our electronics technician, for his photographic work presented in this thesis

and to Kesia Cheng for his assistance with our vacuum stations.

This research was supported financially by the Natural Sciences and Engineering Research Council of Canada (NSERC) through a post-graduate scholarship and an operating grant and by the Fonds Pour La Formation De Chercheurs Et L'Aide A La Recherche (FCAR) of Quebec through a doctoral scholarship. In addition, a fellowship from McGill's Faculty of Graduate Studies is acknowledged.

Definition of Greek Symbols

α	complement of the mobility ratio, $1 - \mu_K/\mu_{Na}$
$\alpha_{1,2}$	EPMA holder tilt angles
α_c	attenuation constant of photodetector
α_p	prism angle
α_r	TBC relaxation parameter
α_{TI}	TRT evanescent wavenumber
β	propagation constant
β^c	complex propagation constant
β'	real part of β^c
β''	imaginary part of β^c
β_m	real quantity used in Von Neumann analysis
γ	complex quantity used in Von Neumann analysis
γ_s	parameter in $S(x, y)$
Γ	right-hand side function in RK method
δ	deviation
Δx	step size in x
Δy	step size in y
Δz	step size in z
Δt	step size in t
ϵ	dielectric constant
ε	Modified Fermi parameter
ε_0	permittivity of free space
ζ	TBC parameter
η_{fg}	fiber-guide mode matching efficiency
η_{max}	maximum power transfer
η_o	end-fire coupling efficiency into detector
θ	bevel angle
θ_i	sunchronous angle
λ	wavelength
μ_K	mobility of K^+ ions
μ_{Na}	mobility of Na^+ ions
μ_o	permeability of free space
μm	micrometer
ξ	normalized depth used in RK method
ρ	local space charge density
$\phi_{1,2}$	phase shifts at interfaces
φ	field component in RK method
χ	parameters in phase shift
Ψ	Fresnel field component
ω	angular frequency

Definition of Alphabetic Symbols

a	Modified Fermi fitting parameter
A	arbitrary amplitude
A_e	amplitude of even mode
A_o	amplitude of odd mode
$\mathcal{A}$	intermediate Fresnel differential operator
$A^l_{i,j}$	2-D and 3-D BPM numerical operator
$A1^l_{i,j}$	3-D BPM numerical operator
$\mathcal{B}$	intermediate Fresnel cross-coupling operator
$B^l_{i,j}$	3-D BPM numerical operator
c_K	concentration of K^+ ions
c_{Na}	concentration of Na^+ ions
c_o	concentration of Na^+ ions prior to exchange
cm	centimeter
$C^l_{i,j}$	3-D BPM numerical operator
$C1^l_{i,j}$	related 3-D BPM numerical operator
d	effective guide depth
d_{pb}	probing depth in EPMA
d_{sub}	substrate thickness
D_e	effective diffusion coefficient
D_K	self-diffusion coefficient of K^+ ions
D_{Na}	self-diffusion coefficient of Na^+ ions
D_2	thin-film thickness
D_3	$GaAs$ detector thickness
e	elementary charge
$\vec{E}$	time dependent vector of electric field
$\vec{H}$	time dependent vector of magnetic field
$\vec{E}_t$	total d.c electric field
$\vec{E}_i$	intrinsic d.c electric field
$\vec{E}_a$	applied d.c electric field
$\vec{E}^T_a$	total applied electric field
f	correlation factor
F	field function of two variables in RK-EIM
F_e	electromigrative coefficient
F_c	Faraday's constant
g	transformation function $\ln(1-\hat{\alpha}c)$
G	field function in RK method
h	hour
h_t	transverse parameter in guiding region
h_K	fraction of exchanged K^+ ions at surface
$HW(z)$	Hanning window function
i	integer index along x
I	ion current density
$I(x,y)$	digitized image data
$I_d(y)$	diffracted intensity pattern

I_i	sample intensity
$I_{(i)}$	standard intensity
j	integer index along y
$\vec{J}_K$	ionic flux of K^+ ions
$\vec{J}_{Na}$	ionic flux of Na^+ ions
$\vec{J}_o$	net ionic flux
k	integer index for t
$k_{1,2,3,4}$	parameters in numerical RK scheme
k_B	Boltzmann constant
k_o	wave number in free space
k_r	$I_i/I_{(i)}$ ratio
$k_{x,y}$	complex proapagation constants in TBC
k_{xi}	TRT guided wavenumber
K_o	constant depth value
K_{sub}	atomic K^+ concentration ratio in substrate
K_{surf}	atomic K^+ concentration ratio at surface
$K1$	maximum integer grid points in t
l	integer index along z
l_s	sampling displacement
$\mathcal{L}$	Fresnel differential operator
L_c	coupling length
L_d	screen distance for diffraction pattern
L_{int}	interaction length
L_{pi}	prism positions
$L1$	maximum integer grid points in z
LBC	left boundary condition
min	minute
m	WKB integer mode number
m_{TBC}	geometric parameter in TBC
mm	millimeter
$M, M1$	maximum integer grid points in x direction
$n(x, y, z)$	refractive index
n_b	substrate refractive index
n_f (n_2)	thin-film index
n_p	prism index
n_{peak}	value of maximum buried refractive index
n_r	reference refractive index
n_s	surface refractive index
n_3	$GaAs$ detector index
nm	nanometer
$N, N1$	maximum integer grid points in y direction
N_{eff}	effective index β/k_0

N_{even}	even mode effective index
N_{odd}	odd mode effective index
Na_{sub}	atomic Na^+ concentration ratio in substrate
p_i	transverse parameter in air region
P_a	normalized power in slab 'a'
P_T	total power
$P(x,y)$	near-field power distribution
$P(z)$	correlation function
$P_d(z)$	propagating power in detector
q_i	transverse parameter in bulk region
r	sputtering rate
r_m	mesh ratio $\Delta t/(\Delta x)^2$
R	ratio of A_a to A_s
$R^l_{i\pm1}$	index parameter across interface in FD-VBPM
s	second
$S(x,y)$	2-D ETF profile
t	time
T	temperature
$T^l_{i\pm1}$	index parameter across interface in FD-VBPM
$u_n(x)$	modal eigenfunction
v	speed of the ions
V	voltage level
V_a	applied voltage
V_o	potential drop across salt melt
x	spatial variable in the depth direction
x_{peak}	location of buried guide index maximum
x_t	turning point in WKB method
X_{max}	computational window size in x direction
y	spatial variable in the width direction
Y_{max}	computational window size in y direction
z	spatial variable in the longitudinal direction
Z_{max}	computational window size in z direction
w	weight value used in BPM
w_f	Gaussian mode field width
W	mask opening (width)
Y_m	location of diffracted intensity minimum
Z_t	wave impedance in TRT

Definition of Acronyms

2-D	two-dimensional
3-D	three-dimensional
ADI	alternating direction implicit
BPM	beam propagation method
C.C.	cold cathode
CCD	charge-coupled device
DC	direct current
D.I.	de-ionized
ELO	epitaxial liftoff
EMP	electron microprobe
EPMA	electron probe microanalysis
ETF	effective transfer function
FD	finite difference
FFT	fast Fourier transform
FV-ADI	full-vector ADI
GRIN	graded-index
H.P.	high purity
H.V.	high vaccuum
LBC	left boundary condition
MSM	metal-semiconductor-metal
PDE	partial differential equation
PSI	pounds per square inch
QV-ADI	quasi-vector ADI
rpm	revolutions per minute
RF	radio frequency
RK-EIM	Runga-Kutta effective index method
STBC	simplified TBC
TBC	transparent boundary condition
TC-1	thermocouple pressure gauge in Foreline
TC-2	thermocouple pressure gauge in Roughing
TE	transverse electric
TM	transverse magnetic
TRT	transverse resonance technique
UV	ultraviolet
VBPM	vector BPM
VDC	vertical directional coupler
WDM	wavelength division multiplexing
WDS	wavelength dispersion spectroscopy
WKB	Wentzel-Kramers-Brillouin
ZAF	Atomic number, absorption, fluorescence

Contents

List of Figures

List of Tables

Chapter 1

Introduction

1.1 Fiber and integrated optics

Optical-fiber communication systems have advanced quite rapidly in the past quarter century. In 1970, Corning Glass Works reported a major breakthrough that reduced optical-fiber transmission loss to $20\,dB/km$. Since then, research and development (R & D) into fiber-optic components and systems has accelerated and completely changed the landscape of telecommunications. There has been a steady evolution in technology from electronics to photonics as the demand for higher-speed voice and data communications intensified. High-frequency lightwaves from newly-developed laser sources began replacing lower frequency microwaves as information carriers. Consequently, smaller-sized dielectric waveguides, such as glass optical fibers with improved losses of $0.2\,dB/km$, became very attractive. Today, fiber-optic photonics technology is prevalent as the backbone of the local and long-distance telephone industry in many countries, providing services that improves the standard of living of its citizens.

Parallel to this phenomenal success, another photonics-based technology was advancing simultaneously (without as much fanfare) that would complement optical fiber. Research and development into integrated optics, first proposed by S.E. Miller of Bell Laboratories, would provide for compact active and passive devices integrated on a common substrate [1]. These optical circuits would act as signal-processing ele-

ments for the optical signal emanating from the fiber. The functional performance of these devices in high-speed modulation, switching, splitting and wavelength division multi/demultiplexing (WDM) would add great benefits to optical communications.

Various technologies have been employed to fabricate the waveguide structures that form the basis of integrated optical devices [2]. Some of these include titanium indiffusion into lithium niobate ($LiNbO_3$) to make electro-optic devices and ion exchange in glass for passive devices. In this thesis, we will focus on the latter fabrication technology.

1.2 Glass integrated optics by ion exchange

Glass is an excellent material as a planar substrate in which to fabricate passive waveguides [3]. Due to its compatibility with optical fibers in material properties, Fresnel losses can be minimized, leading eventually to lower insertion loss. It is also an inexpensive, physically stable material under a wide range of processing and operating conditions. More importantly, it is an ideal medium for a simple diffusion process known as ion exchange. This process is only one example of many processes used for integrated optics in glass. For further details, the reader is asked to consult other sources [2, 4].

The ion-exchange technique [5, 6] has received attention as it creates a higher refractive index waveguiding region by replacing ions in the glass by those of larger size or higher polarizability. The diffusion process is simple and easily amenable to economical batch fabrication on a large scale. Purely thermal and electric-field-assisted ion exchange from a molten ionic bath have led to the fabrication of multimode and single-mode waveguide devices [6]. However, due to the limitation in their information carrying capacity (bandwidth), multimode optical fibers and waveguide devices have been gradually replaced by their single-mode equivalents. Hence, an ion-exchange technology has been developed for this purpose.

The $K^+ - Na^+$ ion-exchange process has by far been the most used for single-

mode device fabrication. This preference is attributed to four main factors:

1. The small refractive index change Δn_s with a pure KNO_3 melt is highly compatible with single-mode fibers.

2. Owing to its small diffusion coefficient, it is a relatively slow and controllable process that is important for good device reproducibility.

3. It has proven to provide low propagation losses [7] because K^+ ions do not reduce to a metallic form in the glass which are the major cause of scattering and absorption centers [6]. This has occurred for pure $AgNO_3$ melts, requiring concentration control (dilution) of Ag^+ ions in the melt.

4. Unlike $Ag^+ - Na^+$ exchange, K^+-ion exchange needs no concentration control of the melt thus simplifying the fabrication process.

Yip and Albert [8, 9, 10] have reported an exhaustive study of purely thermal $K^+ - Na^+$ exchange in soda-lime glass. It includes the determination of the refractive index profile, measurement of the potassium diffusion coefficient and its temperature dependence, the surface index change, and birefringence. Since then, this characterization procedure was repeated by another group to study $K^+ - Na^+$ exchange in BK7 glass [11].

Although surface waveguides have been characterized using potassium, there has been recent interest in fabricating graded-index planar buried waveguides [6]. There are two main reasons for this: the first is that burying a surface waveguide considerably improves the index profile symmetry so as to match that of an optical fiber. The other is that lower propagation losses are attainable because the guided wave does not interact with the surface irregularities which invariably contribute to losses via scattering. These guides are made by a two-step process; the first being an ion exchange that creates a surface guide. This is followed by a backdiffusion process in $NaNO_3$ that replaces the Na^+ ions removed in the first step. The characterization

of such waveguides is necessary in the design and fabrication of passive devices for efficient coupling with optical fibers to minimize the insertion loss.

The field-assisted ion-exchange process is a valuable technology for glass integrated optics. It has been shown to have advantages over the purely thermal exchange for many reasons. Firstly, the application of an electric field across the substrate during ion-exchange considerably speeds up the diffusion time needed to fabricate single and multimode waveguides [12, 13]. In addition, the shape of the index profile can be tailored [13]. Finally, this process can be applied in the fabrication of deep, buried waveguides with the electric field enhancing the backdiffusion process [14].

1.3 Hybrid optoelectronics on glass

From 1970 to 1990, a lion's share of the R & D effort in glass integrated optics has focused on passive components. In fact, these components are now commercially available from companies that include Corning, IOT Schott and NSG. Examples of such passive components include $1 \times N$ branching devices [7], directional-coupler power dividers [15] and wavelength demultiplexers [16]. Since 1990, active functions in glass waveguides have attracted considerable interest. These functions consist of laser and amplifier action in rare-earth doped waveguides [17, 18] and light detection in waveguides combined with semiconductors [19, 20]. Such active components can be fabricated on glass and $LiNbO_3$ by combining waveguides with overlayers of semiconductor material in a hybrid structure. Earlier attempts include the demonstration of a silicon (Si) photodetector coupled to a $LiNbO_3$ waveguide by pressing the detector against the guide [21] or by faceting the $LiNbO_3$ at 45^o to reflect the guided light onto the detector [22]. The techniques used in both these cases required careful mechanical alignment and are difficult to adapt to the small detectors of interest for integrated optics [23]. More recently, research into integrating other semiconductors besides Si has been pursued. Examples of such efforts include the work of Yi-Yan *et al* [19] on grafted $GaAs$ metal-semiconductor-metal (MSM) photodetectors using

epitaxial liftoff (ELO) and integrated with ion-exchanged glass waveguides. Also, the fabrication of p-i-n detectors using $SiGe:H$ [20] and $InGaAs/InP$ on glass waveguides have been reported [24]. These results are of considerable interest because they have created a new application for ion-exchange technology in the arena of hybrid optoelectronic integration [23].

Quite recently, two U.S. companies have begun using this hybrid integration. United Photonics Technology, manufacturers of $LiNbO_3$ integrated-optic components, now offer a detector-on-chip option, which can supply a monitor voltage by placing a detector directly on the waveguide surface [25]. This hybrid approach is advantageous because it shows how each distinct device, best suited for a particular function, can be brought together on the same chip. Also, the Photonics Division of Foster-Miller has developed fabrication techniques to transfer and bond thin epitaxial layers from $GaAs$ wafers onto substrates such as sapphire, glass and prefabricated silicon circuits [26]. One particular device is a $GaAs$ optical modulator placed on a Si substrate that marries the merits of $GaAs$ optical devices with the maturity of Si electronics.

1.4 Vertical integration

To fully exploit hybrid integration for glass integrated optics, one needs to consider vertically integrated structures that would transfer the light signal from the waveguide to the detector located just above it. The concept of vertical integration is well known in the area of semiconductor optical devices [27]. However, for passive components in glass, most of the research efforts have focused on lateral integration of adjacent channel guides. In particular for glass waveguides, only a handful of vertically integrated structures are available. Some of these include a five-layer coupler composed of sputtered Corning 7059 thin-film slabs on Pyrex glass [28] and recently, silicon-on-insulator waveguides on silicon [29]. When this thesis work was undertaken, the goal was to design and fabricate passive waveguide structures made by ion

exchange to be used for efficient coupling from an optical fiber to a photodetector. The work would focus on a vertical directional coupler (VDC) that would allow a fiber-optic signal to be transferred from a buried guide to a surface guide with a high power transfer ratio. The coupling into the detector would be tackled only as a theoretical design problem.

1.5 Thesis organization

The content of this dissertation comprises the study of both waveguide and device fabrication and characterization. The objective of a planar waveguide characterization is to establish a correlation between the propagation characteristics and the ion-exchange fabrication conditions. A systematic study that entails both micro-analytical and optical characterizations is presented in Chapter 5 based on ion-exchange diffusion modeling and electromagnetic wave theory. Chapter 2 presents the theory behind the ion-exchange equation whose solution is used to predict the dopant K^+-ion concentration profile for given fabrication conditions. The waveguide fabrication and measurement procedures are outlined in detail in Chapter 3. The modeling of the propagation characteristics based on electromagnetic wave theory is presented in Chapter 4. As for the device characterization, Chapter 6 presents the planar vertical coupler made by field-assisted ion-exchanged slab waveguides and the improved version, in both planar and channel-guide form, that comprises a buried guide and a dielectric surface guide is detailed in Chapter 7.

1.6 Claim of originality

The original contributions of this work to the advancement of planar glass waveguide technology are summarized as follows:

- the detailed characterization of planar field-assisted K^+-ion exchange glass waveguides including an improved model for the refractive index profile [30]

- the study of the diffusion and propagation properties of single-mode surface and buried guides [31]
- the novel demonstration of a vertical directional coupler in glass made by field-assisted ion-exchanged slab waveguides [32]
- the formulation of an improved two-dimensional (2-D) finite-difference vector beam propagation method (FD-VBPM) that accounts for the gradients of GRIN waveguides [33]
- the design and fabrication of an improved vertical structure used for optimized edge coupling to an embedded photodetector [34] in both planar and channel-guide form
- the experimental and theoretical study of near-field waveguide profiles using a CCD camera, frame grabber digitizer, and including all convolution effects [35]

Bibliography

[1] S.E. Miller. 'Integrated optics: an introduction'. Bell Syst. Tech. Journ., 48 (7), pp. 2059-2069, 1969

[2] T. Tamir. *Guided-Wave Optoelectronics*. Springer-Verlag. Berlin. 1990

[3] A. Beguin, T. Dumas, M.J. Hackert, R. Jansen, and C. Nissim. 'Fabrication and performance of low loss optical components made by ion exchange in glass'. J. Lightwave Technol., 6 (10), pp. 1483-1487, 1988

[4] S.I. Najafi, *Introduction to Glass Integrated Optics*. Artech House, Boston, 1992

[5] T. Findakly, 'Glass waveguides by ion exchange: a review', Opt. Eng., 24 (2), pp. 244-250, 1985

[6] R.V. Ramaswamy and R. Srivastava, 'Ion-exchanged glass waveguides: a review', J. Lightwave Technol., 6 (6), pp. 984-1002, 1988

[7] T. Findakly and B. Chen, 'Single-mode integrated optical $1 \times N$ star coupler', Appl. Phys. Lett., 40 (7), pp. 549-550, 1982

[8] G.L. Yip and J. Albert, 'Characterization of planar optical waveguides by K^+-ion exchange in glass,' Opt. Lett., 10 (3), pp. 151-153, 1985

[9] J. Albert and G.L. Yip, 'Refractive index profiles of planar waveguides made by ion-exchange in glass', Appl. Opt., 24 (22), pp. 3692-3693, 1985

[10] J. Albert and G.L. Yip, 'Stress-induced index change for $K^+ - Na^+$ ion exchange in glass', Electron. Lett., 23 (14), pp. 737-738, 1987

[11] J.E. Gortych and D.G. Hall. 'Fabrication of planar optical waveguides by K^+-ion exchange in BK7 and Pyrex glass', J. Quantum Electron., 22 (6), pp. 892-895, 1986

[12] T. Izawa and H. Nakagome. 'Optical waveguide formed by electrically induced migration of ions in glass plates', Appl. Phys. Lett., 21 (12), pp. 584-586, 1972

[13] G.H. Chartier, P. Jaussaud, A.D. De Oliveira, and O. Parriaux, 'Optical waveguides fabricated by electric field controlled ion-exchange in glass', Electron. Lett., 14 (5), pp. 132-134, 1978

[14] A. Miliou, H. Zhenguang, H.C. Cheng, R. Srivastava, and R.V. Ramaswamy, 'Fiber-compatible $K^+ - Na^+$ ion-exchanged channel waveguides: fabrication and characterization', J. Quantum Electron., 25 (8), pp. 1889-1897, 1989

[15] G.L. Yip and J. Finak, 'Directional-coupler power divider by two-step K^+-ion exchange', Opt. Lett., 9 (9), pp. 423-425, 1984

[16] H.C. Cheng and R.V. Ramaswamy, 'A dual wavelength ($1.32 - 1.56\mu m$) directional coupler demultiplexer by ion exchange in glass', IEEE Photon. Technol. Lett., 2 (9), pp. 637-639, 1990

[17] N.A. Sanford, K.J. Malone, and D.R. Larson, 'Integrated optic laser fabricated by field-assisted ion-exchange in neodymium-doped soda-lime glass', Opt. Lett., 15 (7), pp. 366-368, 1990

[18] M.J. Li and S.I. Najafi, 'Rare-earth-doped glass waveguides and amplifiers', SPIE Proc., 1338, pp. 82-87, 1990

[19] A. Yi-Yan, W.K. Chan, T.J. Gmitter, L.T. Florez, J.L. Jackel, E. Yablonovitch, R. Bhat, and J.P. Harbison, 'Grafted GaAs detectors on lithium niobate and glass optical waveguides', IEEE Photon. Technol. Lett., 1 (11), pp. 379-380, 1989

[20] P.P. Deimel. B.B. Heimhofer. G. Krotz. H.J. Lilienhof. J. Wind. G. Muller. and E. Voges. 'Amorphous $SiGe : H$ photodetectors on glass optical waveguides'. IEEE Photon. Technol. Lett.. 2 (7). pp. 499-501. 1990

[21] T.R. Ranganath and S. Wang. 'Light detection in dielectric waveguides by a photodiode through direct evanescent field coupling'. Appl. Phys. Lett.. 31 (12). pp. 803-806. 1977

[22] L. Goldberg. R. Reedy and S.H. Lee. 'Silicon photodiode for optical channel waveguides'. Appl. Phys. Lett., 37 (2). pp. 195-197. 1980

[23] W.K. Chan and A. Yi-Yan. 'Grafted semiconductor optoelectronics'. J. Quantum Electron.. 27 (3), pp. 717-725. 1991

[24] A. Yi-Yan, W.K. Chan, C.K. Nguyen, T.J. Gmitter. R. Bhat. and J.L. Jackel. '$GaInAs/InP$ *pin* photodetectors integrated with glass waveguide'. Electron. Lett., 27 (1), pp. 87-89, 1991

[25] F.J. Leonberger and S.W. Merritt. 'Technology and applications of commercial $LiNbO_3$ integrated-optic devices', European Conference on Integrated Optics, Delft, 1995

[26] B.N. Gomatam and L.H. Domash, 'Hybrid optoelectronic modulators function without quantum wells', Laser Focus World. pp. 83-86, June 1995

[27] B. Broberg, B.S. Lindgren, M.G. Oberg, and H. Jiang. 'A novel integrated optics wavelength filter in $InGaAsP - InP$', J. Lightwave Technol., 4 (2). pp. 196-203, 1986

[28] A. Ihaya, H. Furuta, and H. Noda, 'Thin-Film Optical Directional Coupler', J. Quantum Electron., 8, pp. 546-547, 1972

[29] R.A. Soref. E. Cortesi. F. Namavar. and L. Friedman. 'Vertically integrated silicon-on-insulator waveguides'. IEEE Photon. Technol. Lett.. 3 (1). pp. 22-24. 1991

[30] G.L. Yip. P.C. Noutsios. and K. Kishioka. 'Characteristics of optical waveguides made by electric-field-assisted K^+-ion exchange in glass'. Opt. Lett.. 15 (14). pp. 789-791. 1990

[31] P.C. Noutsios and G.L. Yip. 'Characterization and modeling of planar surface and buried waveguides made by field-assisted K^+-ion exchange'. Appl. Opt.. 31 (25). pp. 5283-5291, 1992

[32] P.C. Noutsios. G.L. Yip, and J. Albert, 'Novel vertical directional coupler made by field-assisted ion-exchanged slab waveguides', Electron. Lett.. 28 (14). pp. 1340-1342, 1992

[33] G.L. Yip and P.C. Noutsios, 'An improved finite-difference vector beam propagation formulation for graded-index waveguides', IEEE Photon. Technol. Lett.. 6 (4), pp. 543-545, 1994

[34] P.C. Noutsios and G.L. Yip, 'Improved vertical directional coupler for optimum edge coupling to an embedded photodetector'. Opt. Lett.. 20 (21), pp. 2198-2200. 1995

[35] G.L. Yip, P.C. Noutsios, and L. Chen, 'An improved propagation-mode near-field method for refractive index profiling of optical waveguides', accepted by Appl. Opt., Jan. 1996

Chapter 2

Modeling of the Ion-Exchange Process

2.1 Introduction

In this chapter, the theoretical foundations of the ion-exchange process are presented for the purpose of modeling optical waveguide concentration profiles. Section 2.1.1 describes the basic chemical structure of the glass suitable for ion exchange. The kinetics of the process at the microscopic level are detailed and set into a mathematical formulation in Section 2.2. The numerical solutions of the ion-exchange equations for the one and two-dimensional cases are described in the last section of the chapter. These solutions yield the concentration profiles of surface and buried waveguides in both planar and channel form. Although the modelling is quite specific for $K^+ - Na^+$ ion exchange, the methodology is quite general and can be used for other cation pairs and substrate glass.

2.1.1 Structural properties of oxide glass

Glass materials and their related technologies have been known to man since antiquity. The ancient Egyptians and later the Romans developed techniques of making household glass articles [1]. In more recent years, specialty glasses have been made with specific compositions for commercial applications, such as the fabrication of tinted glass for automobiles. Nearly all these glasses are multicomponent compo-

sitions containing a high percentage of silica (SiO_2) and other oxides. These oxide glasses are formed into an amorphous structure whose basic constituents are classified into three types of network molecules [2]. The first type is the network former, such as SiO_2 and GeO_2, that have strong double bonds. The second type is the network intermediate, such as ZnO, that contributes to the strength of the network. Lastly, there are the network modifiers, such as Na_2O, CaO, and K_2O, that are added to the glass to give it some desired surface-mechanical properties. Their respective alkali ions (Na^+, Ca^{++}, K^+) fit into the relatively large voids in the network close to negatively charged non-bridging oxygen atoms, as shown in Fig. 2.1. These modifier ions are attracted rather weakly by ionic bonds to the network and can be replaced quite readily by other ions of the same valence. This replacement, known as ion exchange, can be achieved at sufficiently high temperature by exposing the glass surface to a source of ions from a salt bath (melt) that can occupy the same sites as the modifier ions. Further details of this mechanism will be descibed in the next section.

The multi-component glasses suitable for ion exchange are widely available commercially from companies such as Corning, Schott, and Fisher Scientific. In particular, there are high-quality optical glasses, known as borosilicates, that are named BK7 (from Schott) and Corning 0211. Also, there are good-quality soda-lime silicate glasses available from many companies including Fisher. Both have been quoted widely in the literature [3]. If these substrates are to be used to fabricate good-quality optical waveguides, they must meet some desirable compositional requirements [4]:

- high transparency over a wide wavelength region (0.60 to 1.60 μm) where the low-loss and low-dispersion windows of optical fiber are available
- low optical losses achieved by the removal of foreign impurities, surface defects and any type of inhomogeneity (bubbles, etc.)

Although these commercial glasses have been used by many scientists and engineers, there is yet no standard glass composition agreed upon by manufacturers of waveguide

components. As examples, Corning and IOT Schott fabricate optical glasses suitable for their particular ion-exchange processes. It is interesting to note that this substrate standardization problem does not exist for device manufacturers that use crystalline optical grade substrates, such as $LiNbO_3$ and $LiTaO_3$. The main reason for this may be that the glass IO device companies are also glass manufacturers, making it cheaper for them to use their own substrates, whereas the $LiNbO_3$ device companies are not in the business of growing crystals.

The substrate used in this thesis is the *Fisher*brand microscope slide composed of soda-lime silicate glass. It contains 72 % SiO_2, 14 % sodium oxide (Na_2O), also known as soda, 6 % calcium oxide (CaO), or lime and minor amounts of various oxides including K_2O, Al_2O_3, and MgO, as shown in Table 2.1. (This chemical composition will be looked at again in Chapter 3 along with the instrument used to measure it.) Manufactured by Fisher Scientific, the slide measures 75 mm long, 25 mm wide and 1 mm thick. It has a flame polished surface that is very smooth. The main advantage for using this substrate is its very low cost ($\approx$ \$0.35 per slide) making it ideal for exploratory research in an academic environment. However, it is not of high enough optical quality to be used for the demanding low-loss performance of commercial devices. Another disadvantage is that the manufacturer may change the glass properties without warning. This was experienced first hand in our laboratory with a batch of substrates delivered in January 1995. The measured refractive index of the substrate was found to increase from 1.5125 to 1.5208 at the operating wavelength $\lambda = 0.6328\,\mu m$. Nevertheless, the soda-lime glass slides still provide most of the desirable qualities mentioned earlier making it suitable for university research.

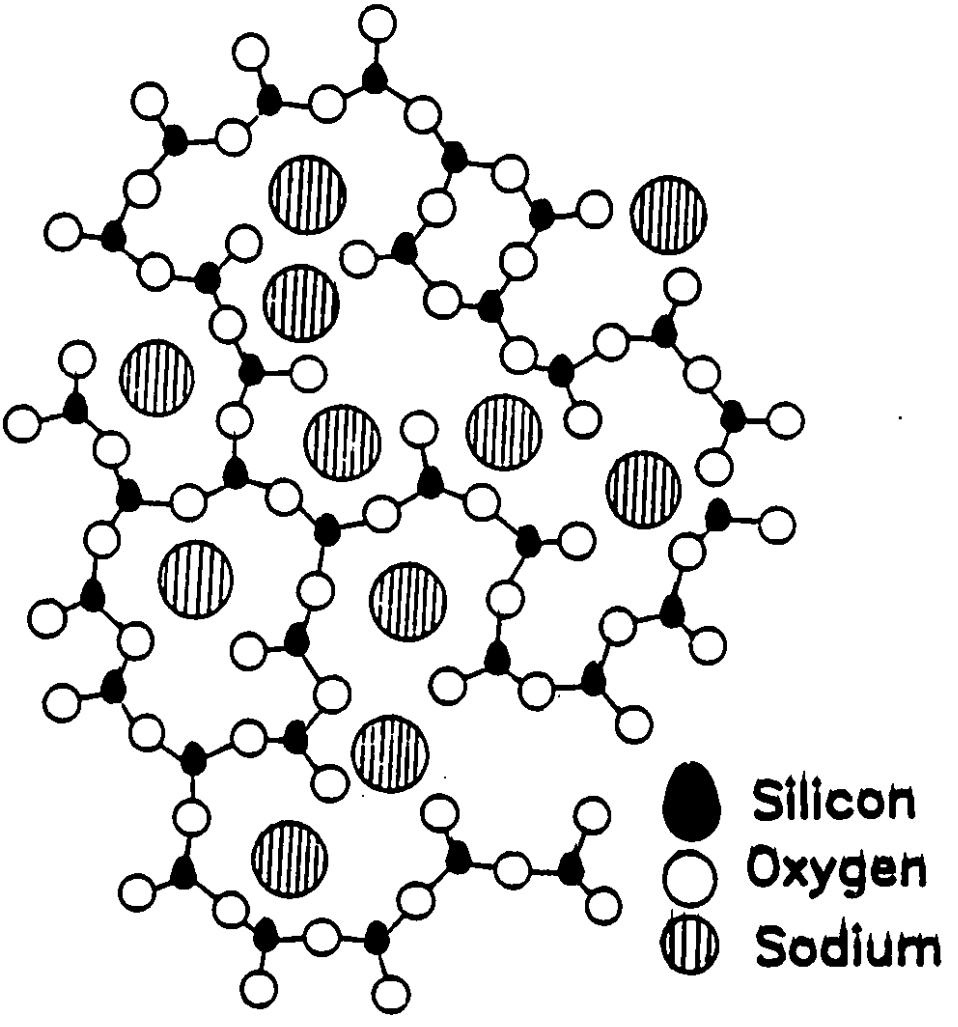

Figure 2.1: Structure of a typical soda-lime glass

Oxide	Substrate glass (weight %)
SiO_2	72.3
Na_2O	14.3
K_2O	1.21
CaO	6.4
Al_2O_3	1.22
MgO	4.31

Table 2.1: Chemical composition of a soda-lime substrate

2.1.2 Ion-exchange kinetics

There are two basic driving mechanisms for ion exchange in glass. The first is due to the thermal agitation of the ions in the glass at high temperatures and the second is due to an externally applied potential difference that is created across the glass causing an ionic current to flow. The former is generally referred to as purely thermal ion exchange and the latter as field-assisted ion exchange. Both processes have been used to fabricate optical waveguide devices in this work.

The purely thermal process proceeds as follows. A glass slide containing Na^+ ions (supplied by Na_2O) is immersed into a salt melt (KNO_3) containing another monovalent ion, such as K^+. At the glass-melt interface, the abundant dopant K^+ ions in the melt "see" the glass as a potassium-free medium and hence, are driven into it by a chemical potential diffusion gradient. Simultaneously, the more mobile Na^+ ions are released into the melt with the K^+ ions replacing them on a one-to-one basis. Actually, there is another force besides the chemical potential at work here. Since potassium and sodium ions have different mobilities, there is a tendency for the smaller Na^+ ions to move faster than the larger K^+ ions, leading to a buildup of electrical charge. There is, however, a gradient in electrical potential along with this charge which acts to slow down the faster Na^+ ions and speed up the slower K^+ ions. Despite the difference in the ion mobilities, the gradient in electrical potential forces the fluxes of the two ions to be equal and opposite thus preserving charge neutrality [5]. In this purely thermal ion exchange, the enriched K^+-ion waveguiding layer is formed on both sides of the substrate, as shown in Fig. 2.2(a).

In the field-assisted case, a potential difference is setup between two melts on either side of the glass that are in contact with the electrodes. When a positive dc electric field is applied, a positive flux of the ions is created. As shown in Fig. 2.2(b), these ions are forced to move in the same direction as the electric field creating a waveguiding layer only on the substrate side facing the positive electrode. To avoid

space-charge buildup, the sum of the ionic fluxes produces a net positive ionic flux with magnitude J_o which is a constant function of position [6]. As in the purely thermal case, the temperature is high enough for ion exchange to occur and hence, there is also a thermal contribution to the field-assisted process.

For two-dimensional (2-D) surface channel waveguides, the purely thermal process is now limited to a narrow opening defined by masking part of the substrate prior to ion exchange. Evaporated aluminum (Al), about $0.2\,\mu m$ thick, was used as the masking material. It is not susceptible to deterioration by the ionic melts and hence, it blocks ion exchange to the rest of the substrate. The resulting 2-D concentration profile has a semi-elliptical shape with lateral dimensions that exceed the width of the mask opening, W, by about twice the exchange depth [2]. This creates difficulties for efficient coupling to optical fibers that have circular symmetry. For field-assisted 2-D exchange, this lateral spreading is further amplified by the quasi-static field lines [7] that emanate from the mask opening and extend to the other side of the substrate. Hence, to minimize lateral spreading, this field-assisted process was avoided for surface channel guide formation. Instead, the purely thermal K^+-ion exchange process was used. For buried channel guide formation, the Al was etched away completely and the above surface channel guide was then field-assisted ion-exchanged in a $NaNO_3$ melt over its entire surface [8]. In this manner, the K^+-ion region is moved deeper into the substrate. Further, the electric field lines are straight and the resulting buried channel guides have improved symmetry. Further experimental details will be given in the Chapters 3 and 5.

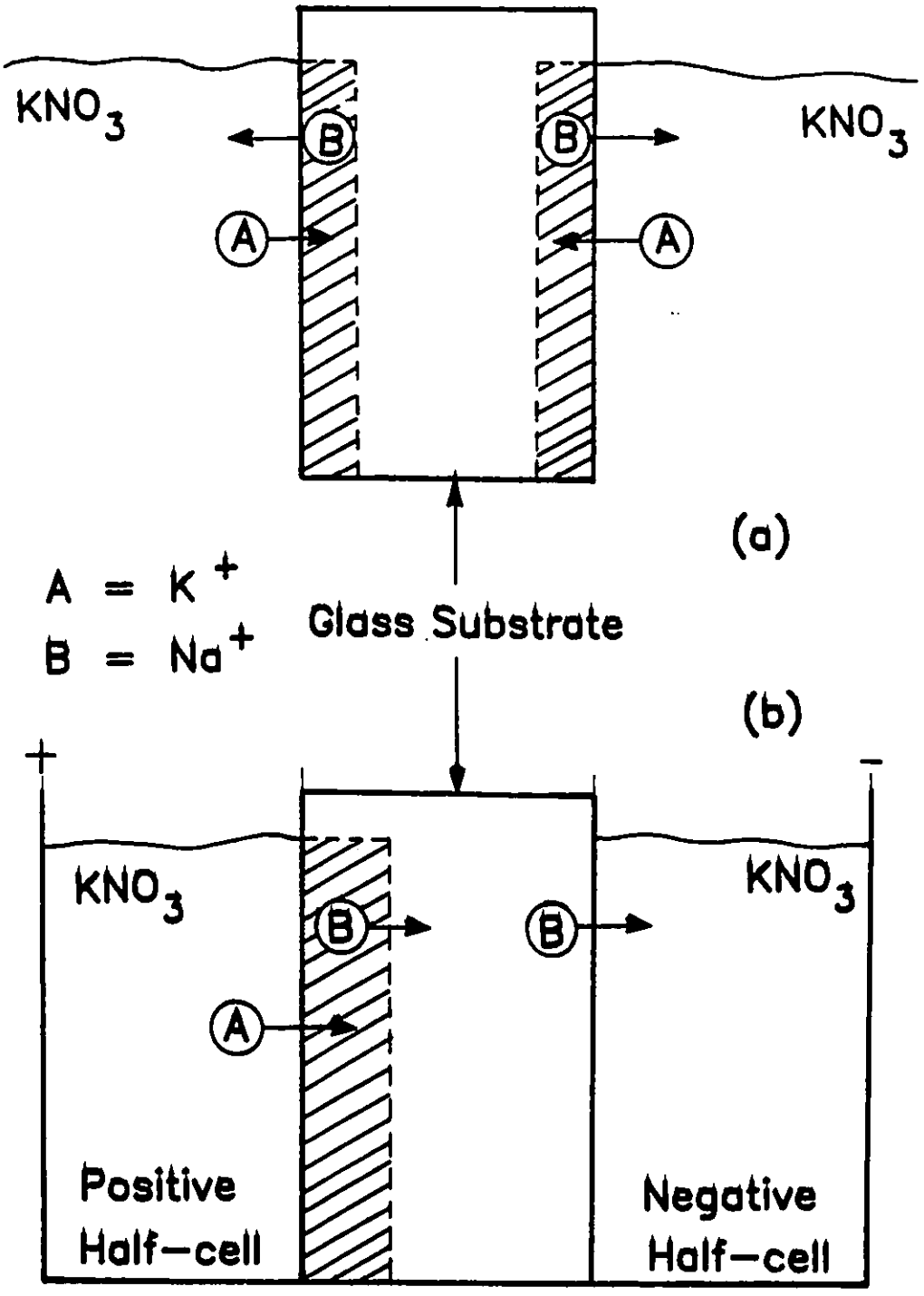

Figure 2.2: Diagram showing the process for (a) purely thermal ion exchange and (b) field-assisted exchange

2.2 Derivation of the ion-exchange equation

In the previous section, a qualitative understanding of the ion-exchange mechanism was developed. The objective of this section is to cast this knowledge into mathematical equations that can be solved numerically and be used to model the dopant concentration profiles which are assumed proportional to the waveguide refractive index profiles. The general field-assisted ion-exchange equation will be derived and the purely thermal equation will be shown to be a special case.

The change in the concentration, c, defined as the number of ions per unit volume, of a given cation is related to the flux of ions $\vec{J}$ by:

$$\frac{\partial c}{\partial t} = -\vec{\nabla} \cdot \vec{J} \tag{2.1}$$

The ionic species are assumed to diffuse isotropically in the $x - y$ domain and the flux obeys Fick's first law of diffusion

$$\vec{J} = -D\vec{\nabla}c = -D\frac{\partial c}{\partial x}\hat{a}_x - D\frac{\partial c}{\partial y}\hat{a}_y \tag{2.2}$$

where D, the diffusion coefficient, is dependent upon c and the fabrication conditions. Substituting (2.2) into (2.1), we get Fick's second law:

$$\frac{\partial c}{\partial t} = \vec{\nabla} \cdot (D\vec{\nabla}c) = \frac{\partial}{\partial x}\left(D\frac{\partial c}{\partial x}\right) + \frac{\partial}{\partial y}\left(D\frac{\partial c}{\partial y}\right)$$

which can be solved for c, given appropriate initial and boundary conditions.

As mentioned in the previous section, there exist two forces that act on the exchanging species. The first is due to the gradient in chemical potential. The other is due to the presence of gradients in electrical potential, one arising intrinsically, $\vec{E}_i$, and the other being applied externally, $\vec{E}_a$. The contribution of the total electric field, $\vec{E}_t = \vec{E}_i + \vec{E}_a$, to the flux is determined as follows. Consider the ratio of the speed of the ions to the magnitude of $\vec{E}_t$ given by the mobility μ,

$$v = \mu E_t \quad (\mu m/min) \tag{2.3}$$

and, according to the Nerst-Einstein definition, the mobility is related to the self-diffusion coefficient, D_K, by:

$$\mu_K = \frac{eD_K}{k_B T} \quad (\mu m^2/V\,min) \tag{2.4}$$

where e is the elementary charge (1.602×10^{-19} Coul), k_B is the Boltzmann constant ($1.381 \times 10^{-23} J/^oK$), and T is the temperature in ^oK. In most glasses, however, the purely thermal migration process is slightly different from the electric field induced transport and (2.4) is not obeyed [3]. Instead, the relation between D_K and μ_K is written as

$$\mu_K = \frac{eD_K}{f k_B T} \tag{2.5}$$

where f is the correlation factor whose value depends on the glass composition [9]. Then,

$$J = cv = c\frac{eD_K}{f k_B T} E_l \tag{2.6}$$

Using (2.2) and (2.5), the total fluxes of the ions become

$$\vec{J}_K = -D_K \vec{\nabla} c_K + \mu_K c_K \vec{E}_l \tag{2.7}$$

$$\vec{J}_{Na} = -D_{Na} \vec{\nabla} c_{Na} + \mu_{Na} c_{Na} \vec{E}_l \tag{2.8}$$

As mentioned previously, the net flux, $\vec{J}_o$, must be constant across the substrate to maintain the neutrality of the glass. Hence,

$$\begin{aligned} \vec{J}_{Na} + \vec{J}_K &= \vec{J}_o = \frac{I}{F_c} \\ \vec{\nabla} \cdot (\vec{J}_K + \vec{J}_{Na}) &= 0 \end{aligned} \tag{2.9}$$

where I is the measured ion current density (mA/mm^2) and F_c is Faraday's constant or 96500 Coul/mole. Also, since the K^+ ions replace the Na^+ ions on a one-to-one basis, the total ion concentrations remain equal to c_o, the concentration of Na^+ ions present in the glass prior to the exchange. Thus,

$$c_K + c_{Na} = c_o = constant \tag{2.10}$$

Defining $\hat{c}_K = c_K/c_o$, $\hat{c}_{Na} = c_{Na}/c_o = 1 - \hat{c}_K$, then

$$\vec{\nabla} \cdot \hat{c}_K = -\vec{\nabla} \cdot \hat{c}_{Na}$$

Substituting (2.7) and (2.8) into (2.9), we get

$$\frac{\vec{J}_o}{c_o} = \mu_K \hat{c}_K \vec{E}_t - D_K \vec{\nabla} \hat{c}_K - D_{Na} \vec{\nabla} \hat{c}_{Na} + \mu_{Na} \hat{c}_{Na} \vec{E}_t \tag{2.11}$$

After a few simple algebraic manipulations,

$$\frac{\vec{J}_o}{c_o D_{Na}} = \frac{e\vec{E}_t}{fk_BT}\left[1 - \left(1 - \frac{D_K}{D_{Na}}\right)\hat{c}_K\right] + \left(1 - \frac{D_K}{D_{Na}}\right)\vec{\nabla}\hat{c}_K$$

and upon letting $\alpha = 1 - D_K/D_{Na} = 1 - \mu_K/\mu_{Na}$, one obtains an expression for the total electric field

$$\vec{E}_t = \vec{E}_a + \vec{E}_i = \frac{fk_BT}{e}\left\{\frac{\vec{J}_o}{c_o D_{Na}(1 - \alpha\hat{c}_K)} - \frac{\alpha\vec{\nabla}\hat{c}_K}{1 - \alpha\hat{c}_K}\right\} \tag{2.12}$$

The externally applied field is

$$\vec{E}_a = \frac{\vec{J}_o}{c_o \mu_{Na}(1 - \alpha\hat{c}_K)} \tag{2.13}$$

using (2.5) for sodium ions. Note that the total field depends on the total flux density $\vec{J}_o$, the concentration c_o and the gradient in chemical potential. This expression explicitly shows that when there is no externally applied field (i.e. the net flux $J_o = 0$), the intrinsic field, E_i is still present. As mentioned, this field arises naturally due to the unequal diffusion rates of the ionic species ($\alpha \neq 0$) and, in particular for $K^+ - Na^+$ exchange, $\vec{E}_i$ depends on α.

Using the equation of continuity (2.1) and (2.7) for $\vec{J}_K$ yields[1]

$$\frac{\partial \hat{c}_K}{\partial t} + \vec{\nabla} \cdot \left(\mu_K \hat{c}_K \vec{E}_t - D_K \vec{\nabla} \hat{c}_K\right) = 0$$

$$\frac{\partial \hat{c}_K}{\partial t} + \mu_K \left(\hat{c}_K \vec{\nabla} \cdot \vec{E}_t + \vec{\nabla}\hat{c}_K \cdot \vec{E}_t\right) = D_K \vec{\nabla}^2 \hat{c}_K$$

The divergence of the total field is deduced from (2.12) to be:

$$\vec{\nabla} \cdot \vec{E}_t = \frac{fk_BT}{e}\left\{\frac{\alpha\vec{\nabla}\hat{c}_K \cdot \vec{J}_o}{c_o D_{Na}(1 - \alpha\hat{c}_K)^2} - \frac{\alpha\vec{\nabla}^2\hat{c}_K}{1 - \alpha\hat{c}_K} - \frac{\alpha^2\vec{\nabla}\hat{c}_K \cdot \vec{\nabla}\hat{c}_K}{(1 - \alpha\hat{c}_K)^2}\right\}$$

[1]The vector identity $\vec{\nabla} \cdot (\hat{c}_K \vec{E}_t) = \hat{c}_K \vec{\nabla} \cdot \vec{E}_t + \vec{\nabla}\hat{c}_K \cdot \vec{E}_t$ is used.

and one obtains, after a few manipulations,

$$\frac{\partial \hat{c}_K}{\partial t} = \frac{D_K}{1-\alpha\hat{c}_K}\left\{\vec{\nabla}^2\hat{c}_K + \frac{\alpha\vec{\nabla}\hat{c}_K\cdot\vec{\nabla}\hat{c}_K}{1-\alpha\hat{c}_K} - \frac{\vec{\nabla}\hat{c}_K\cdot\vec{J}_o}{c_o D_{Na}(1-\alpha\hat{c}_K)}\right\}$$

Now, since

$$\vec{\nabla}\cdot\left(\frac{D_K}{1-\alpha\hat{c}_K}\vec{\nabla}\hat{c}_K\right) = \frac{D_K}{1-\alpha\hat{c}_K}\left(\vec{\nabla}^2\hat{c}_K + \frac{\alpha}{1-\alpha\hat{c}_K}\vec{\nabla}\hat{c}_K\cdot\vec{\nabla}\hat{c}_K\right) \tag{2.14}$$

then the nonlinear partial differential equation describing the general ion-exchange process is

$$\frac{\partial \hat{c}_K}{\partial t} = \vec{\nabla}\cdot\left(\frac{D_K}{1-\alpha\hat{c}_K}\vec{\nabla}\hat{c}_K\right) - \frac{(1-\alpha)\vec{\nabla}\hat{c}_K\cdot\vec{J}_o}{c_o(1-\alpha\hat{c}_K)^2} \tag{2.15}$$

An alternative expression for the above equation can be deduced by incorporating (2.13), so that it becomes independent of the current density J_o:

$$\frac{\partial \hat{c}_K}{\partial t} = \vec{\nabla}\cdot\left(\frac{D_K}{1-\alpha\hat{c}_K}\vec{\nabla}\hat{c}_K\right) - \frac{\mu_K\vec{E}_a\cdot\vec{\nabla}\hat{c}_K}{(1-\alpha\hat{c}_K)} \tag{2.16}$$

Equation (2.15) is used to model current-controlled ion exchange [10] whereas (2.16) is used for voltage-controlled field-assisted ion exchange. Finally, in the case of purely thermal ion exchange, when $J_o = 0$ or $E_a = 0$, the equation becomes:

$$\frac{\partial \hat{c}_K}{\partial t} = \vec{\nabla}\cdot\left(\frac{D_K}{1-\alpha\hat{c}_K}\vec{\nabla}\hat{c}_K\right) \tag{2.17}$$

2.3 Solution of the ion-exchange equations

2.3.1 One-dimensional solutions: planar waveguides

Planar (or slab) waveguides are made by ion exchange without any mask and hence, the process is one-dimensional along the depth direction, x. The gradient terms involve only partial derivatives with respect to x, and (2.16) becomes:

$$\frac{\partial \hat{c}_K}{\partial t} = \frac{\partial}{\partial x}\left(\frac{D_K}{1-\alpha\hat{c}_K}\frac{\partial \hat{c}_K}{\partial x}\right) - \frac{\mu_K E_a}{1-\alpha\hat{c}_K}\frac{\partial \hat{c}_K}{\partial x} \tag{2.18}$$

This nonlinear parabolic partial differential equation (PDE) is second order in the spatial variable x and first order in the time variable t. Hence, it requires two boundary conditions in x and an initial condition in t to be solved uniquely. At time $t = 0$,

there are no K^+ ions in the glass so that

$$\hat{c}_K(x,0) = 0. \tag{2.19}$$

For the boundary conditions, a zero concentration at infinity (i.e. far into the substrate to the right) is expected, while at the surface, a constant value of concentration represents the effect of the KNO_3 melt providing K^+ ions for ion exchange. It was observed that for $K^+ - Na^+$ exchange, the maximum concentration of the exchanged ions is about 90% of the total concentration of available Na^+ sites [11, 12], so that

$$\begin{aligned} \hat{c}_K(0,t) &= c_K(0,t)/c_o = h_K = 0.9 \\ \hat{c}_K(\infty,t) &= 0. \end{aligned} \tag{2.20}$$

Note that with $c_o = c_{Na}(0,0)$, one boundary condition becomes

$$c_K(0,t) = h_K c_{Na}(0,0). \tag{2.21}$$

Since there are negligible amounts of K^+ ions in the substrate prior to exchange, then $c_K(0,0) = 0$. Hence, (2.21) is valid only for $t > 0$ and it takes a finite amount of time for the surface concentration to reach its final equilibrium value. This point will be discussed further in Chapter 5 in the context of EPMA surface concentration measurements of single-mode waveguides.

With these conditions, it is convenient to renormalize $\hat{c}_K$ so that $\hat{c} = \hat{c}_K/h_K$ and the boundary conditions become

$$\hat{c}(0,t) = 1 \ , \ \hat{c}(\infty,t) = 0. \tag{2.22}$$

Hence, (2.18) becomes

$$\frac{\partial \hat{c}}{\partial t} = \frac{\partial}{\partial x}\left(\frac{D_K}{1-\hat{\alpha}\hat{c}}\frac{\partial \hat{c}}{\partial x}\right) - \frac{\mu_K E_a}{1-\hat{\alpha}\hat{c}}\frac{\partial \hat{c}}{\partial x} \tag{2.23}$$

with $\hat{\alpha} = \alpha h_K$. To simplify the numerical procedure, the following transformation is made [13]

$$g = \ln(1 - \hat{\alpha}\hat{c}) \tag{2.24}$$

$$\frac{\partial g}{\partial x} = \frac{-\hat{\alpha}}{1-\hat{\alpha}\hat{c}}\frac{\partial \hat{c}}{\partial x} = -\hat{\alpha}\exp(-g)\frac{\partial \hat{c}}{\partial x}$$

and with similar expresions for $\partial g/\partial t$, we get

$$\frac{\partial g}{\partial t} = \exp(-g)\left\{D_K\frac{\partial^2 g}{\partial x^2} - \mu_K E_a\frac{\partial g}{\partial x}\right\} \tag{2.25}$$

The initial and boundary conditions are the same as those in (2.19) and (2.20), except that, in terms of g, they become:

$$\begin{aligned} g(x,0) &= \ln(1-\hat{\alpha}\hat{c}(x,0)) = 0 \\ g(0,t) &= \ln(1-\hat{\alpha}\hat{c}(0,t)) = \ln(1-\hat{\alpha}) \\ g(\infty,t) &= \ln(1-\hat{\alpha}\hat{c}(\infty,t)) = 0 \end{aligned}$$

The numerical solution of (2.25) is based on an explicit finite-difference (FD) scheme with conditional stability. The partial derivatives are expressed as:

$$\frac{\partial g}{\partial t} = \frac{g_i^{k+1} - g_i^k}{\Delta t} \quad , \frac{\partial g}{\partial x} = \frac{g_{i+1}^k - g_{i-1}^k}{2\Delta x} \tag{2.26}$$

and

$$\frac{\partial^2 g}{\partial x^2} = \frac{g_{i+1}^k - 2g_i^k + g_{i-1}^k}{(\Delta x)^2} \tag{2.27}$$

The solution at the next step g_i^{k+1} becomes:

$$g_i^{k+1} = g_i^k + \Delta t\exp(-g_i^k)\left\{D_K\left(\frac{g_{i+1}^k - 2g_i^k + g_{i-1}^k}{(\Delta x)^2}\right) - \mu_K E_a\frac{(g_{i+1}^k - g_{i-1}^k)}{2\Delta x}\right\} \tag{2.28}$$

The calculation proceeds as follows: first the matrix g_i^k is initialized with zeroes, except at the boundary $x = 0$ where the values are fixed at $\ln(1-\hat{\alpha})$. Note again that $g_o^o = 0$. Then, the values of g_i^1 are calculated using (2.28). This solution replaces g_i^k and the process is repeated for another time step until the desired time has been reached.

As mentioned earlier, the numerical stability of this explicit scheme is conditional. The criterion for Δt can be determined using a standard von Neumann stability analysis [14]. The details are outlined in the Appendix. It is shown that for stability:

$$\Delta t \leq \frac{2D_K(1-\hat{\alpha}\hat{c})(\Delta x)^2}{4D_K^2 + (\mu_K E_a \Delta x)^2} \tag{2.29}$$

By assuming $c = 1$, we obtain a lower bound for Δt. Using typical values of $\hat{\alpha} = 0.898$, $D_K = 0.06429\,\mu m^2/min$, $\mu_K = 20.925\,\mu m^2/V min$, $\Delta x = 0.02\,\mu m$ and $E_a = 0.02\,V/\mu m$, we obtain $\Delta t = 3 \times 10^{-4} min$. Other values for Δt in the range of 10^{-4} were also tried to achieve stability.

An example of a field-assisted ion-exchanged concentration profile is shown in Fig. 2.3 for $E_a = 9.3\,V/mm$, $t = 10\,min$ and $T = 385°C$. Note the Fermi-like nature of the profile with the diffusion depth d located at the half-point of the profile. The values $\hat{\alpha} = 0.898$, $D_K = 0.06429\,\mu m^2/min$, and $\mu_K = 20.925\,\mu m^2/V min$ were used. The diffusion coefficients and mobility values are obtained from optical characterizations to be discussed in Chapter 5. In addition to the field-assisted exchange, a subsequent cooling process, required to avoid substrate cracking, was carried out [15]. During the $10\,min$ cooling time, the temperature T decayes exponentially, with the average measurements yielding $379°C$, corresponding to $D_K = 0.0544 \mu m^2/min$. Here, (2.28) was solved for $t = 10\,min$ with $E_a = 0$ using the first-step exchange concentration profile as the initial condition and (2.22) as the boundary condition. All the other parameters (Δx etc.) remained the same.

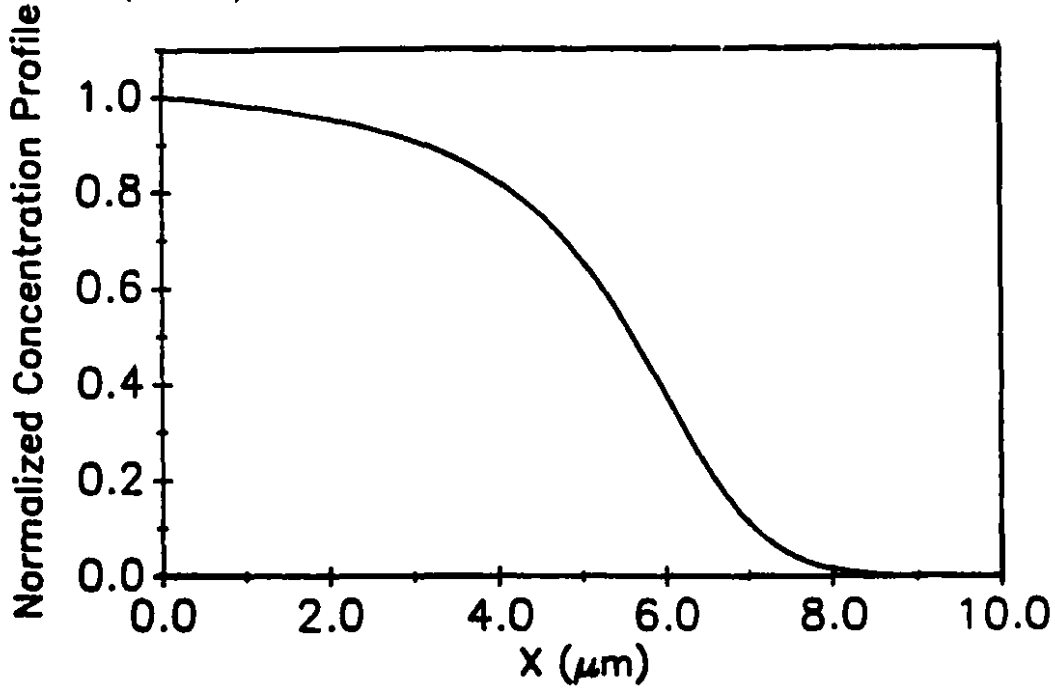

Figure 2.3: Numerical solution for a planar field-assisted ion-exchanged waveguide

2.3.2 Two-dimensional solutions: channel waveguides

The purely thermal ion-exchange process was used to make surface channel guides. Starting from (2.17) and using $c = \hat{c}_K/c_l$ and $\hat{\alpha} = \alpha c_l$, we have

$$\frac{\partial c}{\partial t} = \frac{\partial}{\partial x}\left(\frac{D_K}{1-\hat{\alpha}c}\frac{\partial c}{\partial x}\right) + \frac{\partial}{\partial y}\left(\frac{D_K}{1-\hat{\alpha}c}\frac{\partial c}{\partial y}\right) \tag{2.30}$$

Using the same transformation as in (2.24), we arrive at:

$$\frac{\partial g}{\partial t} = \exp(-g)D_K\left(\frac{\partial^2 g}{\partial x^2} + \frac{\partial^2 g}{\partial y^2}\right) \tag{2.31}$$

Equation (2.31) is solved numerically using the FD explicit method on a 2-D rectangular grid, as shown in Fig. 2.4(a). The time-independent boundary conditions are:

$$\begin{aligned} c(0,y,t) &= 1, \quad |y| \le W/2 \\ \frac{\partial c}{\partial x}(0,y,t) &= 0, \quad |y| > W/2 \end{aligned} \tag{2.32}$$

and all other boundaries are chosen to be far away so that c can be fixed at zero there. Note that since no flux is possible in the x-direction at $x = 0$, due to the presence of the mask, this means that $\partial c/\partial x = 0$. Initially, at $t = 0$, there are no K^+ ions in the glass and $c(x,y,0) = 0$. In terms of g, the initial and boundary conditions become:

$$\begin{aligned} g(0,y,t) &= \ln(1-\hat{\alpha}), \quad |y| \le W/2 \\ \frac{\partial g}{\partial x}(0,y,t) &= 0, \quad |y| > W/2 \\ g(\infty,y,t) &= 0 \\ g(x,\pm\infty,t) &= 0 \\ g(x,y,0) &= 0 \end{aligned} \tag{2.33}$$

To save computing time, the numerical solutions are computed for only the positive half of the spatial domain since the resulting concentration profile is symmetric about $y = 0$. Thus, an additional boundary condition is implemented at $y = 0$:

$$\frac{\partial c}{\partial y}(x,0,t) = 0 = \frac{\partial g}{\partial y}(x,0,t) \tag{2.34}$$

The finite differences that correspond to the above partial derivatives are:

$$\begin{aligned}
\frac{\partial g}{\partial t} &= \frac{g_{i,j}^{k+1} - g_{i,j}^{k}}{\Delta t} \\
\frac{\partial g}{\partial x} &= \frac{g_{i+1,j}^{k} - g_{i-1,j}^{k}}{2\Delta x} \\
\frac{\partial g}{\partial y} &= \frac{g_{i,j+1}^{k} - g_{i,j-1}^{k}}{2\Delta y} \\
\frac{\partial^2 g}{\partial x^2} &= \frac{g_{i+1,j}^{k} - 2g_{i,j}^{k} + g_{i-1,j}^{k}}{(\Delta x)^2} \\
\frac{\partial^2 g}{\partial y^2} &= \frac{g_{i,j+1}^{k} - 2g_{i,j}^{k} + g_{i,j-1}^{k}}{(\Delta y)^2}
\end{aligned} \tag{2.35}$$

The above equations are plugged back into (2.31) to determine the values of $g_{i,j}^{k-1}$ in terms of $g_{i,j}^{k}$ for $i = 0, ...M1$, $j = 0...N1$, and $k = 0. ...L1$. The calculation procedure begins by initializing $g_{i,j}^{0}$ with zero except at the unmasked surface ($i = 0$) where the values are fixed at $\ln(1 - \hat{\alpha})$. Due to the symmetry condition at $y = 0$ ($j = 0$), $g_{i,1}^{0} = g_{i,-1}^{0}$ and $\partial^2 g/\partial y^2$ becomes $2(g_{i,1}^{0} - g_{i,0}^{0})/(\Delta y)^2$. Similarly, under the masked areas at $x = 0$ ($i = 0$), $g_{1,j}^{0} = g_{-1,j}^{0}$ and $\partial^2 g/\partial x^2$ becomes $2(g_{1,j}^{0} - g_{0,j}^{0})/(\Delta x)^2$. All the other interior points for $g_{i,j}^{k+1}$ are calculated explicitly. Then, these values replace those of $g_{i,j}^{k}$ and the process is repeated.

A typical simulation is shown in Fig. 2.5 for $t = 20\,min$, $W = 4.0\,\mu m$, $\hat{\alpha} = 0.898$ and $D_K = 0.01174\,\mu m^2/min$. The spatial dimensions are $X_{max} = 10\,\mu m$ and $Y_{max} = 5\,\mu m$ with the rectangular grid sizes $\Delta x = 0.02\,\mu m$ and $\Delta y = 0.2\,\mu m$. The stability criterion for Δt is chosen to be $4\,s$. The contour plot of Fig. 2.4 was drawn using the commercially available MATLAB software. Note the appreciable side diffusion that occurs under the mask's surface (i.e. $|y| > 2\,\mu m$).

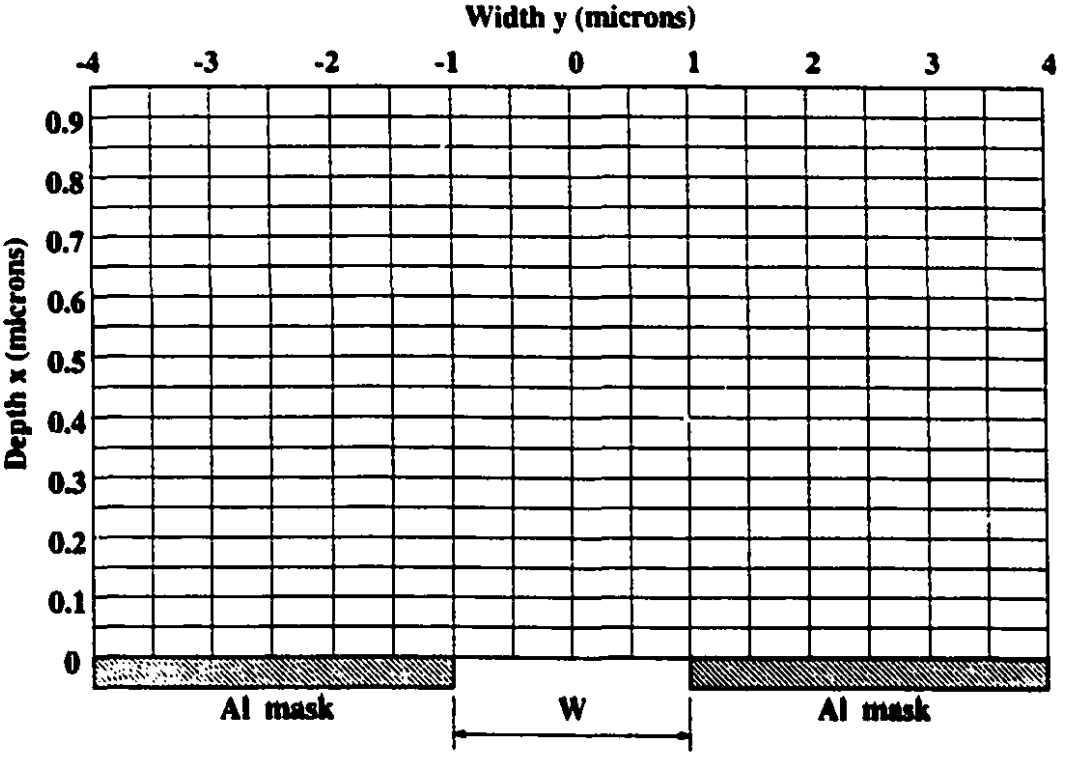

Figure 2.4: Rectangular grid for the calculation of channel waveguide profiles

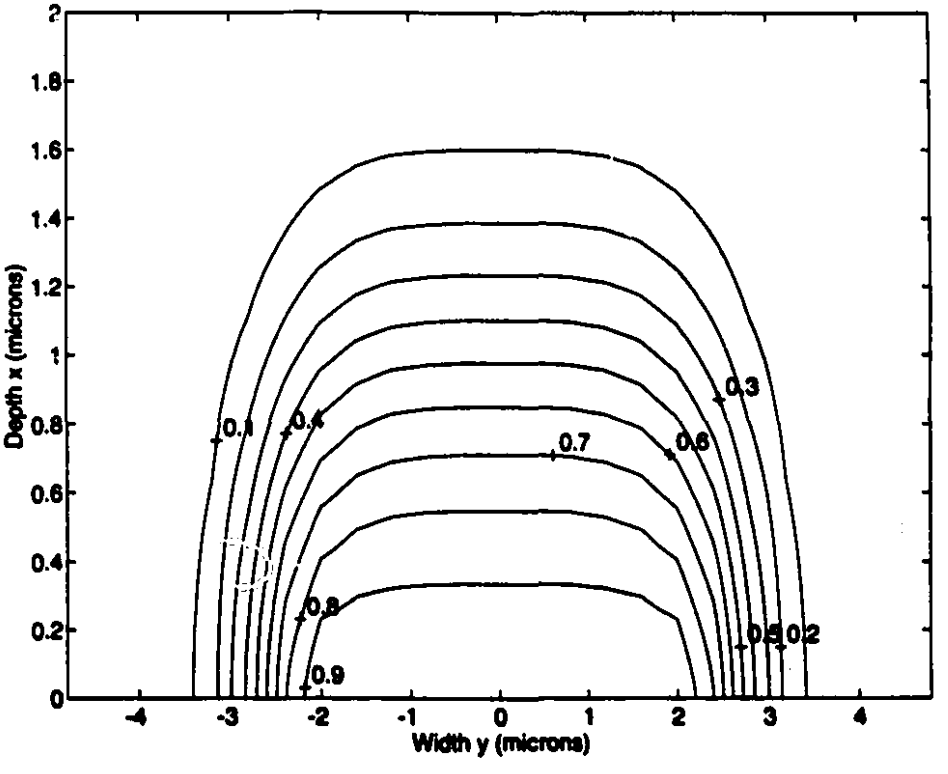

Figure 2.5: Contour plot of surface channel guide profile, $t_1 = 20\,min.$, $W = 4.0\,\mu m$ at $T = 385°C$

2.3.3 The backdiffusion process: buried waveguides

As mentioned in Chapter 1, backdiffusion has become an important fabrication process in the manufacturing of buried optical waveguides. In this technique, a sample with the first exchange surface K^+-ion concentration profile is introduced into a pure melt of $NaNO_3$ for a diffusion time t_2 and applied field E_{a2}. To model this process mathematically for planar waveguides, it is necessary to solve (2.25) and to modify the initial and boundary conditions. The first exchange concentration at time t_1 and applied field E_{a1} are now used as the initial conditions for backdiffusion. In addition, since it is assumed that there are no potassium ions in the $NaNO_3$ melt, the boundary condition is zero at $x = 0$. Hence, $g_0^{k-1} = g_0^k = g_0^{k+1} = 0.0$ and g_i^0 is determined from the numerical solution of the first exchange.

For buried channel guides, the first exchange 2-D profile arises from a purely thermal exchange through a mask opening followed by a second field-assisted exchange in $NaNO_3$ over the whole surface. Mathematically, this corresponds to solving (2.31) for the concentration c for time t_1 and then using c as the initial condition to solve (2.16) with $\vec{E}_{a2} = E_{a2}\hat{a}_x$:

$$\frac{\partial c}{\partial t} = \frac{\partial}{\partial x}\left(\frac{D_K}{1-\hat{\alpha}c}\frac{\partial c}{\partial x}\right) + \frac{\partial}{\partial y}\left(\frac{D_K}{1-\hat{\alpha}c}\frac{\partial c}{\partial y}\right) - \frac{\mu_K E_{a2}}{1-\hat{\alpha}c}\frac{\partial c}{\partial x} \qquad (2.36)$$

Similarly to the planar case, the surface boundary condition $c(0, y, t) = 0$.

For the planar case, profiles are calculated at $E_{a1} = 18.3\,V/mm$, $t_1 = 5\,s$, $E_{a2} = 94.7\,V/mm$, and $t_2 = 100$ and $140\,s$. In this case, we used $\hat{\alpha} = 0.2994$, $D_K = 0.06429\,\mu m^2/min$, and $g_0^k = 0.03$ for reasons to be discussed in a Chapter 5. The cooling effect was included in the simulations after each field-assist process. Figure 2.6 shows the evolution of the buried concentration profile as its concentration peak, located at $x = x_{peak}$, moves deeper into the substrate with increasing t_2. For the channel case, Fig. 2.7 shows a contour plot of a buried guide with $t_2 = 2\,min$, $E_{a2} = 98.5\,V/mm$, $\hat{\alpha} = 0.898$, $D_K = 0.06429\,\mu m^2/min$, and $g_0^k = 0.03$ using the initial conditions quoted in Fig. 2.5 and a cooling simulation as described above.

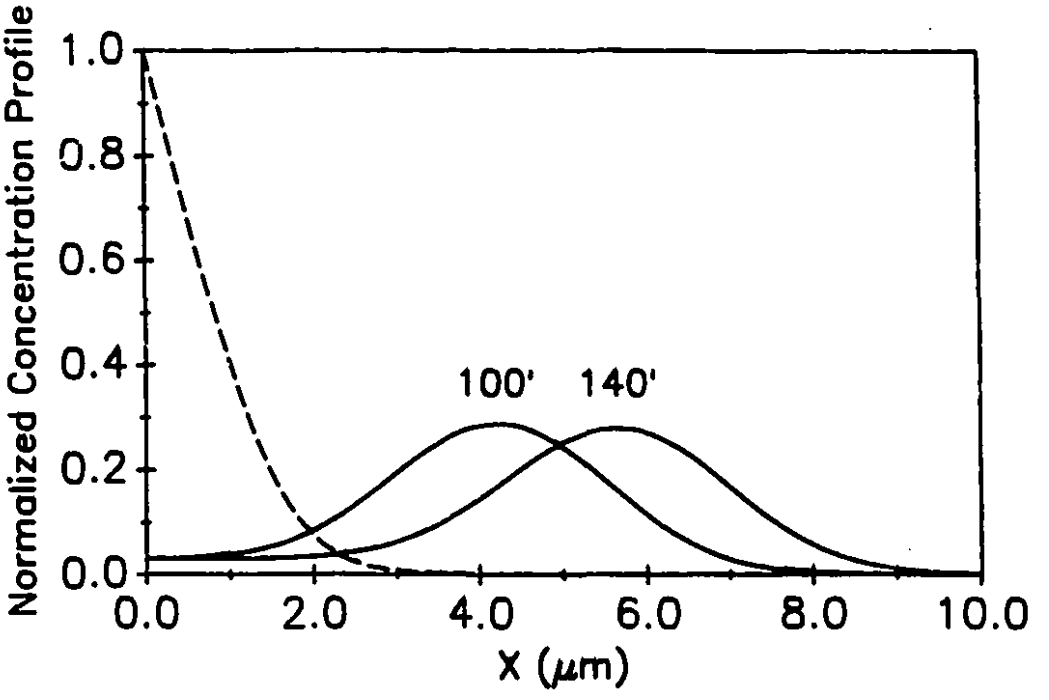

Figure 2.6: Evolution of planar buried concentration profile (solid line) for $t_2 = 100$ and $140\,s$. The initial surface guide (dashed line) is made with $E_{a1} = 18.3\,V/mm$ and $t_1 = 5\,s$

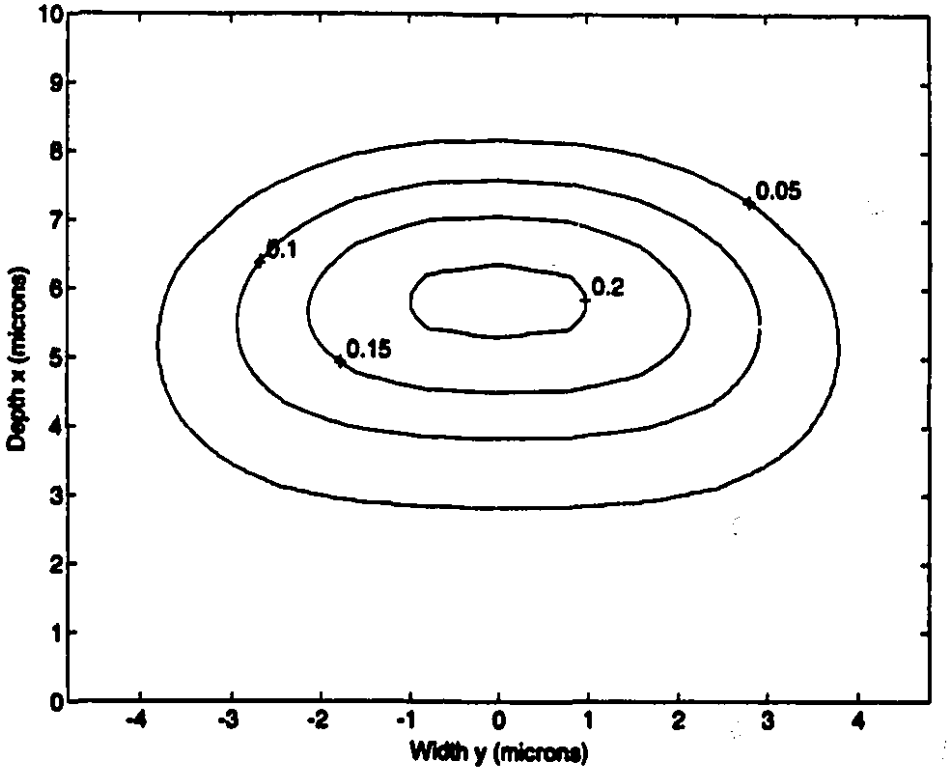

Figure 2.7: Contour plot of buried channel guide profile with $t_2 = 2\,min$, $E_{a2} = 98.5\,V/mm$ at $T = 385°C$

2.4 Conclusions and discussions

Before leaving this chapter, it is worth noting that the equations developed thus far provide us with a theoretical model that is valid only under certain approximations. Although this model takes into account most of the factors affecting the ion-exchange process, there are a few physical phenomena that are not included. These consist of the space charge effect, the mixed alkali effect and the charge depletion observed under the masked areas. Fortunately, as we shall see, these effects do not play any significant role in the modelling of planar and channel K^+-ion exchanged waveguides.

The space charge neutrality conditions expressed in (2.9) and (2.10) are valid only when the local space charge is small. Strictly speaking, the electric field and the ion concentrations should be related via Poisson's equation [3, 16]:

$$\vec{\nabla} \cdot (\epsilon \vec{E}_t) = \rho \tag{2.37}$$

where the local space charge density is:

$$\rho = e(c_K + c_{Na} - c_a) \tag{2.38}$$

For some cases when the change in the dielectric constant ϵ due to ion exchange is very small, (2.37) is replaced by [3]

$$\vec{\nabla} \cdot \vec{E}_t = \frac{\rho}{\epsilon} \tag{2.39}$$

and hence, the space charge neutrality condition becomes:

$$c_K + c_{Na} - c_a = \frac{\rho}{e} = \frac{\epsilon \vec{\nabla} \cdot \vec{E}_t}{e} \tag{2.40}$$

This topic was dealt with recently in a paper by Oven *et al* who showed that the approximate space charge condition (2.10) is still valid for field-assisted ion-exchange over a wide range of fabrication conditions [17]. Their conclusions were based on data of silver-film diffused into soda-lime glass [18] and on our own data for field-assisted K^+-ion exchange [15] to be presented in Chapter 5.

The mixed-alkali or double-alkali effect is basically the reduction in the self-diffusion coefficient of the original alkali ion when a second alkali is added to the glass. This results in a concentration dependence of the self-diffusion coefficients and is believed to be significant only when the size difference between the exchanging ions is large. For example, in $Cs^+ - Na^+$ exchange, this effect has shown to have considerable influence on the diffusion profile [19]. However, for $K^+ - Na^+$ exchange, this effect has not been shown to be significant. In fact, Doremus showed that the diffusion profile modelled with constant diffusion coefficients showed better agreement to experiments than that modelled by the mixed-alkali effect [20].

Finally, there have been some recent experimental findings on the effect of masking films on field-assisted ion-exchange in soda-lime glass [21]. When the first process is a field-assisted exchange, it was found that in the regions under a metal mask, there is a depletion of Na^+ ions that arises from the applied electric field between the metal masking film and the melt (in the negative cell) that acts to drive the mobile Na^+ ions away from these regions. Owing to the extraction of the sodium ions, some structural changes appear in the depleted glass layer that totally inhibits the ability for a second ion exchange. However, this blocking effect is not established in the case of purely thermal ion exchange in the first step or when a dielectric mask is used since the electric field in these cases is too small to form the Na^+ depleted layer. For the purposes of modelling buried channel waveguides presented in this chapter, this depletion layer does not pose any problem since a purely thermal process was used in the first step.

In summary, the theoretical model needed to establish the concentration profiles of planar and channel ion-exchanged waveguides has been presented. These profiles are directly related to the refractive index profiles that will be used in the analysis of the waveguide propagation characteristics to be presented in later chapters.

2.5 Appendix

This is the detailed derivation of the stability criterion using the Von Neumann analysis for the planar field-assisted ion-exchange equation.

We begin with (2.28) and by letting $r_m = \Delta t/(\Delta x)^2$, we obtain:

$$g_i^{k+1} = r_m A g_{i-1}^k + (1 - 2r_m C) g_i^k + r_m B g_{i+1}^k \tag{2.41}$$

where

$$\begin{aligned} A &= \exp(-g_i^k)(D_K + \mu_K E_a \Delta x/2) \\ B &= \exp(-g_i^k)(D_K - \mu_K E_a \Delta x/2) \\ C &= D_K \exp(-g_i^k) \end{aligned} \tag{2.42}$$

Let $g_i^k = \gamma^k \exp(j\beta_m i)$, where β_m is real. Substituting into (2.41), we arrive at:

$$\gamma = r_m(A\exp(-j\beta_m) + B\exp(j\beta_m)) + 1 - 2r_m C \tag{2.43}$$

Assuming that $\exp(-g)$ is locally constant around each grid point, the complex quantity γ can be simplified even further to

$$\gamma = 1 - 4r_m D_K \exp(-g)\sin^2(\beta_m/2) - jr_m \exp(-g)\mu_K E_a \Delta x \tag{2.44}$$

For the scheme to be Von Neumann stable, the magnitude $|\gamma| \leq 1$ and the criterion for r_m reduces to

$$r_m \leq \frac{1 - \hat{\alpha}c}{2D_K + (\mu_K E_a \Delta x)^2/2D_K} \tag{2.45}$$

Plugging back $\Delta t = r_m(\Delta x)^2$, we obtain the stability criterion for the time step Δt:

$$\Delta t \leq \frac{2D_K(1 - \hat{\alpha}c)(\Delta x)^2}{4D_K^2 + (\mu_K E_a \Delta x)^2} \tag{2.46}$$

Bibliography

[1] H. Rawson. 'Glass and its history of service'. IEE Proc. 135 (6). pp. 325-330. 1988

[2] J. Albert. 'Ion Exchange from Salt Melts'. in *Introduction to Glass Integrated Optics*. S.I. Najafi, Ed., Artech House. Boston. 1992

[3] R.V. Ramaswamy and S. Srivastava. 'Ion-exchange Glass Waveguides: A Review', J. Lightwave Technol., 6 (4), pp. 984-1002, 1988

[4] L. Ross, N. Fabricius, and H. Oeste, 'Single-mode integrated optical waveguides by ion-exchange in glass', Euro. Fiber Optic Conf. LAN 87, Basel, 1987

[5] R.H. Doremus, *Glass Science*. Wiley, New York, 1973

[6] M. Abou-el-Liel and A.R. Cooper, 'Analysis of Field-Assisted Binary Ion Exchange', J. Amer. Cer. Soc., 62 (7), pp. 390-395, 1979

[7] H.J. Lilienhof, E. Voges, D. Ritter, and B. Pantschew, 'Field-induced index profiles of multimode ion-exchanged strip waveguides'. J. Quantum Electron., 18 (11), pp. 1877-1883, 1982

[8] T. Izawa and H. Nakagome, 'Optical waveguide formed by electrically induced migration of ions in glass plates', Appl. Phys. Lett. 21, (12), pp. 584-586, 1972

[9] R. Terai and R. Hayami, 'Ionic diffusion in glasses', J. Noncryst. Solids, 18, pp. 217-230, 1975

[10] M. Abou-el-Liel and F. Leonberger. 'Model for ion-exchanged waveguides in glass', J. Amer. Cer. Soc., 71 (6), pp. 497-502. 1988

[11] R.H. Doremus, 'Ion exchange in glasses'. in *Ion-Exchange*. vol. 2. J. A. Marinsky. Ed.. Dekker. New York 1969

[12] H. Ohta and M. Hara, 'Ion Exchange in Sheet Glass by Electrolysis'. Yogyo Kyokai. 78 (5). pp. 158-164. 1970

[13] F. Helfferich and M.S. Plesset, 'Ion-exchange kinetics: a nonlinear problem'. J. Chem. Phys.. 28 (1), pp. 418-424, 1957

[14] P. Duchateau and D.W. Zachmann. *Partial Differential Equations*. Schaum's Outline Series, McGraw-Hill. New York, 1986

[15] G.L. Yip, P.C. Noutsios, and K. Kishioka, 'Characteristics of optical waveguides made by electric-field-assisted K^+-ion exchange in glass', Opt. Lett.. 15 (14). pp. 789-791, 1990

[16] R.G. Walker, C.D.W. Wilkinson and J.A.H. Wilkinson, 'Integrated optical waveguiding structures made by silver ion-exchange in glass. 1: The propagation characteristics of stripe ion-exchanged waveguides: a theoretical and experimental investigation', Appl. Opt.. 22 (12), pp. 1923-1928, 1983

[17] R. Oven, D.G. Ashworth, and M.C. Page, 'On the analysis of field-assisted ion diffusion into glass', J. Phys.: Condens. Matter, 4, pp. 4089-4094. 1992

[18] M.C. Page, R. Oven, and D.G. Ashworth, 'Scaling rules for glass based planar optical waveguides made by field assisted ion diffusion', Electron. Lett., 27 (22), pp. 2073-2076, 1991

[19] V. Neuman, O. Parriaux, and L.M. Walpita, 'Double-alkali effect: Influence of index profile of ion-exchanged waveguides', Electron. Lett., 15 (22), pp. 704-706, 1979

[20] R.H. Doremus. 'Mixed-alkali effect and interdiffusion of Na and K ions in glass'. J. Amer. Cer. Soc.. 57 (11). pp. 478-480. 1974

[21] B. Pantchev, P. Danesh. and Z. Nikolov. 'Field-assisted ion exchange in glass: the effect of masking films'. Appl. Phys. Lett.. 62 (11). pp. 1212-1214. 1993

Chapter 3

Fabrication and Measurement Techniques

3.1 Introduction

The fabrication and measurement techniques of planar and channel optical waveguides are described in this chapter. The experimental apparatus used in both the purely thermal and field-assisted ion-exchange processes is described in detail, including that for the sputtering process. Optical waveguide measurements used to determine relevant propagation characteristics are presented together with the micro-analytical measurement techniques used for the K^+-ion concentration. In addition, near-field imaging techniques used to determine the waveguide mode profile are described.

3.2 Fabrication methods

3.2.1 Substrate cleaning

The soda-lime glass microscope slides are packed 'pre-cleaned' in sealed boxes but they must be cleaned thoroughly if they are to be used as optical substrates. This step is compulsory so as to avoid contamination of the melt and subsequent diffusion of foreign impurities into the waveguide layer. In addition, the surface must be defect-free because imperfections as small as a fraction of a wavelength of the light source can cause scattering losses.

The cleaning procedures are performed in a suitable clean-room environment. The slides are rinsed in flowing de-ionized (D.I.) water ($> 10M\Omega - cm$ resistivity) and then blown dry with high-purity (H.P.) nitrogen gas. Using soft cotton swabs, they are cleaned in a dilute non-abrasive Sparkleen detergent solution and rinsed again with D.I. water. Then, they are placed in an aluminum holder for further cleaning steps that include:

1. a 3 minute wash in an ultrasonic bath containing a few grains of detergent in 300 ml of D.I. water.

2. a rinse in flowing D.I. water.

3. a 3 minute ultrasonic wash in D.I. water.

4. an organic cleaning which consists of placing the holder in an empty beaker containing 20 ml of 2-propanol and then capping it with a Pyrex dish. The setup is then placed on a hot plate ('LO' setting) so that the vaporizing alcohol condenses on the substrate resulting in a cleansing action that is effective for organic decontamination.

5. a final rinse in D.I. water

To assess the substrate cleanliness, a simple inspection technique known as the water break method is used [1]. If the slide is free of organic residue, the D.I. water wets the slide evenly and evaporates slowly, showing interference colours as the layer thins out. When judged clean, it is blown dry and placed in a drying oven kept at 80^oC for about 10 minutes to ensure that it is completely dry before ion-exchange.

3.2.2 Purely thermal ion exchange

In this study, pure potassium nitrate (KNO_3) and sodium nitrate ($NaNO_3$) salt crystals were used as the ionic sources for the K^+ and Na^+ ions, respectively. Since

the melting points are quite high (334°C for KNO_3 and 307°C for $NaNO_3$) [2], a furnace is needed. The Lindberg crucible furnace has a vertical core and a thermocouple controlling the temperature in the 200 – 1200°C range to within 1°C. The KNO_3 crystals are placed in a stainless steel crucible inside the furnace which is closed at the top by an asbestos cover. When molten, the KNO_3 occupies about 200 ml. Two substrates are held vertically in a steel clip which is attached to the end of a brass rod that emerges from a small hole in the cover. Thus, the slides can be lowered into the melt without opening the cover.

The clean substrates are taken from the drying oven and placed in the steel clip which holds them vertically in the furnace. The setup remains suspended over the melt for a warm-up time of 10 min so as to bring the slides into thermal equilibrium with the melt, hence avoiding any thermal shock. They are then lowered slowly into the KNO_3 melt for an exchange time t_1. Once this time has elapsed, they are raised from the melt, the setup is removed from the furnace, and the substrates are taken out of the clip using steel calipers. They fall into a soft bed of tissue paper where they are allowed to cool for about 20 minutes. Since some residual KNO_3 recrystallizes on the glass surface during cooling, the slides must be washed clean of the salt in running D.I. water before they can be measured.

3.2.3 Field-assisted ion exchange

The configuration used for the fabrication of optical waveguides by the field-assisted ion-exchange process is basically comprised of three structures, namely the electrodes and their supporting structures, the molten salt support, and the external electrical equipment. The electrode configuration, as shown in Fig. 3.1(a), is comprised of two 'C' shaped steel blocks which have been milled to form half-cells for holding the salt melt [3]. These cells are made of stainless steel so as to avoid contamination of the salt. They are placed facing each other with the glass substrate and Teflon isolation sheets (see Fig. 3.1(b)) sandwiched between them. The two holes in the corners

of the electrodes are used for attaching Teflon-protected wires to form positive and negative potential. The electrodes are held together by two steel plates which are connected with seven screws and bolts, as shown in Fig. 3.2.

At the top of the electrode configuration, a flat aluminum plate is used to support two stainless steel cones used to funnel the salt into each half-cell. This plate is fastened to the two steel plates by angled brackets. The melt is held in two stainless steel cylindrical containers that lie just above the cones and are supported by a T-section with wire levers (see Fig. 3.3).

The electrode setup, up to the aluminum plate, is then put into a tin can and filled with sand for thermal isolation. This is important to avoid thermal shock and subsequent cracking of the substrate during the cooling process. This can and the whole apparatus is placed in an aluminum cylinder which is then put in the vertical furnace. An asbestos lid with a hole in its center (for the emerging wires) is used to cover the furnace top. The wires are connected to the external electrical equipment which include a voltage-controlled DC power supply and a current meter, as shown in Fig. 3.4. The current meter has a variable DC (mA) current range and the voltage source is internally protected against short circuits that may occur if there is a leakage of salt. The step-by-step fabrication procedure is outlined in Appendix 3A.

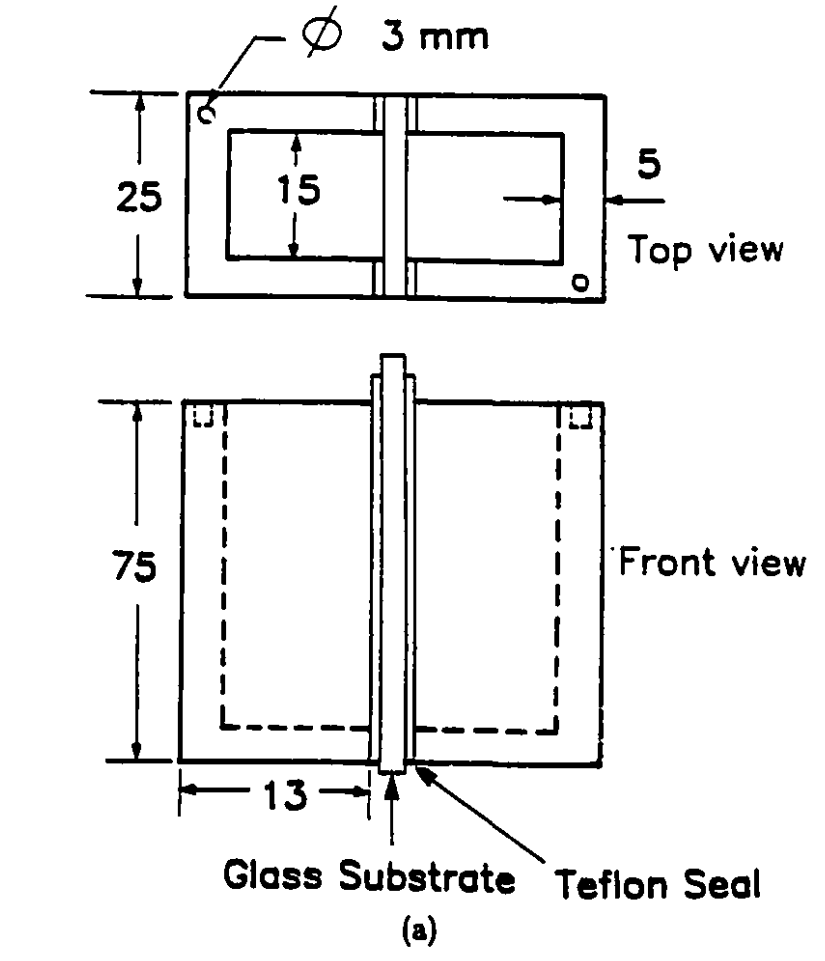

Figure 3.1: Diagram showing (a) half-cell configuration and (b) Teflon seals

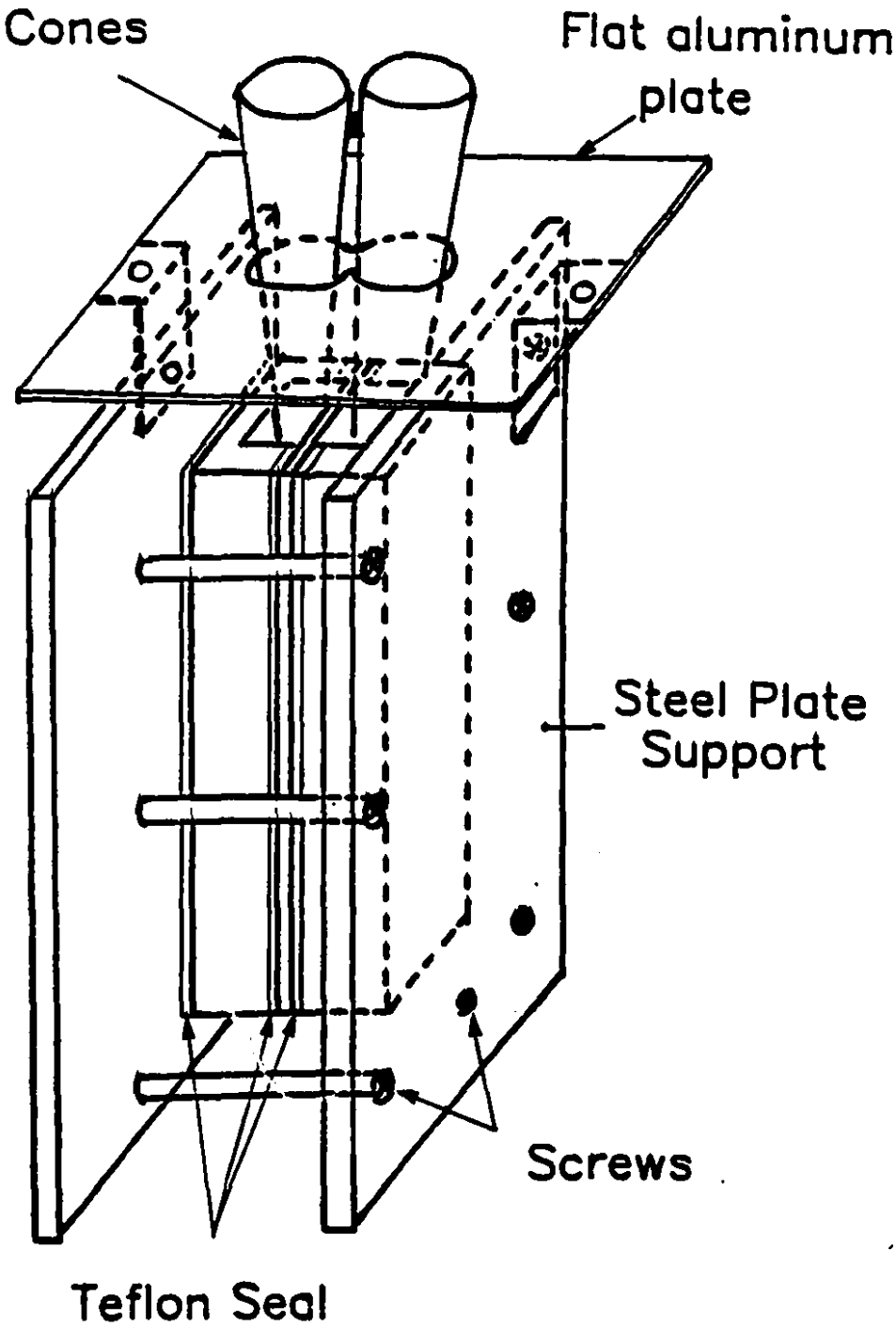

Figure 3.2: Complete electrode configuration

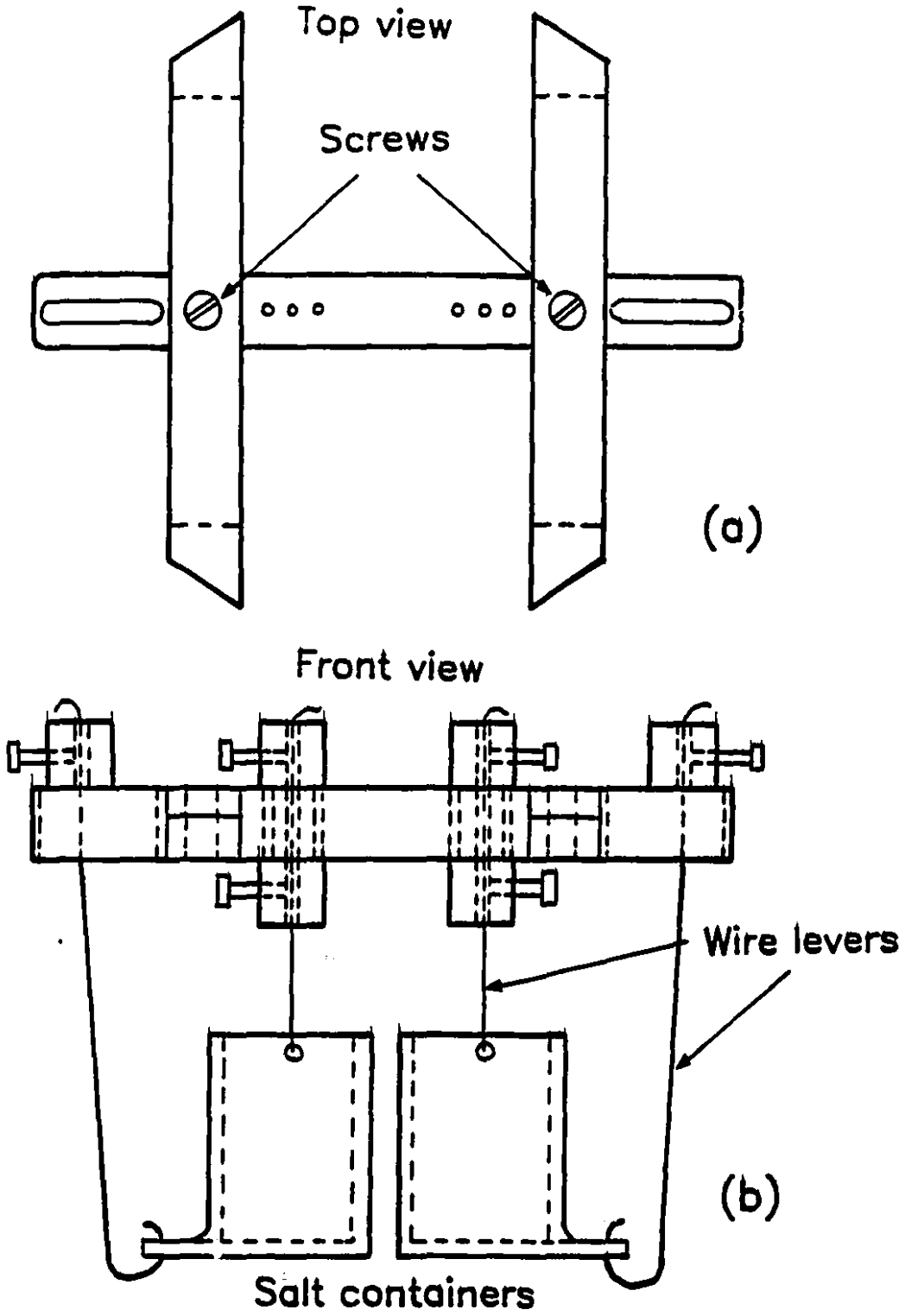

Figure 3.3: Schematic of (a) T-section and (b) wire levels

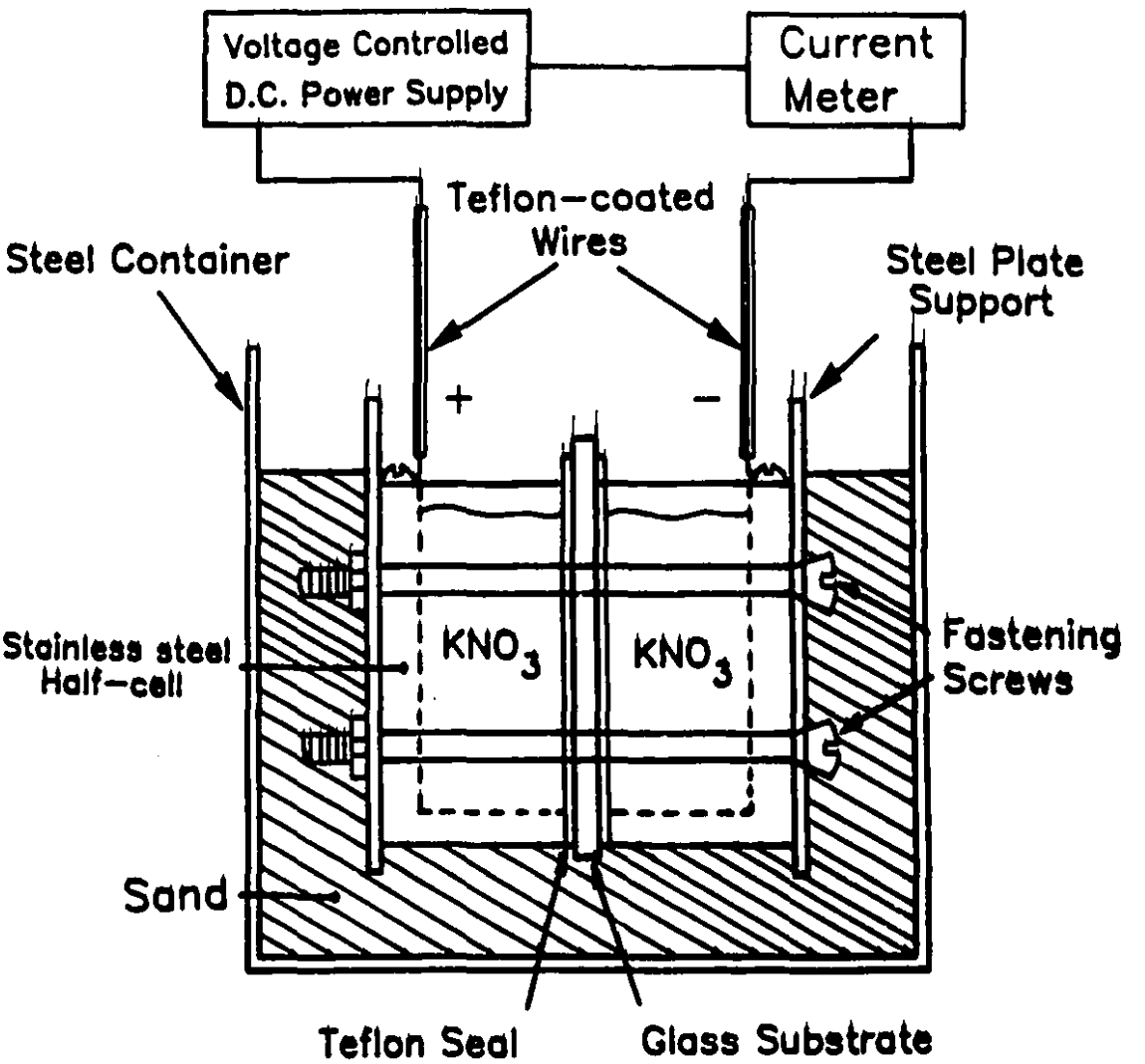

Figure 3.4: Schematic of the electric field-assisted apparatus

3.2.4 RF sputtering

Sputtering is the process in which material is removed from the surface of a target as the result of a bombardment of ions with energies in excess of 30 eV [1]. The particles removed from the target are deposited on a substrate to form a thin film. In this work, the target is a disk of pure aluminum oxide (Al_2O_3) and the ions are generated by the discharge of an argon/oxygen (Ar/O_2) 4:1 mixture (four parts Ar to one part O_2) under an applied rf (13.56 MHz) target voltage. The violet-coloured plasma can be excited under a gas pressure of 2×10^{-2} Torr in a vacuum chamber by applying a high voltage between the target and substrate holders. If the discharge conditions are kept stable, the sputtering rate r is linearly proportional to time t_s with the resulting index n_f being homogeneous throughout the film. Typical sputtering conditions are tabulated below. The Cooke Vacuum CV-300 sputtering system was used and its detailed operation is discussed in Appendix 3B.

We fabricated sputtered Al_2O_3 thin films on soda-lime glass for various power levels and durations in order to characterize the film's refractive index and the sputtering rate. Two input power levels, 12.5 W and 27.5 W corresponding to target voltages 0.5 kV and 0.75 kV were used. The optical measurements of the film's properties will be described in the next section whereas the characterization procedure will be discussed in Chapter 5.

Background pressure	2×10^{-6} Torr
Target	5 inch diameter Al_2O_3 disk
Gas	Ar/O_2 (4:1) mixture
Output pressure	12 PSI
Chamber pressure	20 μm TC-1; 50 μm TC-2
RF target voltage	0.5 - 0.75 kV
RF power	12.5 - 27.5 W at 13.56 MHz
Pre-sputtering	20 min

Table 3.1: Typical Al_2O_3 sputtering conditions

3.2.5 Channel waveguides

The fabrication of channel waveguides is more complicated than that of planar guides because of the high-vacuum metallization and photolithographic processes that are required to define the channel pattern. The metallization of the substrates is the first step of the process. The aluminum (Al) evaporation is performed in a vacuum chamber at a pressure of less than 2×10^{-6}. Two $20\,cm$ long folded wires of high-purity Al (Marz grade) are inserted into two tungsten coils. These coils are then heated by passing a high current through them causing the aluminum to evaporate in the chamber. A part of the evaporated Al condenses on the glass substrate and forms a uniform thin film of about $0.2\,\mu m$. Standard photolithography is now performed to remove the Al from the channel pattern through which the ion exchange is to occur. The following steps are carried out in a clean room environment:

1. **Photoresist coating**: Initially, a coating of Shipley primer was deposited onto the Al surface by spinning the substrate at 3000 rpm for $20\,s$ on a controlled spinning station. Then, a 4:1 mixture of photoresist (Shipley 1450J) and thinner (Microposit) was deposited by spinning at the same rate and time as above. Then, the resist layer was baked for 30 min at 80^oC in a drying oven.

2. **UV exposure**: The photomask was brought into contact with the resist film in a mask aligner station. Ultraviolet (UV) light from a mercury arc lamp was used to expose the mask openings for $90\,s$.

3. **Development**: The photoresist was developed in a 2:1 mixture of Microposit developer and D.I. water for about 1 min. This results in the removal of the resist from the exposed areas. The exact developing time was determined by inspecting the pattern under a microscope until the channels become free of any resist. Then, the sample was baked for 1 h at 120^oC to harden the resist.

4. **Etching**: The Al was clearly etched away from these exposed areas by immersing it in a solution of 16:1:2:1 mixture of phosphoric acid (H_3PO_4), nitric acid (HNO_3), acetic acid (CH_3COOH) and D.I. water, respectively, for 5-10 *min*. As was the case for development, careful inspection of the pattern was needed to ensure that the channels were well defined and clear of Al.

5. **Resist removal**: The photoresist was removed by immersing the sample in a 1:1 solution of Shipley remover and D.I. water. If needed, this solution was set on a hot plate ('LO' setting) and swirled occasionally to remove any residual resist. Then, the sample was dipped in a beaker of D.I. water, blown dry with H.P. nitrogen gas and placed in a drying oven set at 80^oC for 5 *min*. Fig. 3.5 shows a photo of an actual channel guide pattern with $W = 5\,\mu m$.

For surface channel guides made by purely thermal ion exchange, the sample was immersed in a KNO_3 melt for time t_1 at 385^oC, as described in 3.2.2. Then, the Al mask was removed completely using the etching solution (for about 30 *min*) and the sample was cleaned in D.I. water. For buried channel guides, the above sample was ion-exchanged via field assistance over the whole surface as described in 3.2.3 in a $NaNO_3$ melt for time t_2, applied field E_{a2}, at 385^oC. The channel-guide vertical coupling device is made by sputtering a planar layer of Al_2O_3 (see 3.2.4) on top of the above buried channel waveguide. The fabrication steps are illustrated in Fig. 3.6.

Figure 3.5: Photo of channel guide pattern with $W = 5\,\mu m$

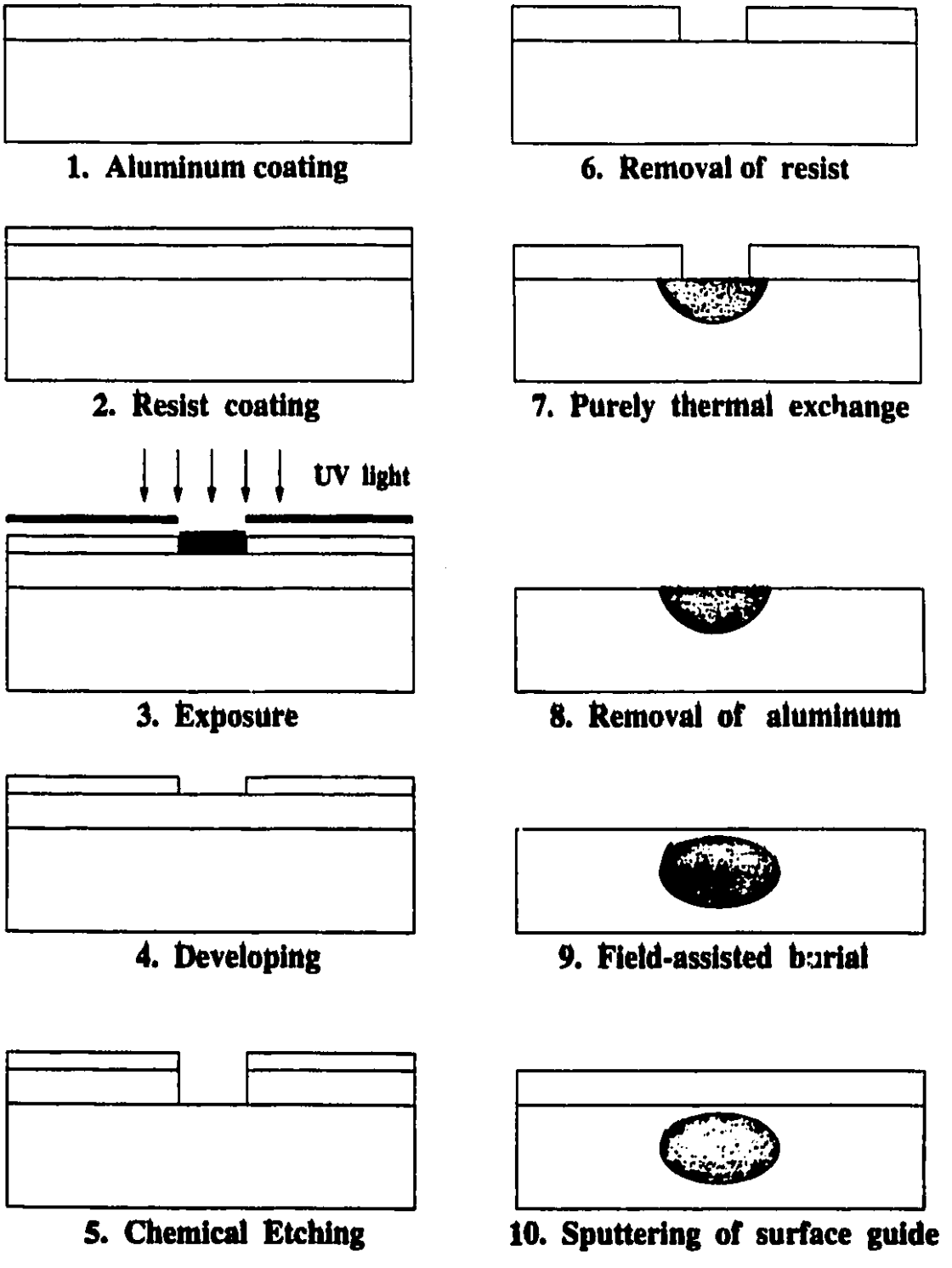

Figure 3.6: Diagram of fabrication procedure of buried channel-guide vertical directional coupler

3.3 Optical waveguide measurements

3.3.1 Introduction

Once these waveguides have been fabricated, their optical propagation characteristics need to be measured. These include the refractive index profile parameters, such as the waveguide dimensions, index change, and the propagation losses. In this thesis, two well-established techniques based on two-prism coupling were used. The first method involves measuring the propagation constants of all the modes that can be excited in a waveguide. It offers an indirect way of determining the index profile. The second method involves measuring the propagation losses of optical waveguides. In addition, an accurate technique based on far-field diffraction is used to determine the channel guide width before ion exchange occurs.

3.3.2 Modal spectroscopy

Modal spectroscopy involves using a two-prism coupler configuration to selectively excite the guided modes of a waveguide so as to measure their effective mode indices [4]. These indices represent the mode's propagation constant β_i normalized with respect to the free-space wavenumber k_o, i.e. $N_{eff,i} = \beta_i / k_o$. The theoretical aspects of the prism coupler have been described often [5] and are not presented here. However, the measurement setup is described below in detail.

To measure the effective mode indices with great accuracy, the coupling 'synchronous' angles, θ_i, must be known precisely. The measurement of these angles was performed using the setup in Fig. 3.7. Laser light from a 5 mW He-Ne source, operating at 0.6328 μm, passes through a polarizer to select TE and TM modes. Then, the incident beam is coupled into the waveguide using a LaF60 glass prism. An identical output prism located a short distance away couples the beam out of the guide. The resulting far-field pattern shows sharp vertical lines, known as m-lines, which can be excited individually (see Fig. 3.8(a)). The prism-waveguide holder, shown in

Fig. 3.9. rests on a precise angular measurement instrument with five degrees of freedom (see Fig. 3.8(b)). It consists (from bottom to top) of a magnetic base, a 3-axis micropositioner (x, y, z) and a rotational stage (θ) with 5 arc-second accuracy. The holder rests on a goniometer (ϕ) that is mounted on top of the complete setup. The θ_m angular measurement at which the m-line appears brightest by eye is recorded. The reference marker is used to measure the zero reference angle θ_r by adjusting the rotational stage until the incoming beam is reflected back onto itself. Hence, the synchronous angles can be determined by $\theta_i = \theta_m - \theta_r$.

The normalized propagation constants, $N_{eff,i}$, are obtained from the angle of incidence using the following formula [1] derived from geometrical optics:

$$N_{eff,i} = \frac{\beta_i}{k_o} = n_p \sin\left\{\alpha_p + \sin^{-1}\left(\frac{\sin\theta_i}{n_p}\right)\right\} \tag{3.1}$$

where n_p is the prism's refractive index and α_p is the prism's base angle. The value of $\alpha_p = 58.37^o$ and $n_p = 1.780$ at the wavelength $\lambda_o = 0.6328\mu m$. This experimental scheme yields an error of $\pm 0.015 - 0.02^o$ in the measurements of θ_i corresponding to an accuracy of $\pm 2 \times 10^{-4}$ in the measured values of $N_{eff,i}$. The accuracy in the value of α_p is $\pm 0.017^o$ and for n_p is equal to $\pm 1 \times 10^{-4}$. In total, this leads to an uncertainty of about $\pm 2 - 3 \times 10^{-4}$ in the measured $N_{eff,i}$.

Another parameter that can be determined rather easily is the substate index n_b. The simplest way is to use the set-up of Fig. 3.7 and to find the incident angle at which the waveguide becomes cut-off by observing the end of the substrate. At a particular angle, one can see the point where the light is no longer confined and starts leaking into the substrate. At this point, the cut-off condition, $N_{eff} = n_b$ is satisfied.

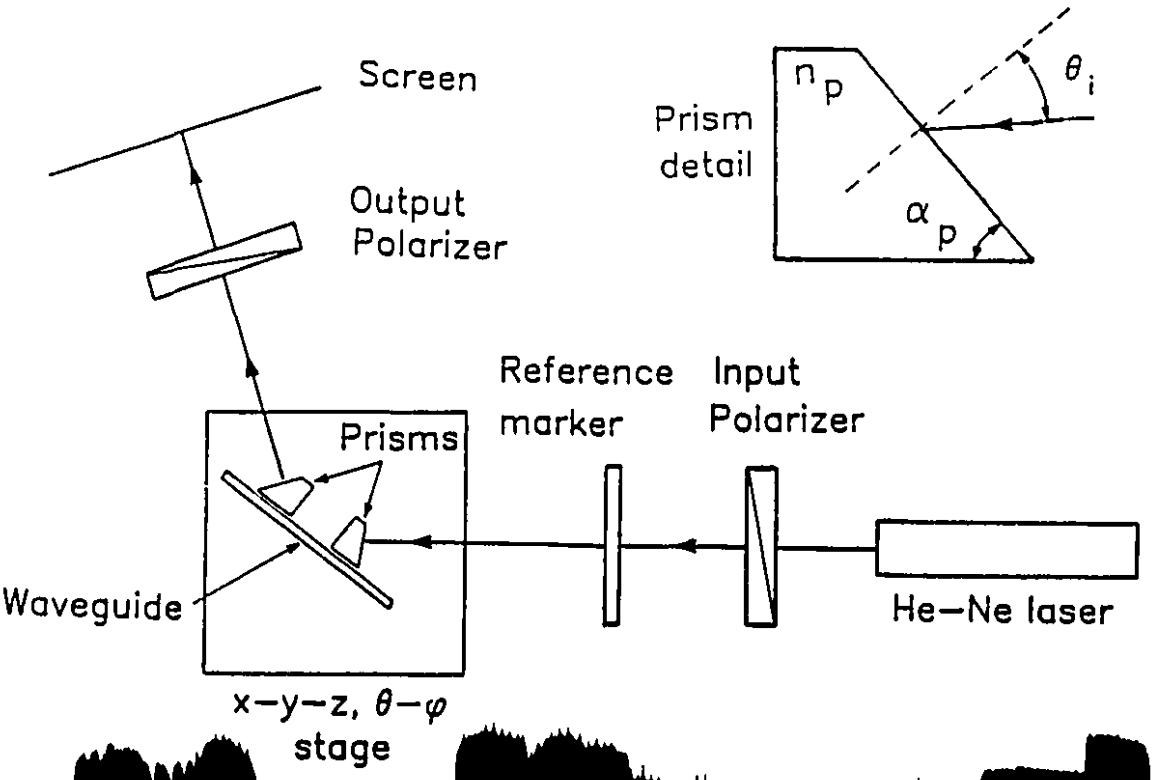

re 3.7: Setup f ective mo

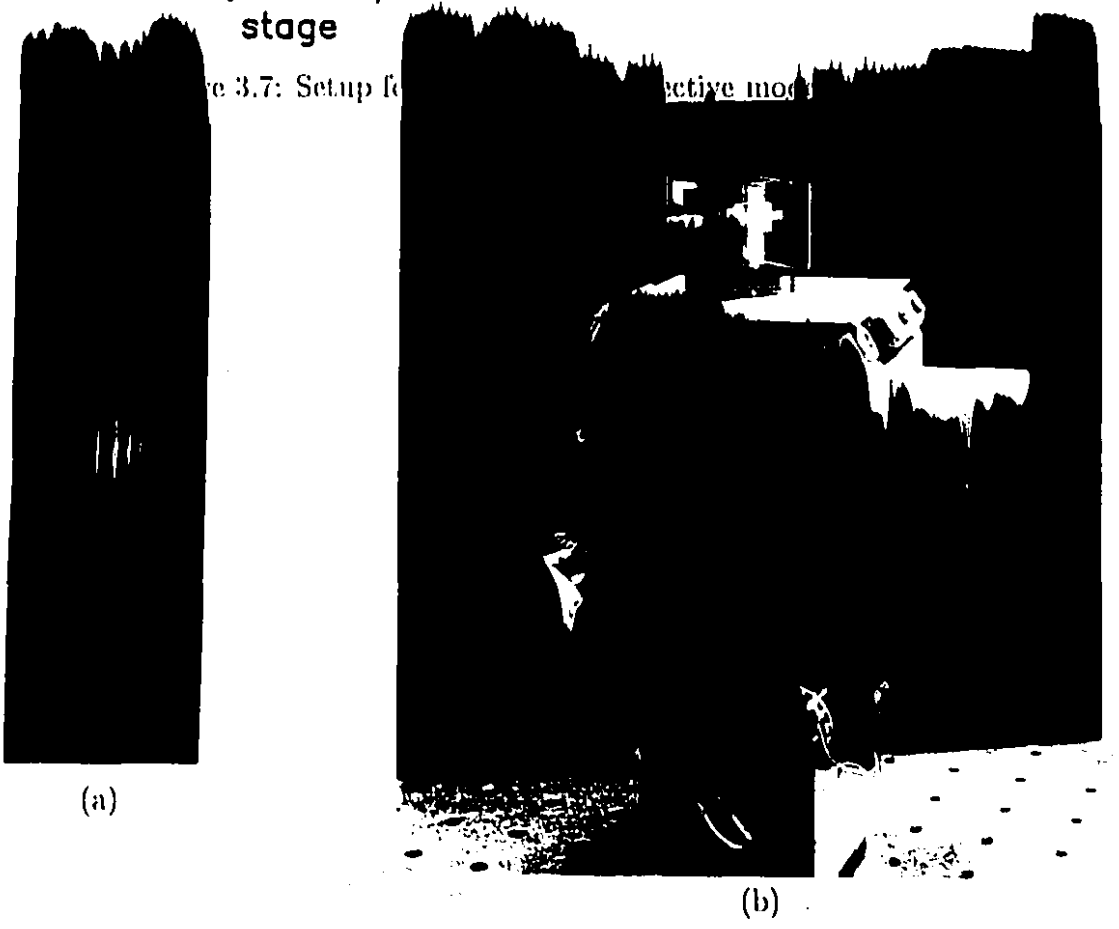

(a) (b)

Figure 3.8: (a) Photo of m-lines from 4-mode sample (b) Complete angular measurement instrument

3.3.3 Propagation loss

Waveguide propagation loss is dominated by absorption (owing to the presence of foreign impurities) and scattering contributions caused by glass inhomogeneity and surface defects. In the literature, a variety of techniques have been developed to measure the propagation loss [6, 7]. Here, the two-prism sliding method [8] was used.

The experimental setup is presented in Fig. 3.10 with the identical prism-coupler configuration of Fig. 3.9. First, the sample and both prisms are cleaned thoroughly as described in 3.2.1; the accuracy of the measurements may be affected by dust particles. The input prism is fixed rigidly to avoid any change in the input coupling efficiency. When a mode is excited, the m-line on the white screen is imaged by a video camera. The camera's output signal is then displayed on a video monitor whose analog output is fed into a channel input of an oscilloscope. The m-line is observed on the scope by scanning the time base in Horizontal Mode A. This allows for one frame of the video signal to be displayed by sharp vertical lines. The voltage level, V, of the line with the largest magnitude is recorded when the mode is excited. The output prism positions, $L_{pi}, i = 1, \ldots, N$, are measured accurately using a Vernier caliper. At each L_{pi}, the voltage is measured and the output prism is moved a few millimeters towards the input prism. This is done repeatedly to get at least 7 data points. The last prism position, L_{pN}, closest to the input prism (roughly 1 mm) is used as the reference to measure the propagation distance $\Delta L_i = L_{pN} - L_{pi}$. At each new output prism position, one must ensure that the coupling between the prism and the waveguide remain constant. This is quite difficult to achieve considering that the point pressure on the prism fluctuates for every measurement. Hence, reproducibility is affected. Propagation losses are evaluated from the slope of the log $|V|^2$ versus ΔL plot using a minimum least-squares linear fitting through the data points. A typical experiment shows that measurement of losses down to about $0.1 dB/cm$ is possible with errors of $\pm 0.01 dB/cm$ [4].

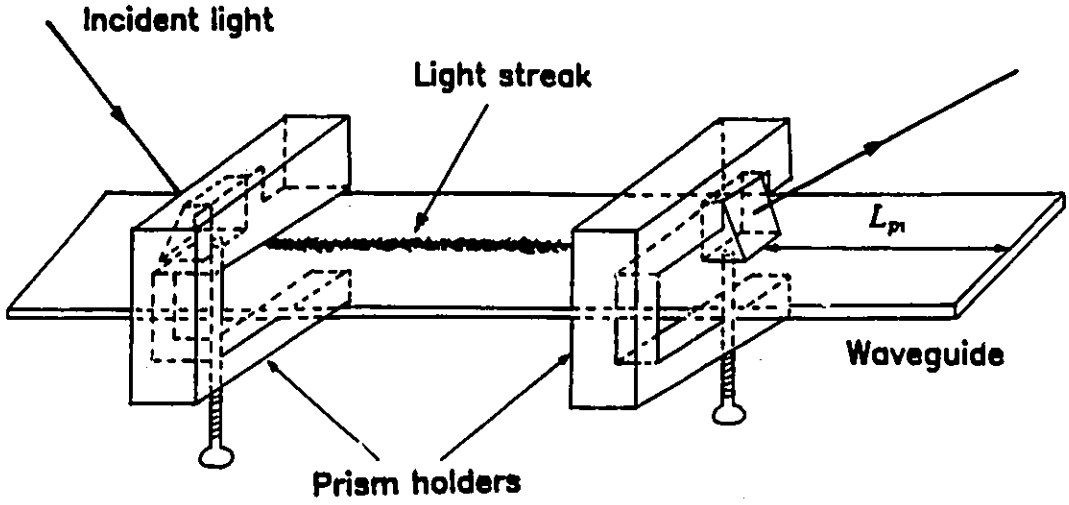

Figure 3.9: Waveguide-prism holder

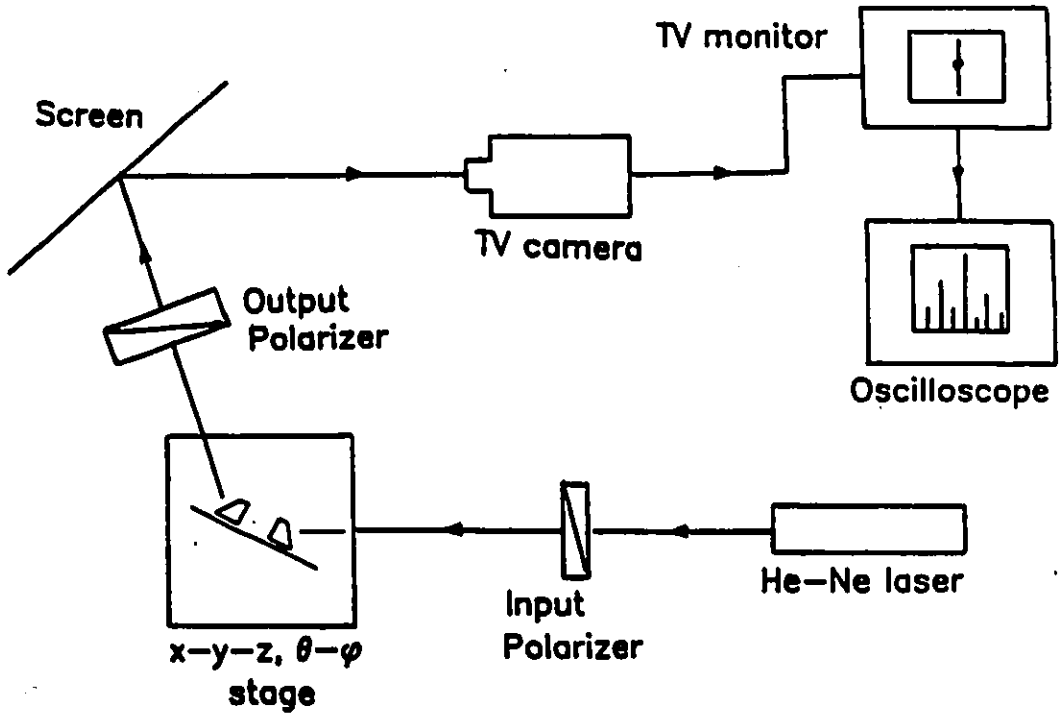

Figure 3.10: Setup for propagation loss measurement

3.3.4 Channel guide width

Due to varying photolithographic processing conditions, the channel width W of the Al channel mask may turn out to be quite different from that of the original photomask. Hence, a measurement method is needed to quantify W accurately prior to any ion-exchange process. The method is based on the classical far-field (Fraunhofer) diffraction pattern that results when the aperture (channel slit) is illuminated by the He-Ne laser at $\lambda_o = 0.6328\,\mu m$. As shown in Fig. 3.11, the light passes through the substrate side of the sample and then through the channel slit where it is diffracted onto a screen that is $L_d = 2\,m$ away. The samples are mounted on a micropositioner allowing vertical movement along the channel slits. On the screen, a one-dimensional diffraction pattern is seen whose intensity is expressed by the well-known formula:

$$I_d(y) = I_o \frac{\sin^2(\pi W \sin\theta_f/\lambda_o)}{(\pi W \sin\theta_f/\lambda_o)^2} \tag{3.2}$$

where θ_f is the angle subtended from $Y = 0$ to Y_m. The intensity minima correspond to $\pi W \sin\theta_f/\lambda_o = n\pi, n = 1, 2, 3....$ By measuring the distance between the first two dark lines, i.e. $2Y_m$ and $n = 1$, and assuming that $Y_m \ll L_d$, then $W = \lambda_o L_d/Y_m$. This measurement was repeated at five different vertical positions for each channel width. The measurements for Y_m ranged between $25\,cm$ and $\quad cm$ with the average being $29\,cm$. By taking the differential of W, $\Delta W = \lambda_o L_d \Delta Y_m / Y_m^2$, we obtain the measurement error in W to be $\pm 0.15\mu m$.

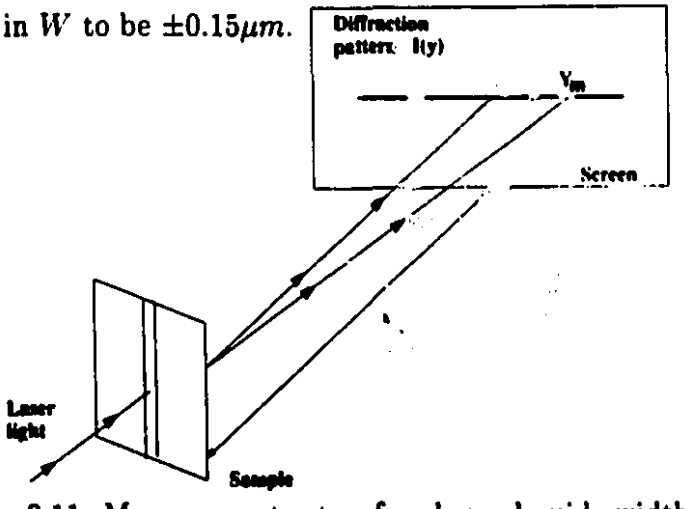

Figure 3.11: Measurement setup for channel guide width

3.4 Near-field mode profile measurements

3.4.1 Introduction

The intensity distribution of a mode, or its mode profile, is another important characteristic of a waveguide. This profile gives us useful information about the waveguide dimensions and symmetry that can be used to determine the coupling efficiency to an optical fiber [9]. In another application, the mode profile can be used to determine the refractive index profile [10]. In this thesis, the near-field mode profile of a buried channel guide was studied. The following sections describe our new experimental approach that uses a linear CCD camera and a frame grabber digitizer to capture the near-field pattern pixel-by-pixel [11] rather than a vidicon camera and digitizing oscilloscope as in [12]. The 8-bit frame grabber can digitize and provide 256 intensity levels to represent the measured data in its entirety. Specifically, the complete near-field pattern can be imaged at once, thereby eliminating the need to perform any transverse scanning of the image as in [12, 13].

3.4.2 Frame grabber calibration

The experimental setup used for measuring the near-field intensity distribution is shown in Fig. 3.12. The near-field pattern appearing on the cleaved edge of the waveguide sample under consideration is magnified by a 40× microscope objective onto the CCD camera. An attenuator, placed between the laser source and the waveguide, is used if necessary, to avoid saturation of the CCD camera. The intensity distribution imaged by the camera is then digitized pixel-by-pixel by the frame grabber signal processing board and stored in the computer memory for future use. In particular, the frame grabber stores the image obtained by the CCD camera in a two-dimensional array: the spatial coordinates of the image correspond to the array elements while the array entry represents the intensity level. Note further that each array entry represents one pixel.

The CCD camera we used provides excellent linearity in the region $0.4 - 1.1\mu m$. provided that it has not been saturated. Saturation occurs when the intensity level measured by each pixel is a maximum (for the 8-bit frame grabber, FF_{16} is the maximum level obtainable). To avoid saturation, the attenuator is adjusted so that the intensity levels digitized by the frame grabber are not near this maximum value. This does not affect the near-field pattern since the CCD camera provides relative, and not absolute, measurements of intensity levels. In fact, the units are arbitrary and the data may be normalized with respect to the maximum value.

Calibration of the frame grabber is vital: this is the only means available to obtain knowledge of the spatial dependence of the near-field distribution. More precisely, we need to determine the number of pixels/μm. To do so, the distance between the microscope objective and the CCD camera is fixed. Then, a micro-ruler is mounted onto the stage and back-illuminated by a white lamp. It is in then adjusted until the micro-ruler is properly focused. The image, which can simultaneously be viewed on the display monitor, is then stored by the frame grabber. The micro-ruler is chosen here with a particular known spacing, namely every 10 μm. The image of the micro-ruler will consist of a series of bright bands separated by dark fringes in the horizontal (y) direction. These bright bands represent the grid markings and the dark fringes represent the spacings, as shown in Fig. 3.13. The distance between two consecutive bright bands corresponds to the known spacing. The data stored by the frame grabber in a two-dimensional array reflects the viewed image. Specifically, the array will consist of columns of high intensity levels corresponding to the bright bands separated by columns of low intensity levels, reflecting the dark fringes. Since each pixel represents one entry in the two-dimensional array, the number of columns between successive high intensity level bands yields the desired result: the number of pixels per μm. Following this calibration procedure, we obtained a scale of 50 pixels / $10\mu m$, or 0.2 μm / pixel.

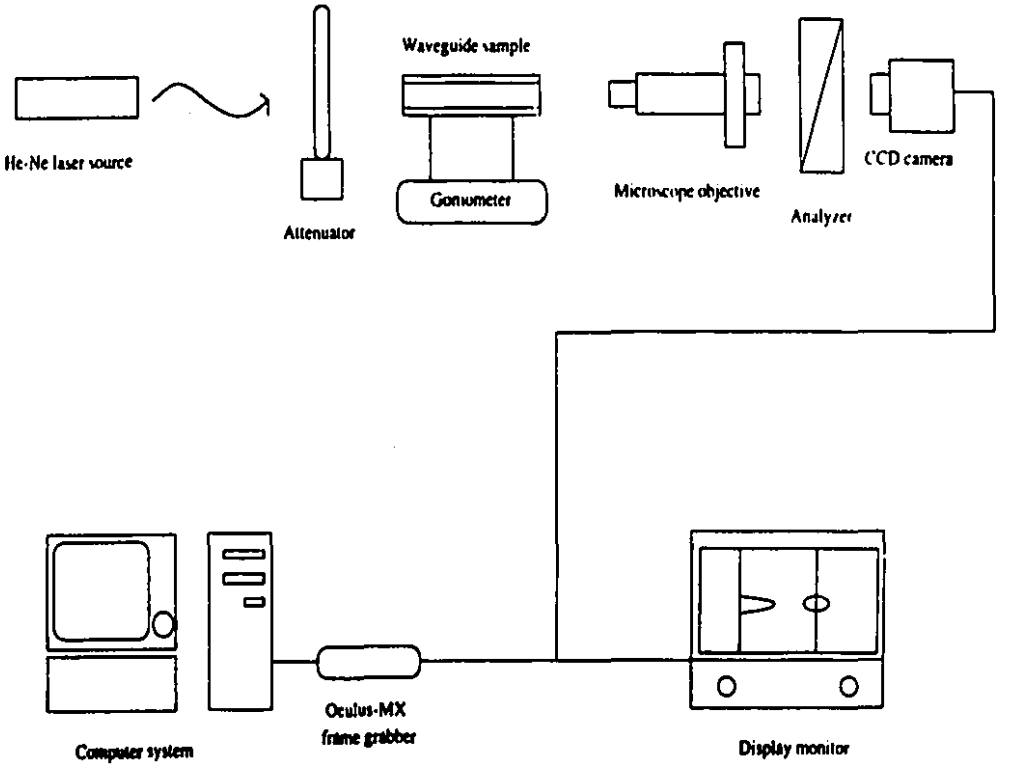

Figure 3.12: Experiment setup for near-field measurements

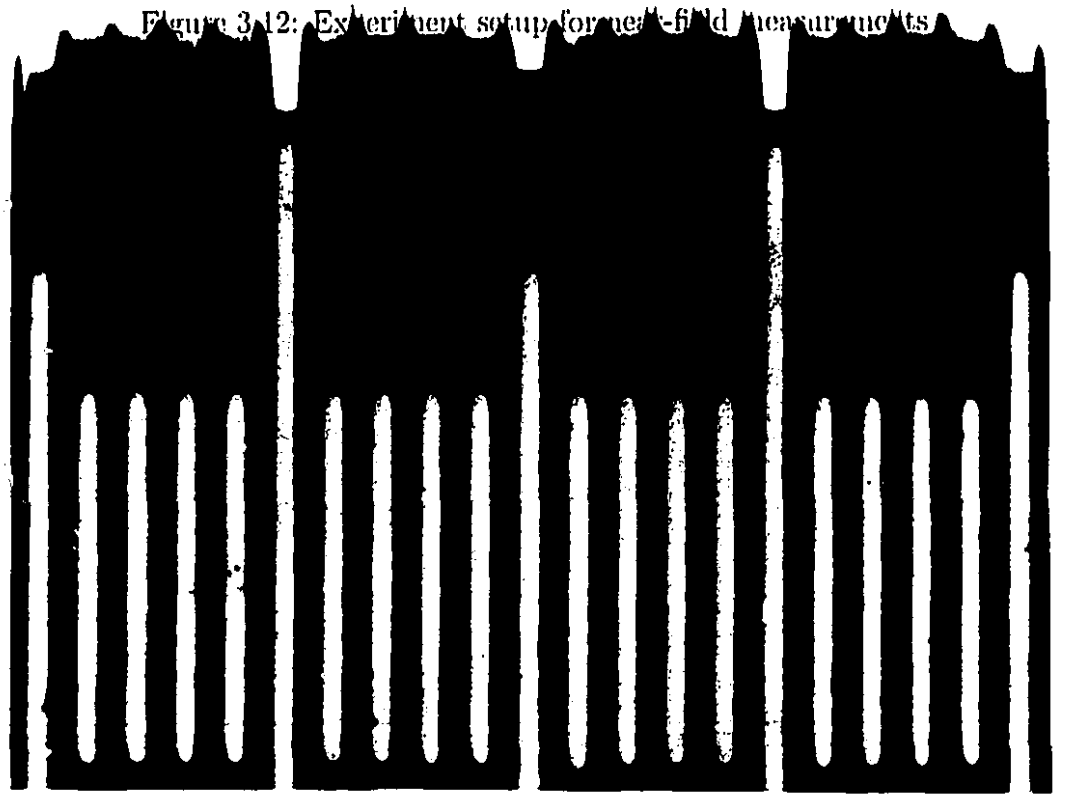

Figure 3.13: Photograph of the micro-ruler bands

3.4.3 Imaging system transfer function

It is well known that any imaging system distorts the actual object due to diffraction and aberration of the optical components [13, 14]. In our case, the microscope objective, CCD camera, and frame grabber system distort the actual near-field profile (object). The stored image does not correspond exactly to the near-field profile emerging from the waveguide. The image is in fact a convolution of the object with the system transfer function [11] given by the following convolution product

$$I(x,y) = S_3(x,y) * S_2(x,y) * S_1(x,y) * P(x,y) \tag{3.3}$$

where $I(x,y)$, $S_3(x,y)$, $S_2(x,y)$, $S_1(x,y)$, and $P(x,y)$ represent respectively the digitized image or the measured data, the effects of near-field (Fresnel) diffraction at the cleaved waveguide edge, the microscope objective transfer function, the transfer function of the CCD camera and frame grabber system, and the actual near-field power distribution (se Fig. 3.14). Alternatively, if $S(x,y) = S_3(x,y) * S_2(x,y) * S_1(x,y)$ represents the effective transfer function (ETF) of the optical imaging system, then

$$I(x,y) = S(x,y) * P(x,y) \tag{3.4}$$

To recover $P(x,y)$, a deconvolution process in the spatial domain, or an inverse Fourier transform in the spatial frequency domain may be needed. Deconvolution algorithms are readily available [15] as are inverse FFT techniques [16].

The ETF $S(x,y)$ was determined from measurements of the system's input and output. We used a process similar to that used to calibrate the frame grabber. The image of a simple inverted photomask consisting of dark fringes of known widths on a transparent background was grabbed and stored in memory. Theoretically, an intensity plot of the inverted mask would have a step-like form as shown in Fig. 3.15. However, due to the convolution of the imaging system transfer function, the measured data is not step-like at all. The ETF can now be determined using an iterative minimization procedure. A first estimate to the transfer function is made

and convoluted with the theoretical step-like input to give an estimate of the output. After each iteration, the ETF $S(x, y)$ is modified so as to minimize the mean-square error between the measured data and each successive estimate of the output. Once a prescribed error criterion has been achieved ($< 1 \times 10^{-8}$), the process terminates. This process, though described in the spatial domain, can also be carried out in the spatial frequency domain. In fact, our computations were made on MATLAB which computes convolutions as the inverse of FFT processes. Following this iterative procedure, we determined the effective transfer function to be of the form

$$S(y) = A\left\{\frac{J_1(\gamma_s y)}{\gamma_s y}\right\}^2 \tag{3.5}$$

where $A = 4.00$, $\gamma_s = 2.50$, $J_1(y)$ is the first order Bessel function, and y is a variable in the horizontal direction. This particular function, sometimes referred to as the *Sombrero* function, was chosen since microscope objective transfer functions generally have this form [17]. The same functional form was used in the vertical direction.

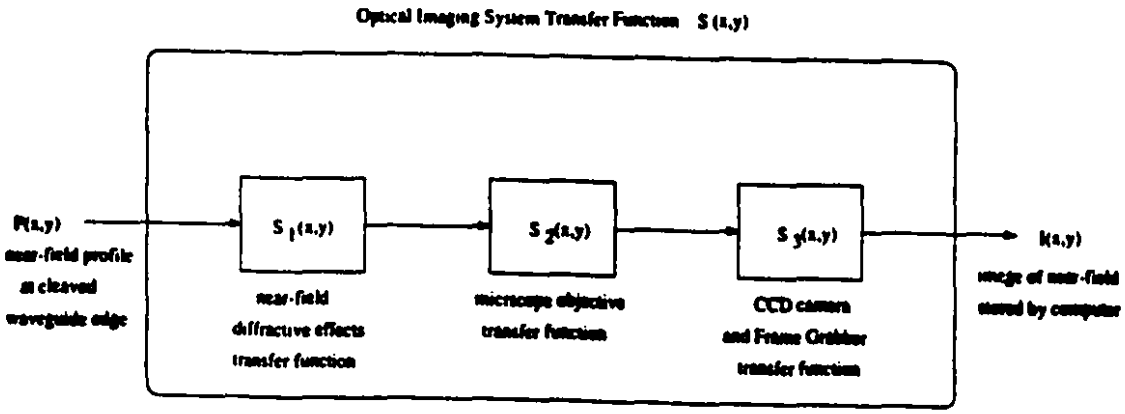

Figure 3.14: Optical imaging system

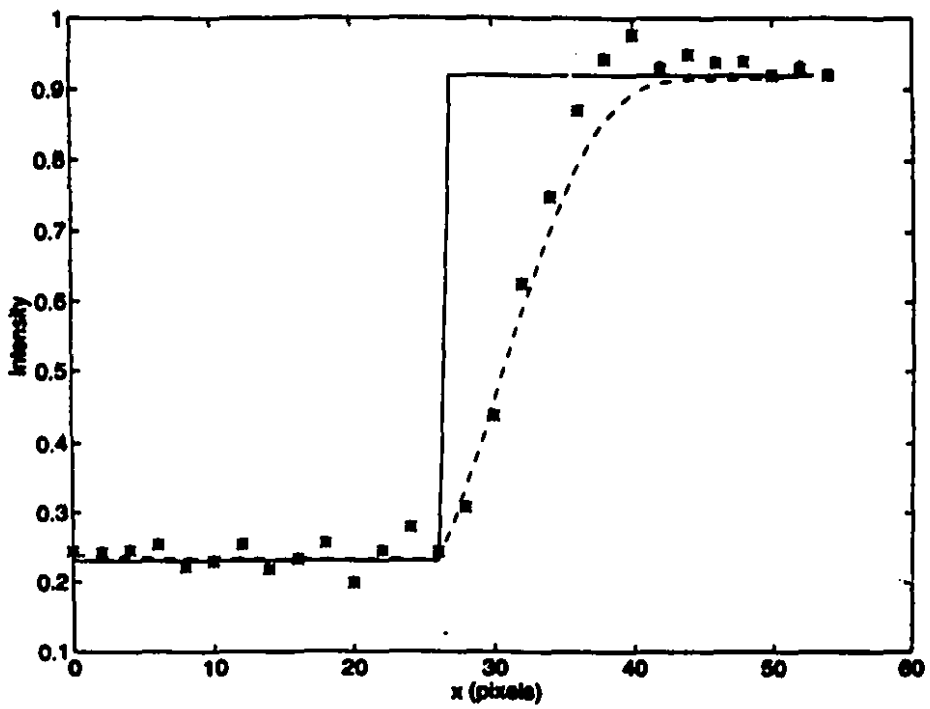

Figure 3.15: Determining the ETF: Solid line represents theoretical step-like intensity levels of inverted photomask, asterisks represent the measured levels and the dashed line represents convolution of the step-like profile with the ETF

3.5 Electron microprobe measurements

3.5.1 Introduction

The electron microprobe (EMP), also known as electron probe microanalysis (EPMA) was first described by Castaing in his doctoral thesis in 1948 [18]. The basic principle of the method consists of the electron beam bombardment of a sample and the subsequent study of its X-ray emission. Of all the signals generated by the interaction of the primary electron beam with the sample in the EMP, X-rays are most commonly used for material characterization [19]. The X-rays have energies characteristic of the element from which they originate leading to elemental identification. The X-ray intensity can be compared with intensities from a known sample (called a standard) and the ratio of the sample intensity to that of the standard is used to measure the amount of a given element in the sample. The highest accuracy in quantitative concentration determination is obtained if the standard is identical or at least very similar in composition to the sample under investigation. Further details of the EMP and its applications are presented in many textbooks [19, 20, 21, 22].

This section presents the quantitative electron microprobe analysis (EPMA) of soda-lime glass substrates and K^+-ion exchanged waveguide compositions. Two types of analysis were performed: surface and bevelled. The surface analysis was done at the samples' planar surface at different locations while the bevelled analysis was performed along the samples' angle-lapped surface to determine its spatial variation in depth using an angle lapping polishing method. The CAMECA electron microprobe was used for the experiments and its operation is explained as follows. An electron beam is focused onto a small ($\approx 10\,\mu m$ diameter) spot on the surface of the sample from which X-rays characteristic of the chemical composition are generated and emitted. The spot analysis time usually takes about one minute. Provision must be made so that the area is small enough to resolve spatial chemical variation.

Fig. 3.16 shows the schematic diagram of the entire setup. The wavelength

dispersive X-ray spectrometer consists of a bent crystal monochromator, a gas-filled detector and a single-channel (pulse-height) analyzer [21]. In the fully-focusing spectrometer, the sample, crystal and detector all lie on the same focusing Rowland circle. The X-rays emitted by the sample are analyzed by the crystal. If this latter is set at the Bragg angle for a given wavelength, the X-rays are reflected and focused onto the detector. These X-ray wavelengths and their intensities depend on the concentration of the element in the sample and are measured quantitatively in an X-ray detector, that is an argon/methane gas proportional counter. The output signal is amplified and the elemental and oxide concentrations (determined from relative intensities with the standard) are printed on an output device. This technique is usually referred to as wavelength dispersion spectroscopy (WDS), since it is the wavelength of the characteristic X-ray lines that is being measured [20].

In actual practice, the analysis does not give the concentration exactly at the sample surface. EMP is not a true surface technique because the X-rays are emitted from within the sample volume. Hence, it gives a statistical average of the concentration over a small depth of up to $0.5\,\mu m$ near the surface. Fig. 3.17 shows a theoretical prediction of the probabilistic penetration depth calculated by Monte-Carlo simulations [22]. The calculations, provided by CAMECA software, are based on the chemical composition of the soda-lime glass and its density. Two bounding curves describe the signal information. The upper curve is the intensity of the X-rays generated by the electron beam and the lower curve is that of the X-ray intensity emitted from the sample. Although the penetration depth is up to about $1.3\,\mu m$, the major part of the information exists up to about $0.5\,\mu m$. For larger accelerating voltages, the penetration depth increases. Hence, the voltage should be kept as low as possible so as to provide for accurate results near the surface yet be high enough to excite the X-rays of all the glass constituents. For the soda-lime silicate glasses used in the experiments, the accelerating voltage was set at $10\,kV$ to satisfy the aforementioned requirements.

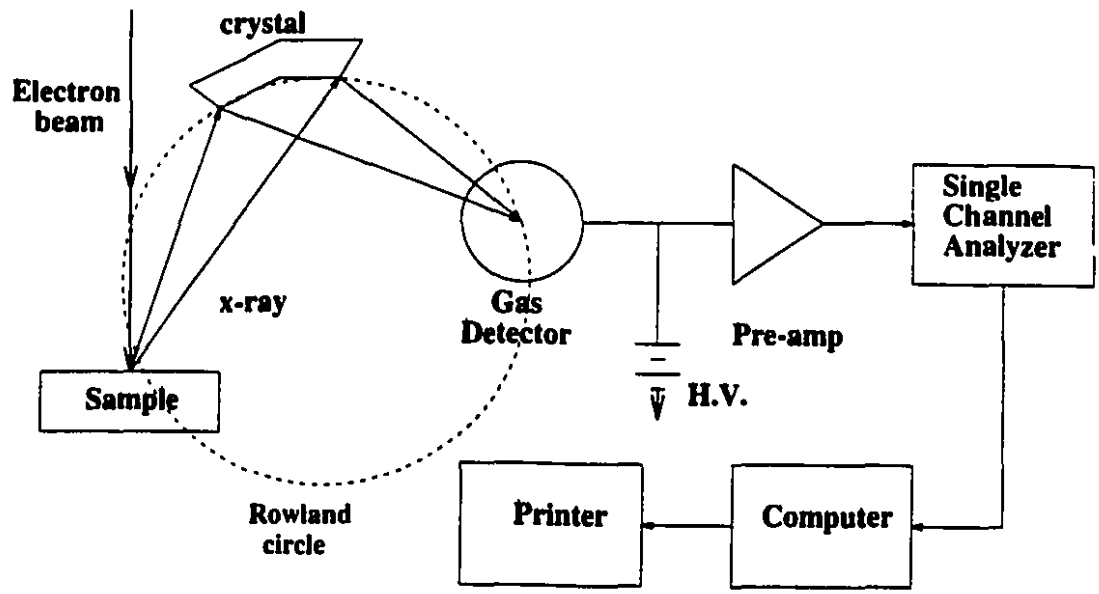

Figure 3.16: Schematic of the EPMA X-ray apparatus

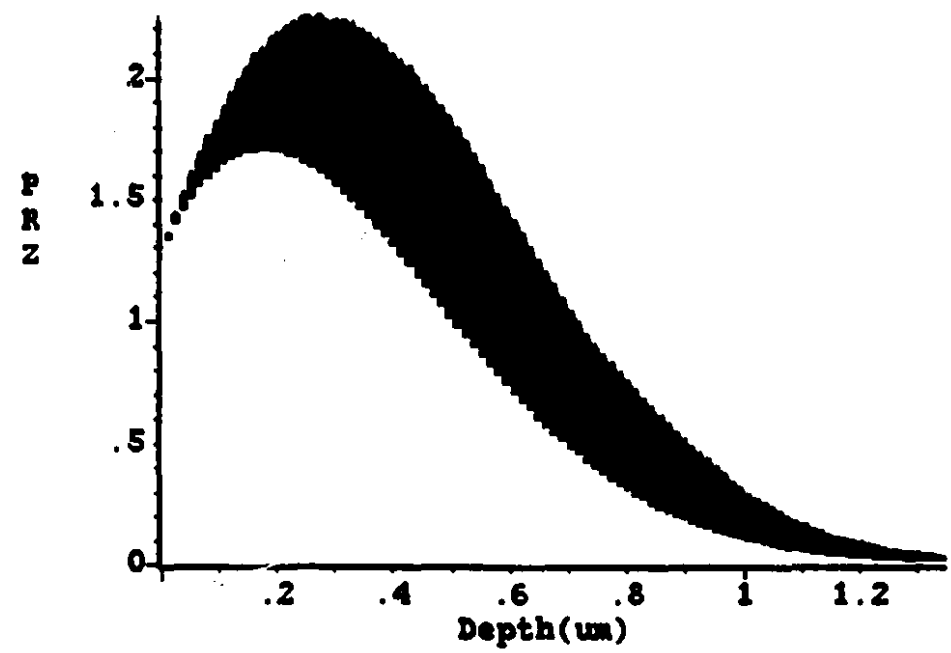

Figure 3.17: Probabilistic curve vs. penetration depth for a Fisher glass substrate

For the surface analysis, the focused electron beam was not suitable for the soda-lime glasses. Due to the long spot analysis time and the high energy density of the beam, the soda (Na_2O) was 'burned off' (i.e. Na was dislodged from the glass structure) during the measurements, hence destroying the samples' composition. The solution to this problem was to use a defocused beam of $20\,\mu m$ in diameter that provided for much lower energy density and spatial resolution. Consequently, another type of surface analysis to be discussed below is called for to accommodate the defocused beam resolution.

3.5.2 Sample preparation

For the EMP surface analysis, the waveguide side of the sample was cut into $3 \times 5\,cm$ pieces so as to fit into a special holder. These samples were then carbon coated under high vacuum with a $15\,nm$ thin film so as to prevent charge buildup on the dielectric sample from the electron beam during the spot analysis. The carbon coating provides a conductive path for the e-beam.

The sample preparation for the bevelled analysis is more elaborate. An angle-lapping polishing technique, popular in semiconductor work, is used to expose the varying potassium concentration. This approach provides for an accurate measurement of the concentration in the depth direction which has been effectively 'stretched' out by polishing at a desired angle θ, as shown in Fig. 3.18. This method is known to provide for better results than simple butt polishing in which the defocused electron beam is incident perpendicular to the polished edge. For our waveguides, with depths less than $10\,\mu m$, the defocused electron beam resolution (with $20\,\mu m$ diameter) would have been inadequate for butt polishing. Fortunately, the resolution can be substantially improved by the angle-lapping approach. As an example, if $\theta = 1^{\circ}$ and the spatial sampling displacement along y $l_s = 25\,\mu m$, then the depth d can be resolved for $d = l_s \tan(\theta) = 0.44\,\mu m$. A more accurate expression for this depth will be presented in the next section.

A simple bevelled polishing chuck made of aluminum was designed and built to hold the sample during polishing. The waveguide was first cut to a suitable size of 5 *cm* and then epoxied to the metal chuck. The epoxied sample protruded about 2 *cm* on the flat side of the chuck and was ground to remove the protrusion, as shown in Fig. 3.19(a) and (b). It was then polished on a variable speed machine, set at 100 rpm, in the following manner to achieve a flat, smooth surface:

- a 240 grit disk for 15-20 *min* to remove the protrusion
- a 400 grit disk for 5-10 *min* to remove the scratches
- a 600 grit disk for 5-10 *min* for the final grinding
- alumina suspension for about 10 *min* for the intermediate polishing
- colloidal silica for about 10 *min* for the final polishing

Finally, the sample was carbon coated as before. The total polishing procedure provided a smooth surface, as photographed in Fig. 3.19(c).

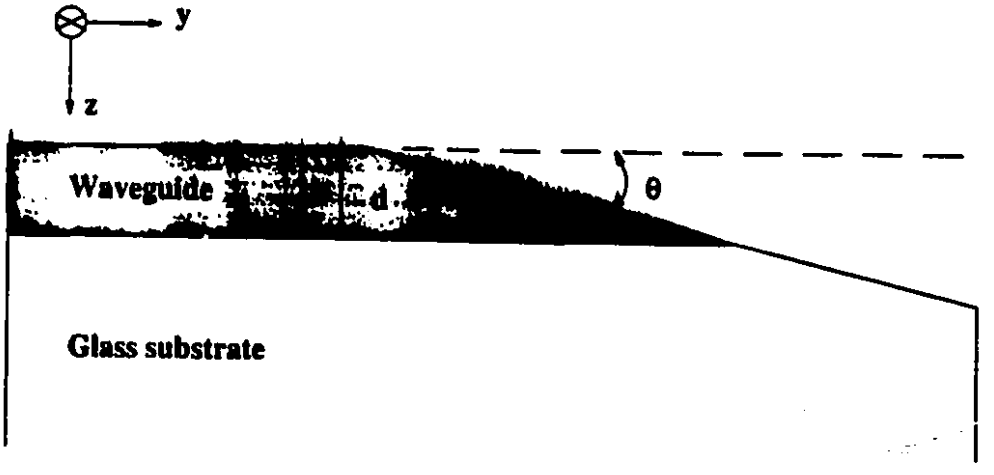

Figure 3.18: Potassium concentration measurement by angle lapping

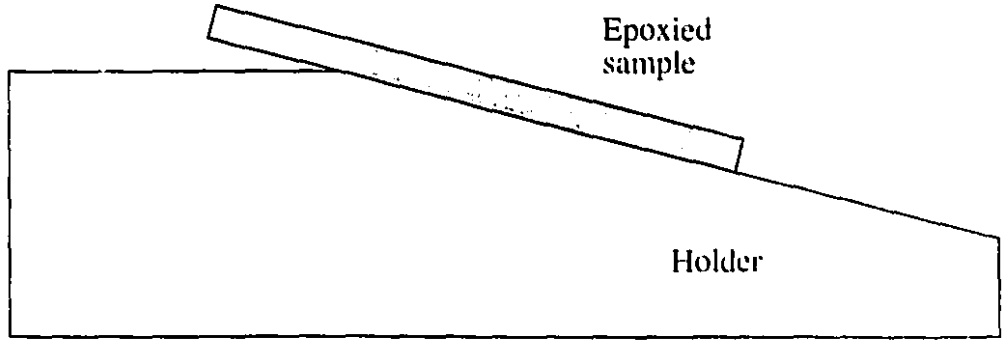

(a)

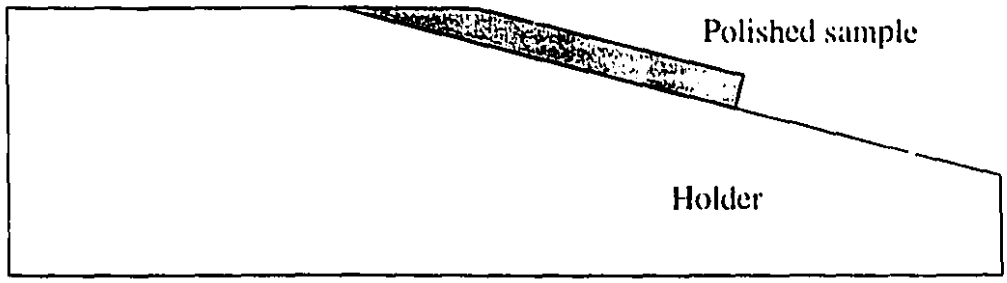

(b)

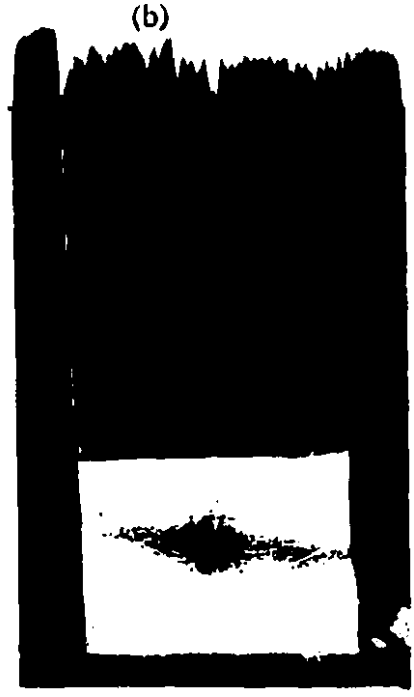

(c)

Figure 3.19: Epoxied sample on bevelled chuck (a) before and (b) after polishing. (c) a photograph of a smooth angle-polished sample

3.5.3 Data reduction

Quantitative EMP analysis seems to be extremely simple at first. All that needs to be done is to form the ratio k_r of the characteristic X-ray intensity measured from the sample (I_i) and the standard ($I_{(i)}$) where $k_r = I_i/I_{(i)}$. This k_r-value is assumed to be equal to the concentration ratio $c_i/c_{(i)}$ between the sample and the standard. It forms the most basic experimental measurement that underlies all quantitative analyses [20]. However, in most practical cases, the measured intensities from sample and standard need to be corrected for differences in the electron backscatter, density, X-ray cross section, and energy loss as well as absorption within the solid in order to arrive at the ratio of generated intensities and hence the value of c_i. These matrix effects are divided up into atomic number (Z), X-ray absorption (A) and x-ray fluorescence (F) and the correction to $c_i/c_{(i)} = (ZAF)_i k_i$ is known as ZAF correction. It is done internally by the CAMECA software.

After ZAF correction, the electron microprobe analysis gives the concentration of the elemental oxides in the soda-lime glass in terms of its weight fraction. The atomic concentration of the constituent elements (K, Na, Si, Ca, Mg, Al) are also provided in terms of atomic concentration ratios. These ratios are useful in determining the fraction of exchanged potassium ions (occuring at the surface) with the available concentration of sodium ions. This value h_K is calculated as:

$$h_K = \frac{K_{surf} - K_{sub}}{Na_{sub}} \tag{3.6}$$

where K_{surf} is the atomic potassium concentration ratio at the sample surface. K_{sub} and Na_{sub} are the concentrations of the potassium and sodium in the substrate, respectively, before ion exchange. Note that the background K in the substrate must be subtracted from the K at the surface to give an accurate measurement of h_K.

For the surface analysis of the soda-lime glass substrate, at least five spot analyses, randomly chosen on the surface, were performed with the average measurements and deviations presented in Table 3.2. The chemical composition of the bulk sub-

strate, measured by our EMP (third column), is shown to be in excellent agreement to that published by Fisher Scientific (second column). The $N620$ glass sample, provided by the National Institute of Standards and Technology (NIST) was used as the standard sample in our experiments since its chemical composition is very similar to that of our substrate (see Table 3.2). In addition, the $KN9$ standard was used in the elemental analysis of potassium because its higher K content provided for accurate measurement of K in the exchanged guides.

An example of a surface analysis to determine h_K is performed on a K^+-ion-exchanged surface guide (8-92D), fabricated at $E_a^T = 19.81 V/mm$ for $t = 20 min$. The atomic concentration ratios of the elements are presented in Table 3.3 for the waveguide and substrate. Only the potassium and sodium values are of interest because they are the only elements that participate in the ion-exchange; note that the other elemental ratios remain unchanged within experimental error. Hence, we obtain

$$h_K = \frac{0.0894 - 0.0042}{0.0941} = 90.5 \pm 1\%$$

which is typical of $K^+ - Na^+$ ion-exchange in glass and is in excellent agreement to the 90% value published by Doremus [23]. The results of this surface analysis also suggests that there is no effect from other impurities on the field-assisted ion-exchanged sample. Other surface analyses done on both surface and buried guides are to be presented in Chapter 5.

The analysis becomes more complicated for the bevelled sample because the bevel angle and interface location must be determined accurately. In addition, an automated line scan with auto-focusing of the direction perpendicular to the sample surface (z direction) is very desirable in the analysis. In general, the sample may be tilted by an angle α_1, while in the EMP holder, as shown in Fig. 3.20. The probe does a spot analysis at a given y position, then the holder stage moves horizontally along y by a small amount and the process is repeated until the whole sample has been scanned. By geometry, we see that $d_{pb} = y' \tan(\theta)$, where $\theta = \alpha_2 - \alpha_1$, and

$y' = y/\cos(\alpha_1)$ to yield the probing depth d_{pb}

$$d_{pb} = \frac{y\tan(\theta)}{\cos(\alpha_1)} = \frac{y\tan(\alpha_2 - \alpha_1)}{\cos(\alpha_1)} \tag{3.7}$$

This variable depth, perpendicular to the sample surface, is along the sample's z direction and hence, $z = d_{pb}$. The variation of the atomic K with z gives an accurate measure of the concentration profile. An example is presented for sample 8-92D. A plot of the z-focus distance versus displacement y is shown in Fig. 3.21. From this plot, the interface location (to be used as the $z = 0$ reference) and the bevel angle can be determined. The dark circles, representing actual focusing measurements, can be fitted by linear regression to find the intersection point and the angles α_1 and α_2. For this sample, we find that $\theta = 1.0115^o$ which provides for good resolution in depth of about $0.5\,\mu m$. This angle is then used with (3.7) and the atomic K concentration to determine the profile.

Oxide	Fisher glass (wt. %)	EMP measured (wt. %)	$N620$ (wt. %)	$KN9$ (wt. %)
SiO_2	72.25	72.35 ± 0.32	72.08	74.70
Na_2O	14.31	14.04 ± 0.11	14.39	5.48
K_2O	1.20	0.95 ± 0.02	0.41	4.40
CaO	6.40	6.18 ± 0.10	7.11	0.14
Al_2O_3	1.20	1.27 ± 0.01	1.80	10.74
MgO	4.30	4.22 ± 0.05	3.69	0.01

Table 3.2: Quantitative electron-probe microanalysis

Element	substrate	8-92D
Si	0.2501 ± 0.0004	0.2538 ± 0.0005
Na	0.0941 ± 0.0008	0.0003 ± 0.0001
K	0.0042 ± 0.0001	0.0894 ± 0.0013
Ca	0.0229 ± 0.0004	0.0237 ± 0.0001
Al	0.0052 ± 0.0001	0.0052 ± 0.0001
Mg	0.0217 ± 0.0003	0.0219 ± 0.0002

Table 3.3: Atomic concentration ratios of the elements

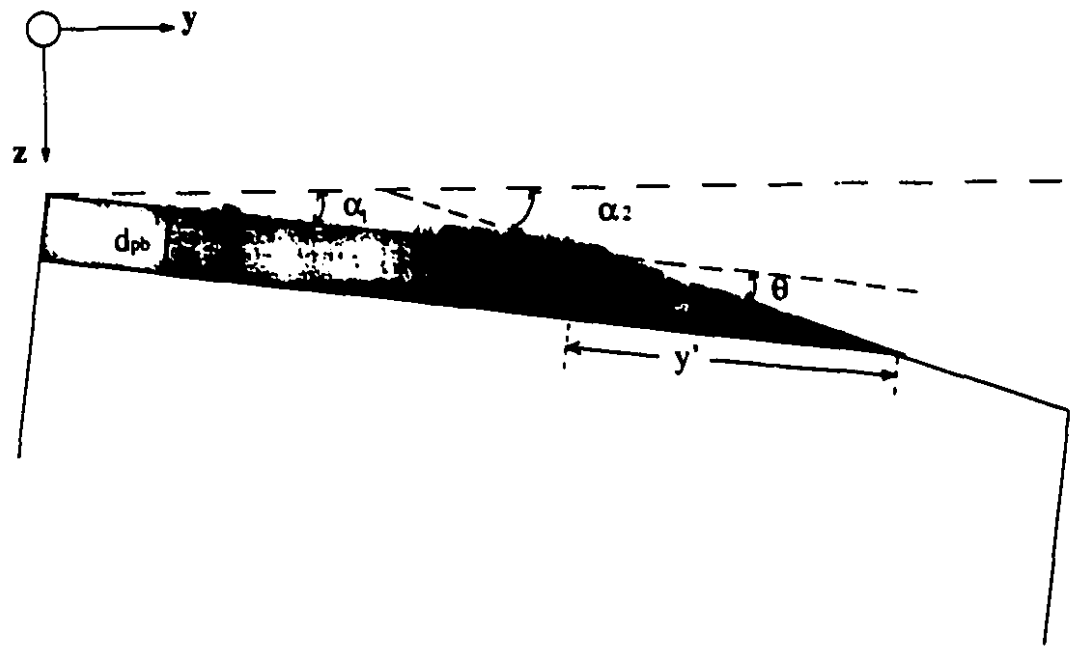

Figure 3.20: Schematic of bevelled sample in EMP holder

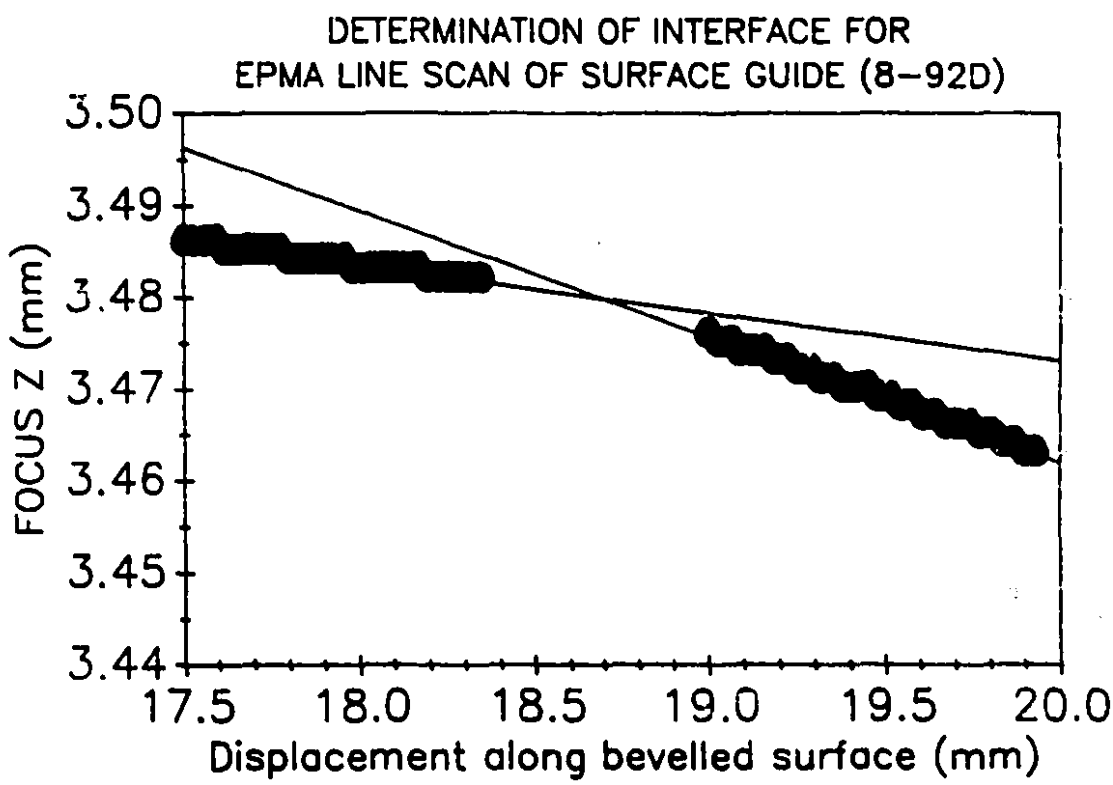

Figure 3.21: Plot of z-focus vs. horizontal displacement

3.6 Appendix 3A

The field-assisted ion-exchange fabrication procedure is described below.

1. The Teflon sheets are needed to electrically isolate the electrode and substrate. Two "U" shaped pieces and one rectangular piece are cut, as shown in Fig. 3.1(b). The Teflon can withstand the high temperatures of the furnace, although it shows signs of degradation after each process. New sheets must be used for every procedure.

2. **Electrode sandwich.** The rectangular sheet is placed on one steel plate. Then one electrode is put on top of it, followed by a "U" sheet, the glass substrate, another "U" sheet, the other electrode and the other steel plate in a sandwich-like process. One must ensure that the smooth part of the glass substrate is facing the bottom (positive) electrode. Also, the steel plates should always be flat and smooth; 600 grit polishing paper should be used. The seven screws and bolts are inserted in the plates and tightened gently. Tightening too hard will cause the substrate to crack during cooling however, if the setup is too loose, the molten salt will leak into the sand. Practice is needed to develop the correct tightness.

3. One Teflon-coated wire is fastened by screw into a small hole located at the corner of the positive electrode.

4. Then, the aluminum plate with the attached angled brackets is fastened to both steel plates by two small screws. The other wire is now attached to one of these screws on the steel plate that is in contact with the other electrode.

5. At this point, a simple resistance check is needed to ensure electrical isolation. This is done by measuring the resistance between the two electrodes. A high resistance ($> 20\,M\Omega$) signifies good electrical isolation.

6. The whole setup is now placed in a tin can which is then filled with ordinary sand using a funnel.

7. The melt containers, attached to the T-section wire levers, are then filled with salt crystals. About $10-12\,g$ of salt is measured and placed into each container. This amount may be decreased in order to obtain a smaller ionic current, if desired.

8. The tin can and the T-section configuration is then fitted into the special black-anodized aluminum cylinder and placed carefully in the furnace using a U-shaped wire. The furnace is then covered with the lid with two wires emanating from a hole in the center.

9. The electric circuit is completed as shown in Fig. 3.4.

10. The furnace is turned on and a waiting period of about $3\,h$ is needed for the temperature to reach 385^oC.

11. After this time, the lid is removed and the containers holding the molten salt are tilted by lifting the wire levers with a steel caliper so that the salt is poured into the cones. Cotton gloves should be used to avoid any burns.

12. After pouring the melt, the containers and the cones are removed immediately and the lid is replaced. The voltage source is turned on and the ammeter begins recording the ionic current in desired intervals of time. If a short occurs, the voltage will be low and the current high. Turn off the furnace and voltage source and return to step 1 after the furnace has cooled down.

13. When the exchange time is reached, the power supply and furnace are turned off and the asbestos lid is removed by placing it near the side of the furnace opening. A steel caliper is helpful to remove the lid.

14. Wait for ten minutes. This step avoids thermal shock and subsequent cracking of the substrate. However, it means that the waveguides are still being influenced by ion exchange. During these ten minutes, the temperature decreases and the average temperature is measured to be 379°C. This cooling step must be included in the concentration profile modeling (see Chapter 2). Future improvement of this step is needed to simplify the process.

15. Finally, the whole setup is removed from the furnace using the U-shaped wire and is allowed to cool down for one hour.

16. After cooling, the tin can is removed, the sand is poured back in its place and the seven screws and bolts are undone. The electrodes are still quite hot, so cotton gloves should be used. Then, the electrode structure is placed into a pan filled with boiling hot water. Within a few minutes, the salt has mostly dissolved and the substrates can be removed easily. They should be rinsed with D.I. water to remove any residue.

3.7 Appendix 3B

The sputtering procedure is described below in detail. The Cooke Vacuum sputtering system is shown in Fig. 3.22. It consists of a substrate holder, a J-head target holder, a rf matching network, a rf generator, and a water cooling system. Further details may be obtained from the Cooke CV-300 manual and an internal lab report [24].

1. Follow the instructions for setting the metal ring for GLO-discharge, connecting the electrical terminals, and grounding the mesh guard of the bell jar to the vacuum system chassis [24].

2. Make sure all valves are closed, turn on a mechanical pump and open a water valve. Switch to the Foreline position and allow the vacuum system to reach equilibrium. A thermocouple gauge located on the adjacent unit is switched to

TC-1 and should indicate less than 25 μm. Switch on a diffusion pump that takes 20 min to warm up.

3. The J-head target holder should be turned over and lying on a desk. Open a fan-type shutter and turn the J-head clockwise by 2", enough to fix the substrate with the steel strips. Turn back the shutter and the J-head. Clean the baseplate of the rf matching network with acetone. Using H.P. nitrogen gas, spray the substrate to remove any dust.

4. Grab the neck of the J-head and lift the module so as to place it carefully on the bell jar. Fasten the suspended metal cover to the box housing and connect the wires on the mesh guard to one of the four steel fasteners. Connect the plastic water tubing for the J-head target and turn on a second water valve.

5. Unlock a counterweight by removing a screw and lift up the module slowly.

6. Place the Al_2O_3 target on the J-head holder and adjust its position so that it is flush with the holder.

7. Push down the module slowly and lock the counterweight. Ensure that the baseplate of the module covers completely the upper rubber seal of the bell jar. Also re-check the target position to ensure it hasn't moved.

8. The vacuum system should now have reached full operation with TC-1 being lower than 25 μm.

9. Switch to the Roughing position and turn the gauge to TC-2. After 15-20 min, TC-2 should reach 20 μm.

10. When TC-2 reaches 20 μm, open the main valve of the Ar/O_2 gas cylinder and set an output pressure of 12 PSI. Then, push up a toggle valve on the left-hand side of the vacuum system and open fully a needle valve. Keep the two valves

open for two minutes to exhaust air in a gas inlet line with the mechanical pump.

11. TC-2 should return to less than 20 μm about two minutes after the toggle and needle valves are closed.

12. Move the switch back to the Foreline position. After TC-1 returns to less than 25 μm, open the high-vacuum (H.V.) valve.

13. After TC-1 recovers to about 30 μm, turn off the thermocouple gauge and switch on the cold cathode (C.C.) gauge. The vacuum level should reach 3-4 $\times 10^{-5}$ Torr in about 30 min.

14. Pour about 1 l of liquid nitrogen into the cold trap of the diffusion pump. Within 2 min, the vacuum level should reach less than 2×10^{-6} Torr, which is necessary background presure for sputtering.

15. Turn off the C.C. gauge and close the H.V. valve.

16. Push up the toggle valve and turn the needle valve four and a half turns counterclockwise.

17. Open the H.V. valve in small increments until TC-2 reaches 20 μm.

18. Check TC-1. Ideally, it should be around 50 μm; if it is lower, open the needle valve slightly. Adjust the H.V. and needle valves so that TC-1 and TC-2 read 50 μm and 20μm, respectively.

19. Turn off the thermocouple gauge and turn on the rf generator. After three minutes, the 'ready' lamp should be on. Wait about three minutes more and then turn on a rf switch.

20. Slowly begin to turn the 'output control' dial clockwise until the forward and reflected power begin to increase. Also, check the target voltage on the box

housing of the module. Adjust capacitors C1 and C2 until a dip in the reflected power is noted and a violet-coloured plasma is ignited. One can also try to open slightly the fan-type shutter to excite the plasma. After plasma ignition, close the shutter, increase the power and re-tune C1 and C2 until the reflected power is zero. Check the target voltage to be close to 0.5 *kV*.

21. A pre-sputtering process of about 20 *min* is needed to clean the target surface.

22. After pre-sputtering, open the shutter fully and re-tune C1, C2, and the output control to obtain the desired target voltage and zero reflected power. The sputtering process is now started. Monitor the process every 10 *min* to ensure proper behaviour.

23. When the sputtering is complete,

    (a) turn the control dial counterclockwise to decrease the power

    (b) turn off the rf power upon which the plasma disappears

    (c) close the toggle and needle valves completely

    (d) close the main valve of the gas cylinder

    (e) wait for 2 *min*

    (f) open the H.V. valve fully to cool down the chamber (wait 45 *min*)

24. After cooling,

    (a) close the fan-type shutter

    (b) close the H.V. valve

    (c) turn off the diffusion pump

    (d) open the vent valve

    (e) close the second water valve and remove the tubing

As soon as the sputtering module can be detached from the rubber ring of the bell jar, close the vent valve.

25. Unlock the counterweight and lift up the module slowly. Remove the target from the J-head holder carefully and place it in its cover.

26. Push down the module and lock the counterweight again.

27. Unfasten the metal cover and the grounding wires from the module. Lift up the module from its edge, grab the neck of the J-head and turn it over on the desk. Turn the J-head slightly to remove the substrate with the sputtered film.

28. Turn off the mechanical pump and the water valve and vent the system.

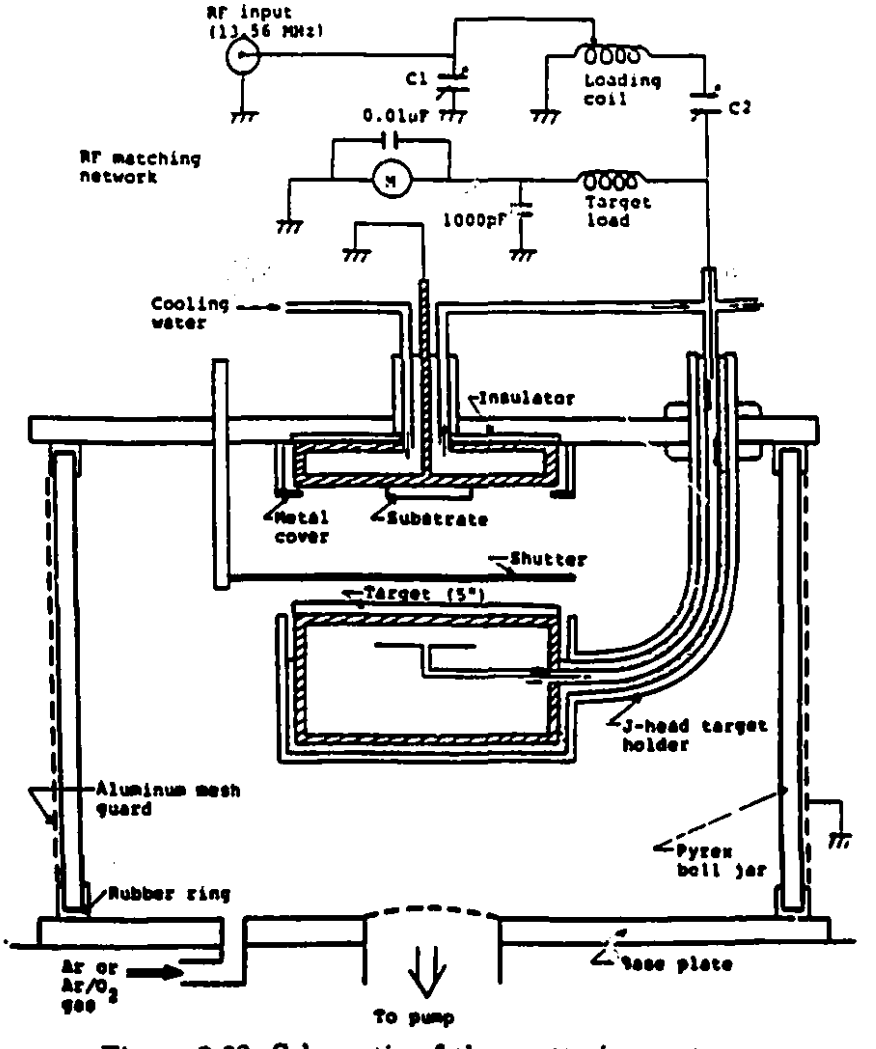

Figure 3.22: Schematic of the sputtering system

Bibliography

[1] F. Zernike. 'Fabrication and measurement of passive components'. in *Integrated Optics*. T. Tamir. Ed.. Springer Verlag. Berlin. 1975

[2] T. Findakly. 'Glass waveguides by ion-exchange: a review'. SPIE Opt. Eng.. 24 (2). pp. 244-250. 1985

[3] S. Urnes. 'Na-K Exchange in Silicate Glasses'. J. Amer. Cer. Soc.. 56 (10). pp. 514-519. 1973

[4] H. Nishihara. M. Haruna. T. Suhara. *Optical Integrated Circuits*. McGraw-Hill. New York. 1989

[5] P.K. Tien and R. Ulrich. 'Theory of prism-film coupler and thin-film light guides'. J. Opt. Soc. Amer.. 60 (8). pp. 1007-1015. 1970

[6] I.P. Kaminow and L.W. Stulz. 'Loss in cleaved Ti-diffused $LiNbO_3$ waveguides'. Appl. Phys. Lett.. 33 (1). pp. 62-63. 1978

[7] Y. Okamura. S. Yoshinaka. and S. Yamamoto. 'Measuring mode propagation losses of integrated optical waveguides: a simple method'. Appl. Opt.. 22 (23). pp. 3892-3894. 1983

[8] H.P. Weber, F.A. Dunn and W.N. Leibolt, 'Loss measurements in thin film optical waveguides', Appl. Opt., 12 (4), pp. 755-760, 1973

[9] W.K. Burns and G.B. Hocker, 'Endfire coupling between optical fibers and diffused channel waveguides', Appl. Opt., 16 (8), pp. 2048-2051, 1977

[10] K. Moroshita. 'Refractive-index-profile determination of single-mode optical fibers by a propagation-mode near-field scanning technique', J. Lightwave Technol., 1 (3), pp. 445-449, 1983

[11] G.L. Yip, P.C. Noutsios, and L. Chen. 'An improved propagation-mode near-field method for refractive index profiling of optical waveguides', accepted by Appl. Opt., Jan. 1996

[12] K. Morishita. 'Index profiling of three-dimensional optical waveguides by the propagation-mode near-field method', J. Lightwave Technol., 4 (8), pp. 1120-1124, 1986

[13] M. Halfmann, A. Kunz, and W. Heinlein. 'Comparison of measured and simulated mode fields in InP waveguides', Integrated Photonics Research IPR'94, San Fransisco, pp. 121-123, 1994

[14] J.R. Meyer-Arendt, *Introduction to Classical and Modern Optics*, 2nd ed., Prentice-Hall, New Jersey, 1984

[15] P.B. Crilly, 'A quantitative evaluation of various iterative deconvolution algorithms', IEEE Trans. Instrument. Meas., 40 (3), pp. 558-562, 1988

[16] J.C. Sprott, *Numerical Recipes: the Art of Scientific Computing*, Cambridge University Press, Cambridge, 1991

[17] W.B. Wetherell. 'The calculation of image quality', in *Applied Optics and Optical Engineering*, R.R. Shannon and J.C. Wyant, Eds., Academic Press, New York, 1980

[18] R. Castaing, Thesis, Univ. of Paris, France, 1948; 'Electron Probe Microanalysis,' in *Advances in Electronics and Electron Physics*, L. Marton, Ed., Academic Press, New York, 1960

[19] D.K. Schroder. *Semiconductor Material and Device Characterization*. Wiley & Sons. New York. 1990

[20] J.I. Goldstein. D.E. Newbury. P. Echlin. D.C. Joy. A.D. Romig. Jr.. C.E. Lyman. C. Fiori. and E. Lifshin. *Scanning Electron Microscopy and X-Ray Microanalysis*. Plenum Press. New York. 1990

[21] F. Maurice. L. Meny and R. Tixier *Microanalysis and Scanning Electron Microscopy*. Les Editions de Physique. Orsay. 1979

[22] V.D. Scott and G. Love. *Quantitative Electron-Probe Microanalysis*. Ellis Horwood Series in Physics. Wiley & Sons. New York. 1983

[23] R. H. Doremus. 'Ion exchange in glasses'. in *Ion-Exchange*. vol. 2. J.A. Marinsky. Ed.. Dekker. New York. 1969

[24] M. Masuda and G.L. Yip. 'Fabrication techniques of thin film optical waveguides using McGill facilities', Dept. of Electrical Engineering. McGill University. 1980

Chapter 4

Modeling of the Waveguide Characteristics

4.1 Introduction

In this chapter, the theoretical aspects of the optical waveguide propagation characteristics are presented. The planar and channel guide structures are described followed by the dispersion relations that are used to calculate the effective mode indices as a function of the waveguide dimensions. The general vector Helmholtz and Fresnel equations are also derived and their numerical solution is presented based on the Runga-Kutta technique and the vector beam propagation method.

4.1.1 Waveguide structures

Here, both planar and channel guide structures are studied. The planar guide structures of Figs. 4.1(a) and (b), are of the step-index and graded-index type, respectively. They are used to confine and propagate light along the z direction. The geometries are asymmetric since the bulk index n_b is different from that of the air-cover region, $n_o = 1.0$. For the step-index guides, the film index n_f is homogeneous throughout its film thickness d, whereas the graded-index guides have an inhomogeneous refractive index distribution $n(x) = n_b + \Delta n_s f(x)$ where $\Delta n_s = n_s - n_b$ is the maximum index change and $f(x)$ is any function describing the profile shape. For graded-index channel guides, shown in Fig. 4.2, the index distribution $n(x, y) = n_b + \Delta n_s f(x, y)$.

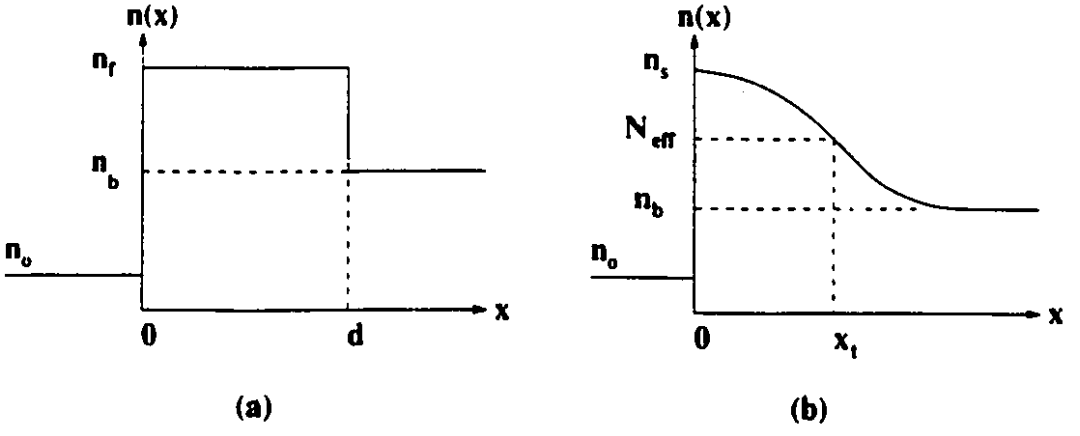

Figure 4.1: Planar waveguide structures: (a) step-index (b) graded-index

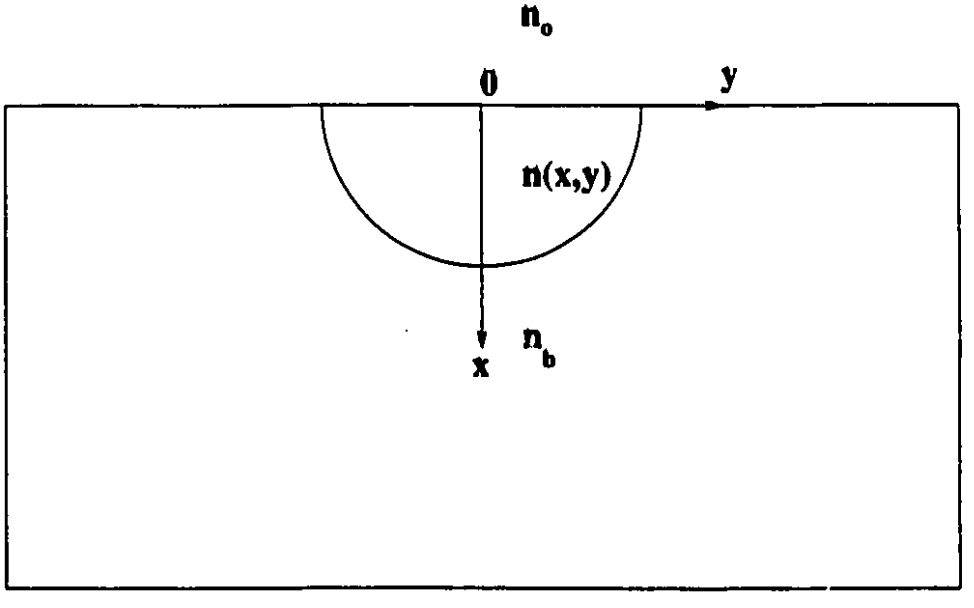

Figure 4.2: Graded-index channel guide structure

4.1.2 Helmholtz wave equations

The propagation of electromagnetic lightwaves in an inhomogeneous, source-free medium is governed by Maxwell's equations:

$$\vec{\nabla} \times \vec{H} - j\omega\epsilon\vec{E} = 0 \tag{4.1}$$

$$\vec{\nabla} \times \vec{E} + j\omega\mu_o\vec{H} = 0 \tag{4.2}$$

$$\vec{\nabla} \cdot (\epsilon\vec{E}) = 0 \tag{4.3}$$

$$\vec{\nabla} \cdot \vec{H} = 0 \tag{4.4}$$

with the fields having an exponential time dependence $\exp(j\omega t)$. Taking the curl of (4.2) and replacing (4.3) in the result, the vector Helmholtz equation for $\vec{E}$ can be derived as:

$$\vec{\nabla}^2\vec{E} + \vec{\nabla}\left(\frac{\vec{\nabla}\epsilon \cdot \vec{E}}{\epsilon}\right) + \omega^2\mu_o\epsilon\vec{E} = 0 \tag{4.5}$$

with $\vec{\nabla}\epsilon \neq 0$ since the dielectric term $\epsilon = \epsilon_o n^2(x, y, z)$ is inhomogeneous. If the refractive index is uniform along z, the transverse electric field components can be written separately as Helmholtz wave equations:

$$\nabla^2 E_x + n^2 k_o^2 E_x = -\frac{\partial}{\partial x}\left(\frac{1}{n^2}\frac{\partial n^2}{\partial x}E_x\right) - \frac{\partial}{\partial x}\left(\frac{1}{n^2}\frac{\partial n^2}{\partial y}E_y\right) \tag{4.6}$$

$$\nabla^2 E_y + n^2 k_o^2 E_y = -\frac{\partial}{\partial y}\left(\frac{1}{n^2}\frac{\partial n^2}{\partial x}E_x\right) - \frac{\partial}{\partial y}\left(\frac{1}{n^2}\frac{\partial n^2}{\partial y}E_y\right) \tag{4.7}$$

A waveguide mode describes a set of electromagnetic field components that satisfy Maxwell's equations and the appropriate boundary conditions. These field components maintain their spatial distribution as they propagate along z with the propagation constant β: the phase term $\exp(-j\beta z)$ is understood to be included. Thus, (4.6) and (4.7) reduce to:

$$\frac{\partial^2 E_x}{\partial x^2} + \frac{\partial^2 E_x}{\partial y^2} + (n^2(x,y)k_o^2 - \beta^2)E_x = -\frac{\partial}{\partial x}\left(\frac{1}{n^2}\frac{\partial n^2}{\partial x}E_x\right) - \frac{\partial}{\partial x}\left(\frac{1}{n^2}\frac{\partial n^2}{\partial y}E_y\right) \tag{4.8}$$

$$\frac{\partial^2 E_y}{\partial x^2} + \frac{\partial^2 E_y}{\partial y^2} + (n^2(x,y)k_o^2 - \beta^2)E_y = -\frac{\partial}{\partial y}\left(\frac{1}{n^2}\frac{\partial n^2}{\partial x}E_x\right) - \frac{\partial}{\partial y}\left(\frac{1}{n^2}\frac{\partial n^2}{\partial y}E_y\right) \tag{4.9}$$

These are the vector Helmholtz equations for the transverse electric field components: a similar set can be derived for the magnetic field. Note the coupled nature of the orthogonal components E_x and E_y that occurs due to the graded-index profiles.

The above equations can be classified generally into two types of mode solutions. If we consider a 1-D planar guide with $n = n(x)$ and $\partial/\partial y = 0$, then it can support transverse electric (TE) modes with $E_z = 0$ and transverse magnetic (TM) modes with $H_z = 0$. For TE modes, the non-trivial field components are (E_y, H_x, H_z) with

$$H_x = -\frac{\beta E_y}{\omega \mu_o} \tag{4.10}$$

$$H_z = \frac{j}{\omega \mu_o}\frac{\partial E_y}{\partial x} \tag{4.11}$$

and for TM modes, the non-trivial components are (H_y, E_x, E_z) [1] with

$$E_x = \frac{\beta H_y}{\omega \epsilon_o n^2(x)} \tag{4.12}$$

$$E_z = -\frac{j}{\omega \epsilon_o n^2(x)}\frac{\partial H_y}{\partial x} \tag{4.13}$$

Equations (4.9) and (4.10) are now simplified into

$$\frac{\partial^2 E_x}{\partial x^2} + (n^2(x)k_o^2 - \beta^2)E_x = -\frac{\partial}{\partial x}\left(\frac{1}{n^2}\frac{\partial n^2}{\partial x}E_x\right), \quad TM \tag{4.14}$$

$$\frac{\partial^2 E_y}{\partial x^2} + (n^2(x)k_o^2 - \beta^2)E_y = 0 \quad TE \tag{4.15}$$

For 2-D channel guide profiles, $n = n(x, y)$, (4.8) and (4.9) represent the coupled E_x (TM) and E_y (TE) equations. If we neglect this cross coupling, the modes can be classified as either quasi-TM or quasi-TE:

$$\frac{\partial^2 E_x}{\partial x^2} + \frac{\partial^2 E_x}{\partial y^2} + (n^2(x,y)k_o^2 - \beta^2)E_x = -\frac{\partial}{\partial x}\left(\frac{1}{n^2}\frac{\partial n^2}{\partial x}E_x\right), \quad quasi - TM \tag{4.16}$$

$$\frac{\partial^2 E_y}{\partial x^2} + \frac{\partial^2 E_y}{\partial y^2} + (n^2(x,y)k_o^2 - \beta^2)E_y = -\frac{\partial}{\partial y}\left(\frac{1}{n^2}\frac{\partial n^2}{\partial y}E_y\right), \quad quasi - TE \tag{4.17}$$

4.1.3 Fresnel wave equations

The Fresnel wave equations are an approximation to the full vector Helmholtz equations. These Fresnel equations assume that the wave propagation is paraxial. Let us presume that the transverse field components E_t (E_x or E_y) can be expressed as plane waves:

$$E_t = \Psi_t e^{-jn_r k_o z} \tag{4.18}$$

travelling along z in a homogeneous medium where n_r is a reference refractive index. Substituting (4.18) into (4.6) or (4.7) and assuming the fields are slowly varying with respect to z, i.e. $\partial^2\Psi_t/\partial z^2 \approx 0$, we obtain the coupled set of parabolic partial differential equations:

$$j2n_r k_o \frac{\partial \Psi_x}{\partial z} = \mathcal{L}_{xx}\Psi_x + \mathcal{L}_{xy}\Psi_y \tag{4.19}$$

$$j2n_r k_o \frac{\partial \Psi_y}{\partial z} = \mathcal{L}_{yx}\Psi_x + \mathcal{L}_{yy}\Psi_y \tag{4.20}$$

where the differential operators are defined by:

$$\mathcal{L}_{xx}\Psi_x = \frac{\partial}{\partial x}\left[\frac{1}{n^2}\frac{\partial}{\partial x}(n^2\Psi_x)\right] + \frac{\partial^2\Psi_x}{\partial y^2} + (n^2 - n_r^2)k_o^2\Psi_x \tag{4.21}$$

$$\mathcal{L}_{yy}\Psi_y = \frac{\partial}{\partial y}\left[\frac{1}{n^2}\frac{\partial}{\partial y}(n^2\Psi_y)\right] + \frac{\partial^2\Psi_y}{\partial x^2} + (n^2 - n_r^2)k_o^2\Psi_y \tag{4.22}$$

$$\mathcal{L}_{xy}\Psi_y = \frac{\partial}{\partial x}\left[\frac{1}{n^2}\frac{\partial}{\partial y}(n^2\Psi_y)\right] - \frac{\partial^2\Psi_y}{\partial x \partial y} \tag{4.23}$$

$$\mathcal{L}_{yx}\Psi_x = \frac{\partial}{\partial y}\left[\frac{1}{n^2}\frac{\partial}{\partial x}(n^2\Psi_x)\right] - \frac{\partial^2\Psi_x}{\partial y \partial x} \tag{4.24}$$

The right-hand side of (4.19) and (4.20) can be expanded out and written more conveniently using intermediate operators:

$$j2n_r k_o \frac{\partial \Psi_x}{\partial z} = (\mathcal{A}_x + \mathcal{A}_{xn} + \mathcal{A}_y + \mathcal{A}_o)\Psi_x + \mathcal{B}_{xy}\Psi_y \tag{4.25}$$

$$j2n_r k_o \frac{\partial \Psi_y}{\partial z} = (\mathcal{A}_y + \mathcal{A}_{yn} + \mathcal{A}_x + \mathcal{A}_o)\Psi_y + \mathcal{B}_{yx}\Psi_x \tag{4.26}$$

where

$$\mathcal{A}_x = \frac{\partial^2}{\partial x^2}$$

$$\mathcal{A}_y = \frac{\partial^2}{\partial y^2}$$

$$\mathcal{A}_o = (n^2 - n_r^2)k_o^2$$

$$\mathcal{A}_{xn} = \frac{2}{n}\left[\frac{\partial^2 n}{\partial x^2} + \frac{\partial n}{\partial x}\frac{\partial}{\partial x} - \frac{1}{n}\left(\frac{\partial n}{\partial x}\right)^2\right]$$

$$\mathcal{A}_{yn} = \frac{2}{n}\left[\frac{\partial^2 n}{\partial y^2} + \frac{\partial n}{\partial y}\frac{\partial}{\partial y} - \frac{1}{n}\left(\frac{\partial n}{\partial y}\right)^2\right]$$

$$\mathcal{B}_{xy} = \frac{2}{n}\left[\frac{\partial^2 n}{\partial x \partial y} + \frac{\partial n}{\partial y}\frac{\partial}{\partial x} - \frac{1}{n}\left(\frac{\partial n}{\partial x}\right)\left(\frac{\partial n}{\partial y}\right)\right]$$

$$\mathcal{B}_{yx} = \frac{2}{n}\left[\frac{\partial^2 n}{\partial y \partial x} + \frac{\partial n}{\partial x}\frac{\partial}{\partial y} - \frac{1}{n}\left(\frac{\partial n}{\partial x}\right)\left(\frac{\partial n}{\partial y}\right)\right]$$

These are the general vector differential operators for three-dimensional (x, y, z) structures. The vector properties are responsible for the polarization dependent propagation of the optical guided waves due to the inequality of the $\mathcal{L}_{xx}$ and $\mathcal{L}_{yy}$ operators. The coupling between the two orthogonal polarizations occurs through the $\mathcal{L}_{xy}$ and $\mathcal{L}_{yx}$ operators. These general Fresnel equations will be used in the beam propagation algorithms in the following sections. The cross coupling polarization effects and the refractive index gradients are taken fully into consideration. The only aproximation made is that of paraxial propagation. Note that for planar waveguides with $n = n(x)$, the cross coupling between Ψ_x and Ψ_y vanishes and the waves are decomposed into purely TE and TM modes that can be treated separately:

$$j2n_r k_o \frac{\partial \Psi_x}{\partial z} = (\mathcal{A}_x + \mathcal{A}_{xn} + \mathcal{A}_o)\Psi_x, \quad TM \tag{4.27}$$

$$j2n_r k_o \frac{\partial \Psi_y}{\partial z} = (\mathcal{A}_x + \mathcal{A}_o)\Psi_y, \quad TE \tag{4.28}$$

4.2 Dispersion relations

Waveguide dispersion relations are important in the design of integrated optical devices because they convey the relationship between the effective mode indices and the waveguide dimension. These relations are presented in many textbooks [1, 2]. Here, the dispersion relations for step-index and graded-index profiles are stated only.

4.2.1 Step-index profiles

For the special case of planar surface guides fabricated by rf sputtering, the index profile has been shown to be step-like [3] with film index, n_f, as shown in Fig. 4.1(a). The well-established relations for such slab waveguides can be solved by applying the continuity of the relevant field components to obtain [1]:

$$d = \frac{\phi_1 + \phi_2 + m\pi}{k_o\sqrt{n_f^2 - N_{eff}^2}},\ m = 0, 1, 2, \ldots \tag{4.29}$$

where the phase shifts ϕ_1 and ϕ_2 at the guide-substrate and air-substrate interfaces, respectively, are:

$$\phi_1 = \tan^{-1}\left(\chi^*\sqrt{N_{eff}^2 - n_b^2/n_f^2 - N_{eff}^2}\right);\phi_2 = \tan^{-1}\left(\chi\sqrt{N_{eff}^2 - 1.0/n_f^2 - N_{eff}^2}\right) \tag{4.30}$$

and

$$\chi^* = \begin{cases} 1 & \text{TE modes} \\ (n_f/n_b)^2 & \text{TM modes} \end{cases} \quad \chi = \begin{cases} 1 & \text{TE modes} \\ n_f^2 & \text{TM modes} \end{cases}$$

The exact TM mode field solution for this three-layer structure, shown in Fig. 4.3(a), is:

$$H_y(x) = \begin{cases} A\exp(-q_i x) & 0 < x < \infty \\ A\left\{(\cos(h_i x) - \frac{q_i}{h_i}\sin(h_i x)\right\} & -D_2 < x < 0 \\ A\left\{\cos(h_i D_2 + \frac{q_i}{h_i}\sin(h_i D_2)\right\}\exp(p_i(x + D_2)) & -\infty < x < -D_2 \end{cases} \tag{4.31}$$

where $q_i = k_o\sqrt{N_{eff}^2 - n_b^2}, p_i = k_o\sqrt{N_{eff}^2 - n_1^2}$, $h_i = k_o\sqrt{n_2^2 - N_{eff}^2}$ and $\bar{q}_i \equiv n_2^2 q_i/n_b^2$. Using (4.12), the corresponding electric field component $E_x = \beta H_y(x)/\omega\epsilon_o n^2$ with $\beta = k_o N_{eff}$.

4.2.2 Graded-index profiles

The WKB method can be used to obtain approximate solutions of the Helmholtz equation for slowly varying inhomogeneous profiles. This method is well-known, especially in the quantum mechanics literature, and its applications to planar waveguides has been discussed by many researchers [4].

For planar surface guides, the WKB integral relation

$$k_o d \int_0^{\hat{x}_t} \sqrt{n^2(\hat{x}) - N_e^2} d\hat{x} = \phi_1 + \phi_2 + m\pi. \quad m = 0, 1, 2, \ldots \tag{4.32}$$

with ϕ_1 and ϕ_2 similar to (4.30) except that n_f is replaced by n_s (see Fig. 4.1(b)). The other parameter $\hat{x} = x/d$, and x_t is the turning point defined by $n(x_t) = N_{eff}$. The dispersion curves for the surface planar guides are generated by this method.

4.2.3 Four-layer step-index relations

The dispersion relation of a four-layer structure, used to model the $GaAs$ photodetector embedded in Al_2O_3, can be derived using the well-known transverse resonance technique (TRT). It is based on the transmission line model of the transverse cross section [5], shown in Fig. 4.4. The TRT condition requires that the total impedance looking towards the cover region and the substrate region is zero, i.e. $Z_1' + Z_2' = 0$. The TE and TM dispersion relations and further details are provided in Appendix 4A. Since this method offers the dispersion relation only, the field profiles can be determined by solving the Helmholtz equation with the appropriate boundary conditions [6]. The TM solution for the four-layer structure shown in Fig. 4.3(b) yields:

$$H_y(x) = \begin{cases} A\exp(-q_j x) & 0 < x < \infty \\ A\left(\cos(h_j x) - \frac{\bar{q}_j}{h_j}\sin(h_j x)\right) & -D_3 < x < 0 \\ A\left(\cos(h_j D_3) + \frac{\bar{q}_j}{h_j}\sin(h_j D_3)\right)\cos(r_j(x+D_3)) + & \\ \left(\frac{\bar{h}_j}{r_j}\sin(h_j D_3) - \left(\frac{n_2}{n_4}\right)^2 \frac{\bar{q}_j}{r_j}\cos(h_j D_3)\right)\sin(r_j(x+D_3)) & -D_T < x < -D_3 \\ AH_y(-D_T)\exp(p_d(x+D_T)) & x < -D_T \end{cases} \tag{4.33}$$

where $D_T = D_2 + D_3$, $q_j = k_o\sqrt{N_{eff}^2 - n_b^2}$, $p_d = k_o\sqrt{N_{eff}^2 - n_1^2}$, $h_j = k_o\sqrt{n_3^2 - N_{eff}^2}$, $r_j = k_o\sqrt{n_2^2 - N_{eff}^2}$, $\bar{h}_j \equiv n_2^2 h_j/n_3^2$ and $\bar{q}_j \equiv n_2^2 q_j/n_b^2$.

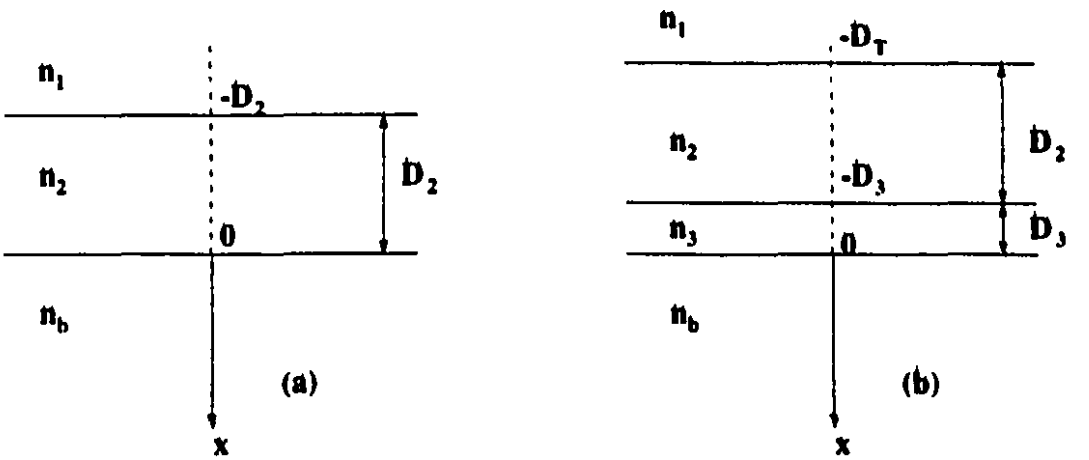

Figure 4.3: (a) Three-layer and (b) four-layer structure

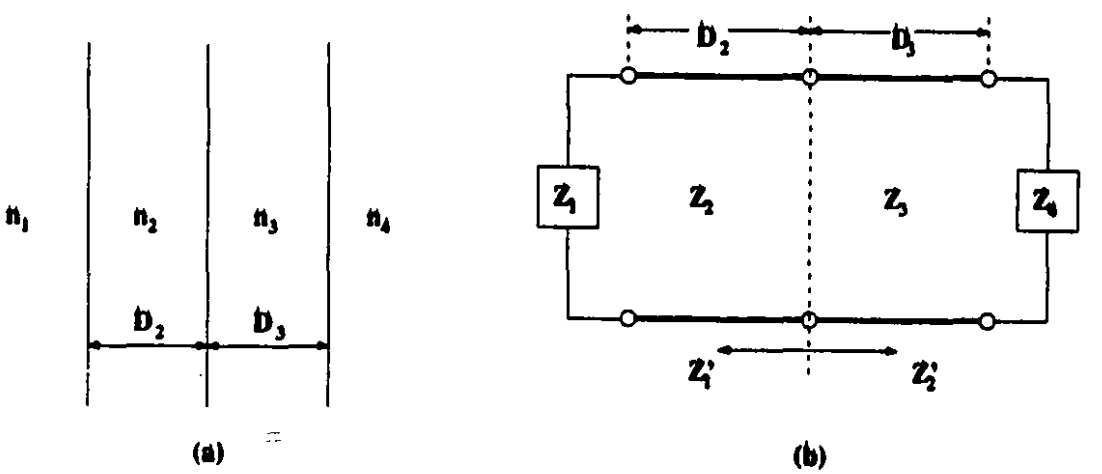

Figure 4.4: (a) Transverse cross section (b) TRT transmission line model

4.3 Runga-Kutta solutions

4.3.1 Background

As we have seen, the propagation constant and modal field distribution can in general be obtained from the solution of the vector Helmholtz equation. However, except for a few refractive index profiles [1], analytical solutions do not exist. Hence, one uses either approximate methods such as the variational method and the WKB method or uses numerical methods to obtain the solution [7]. It has been shown that the WKB method does not give accurate results for lower order modes close to cutoff [8]. Hence, one must try another method to obtain more accurate dispersion curves, especially in the single-mode region. One numerical method that yields promising results [9] uses a simple Runga-Kutta technique after transforming the Helmholtz equation into a first order linear (Ricatti) differential equation. Results show that more accurate effective index values are obtained than by using WKB.

4.3.2 Computation of the effective mode indices

For a planar waveguide with $n = n(x)$, the Helmholtz equations (4.14) and (4.15) can be written as [9]

$$\frac{d^2\phi}{d\xi^2} + k_o^2 d^2[n^2(\xi) - N_{eff}^2]\phi = 0, \quad TE \tag{4.34}$$

$$\frac{d^2\phi}{d\xi^2} + k_o^2 d^2[n^2(\xi) - N_{eff}^2]\phi = \left[\frac{3}{4}\left(\frac{1}{n^2}\frac{dn^2}{d\xi}\right)^2 - \frac{1}{2n^2}\frac{d^2n^2}{d\xi^2}\right]\phi, \quad TM \tag{4.35}$$

where $\phi = E_y$ for TE and $\phi = n(x)E_x$ for TM with $\xi = x/d$. Using

$$G = \frac{1}{\phi}\frac{d\phi}{d\xi}$$

(4.34) and (4.35) reduce to first-order Ricatti differential equations:

$$\frac{dG}{d\xi} = -G^2 - k_o^2 d^2[n^2(\xi) - N_{eff}^2] \tag{4.36}$$

$$\frac{dG}{d\xi} = -G^2 - k_o^2 d^2\left[n^2(\xi) - \frac{3}{4k_o^2 d^2}\left(\frac{1}{n^2}\frac{dn^2}{d\xi}\right)^2 + \frac{d^2n^2/d\xi^2}{2k_o^2 d^2 n^2} - N_{eff}^2\right] \tag{4.37}$$

which are solved using Runga-Kutta techniques with appropriate boundary conditions. To obtain the boundary conditions on G, we observe that for TE modes, both ϕ and $d\phi/d\xi$ (proportional to tangential fields) are continuous everywhere, including the boundaries. Thus, G is continuous everywhere. In air ($n = 1.0$ and $\xi < 0$), (4.36) and (4.37) become:

$$\frac{d^2\phi}{d\xi^2} - k_o^2 d^2[N_{eff}^2 - 1]\phi = 0$$

with general solution

$$\phi(\xi) = C_1 \exp\left[k_o d\xi\sqrt{N_{eff}^2 - 1}\right] + C_2 \exp\left[-k_o d\xi\sqrt{N_{eff}^2 - 1}\right]$$

Since the modal field must vanish away from the surface, then $\phi \to 0$ as $\xi \to -\infty$, so that the second solution must be rejected, leaving us with

$$\phi \propto \exp\left[k_o d\xi\sqrt{N_{eff}^2 - 1}\right]$$

Hence, the boundary condition on G is

$$G(\xi = 0^+) = G(\xi = 0^-) = \frac{1}{\phi}\frac{d\phi}{d\xi}\bigg|_{\xi=0^-} = k_o d\sqrt{N_{eff}^2 - 1} \tag{4.38}$$

However, for TM modes, H_y and $(1/n^2)dH_y/d\xi$ (proportional to tangential field E_z) are continuous everywhere, and using (4.13) we get for H_y continuity:

$$n(\xi = 0^+)\phi(\xi = 0^+) = n(\xi = 0^-)\phi(\xi = 0^-) \tag{4.39}$$

Similarly, using the above condition, we get:

$$\frac{1}{n^2(\xi)}\frac{dH_y}{d\xi}\bigg|_{\xi=0^+} = \frac{1}{n^2(\xi)}\frac{dH_y}{d\xi}\bigg|_{\xi=0^-}$$

and after some manipulations we get,

$$G(\xi = 0^+) = k_o d(n_b + \Delta n_s f(0))^2\sqrt{N_{eff}^2 - 1} - \frac{\Delta n_s}{n_b + \Delta n_s f(0)}\frac{df}{d\xi}\bigg|_{\xi=0^+} \tag{4.40}$$

Since the refractive index saturates to n_b far into the substrate (i.e. $\xi \to \xi_o$, $\xi_o \to \infty$), the field is expected to tend as $\exp(-k_o d\xi\sqrt{N_{eff}^2 - n_b^2})$ and thus,

$$G(\xi)|_{\xi\to\xi_o} = -k_o d\sqrt{N_{eff}^2 - n_b^2} \tag{4.41}$$

To summarize, for a planar surface or buried waveguide with given values of k_o, d (or x_{peak}), n_s, Δn_s, and $f(\xi)$, the problem of computing N_{eff} for a particular mode is reduced to the solution of the differential equation (4.36) or (4.37) with boundary conditions given by (4.38) or (4.40) and (4.41).

4.3.3 Single-mode field profiles

The numerical model is also useful for deducing the transverse modal fields E_y and H_y as functions of ξ. Since ϕ satisfies a linear differential equation, the solution is unique apart from a constant multiplier. Hence, without loss of generality, we may assume the field to be unity at the air-guide interface (i.e. $\phi(0) = 1.0$). Since,

$$\frac{d\phi}{d\xi} = G\phi,$$

the separable differential equation can be solved at any arbitrary value of ξ as:

$$\phi(\xi) = \exp\left\{\int_0^{\xi} G(\xi')d\xi'\right\} \tag{4.42}$$

Once N_{eff} is determined, the integral is computed numerically using Simpson's rule [10] with the integrand $G(\xi')$.

4.3.4 Numerical methodology

Equation (4.36) or (4.37) can be solved numerically using a fourth order Runga-Kutta method [10] as follows:

$$\begin{aligned} G_1 &= G_o + \frac{1}{6}(k_1 + 2k_2 + 2k_3 + k_4) \qquad (4.43)\\ k_1 &= \Delta x \Gamma(\xi_o, G_o)\\ k_2 &= \Delta x \Gamma\left(\xi_o + \frac{\Delta x}{2}, G_o + \frac{k_1}{2}\right)\\ k_3 &= \Delta x \Gamma\left(\xi_o + \frac{\Delta x}{2}, G_o + \frac{k_2}{2}\right)\\ k_4 &= \Delta x \Gamma(\xi_o + \Delta x, G_o + k_3) \end{aligned}$$

where G_1 is the value of G after a step of size Δx has been taken. G_o is the boundary condition expressed in (4.38) or (4.40). The function $\Gamma(\xi, G)$ represents the right hand side of (4.36) or (4.37). The associated truncation error is $\sim (\Delta x)^5$.

The differential equation for G must be solved simultaneously while 'shooting' [10] for the boundary condition at infinity (4.41). This transcendental equation can be tackled using the Secant root search method [10]. The accuracy of the solution depends on the value of ξ_o which can be chosen arbitrarily. Hence, before proceeding, one has to choose a value of ξ_o and two initial guesses for N_{eff}. These two values are related in the sense that, if N_{eff} is not sufficiently close to the true value of N_{eff} (which must be determined), the solution may blow up even before ξ reaches ξ_o. Hence, the correct choice of the initial values of N_{eff} and ξ_o is quite important in the analysis [11]. The following steps have been taken to solve the problem:

- Choose a low enough value of ξ_o, say $1.0 \leq \xi_o \leq 1.5$, and two initial guesses for N_{eff} ($n_b < N_e < n_b + \Delta n_s$). The step size Δx is 0.005 and the new value of N_{eff} is determined by the Secant method.

- Increase the value of ξ_o by 0.1, using the N_{eff} obtained above as the initial guess to solve N_{eff} with better accuracy.

- The process is repeated until the desired accuracy of N_{eff} (about 1×10^{-6}) is reached.

These steps can be easily programmed to determine the effective index of the mode and its field profile. Typical computing times for these simulations, that depend on the chosen value of Δx, ranged from $30\,s$ to $1\,min$ on a SunSparc5 station.

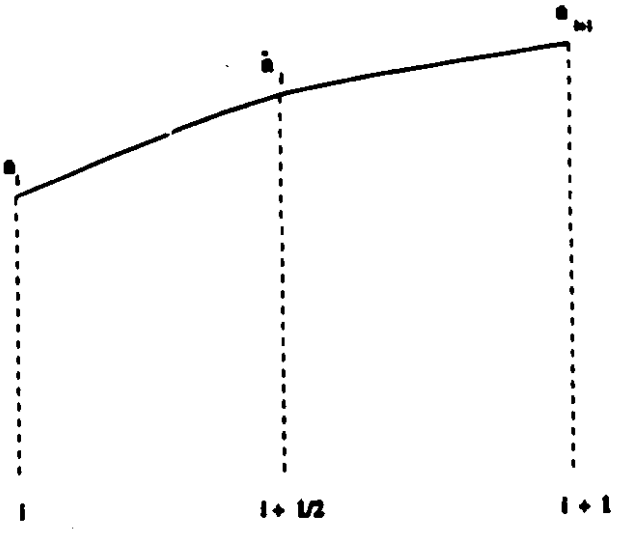

Figure 4.5: Discrete form of index at $\Delta x/2$

On a final note, it is worth mentioning that (4.43) can be used to accommodate for index profiles that can be represented analytically, such as the Gaussian and exponential. However, in the event that $n(x)$ is provided in discrete form, i.e. $n(x_i)$ with $x_i = i\Delta x$, $i = 0, 1, 2..$, then some small changes to (4.43) need to be made. For k_1 and k_4, $n(x_i)$ and $n(x_i + \Delta x)$ are needed and can be discretized in the spatial domain to yield derivatives:

$$\frac{dn}{dx} = \frac{n_{i+1} - n_i}{\Delta x} \qquad \frac{d^2n}{dx^2} = \frac{n_{i+1} - 2n_i + n_{i-1}}{(\Delta x)^2}$$

However, for k_2 and k_3, $n(x_i + \Delta x/2)$ is needed and not available in discrete form. Hence, we define the index in between two discrete points as the average $\bar{n}_i = (n_i + n_{i+1})/2$ (see Fig. 4.5) and the derivatives (in central-difference form) now become:

$$\frac{dn}{dx} = \frac{n_{i+1} - n_i}{\Delta x} \qquad \frac{d^2n}{dx^2} = \frac{n_{i+1} - 2\bar{n}_i + n_i}{(\Delta x/2)^2}$$

Finally, we note that the forward-difference form for dn/dx used for k_1 and k_4 and the central-difference form used for k_2 and k_3 was implemented in this way solely for the convenience of numerical implementation.

4.3.5 Effective index method

The effective index method (EIM) is a widely used analytical tool in integrated optics. First proposed by Knox and Toulios in 1970 [12], it has been improved and extended to inhomogeneous channel guides by many researchers including Hocker and Burns [13]. Basically, the method describes the reduction of the 2-D Helmholtz equation into two simpler 1-D equations. The version described below has been modified to create a vertical effective index profile instead of the conventional lateral profile. In this thesis, the EIM was used to complement the 3-D BPM by providing the initial 2-D field profile. In addition, this profile is used in mode mismatch loss calculations to be presented in Chapter 5.

We begin with the vector Helmholtz equation for the quasi-TM mode represented by $E_x(x,y)$ that satisfies (4.16). A separation of variables approach is then used:

$$E_x(x,y) = F(x,y)G(x) \tag{4.44}$$

and (4.16) becomes:

$$G\frac{\partial^2 F}{\partial x^2}+F\frac{\partial^2 G}{\partial x^2}+G\frac{\partial^2 F}{\partial y^2}+2\frac{\partial F}{\partial x}\frac{\partial G}{\partial x}+(k_o^2 n^2(x,y)-\beta^2)FG = \frac{2}{n^2}\left(\frac{\partial n}{\partial x}\right)^2 FG-\frac{2}{n}\frac{\partial^2 n}{\partial x^2}FG \tag{4.45}$$

Since most of the gradient in x is taken up by $G(x)$ then the first and fourth terms of (4.45) can be neglected. Defining an effective index function in the depth direction $N_{eff}(x)$ by:

$$\frac{\partial^2 G}{\partial x^2} + (k_o^2 N_{eff}^2(x) - \beta^2)G = \frac{2}{n^2}\left(\frac{\partial n}{\partial x}\right)^2 G - \frac{2}{n}\frac{\partial^2 n}{\partial x^2}G \tag{4.46}$$

and substituting it back into (4.45) reduces to:

$$\frac{\partial^2 F}{\partial y^2} + k_o^2\left(n^2(x_i,y) - N_{eff}^2(x_i)\right)F = 0 \tag{4.47}$$

Equation (4.47) is solved using the Runga-Kutta method, described in Section 4.3, along the lateral y direction for each different value of x_i in the vertical direction. This is analogous to solving a planar, one-dimensional waveguide problem extending

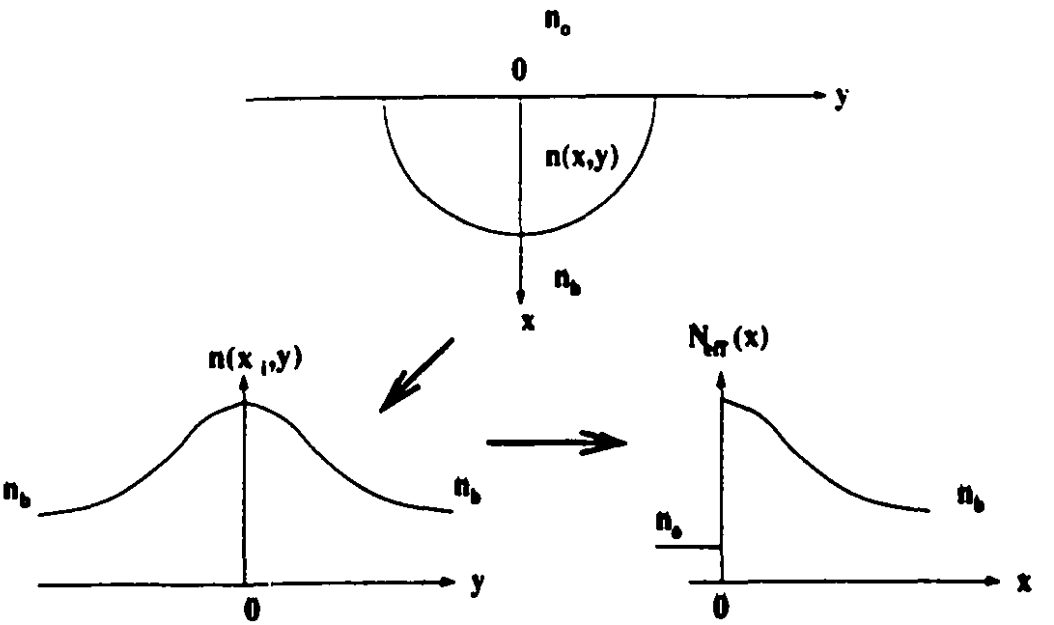

Figure 4.6: Schematic of the EIM

infinitely along y. The root-searching technique provides for the vertical effective index function $N_{eff}(x)$ and $F(x,y)$ for all the x values. Then, (4.46) is solved to yield $G(x)$ and β for the planar waveguide problem extending along x. To calculate β for a particular polarization, one must be careful to choose the proper modes for the two one-dimensional problems. For example, the calculation of the TM mode ($E_x(x,y)$) channel guide propagation constant entails the solution of the TE mode planar problem along y in the first stage and the TM mode problem along x in the second stage. This is because the E_x field, normal to the waveguide surface of the 2-D problem, becomes equivalent to a TE mode field parallel to the x direction of the first 1-D problem and a TM mode field normal to the surface of the second 1-D problem. Fig. 4.6 outlines the method graphically.

4.4 2-D finite-difference vector BPM

4.4.1 Introduction

In 1978, Feit and Fleck developed the beam propagation method (BPM) to calculate the modal properties of multi-mode optical fibers [14]. In the original BPM scheme, the wave propagation was modeled as a spectrum of plane waves in the spectral domain. Then the fast Fourier transform (FFT) was used to solve the paraxial wave equation linking the spatial and spectral domains. This method has come to be known as the FFT-BPM and its accuracy and applicability have been studied extensively [15, 16]. The paraxial (Fresnel) wave equation may also be solved directly in the spatial domain by a finite-difference scheme involving a split-step technique. The beam propagation method using finite differences (FD-BPM) to solve the **scalar** paraxial wave equation has been compared to the FFT-BPM and shown to be superior [17, 18].

Although these schemes have been used extensively in the literature, they can only solve the wave equation under the scalar approximation in which the electric and magnetic fields are simply assumed to be continuous across all boundaries. This may be adequate for some devices, but not for those with birefrigence and abrupt index changes [19]. One cannot neglect the vectorial nature of the guided waves in these cases. A **vector** beam propagation method based on finite difference schemes (FD-VBPM) has been developed [20] with a detailed analysis and assessment performed for a 2-D step-index slab waveguide directional coupler structure [21]. In this section, we describe the 2-D FD-VBPM formulation, our new improvements to account for GRIN structures [22] and the method used to calculate the propagation constants and modal eigenfunctions. In addition, some numerical results are included and compared to those computed by the Runga-Kutta technique.

4.4.2 Numerical algorithm

The paraxial wave equations (4.27) and (4.28) are solved using a finite difference method in which the spatial domain is discretized into a lattice structure defined in the computation region. The fields at the lattice point (x, z) is given by $x = i\Delta x$ and $z = l\Delta z$ and represented by $\Psi_x^l(i)$ and $\Psi_y^l(i)$, for TM and TE modes, respectively. As presented in [21, 23], the operators $\mathcal{L}_{xx}$ and $\mathcal{L}_{yy}$ can be approximated with

$$\frac{\partial^2 \Psi_x}{\partial x^2} = \frac{T_{i+1}^l \Psi_x^l(i+1) - [2 - R_{i+1}^l - R_{i-1}^l]\Psi_x^l(i) + T_{i-1}^l \Psi_x^l(i-1)}{(\Delta x)^2} \tag{4.48}$$

where

$$T_{i\pm1}^l = \frac{2(n_{i\pm1}^l)^2}{(n_{i\pm1}^l)^2 + (n_i^l)^2} \tag{4.49}$$

$$R_{i\pm1}^l = T_{i\pm1}^l - 1 \tag{4.50}$$

are index parameters across the interfaces between $i\Delta x$ and $(i \pm 1)\Delta x$. In addition, the other operator is given by

$$2n_r k_o \mathcal{L}_{yy}\Psi_y = \frac{\Psi_y^l(i+1) - 2\Psi_y^l(i) + \Psi_y^l(i-1)}{(\Delta x)^2} + ((n_i^l)^2 - n_r^2)k_o^2 \Psi_y^l(i) \tag{4.51}$$

An implicit weighted finite difference scheme (with weight w) [24] can be used to solve (4.27) resulting in a tridiagonal system of linear equations

$$\begin{aligned} A_i^{l+1}\Psi_x^{l+1}(i) \; &+A_{i+1}^{l+1}\Psi_x^{l+1}(i+1) + A_{i-1}^{l+1}\Psi_x^{l+1}(i-1) \\ = \quad & A_i^l \Psi_x^l(i) + A_{i+1}^l \Psi_x^l(i+1) + A_{i-1}^l \Psi_x^l(i-1) \end{aligned} \tag{4.52}$$

where

$$A_i^{l+1} = 1 - j\frac{w\Delta z}{2k_o n_r}\left\{\frac{2 - R_{i+1}^{l+1} - R_{i-1}^{l+1}}{(\Delta x)^2} - ((n_i^{l+1})^2 - n_r^2)k_o^2\right\}$$

$$A_{i\pm1}^{l+1} = j\frac{wT_{i\pm1}^{l+1}\Delta z}{2n_r k_o(\Delta x)^2}$$

$$A_i^l = 1 + j\frac{(1-w)\Delta z}{2k_o n_r}\left\{\frac{2 - R_{i+1}^l - R_{i-1}^l}{(\Delta x)^2} - ((n_i^l)^2 - n_r^2)k_o^2\right\}$$

$$A_{i\pm1}^l = -j\frac{(1-w)T_{i\pm1}^l\Delta z}{2n_r k_o(\Delta x)^2}$$

For TE modes, the tangential transverse fields are continuous across the interfaces and hence, $T^l_{m\pm1} = 1$ and $R^l_{m\pm1} = 0$. This tridiagonal system is solved using an elimination method [10].

4.4.3 Improved GRIN formulation

Although this scheme works well for step-index structures [21], improvements must be made for the TM mode in GRIN structures [22]. The main reason for this is that the operator $\mathcal{L}_{xx}$ in finite difference form has not been represented accurately for inhomogeneous index profiles. The first term on the right-hand side of (4.21) as expressed by (4.48) is insufficiently accurate since:

$$\frac{\partial}{\partial x}\left(\frac{1}{n^2(x)}\frac{\partial}{\partial x}(n^2(x)\Psi_x)\right) \neq \frac{\partial^2\Psi_x}{\partial x^2}$$

To correctly account for the index inhomogeneity, the partial derivates of $n(x)$ must be included. This modification results in an improved operator $\mathcal{L}_{xx}$:

$$2n_r k_o \mathcal{L}_{xx}\Psi_x = \frac{T^l_{i+1}\Psi^l_x(i+1) - (2 - R^l_{i+1} - R^l_{i-1})\Psi^l_x(i) + T^l_{i-1}\Psi^l_x(i-1)}{(\Delta x)^2} \tag{4.53}$$

$$+\frac{2(n^l_{i+1} - 2n^l_i + n^l_{i-1})}{n^l_i(\Delta x)^2}\Psi^l_x(i) + \frac{2(n^l_{i+1} - n^l_i)(\Psi^l_x(i+1) - \Psi^l_x(i))}{n^l_i(\Delta x)^2}$$

$$-\frac{2(n^l_{i+1} - n^l_i)^2}{(n^l_i\Delta x)^2}\Psi^l_x(i) + ((n^l_i)^2 - n_r^2)k_o^2\Psi^l_x(i)$$

with $\mathcal{L}_{yy}$, $T^l_{i\pm1}$, and $R_{i\pm1}$ remaining unchanged. These three new terms are now incorporated into (4.52) leading to an improved tridiagonal system: where

$$A^{l+1}_i = 1 - j\frac{w\Delta z}{2k_o n_r}\left\{\frac{2 - R^{l+1}_{i+1} - R^{l+1}_{i-1}}{(\Delta x)^2} - ((n^{l+1}_i)^2 - n_r^2)k_o^2\right\}$$

$$+j\frac{w\Delta z}{k_o n_r(\Delta x)^2}\left\{\left(\frac{n^{l+1}_{i-1} - n^{l+1}_i}{n^{l+1}_i}\right) - \left(\frac{n^{l+1}_{i+1} - n^{l+1}_i}{n^{l+1}_i}\right)^2\right\}$$

$$A^{l+1}_{i+1} = j\frac{w\Delta z}{2n_r k_o(\Delta x)^2}\left\{T^{l+1}_{i+1} + 2\left(\frac{n^{l+1}_{i+1} - n^{l+1}_i}{n^{l+1}_i}\right)\right\}$$

$$A^{l+1}_{i-1} = j\frac{w\Delta z T^{l+1}_{i-1}}{2n_r k_o(\Delta x)^2}$$

$$A_i^l = 1 + j\frac{(1-w)\Delta z}{2k_o n_r}\left\{\frac{2 - R_{i-1}^l - R_{i-1}^l}{(\Delta x)^2} - ((n_i^l)^2 - n_r^2)k_o^2\right\}$$
$$-j\frac{(1-w)\Delta z}{k_o n_r(\Delta x)^2}\left\{\left(\frac{n_{i-1}^l - n_i^l}{n_i^l}\right) - \left(\frac{n_{i+1}^l - n_i^l}{n_i^l}\right)^2\right\}$$
$$A_{i-1}^l = -j\frac{(1-w)\Delta z}{2n_r k_o(\Delta x)^2}\left\{T_{i-1}^l + 2\left(\frac{n_{i-1}^l - n_i^l}{n_i^l}\right)\right\}$$
$$A_{i-1}^l = -j\frac{(1-w)\Delta z T_{i-1}^l}{2n_r k_o(\Delta x)^2}$$

No adjustment is needed for TE modes since the partial derivative $\partial^2\Psi_y/\partial x^2$ does not include $n(x,z)$ as shown in (4.28).

4.4.4 Transparent boundary condition (TBC)

At the edges of the computational window, a numerical transparent boundary condition (TBC) that allows the traveling waves toward the edges to pass through freely without reflection is implemented [25]. For example, near the boundary at the right end of the computational window along the x axis (i.e. $x = M\Delta x$), the field amplitudes should satisfy

$$\frac{\partial\Psi_x}{\partial x} = jk_x\Psi_x \tag{4.54}$$

or in finite-difference form

$$\Psi_x^{l+1}(M) = \Psi_x^{l+1}(M-1)e^{jk_x\Delta x} \tag{4.55}$$

where the transverse complex wave vector k_x is computed from the previous step by calculating the ratio $\Psi_x^l(M-1)/\Psi_x^l(M-2)$. As long as the real part of k_x is positive, there will be radiative energy flowing out of the problem region. The TBC's are shown to be superior to the conventional absorbing boundary conditions. In addition, their implementation is relatively independent of the waveguide structures.

4.4.5 Propagation constants and modal eigenfunctions

The computation of the modal eigenfunctions and propagation constants are very useful in the design stages of the device. The field distribution that satisfies (4.27)

can be represented by the superposition of a mode eigenfunction

$$\Psi_x(x,z) = \sum_n A_n u_n(x) \exp(-j\beta_{pn} z). \tag{4.56}$$

The paraxial eigenfunction $u_n(x)$ of the nth mode is identical to that of the Helmholtz equation though this is not the case for the eigenvalues. The Helmholtz propagation constants β_h are related to the paraxial ones β_p by the relation [26]:

$$\beta_h = k_o n_r \sqrt{1 + 2\beta_p / k_o n_r}. \tag{4.57}$$

In the course of the BPM calculation, the correlation function

$$P(z) = \int \Psi_x^*(x,0)\Psi_x(x,z)dx \tag{4.58}$$

is computed and multiplied by the Hanning window function

$$HW(z) = 1 - \cos(2\pi z / Z_{max}) \tag{4.59}$$

where Z_{max} is the maximum propagation distance. The Fourier transform of the product of (4.58) and (4.59) is performed at the end of the computational run using a standard FFT algorithm. The eigenvalues β_p are determined by locating the resonant peaks of this modal power spectrum. The eigenfunction is determined by computing numerically the integral [27]

$$u_n(x) = constant \times \int_0^{Z_{max}} \Psi_x(x,z) HW(z) \exp(j\beta_{pn} z) dz. \tag{4.60}$$

The eigenfunction computation can proceed simultaneously with the FD-VBPM solution for Ψ_x using the calculated eigenvalue.

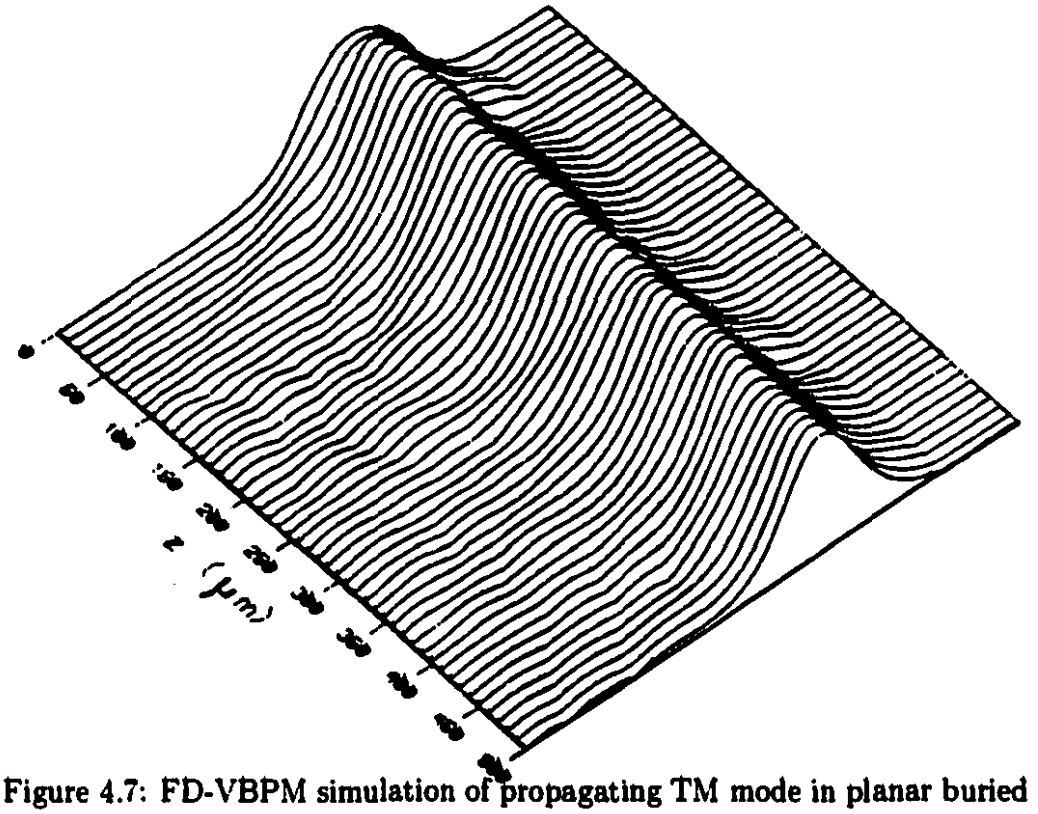

Figure 4.7: FD-VBPM simulation of propagating TM mode in planar buried guide

4.4.6 Results and discussions

A typical 2-D improved FD-VBPM simulation of the propagating TM wave in a planar buried waveguide is shown in Fig. 4.7. The index profile $n(x)$ was calculated using the concentration profile of Fig. 2.6 with $t_2 = 100\,s$ (see Section 2.3), $\Delta n_s(TM) = 0.0134$ and $n_b = 1.5125$. The initial field profile at $z = 0$ was calculated using the three-layer TM field solution of (4.31) with $n_b = n_1$, $n_2 = max(n(x)) = 1.5162888$ occuring at $x = x_{peak}$, $D_2 = 5.0\,\mu m$, and $N_{eff} = 1.5156$ deduced using (4.29). The value of D_2 was chosen roughly to account for the buried guide field width. Also, the midpoint of this 3-layer structure was chosen to match that of the GRIN buried profile in the BPM program. The chosen step sizes are $\Delta z = 0.5\,\mu m$ and $\Delta x = 0.02\,\mu m$. The computational window sizes are $X_{max} = 20\,\mu m$ and $Z_{max} = 500\,\mu m$. The weight $w = 0.53$ and the reference index $n_r = 1.5125 = n_b$ were chosen for this weakly-guiding structure [21] with $\Delta n_s(TM) = 0.0134$. This particular run took about $55\,s$ on a SunSparc5.

The improved scheme was assessed in the calculation of single-mode TM propagation constants for two GRIN profiles, namely Gaussian and exponential. The step sizes Δz and Δx were chosen as $0.025\,\mu m$ with the lateral and longitudinal computational windows equal to $25\,\mu m$ and $1638\,\mu m$, respectively. The chosen w was 0.53 and the optimum $n_o = N_{eff}$ was calculated by the Runga-Kutta (exact) method [9] that provides for an accuracy of $< 10^{-8}$ in the value of the effective index. A transparent boundary condition was used at the window edges [25]. Both strongly and weakly guiding samples were tested for cases close to and far from cutoff. The surface index changes Δn_s varied from 0.0113 to 0.13 that are typical of ion exchange in glass (bulk index $n_b = 1.5125$) and of annealed proton-exchange in $LiNbO_3$ ($n_b = 2.20$) at $\lambda_o = 0.6328\,\mu m$. The results (see Table 4.1) show that there is no difference between the existing and modified schemes for the weakly-guiding case. However, the deviation δ between them is more evident for the guides with the larger index change and even more serious for those operating close to cutoff. Fig. 4.8 illustrates the modal power spectrum for a Gaussian profile defined as $n(x) = n_b + \Delta n_s \exp(-x^2/d^2)$ with the effective depth $d = 0.30\,\mu m$ and $\Delta n_s = 0.13$. The improved scheme shows closer agreement to the exact effective index in comparison to the existing scheme. These deviations were also verified using the Runge-Kutta method, with and without the index gradient terms, and were found to vary from $2 - 4 \times 10^{-4}$ for the strongly guiding case and about 1×10^{-6} for the weakly guiding case. Although only Gaussian and exponential profiles were tested here, such improved accuracy is believed to occur also for other GRIN profiles.

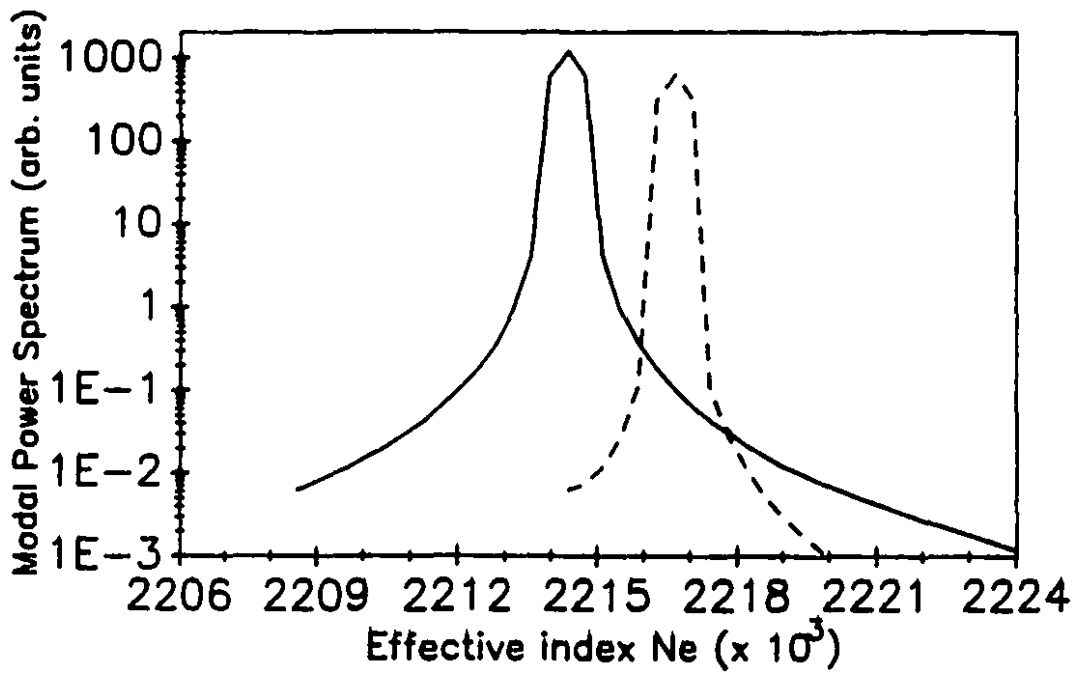

Figure 4.8: Modal power spectrum of single-mode guide with Gaussian profile using existing (dashed line) and improved (solid line) schemes

Δn_s (profile)	d (μm)	N_{eff} (exact)	N_{eff} (old BPM)	N_{eff} (new BPM)	$\lvert\delta\rvert$ ($\times 10^{-4}$)
0.0113	1.10	1.5131200	1.5135062	1.5135062	0.0
(Gaussian)	2.00	1.5164097	1.5167959	1.5167959	0.0
0.1300	0.30	2.2139642	2.2166662	2.2143505	23.16
(Gaussian)	0.50	2.2472587	2.2495748	2.2476448	19.30
0.10	0.40	1.5257407	1.5272848	1.5268989	3.86
(exponential)	0.55	1.5356583	1.5372024	1.5368165	3.86

Table 4.1: Comparison of N_{eff} using existing and improved FD-VBPM schemes

4.5 3-D vector ADI-BPM formulation

4.5.1 Introduction

Recently, there have been a number of 3-D vectorial BPM schemes reported. A full vector FD-BPM based on an explicit scheme has been studied, although it is only conditionally stable for a small propagation step Δz [28]. A numerical scheme based on the alternating-direction implicit (ADI) method has been applied to rib waveguides although only in the quasi-vectorial approximation [29]. A full vector BPM based on a block iterative ORTHOMIN matrix solver has been implemented [30]. Recently, a 3-D BPM based on a joint FFT and FD scheme was also studied [31]. All the above 3-D schemes that treat the full vectorial nature of the fields have been applied numerically on step-index waveguide structures. However, the Fresnel operators in a finite-difference form do not include the terms that account for ∇n^2. Although this approximation may be valid for weakly guiding structures, it causes significant deviation for single-mode guides with large index changes. In this section, 3-D GRIN strucutures are studied using the full vector ADI BPM. The cross coupling effects between the transverse electric field components and the refractive index gradients are taken fully into consideration.

4.5.2 Finite-difference scheme

The Fresnel wave equations (4.25) and (4.26) are solved using a finite-difference method in which the 3-D spatial domain is discretized into a lattice structure. The fields at the lattice point (x, y, z), where $x = i\Delta x$, $y = j\Delta y$ and $z = l\Delta z$, are represented by $\Psi^l_{x,i,j}$ and $\Psi^l_{y,i,j}$. As discussed in [21, 23], the second-order intermediate operator can be approximated by a five-point central-difference scheme

$$\mathcal{A}_x\Psi_x = \frac{T^l_{i+1,j}\Psi^l_{x,i+1,j} - [2 - R^l_{i+1,j} - R^l_{i-1,j}]\Psi^l_{x,i,j} + T^l_{i-1,j}\Psi^l_{x,i-1,j}}{(\Delta x)^2} \qquad (4.61)$$

where

$$T^l_{i\pm1,j} = \frac{2(n^l_{i\pm1,j})^2}{(n^l_{i\pm1,j})^2 + (n^l_{i,j})^2} \tag{4.62}$$

$$R^l_{i\pm1,j} = T^l_{i\pm1,j} - 1 \tag{4.63}$$

with the transmission ($T^l_{i\pm1,j}$) and reflection ($R^l_{i\pm1,j}$) parameters across the refractive index interfaces between $i\Delta x$ and $(i \pm 1)\Delta x$. In addition, the other operators are:

$$\mathcal{A}_y\Psi_x = \frac{\Psi^l_{x,i,j-1} - 2\Psi^l_{x,i,j} + \Psi^l_{x,i,j-1}}{(\Delta y)^2} \tag{4.64}$$

$$\mathcal{A}_x\Psi_y = \frac{\Psi^l_{y,i+1,j} - 2\Psi^l_{y,i,j} + \Psi^l_{y,i-1,j}}{(\Delta x)^2} \tag{4.65}$$

$$\mathcal{A}_y\Psi_y = \frac{T^l_{i,j+1}\Psi^l_{y,i,j+1} - [2 - R^l_{i,j+1} - R^l_{i,j-1}]\Psi^l_{y,i,j} + T^l_{i,j-1}\Psi^l_{y,i,j-1}}{(\Delta y)^2} \tag{4.66}$$

Note that in (4.66), the transmission ($T^l_{i,j\pm1}$) and reflection ($R^l_{i,j\pm1}$) parameters across the refractive index interfaces between $j\Delta y$ and $(j\pm1)\Delta y$. The other GRIN and cross coupling operators are derived as:

$$\begin{aligned}\mathcal{A}_{xn}\Psi_x &= \frac{2}{(\Delta x)^2}\left[\left(\frac{n^l_{i-1,j} - n^l_{i,j}}{n^l_{i,j}}\right) - \left(\frac{n^l_{i+1,j} - n^l_{i,j}}{n^l_{i,j}}\right)^2\right]\Psi^l_{x,i,j} \\ &+ \frac{2}{(\Delta x)^2}\left(\frac{n^l_{i+1,j} - n^l_{i,j}}{n^l_{i,j}}\right)\Psi^l_{x,i+1,j}\end{aligned} \tag{4.67}$$

$$\begin{aligned}\mathcal{A}_{yn}\Psi_y &= \frac{2}{(\Delta y)^2}\left[\left(\frac{n^l_{i,j-1} - n^l_{i,j}}{n^l_{i,j}}\right) - \left(\frac{n^l_{i,j+1} - n^l_{i,j}}{n^l_{i,j}}\right)^2\right]\Psi^l_{y,i,j} \\ &+ \frac{2}{(\Delta y)^2}\left(\frac{n^l_{i,j+1} - n^l_{i,j}}{n^l_{i,j}}\right)\Psi^l_{y,i,j+1}\end{aligned} \tag{4.68}$$

$$\begin{aligned}\mathcal{B}_{xy}\Psi_y &= \frac{2}{\Delta x\Delta y}\left[\frac{n^l_{i,j}n^l_{i+1,j+1} - n^l_{i,j}n^l_{i,j+1} - n^l_{i+1,j}n^l_{i,j+1} + (n^l_{i,j})^2}{(n^l_{i,j})^2}\right]\Psi^l_{y,i,j} \\ &+ \frac{2}{\Delta x\Delta y}\left(\frac{n^l_{i,j+1} - n^l_{i,j}}{n^l_{i,j}}\right)\Psi^l_{y,i+1,j}\end{aligned} \tag{4.69}$$

$$\begin{aligned}\mathcal{B}_{yx}\Psi_x &= \frac{2}{\Delta x\Delta y}\left[\frac{n^l_{i,j}n^l_{i+1,j+1} - n^l_{i,j}n^l_{i+1,j} - n^l_{i+1,j}n^l_{i,j+1} + (n^l_{i,j})^2}{(n^l_{i,j})^2}\right]\Psi^l_{x,i,j} \\ &+ \frac{2}{\Delta x\Delta y}\left(\frac{n^l_{i+1,j} - n^l_{i,j}}{n^l_{i,j}}\right)\Psi^l_{x,i,j+1}\end{aligned} \tag{4.70}$$

In Section 4.4, an implicit weighted finite-difference scheme (with weight w) was used to solve the Fresnel equations resulting in a tridiagonal system of linear

equations. ADI methods used for 3-D problems preserve the tridiagonal feature of the 2-D scheme by first solving a sequence of 1-D equations along x, then another along y for every Δz. The operators in (4.25) and (4.26) must be split carefully into two steps [29, 32]. The first equation is solved for $\Psi_x^{l+1/2}$ using Ψ_x^l and Ψ_y^l along x for $j = 0, ...N$:

$$A_{x,i,j}^{l+1/2}\Psi_{x,i,j}^{l+1/2} + A_{x,i+1,j}^{l+1/2}\Psi_{x,i+1,j}^{l+1/2} + A_{x,i-1,j}^{l+1/2}\Psi_{x,i-1,j}^{l+1/2} = \tag{4.71}$$

$$A_{y,i,j}^{l}\Psi_{x,i,j}^{l} + A_{y,i,j+1}^{l}\Psi_{x,i,j+1}^{l} + A_{y,i,j-1}^{l}\Psi_{x,i,j-1}^{l} + B_{x,i,j}^{l}\Psi_{y,i,j}^{l} + B_{x,i+1,j}^{l}\Psi_{y,i-1,j}^{l}$$

where

$$A_{x,i,j}^{l+1/2} = 1 - j\frac{w\Delta z}{2k_o n_r}\left\{\frac{(2 - R_{i+1,j}^{l+1/2} - R_{i-1,j}^{l+1/2})}{(\Delta x)^2} - \frac{((n_{i,j}^{l+1/2})^2 - n_r^2)k_o^2}{2}\right\}$$

$$+j\frac{w\Delta z}{k_o n_r(\Delta x)^2}\left\{\left(\frac{n_{i-1}^{l+1/2} - n_{i,j}^{l+1/2}}{n_{i,j}^{l+1/2}}\right) - \left(\frac{n_{i+1,j}^{l+1/2} - n_{i,j}^{l+1/2}}{n_{i,j}^{l+1/2}}\right)^2\right\}$$

$$A_{x,i+1,j}^{l+1/2} = j\frac{w\Delta z}{2n_r k_o(\Delta x)^2}\left\{T_{i+1,j}^{l+1/2} + 2\left(\frac{n_{i+1,j}^{l+1/2} - n_{i,j}^{l+1/2}}{n_{i,j}^{l+1/2}}\right)\right\}$$

$$A_{x,i-1,j}^{l+1/2} = j\frac{w\Delta z T_{i-1,j}^{l+1/2}}{2n_r k_o(\Delta x)^2}$$

$$A_{y,i,j}^{l} = 1 + j\frac{(1-w)\Delta z}{2k_o n_r}\left\{\frac{2}{(\Delta y)^2} - \frac{((n_{i,j}^{l})^2 - n_r^2)k_o^2}{2}\right\}$$

$$A_{y,i,j+1}^{l} = -j\frac{(1-w)\Delta z}{2n_r k_o(\Delta y)^2} = A_{y,i,j-1}^{l}$$

$$B_{x,i,j}^{l} = -j\frac{\Delta z}{n_r k_o \Delta x \Delta y}\left\{\frac{n_{i,j}^{l}n_{i+1,j+1}^{l} - n_{i,j}^{l}n_{i,j+1}^{l} - n_{i+1,j}^{l}n_{i,j+1}^{l} + (n_{i,j}^{l})^2}{(n_{i,j}^{l})^2}\right\}$$

$$B_{x,i+1,j}^{l} = -j\frac{\Delta z}{n_r k_o \Delta x \Delta y}\left\{\frac{n_{i,j+1}^{l} - n_{i,j}^{l}}{n_{i,j}^{l}}\right\}$$

Then, the second equation is solved for Ψ_x^{l+1} using $\Psi_x^{l+1/2}$ and Ψ_y^l along y for $i = 0, ..M$:

$$A_{y,i,j}^{l+1}\Psi_{x,i,j}^{l+1} + A_{y,i,j+1}^{l+1}\Psi_{x,i,j+1}^{l+1} + A_{y,i,j-1}^{l+1}\Psi_{x,i,j-1}^{l+1} = \tag{4.72}$$

$$A1_{x,i,j}^{l+1/2}\Psi_{x,i,j}^{l+1/2} + A1_{x,i+1,j}^{l+1/2}\Psi_{x,i+1,j}^{l+1/2} + A1_{x,i-1,j}^{l+1/2}\Psi_{x,i-1,j}^{l+1/2} + B_{x,i,j}^{l}\Psi_{y,i,j}^{l} + B_{x,i+1,j}^{l}\Psi_{y,i+1,j}^{l}$$

where

$$A_{y,i,j}^{l+1} = 1 - j\frac{w\Delta z}{2k_o n_r}\left\{\frac{2}{(\Delta y)^2} - \frac{((n_{i,j}^{l-1})^2 - n_r^2)k_o^2}{2}\right\}$$

$$A_{y,i,j+1}^{l+1} = j\frac{w\Delta z}{2n_r k_o(\Delta y)^2} = A_{y,i,j-1}^{l+1}$$

$$A1_{x,i,j}^{l+1/2} = 1 + j\frac{(1-w)\Delta z}{2k_o n_r}\left\{\frac{(2 - R_{i+1,j}^{l+1/2} - R_{i-1,j}^{l+1/2})}{(\Delta x)^2} - \frac{((n_{i,j}^{l+1/2})^2 - n_r^2)k_o^2}{2}\right\}$$

$$-j\frac{(1-w)\Delta z}{k_o n_r(\Delta x)^2}\left\{\left(\frac{n_{i-1}^{l+1/2} - n_{i,j}^{l+1/2}}{n_{i,j}^{l+1/2}}\right) - \left(\frac{n_{i+1,j}^{l+1/2} - n_{i,j}^{l+1/2}}{n_{i,j}^{l+1/2}}\right)^2\right\}$$

$$A1_{x,i+1,j}^{l+\frac{1}{2}} = -j\frac{(1-w)\Delta z}{2n_r k_o(\Delta x)^2}\left\{T_{i+1,j}^{l+1/2} + 2\left(\frac{n_{i+1,j}^{l+1/2} - n_{i,j}^{l+1/2}}{n_{i,j}^{l+1/2}}\right)\right\}$$

$$A1_{x,i-1,j}^{l+\frac{1}{2}} = -j\frac{(1-w)\Delta z T_{i-1,j}^{l+1/2}}{2n_r k_o(\Delta x)^2}$$

The solution Ψ_x^{l+1} is now used in another similar set of ADI equations to determine Ψ_y^l. As before, the first set of equations are along x for $j = 0,..N$:

$$C_{x,i,j}^{l+1/2}\Psi_{y,i,j}^{l+1/2} + C_{x,i+1,j}^{l+1/2}\Psi_{y,i+1,j}^{l+1/2} + C_{x,i-1,j}^{l+1/2}\Psi_{y,i-1,j}^{l+1/2} = \tag{4.73}$$

$$C_{y,i,j}^{l}\Psi_{y,i,j}^{l} + C_{y,i,j+1}^{l}\Psi_{y,i,j+1}^{l} + C_{y,i,j-1}^{l}\Psi_{y,i,j-1}^{l} + B_{y,i,j}^{l}\Psi_{x,i,j}^{l} + B_{y,i,j+1}^{l}\Psi_{x,i,j+1}^{l}$$

where

$$C_{x,i,j}^{l+1/2} = 1 - j\frac{w\Delta z}{2k_o n_r}\left\{\frac{2}{(\Delta x)^2} - \frac{((n_{i,j}^{l+1/2})^2 - n_r^2)k_o^2}{2}\right\}$$

$$C_{x,i+1,j}^{l+1/2} = j\frac{w\Delta z}{2n_r k_o(\Delta x)^2} = C_{x,i-1,j}^{l+1/2}$$

$$C_{y,i,j}^{l} = 1 + j\frac{(1-w)\Delta z}{2k_o n_r}\left\{\frac{(2 - R_{i,j+1}^{l} - R_{i,j-1}^{l})}{(\Delta y)^2} - \frac{((n_{i,j}^{l})^2 - n_r^2)k_o^2}{2}\right\}$$

$$-j\frac{(1-w)\Delta z}{k_o n_r(\Delta y)^2}\left\{\left(\frac{n_{i-1}^{l} - n_{i,j}^{l}}{n_{i,j}^{l}}\right) - \left(\frac{n_{i+1,j}^{l} - n_{i,j}^{l}}{n_{i,j}^{l}}\right)^2\right\}$$

$$C_{y,i,j+1}^{l} = -j\frac{(1-w)\Delta z}{2n_r k_o(\Delta y)^2}\left\{T_{i,j+1}^{l} + 2\left(\frac{n_{i+1,j}^{l} - n_{i,j}^{l}}{n_{i,j}^{l}}\right)\right\}$$

$$C_{y,i,j-1}^{l} = -j\frac{(1-w)\Delta z T_{i,j-1}^{l}}{2n_r k_o(\Delta y)^2}$$

$$B_{y,i,j}^{l} = -j\frac{\Delta z}{n_r k_o \Delta x \Delta y}\left\{\frac{n_{i,j}^{l}n_{i+1,j+1}^{l} - n_{i,j}^{l}n_{i+1,j}^{l} - n_{i+1,j}^{l}n_{i,j+1}^{l} + (n_{i,j}^{l})^2}{(n_{i,j}^{l})^2}\right\}$$

$$B^{l}_{y,i,j-1} = -j\frac{\Delta z}{n_r k_o \Delta x \Delta y}\left\{\frac{n^{l}_{i-1,j} - n^{l}_{i,j}}{n^{l}_{i,j}}\right\}$$

followed by equations along y for $i = 0...M$:

$$C^{l+1}_{y,i,j}\Psi^{l+1}_{y,i,j} + C^{l+1}_{y,i,j+1}\Psi^{l+1}_{y,i,j+1} + C^{l+1}_{y,i,j-1}\Psi^{l+1}_{y,i,j-1} = \tag{4.74}$$
$$C1^{l+1/2}_{x,i,j}\Psi^{l+1/2}_{y,i,j} + C1^{l+1/2}_{x,i+1,j}\Psi^{l+1/2}_{y,i+1,j} + C1^{l+1/2}_{x,i-1,j}\Psi^{l+1/2}_{y,i-1,j} + B^{l}_{y,i,j}\Psi^{l-1/2}_{x,i,j} + B^{l}_{y,i,j-1}\Psi^{l-1/2}_{x,i,j+1}$$

where

$$C^{l+1}_{y,i,j} = 1 - j\frac{w\Delta z}{2k_o n_r}\left\{\frac{(2 - R^{l+1}_{i,j+1} - R^{l+1}_{i,j-1})}{(\Delta y)^2} - \frac{((n^{l+1}_{i,j})^2 - n_r^2)k_o^2}{2}\right\}$$
$$+j\frac{w\Delta z}{k_o n_r(\Delta y)^2}\left\{\left(\frac{n^{l+1}_{i,j-1} - n^{l+1}_{i,j}}{n^{l+1}_{i,j}}\right) - \left(\frac{n^{l+1}_{i,j+1} - n^{l+1}_{i,j}}{n^{l+1}_{i,j}}\right)^2\right\}$$

$$C^{l+1}_{y,i,j+1} = j\frac{w\Delta z}{2n_r k_o(\Delta y)^2}\left\{T^{l+1}_{i,j+1} + 2\left(\frac{n^{l+1}_{i,j+1} - n^{l+1}_{i,j}}{n^{l+1}_{i,j}}\right)\right\}$$

$$C^{l+1}_{y,i,j-1} = j\frac{w\Delta z T^{l+1}_{i,j-1}}{2n_r k_o(\Delta y)^2}$$

$$C1^{l+1/2}_{x,i,j} = 1 + j\frac{(1-w)\Delta z}{2k_o n_r}\left\{\frac{2}{(\Delta x)^2} - \frac{((n^{l+1/2}_{i,j})^2 - n_r^2)k_o^2}{2}\right\}$$

$$C1^{l+1/2}_{x,i+1,j} = -j\frac{(1-w)\Delta z}{2n_r k_o(\Delta x)^2} = C1^{l+1/2}_{x,i-1,j}$$

As an example, one can model TM mode propagation by initially calculating Ψ_x at $z = 0$ by the EIM described in Section 4.3 and setting Ψ_y to zero. Then, using (4.71), one solves for $\Psi_x^{l+1/2}$ which in turn is used to calculate Ψ_x^{l+1} via (4.72). To calculate Ψ_y, one solves (4.73) for $\Psi_y^{l+1/2}$ using Ψ_x^{l} just calculated which in turn are used to determine Ψ_y^{l+1} via (4.74). The assessment of this 3-D scheme on our GRIN channel-guide devices will be presented in Chapter 7.

4.5.3 3-D implementation of the TBC

The TBC is also used in our vector 3-D ADI scheme [33]. This condition accounts for plane waves that impinge on the boundary at an angle which is an improvement over the simplified TBC [25] (referred to as STBC). We have found that the STBC alone is not sufficient in the 3-D scheme leading to numerical instability.

Let us look at this in more detail. The method proposes to select the complex propagation constant k_x that is dependent on the angle at which the wavefront impinges on the boundary and the relative mesh spacings, as shown in Fig. 4.9. The right boundary is considered here; the treatment of the other boundary is essentially identical. We first consider the case depicted in Fig. 4.9(a) where we are looking at a cross-sectional view of the waveguide structure in the $x-z$ plane. The value of k_x is computed as

$$\exp(jk_x\Delta x) = \frac{\Psi_{x,M-m_{TBC},j}}{\Psi_{x,M-m_{TBC}-1,j}} \tag{4.75}$$

where m_{TBC} is found by simple geometrical considerations to be

$$m_{TBC} = \frac{\Delta z}{\Delta x}\frac{k_x}{\sqrt{k_o^2 - k_x^2}} \tag{4.76}$$

and the value to be inserted for k_x in (4.76) is that determined from the previous step. Note that the field is computed at mesh points further from the boundary, reflecting the steeper angle made by the phase front, or possibly a larger step size. Next, consider the opposite case shown in Fig. 4.9(b). Here, the value of k_x computed from mesh points $M-1$ and $M-2$ are expected to provide a good estimate for propagation. Thus, we underrelax the updating of k_x according to

$$\zeta^{l+1} = \alpha_r\frac{\Psi_{x,M-1,j}}{\Psi_{x,M-2,j}} + (1-\alpha_r)\zeta^l \tag{4.77}$$

where the parameter ζ is related to k_x via the relation

$$\zeta = \exp(jk_x\Delta x). \tag{4.78}$$

The relaxation parameter α_r is taken as

$$\alpha_r = \frac{\Delta z}{\Delta x}\frac{k_x}{\sqrt{k_o^2 - k_x^2}} \tag{4.79}$$

As for the other direction along y, a similar procedure is implemented by solving for k_y. Both of these TBC algorithms are also used for the ADI equations to solve Ψ_y.

Thus, in practice, the following procedure is implemented for the 3-D TBC:

- Compute the right-hand side of (4.79) and test its magnitude
- If it is greater than or equal to unity, we round it to the nearest integer, interpret it as m_{TBC} and apply (4.75)
- If it is less than unity, we interpret it as α_r and use (4.77) to compute k_x
- If the real part of k_x is negative, it is reset to zero
- The value of Ψ_x at the boundary point is redefined to satisfy

$$\Psi^l_{x,M,j} = \Psi^l_{x,M-1,j} \exp(jk_x \Delta x)$$

  using the value of k_x just calculated

- The next propagation step is performed using the simple condition

$$\Psi^{l+1}_{x,M,j} = \Psi^{l+1}_{x,M-1,j} \exp(jk_x \Delta x)$$

The above procedure has been used successfully with the TBC algorithm being applied along each row and column. In this case, the values of k_x and k_y are allowed to be different for each row and column accounting for variations of phase tilt along the boundaries.

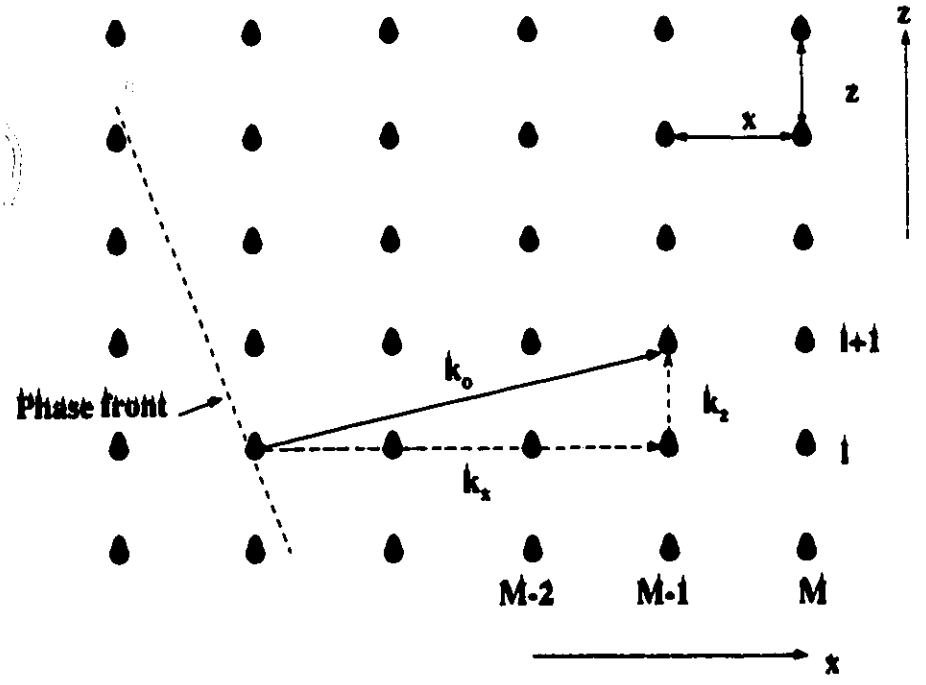

(a)

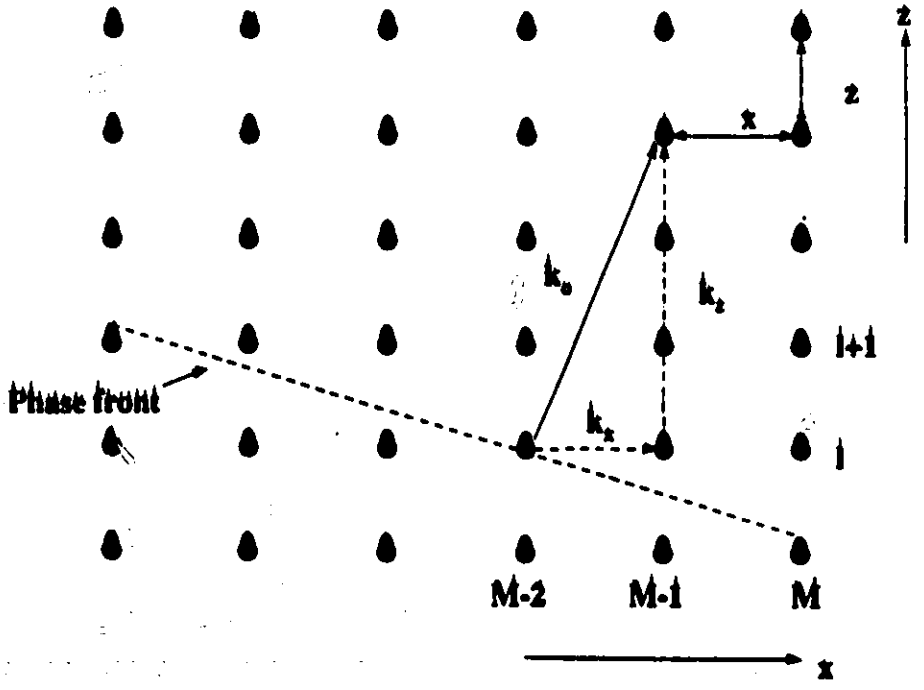

(b)

Figure 4.9: (a) Schematic illustration for the determination of k_z using more lateral points. In (b), several propagation steps are used (see Fig. 1 of [33])

4.5.4 Typical simulations

The full vector BPM (FV-ADI) was tested on a weakly-guiding buried channel guide with parameters $W = 4.0\,\mu m$, $t_1 = 20\,min$, $t_2 = 2.0\,min$. $E_a^T = 98.5\,V/mm$ and $T = 385°C$. The concentration profile $c(x, y)$, calculated in Chapter 2, is used to determine the index profile $n(x, y)$ with $c(x, y) = f(x, y)$ as described in Section 4.1, with $\Delta n_s(TM) = 0.0108$ and $n_b = 1.5208$. The initial TM mode field profile $E_x(x, y)$ at $z = 0$ was calculated by the EIM. The step sizes are $\Delta z = 0.5\,\mu m$, $\Delta x = 0.02\,\mu m$ and $\Delta y = 0.2\,\mu m$. The computational window sizes were $X_{max} = 20\,\mu m$, $Y_{max} = 10\,\mu m$ and $Z_{max} = 500\,\mu m$ with weight $w = 0.53$ and reference index $n_r = 1.5208$. For this weakly-guiding case ($\Delta n_s \ll 1$), the cross-coupling terms are neglected [21] yielding a much simpler numerical quasi-vectorial (QV-ADI) scheme for quasi-TM propagation using (4.25) only with $\mathcal{B}_{xy} = 0$. The contour plot of the buried field profile is shown in Fig. 4.10(a). This particular run took $72min$ to complete on a SunSparc5. Identical results are obtained for the more accurate FV-ADI, however, at the penalty of twice the computation time.

On a final note, it is also interesting to compare this field profile to that of a circularly symmetric optical fiber in the Gaussian mode approximation, $\exp(-(x^2 + y^2)/w_f^2)$ [34] with $w_f = 2.30\,\mu m$ centered at the same position as the buried channel guide, as shown in Fig. 4.10(b). Note the similarity between the two profiles.

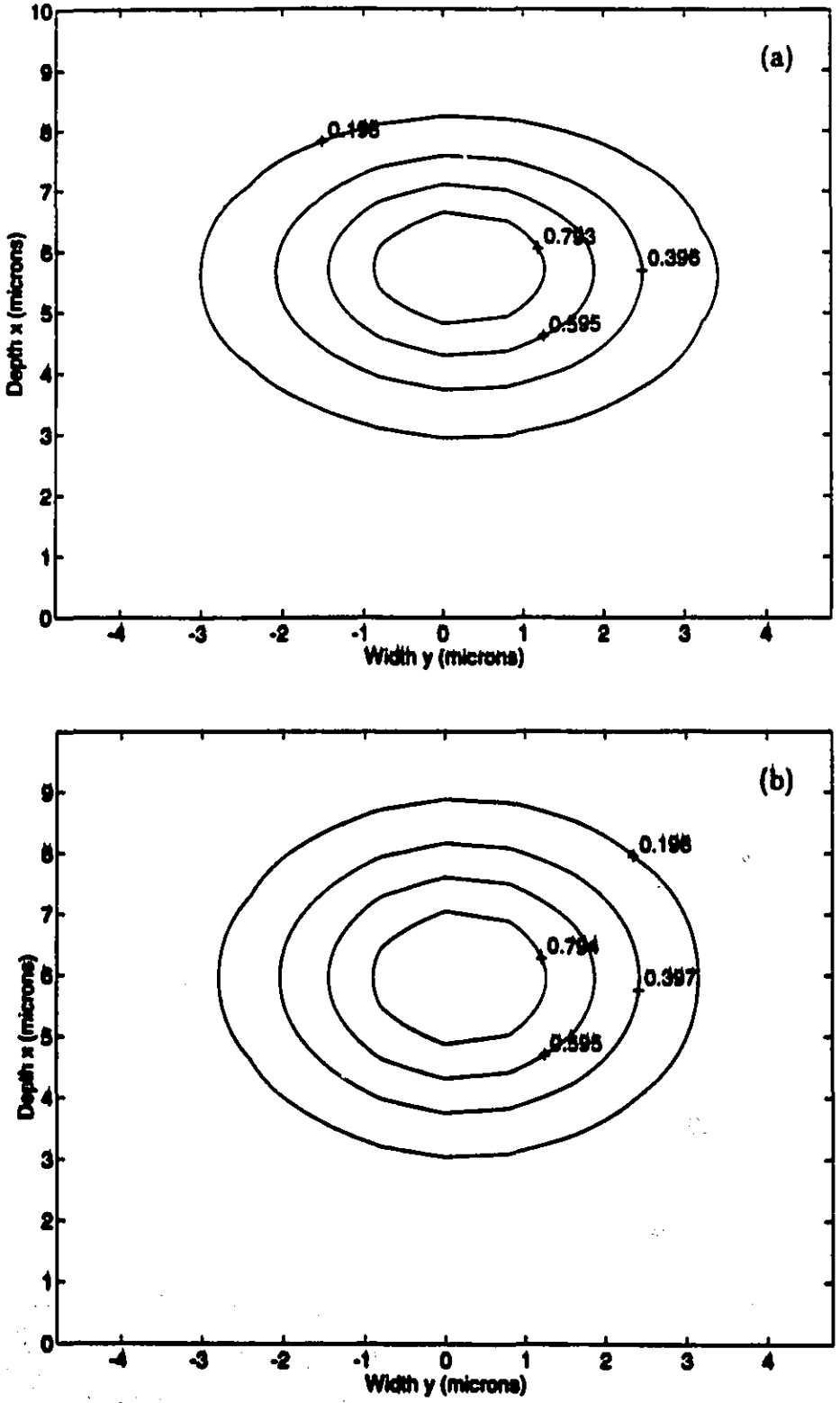

Figure 4.10: 2-D field profiles of a (a) channel buried guide and (b) circularly symmetric single-mode fiber

4.6 Appendix 4A

The TRT is used to derive the dispersion relation for the four-layer complex index structure. First, we write the wave impedances for TE and TM modes as:

$$Z_i = \begin{cases} \omega\mu_o/k_{xi}, & \text{TE} \\ k_{xi}/\omega\epsilon_o^2 n_i^2, & \text{TM} \end{cases}$$

where $k_{xi} = k_o\sqrt{(n_i)^2 - (N_{eff}^c)^2}$ and $i = 1, 2, 3, 4$. If we assume field guidance in regions 2 and 3, then $Re(N_{eff}^c) < Re(n_2), n_3$. Using impedance transformation:

$$\begin{aligned} Z_1' &= Z_2\frac{Z_1 + jZ_2\tan(k_{x2}D_2)}{Z_2 + jZ_1\tan(k_{x2}D_2)} \\ Z_2' &= Z_3\frac{Z_4 + jZ_3\tan(k_{x3}D_3)}{Z_3 + jZ_4\tan(k_{x3}D_3)} \end{aligned} \tag{4.80}$$

and since $Z_1' + Z_2' = 0$, we arrive at the TE mode dispersion relation:

$$(k_{x2} + k_{x3})(k_{x2}k_{x3} - \alpha_{x1}\alpha_{x4})\sin(k_{x2}D_2 + k_{x3}D_3) \quad + \tag{4.81}$$

$$(k_{x2} - k_{x3})(k_{x2}k_{x3} + \alpha_{x1}\alpha_{x4})\sin(k_{x2}D_2 - k_{x3}D_3) \quad - \tag{4.82}$$

$$(k_{x2} + k_{x3})(\alpha_{x1}k_{x3} + k_{x2}\alpha_{x4})\cos(k_{x2}D_2 + k_{x3}D_3) \quad - \tag{4.83}$$

$$(k_{x2} - k_{x3})(\alpha_{x1}k_{x3} - k_{x2}\alpha_{x4})\cos(k_{x2}D_2 - k_{x3}D_3) \quad = \quad 0 \tag{4.84}$$

where $k_{xi} = k_0\sqrt{n_i^2 - (N_{eff}^c)^2}$ for the regions $i = 2, 3$ and for regions 1 and 4, with field evanescence, $\alpha_{xi} = k_0\sqrt{(N_{eff}^c)^2 - n_i^2}$ and $k_{xi} = -j\alpha_{xi}$ with $i = 1, 4$. Similarly, for the TM mode:

$$(K_{x2} + K_{x3})(K_{x2}K_{x3} - A_{x1}A_{x4})\sin(k_{x2}D_2 + k_{x3}D_3) \quad + \tag{4.85}$$

$$(K_{x2} - K_{x3})(K_{x2}K_{x3} + A_{x1}A_{x4})\sin(k_{x2}D_2 - k_{x3}D_3) \quad - \tag{4.86}$$

$$(K_{x2} + K_{x3})(A_{x1}K_{x3} + K_{x2}A_{x4})\cos(k_{x2}D_2 + k_{x3}D_3) \quad - \tag{4.87}$$

$$(K_{x2} - K_{x3})(A_{x1}K_{x3} - K_{x2}A_{x4})\cos(k_{x2}D_2 - k_{x3}D_3) \quad = \quad 0 \tag{4.88}$$

where $K_{xi} = k_{xi}/n_i^2$ and , $k_{xi} = k_0\sqrt{n_i^2 - (N_e^c)^2}$ for the regions $i = 2, 3$. For regions 1 and 4, with field evanescence, $A_{xi} = \alpha_{xi}/n_i^2$, $k_{xi} = k_0\sqrt{n_i^2 - (N_e^c)^2}$ and $\alpha_{xi} = jk_{xi}$ with $i = 1, 4$.

Bibliography

[1] H. Kogelnik. 'Theory of optical waveguides'. in *Guided-Wave Optoelectronics*. T. Tamir. Ed., Springer-Verlag, Berlin. 1990

[2] H. Nishihara. M. Haruna, T. Suhara. *Optical Integrated Circuits*. McGraw-Hill. New York. 1989

[3] F. Zernike, 'Fabrication and measurement of passive components'. in *Integrated Optics*, T. Tamir. Ed., Springer Verlag, Berlin. 1975

[4] R.V. Ramaswamy and R. Srivastava, 'Ion-exchanged glass waveguides: A review'. J. Lightwave Technol., 6 (6), pp. 984-1002, 1988

[5] R.E. Collin, *Microwave Engineering*, McGraw Hill, New York. 1966

[6] J.F. Vinchant, F. Mallecot, D. Decoster, and J.P. Vilcot, 'Effects of absorbing layers on the propagation constants: a four layer model on desktop-computer applied to photodetectors monolithically integrated with optical waveguides', Optics Comm., 67 (4), pp. 266-270, 1988

[7] G.L. Yip and H. H. Yao, 'Numerical study of inhomogeneous optical waveguide problems using predictor-corrector method', Electron. Lett., 17 (6), pp. 229-230, 1981

[8] A. Gedeon, 'Comparison between rigorous theory and WKB analysis of modes in graded-index waveguides', Opt. Comm., 12 (3), pp. 329-332, 1974

[9] A.N. Kaul. S.I. Hosain. and K. Thyagarajan. 'A simple numerical method for studying the propagation characteristics of single-mode graded-index planar optical waveguides', IEEE Trans. Microwave Theory and Tech., 34 (2), pp. 288-292, 1986

[10] G.G. Bach, *Numerical Analysis*. Department of Mechanical Engineering. McGill University, 1982

[11] P.K. Mishra and A. Sharma. 'Analysis of single mode inhomogeneous planar waveguides', J. Lightwave Technol., 4 (2), pp. 204-211, 1986

[12] R.M Knox and P.P. Toulios. 'Integrated circuits for millimeter through optical frequency range', in *Proceedings on Submillimeter Waves*, J. Fox, Ed., Polytechnic Press, Brooklyn, 1970

[13] G.B. Hocker and W.K. Burns, 'Mode dispersion in diffused channel waveguides by the effective index method', Appl. Opt., 16 (1), pp. 113-118, 1977

[14] M.D. Feit and J.A. Fleck, Jr., 'Light propagation in graded-index optical fibers', Appl. Opt., 17 (24), pp. 3990-3998, 1978

[15] L. Thylen, 'The beam propagation method: an analysis of its applicability', Opt. Quantum Electron., 15 (5), p. 433-439, 1983

[16] J. Van Roey, J. van der Donk, and P.E. Lagasse, 'Beam propagation method: Analysis and assessment' J. Opt. Soc. Amer., 71 (7), pp. 803-810, 1981

[17] Y. Chung amd N. Dagli, 'Explicit finite difference beam propagation method: application to semiconductor rib waveguide Y-junction analysis', Electron. Lett., 26 (11), pp. 711-713, 1990

[18] R. Scarmozzino and R.M. Osgood, Jr., 'Comparison of finite difference and Fourier transform solutions of the parabolic wave equation with emphasis on integrated optics applications', J. Opt. Soc. Amer. A, 8 (5), pp. 724-731, 1991

[19] P.L. Liu and B.J. Li. 'Study of form birefringence in waveguide devices using the semivectorial beam propagation method'. IEEE Phot. Tech. Lett.. 3 (10). pp. 913-915, 1991

[20] W.P. Huang. C.L. Xu. S.T. Chu. and S.K. Chaudhuri. 'A vector beam propagation method for guided-wave optics'. IEEE Phot. Tech. Lett.. 3 (10). pp. 910-913, 1991

[21] W.P. Huang. C.L. Xu, S.T. Chu. and S.K. Chaudhuri. 'The finite difference vector beam propagation method: analysis and assessment'. J. Lightwave Technol.. 10 (3), pp. 295-305, 1992

[22] G.L. Yip and P.C. Noutsios, 'An improved finite-difference vector beam propagation formulation for graded-index waveguides', IEEE Photon. Technol. Lett., 6 (4), pp. 543-545, 1994

[23] M.S. Stern, 'Semivectorial polarised finite difference method for optical waveguides with arbitrary index profiles', IEE Proc., Pt. J. 135 (1), pp. 56-63, 1988

[24] P. Duchateau and D.W. Zachmann, *Partial Differential Equations*. Schaum's Outline Series, McGraw-Hill, New York, 1986

[25] G.R. Hadley, 'Transparent boundary condition for beam propagation methods', Opt. Lett., 16 (9), pp. 624-626, 1991

[26] M.D. Feit and J.A. Fleck, Jr. 'Computation of mode properties in optical fiber waveguides by a propagating beam method', Appl. Opt., 19 (7), pp. 1154-1163, 1980

[27] M.D. Feit and J.A. Fleck, Jr., 'Computation of mode eigenfunctions in graded-index optical fibers by the propagating beam method', Appl. Opt., 19 (13), pp. 2240-2246, 1980

[28] Y. Chung, N. Dagli, and L. Thylen, 'Explicit finite difference vectorial beam propagation method', Electron. Lett., 27 (23), pp. 2119-2121, 1991

[29] P.L. Liu and B.J. Li, "Semivectorial beam-propagation method for analyzing polarized modes of rib waveguides", IEEE J. Quantum Electron., 28 (4), pp. 778-782, 1992

[30] W.P. Huang, C.L. Xu, and S.K. Chaudhuri, 'A finite- difference vector beam propagation method for three-dimensional waveguide structures', IEEE Photon. Technol. Lett., 4 (2), pp. 148-151, 1992

[31] E.E. Kriezis and A.G. Papagiannakis, 'A joint finite-difference and FFT full vectorial beam propagation scheme', J. Lightwave Technol., 13 (4), pp. 692-700, 1995

[32] D. Yevick and B. Hermansson, 'Efficient beam propagation techniques', J. Quantum Electron., 26 (1), pp. 109-112, 1990

[33] G.R. Hadley, 'Transparent boundary condition for the beam propagation method', J. Quantum Electron., 26 (1), pp. 363-370, 1992

[34] D. Marcuse, *Light Transmission Optics*, 2nd ed., Van Nostrand Reinhold, New York, 1982

Chapter 5

Waveguide Characterization

5.1 Introduction

In this chapter, the theoretical modeling and experimental characterizations of the planar field-assisted ion-exchanged waveguides and the Al_2O_3 sputtered guides are presented. The propagation characteristics, such as the refractive index profile and dispersion curves, are determined and compared to the effective mode index measurements. Parallel to this, the diffusion characteristics measured by EPMA, such as the K^+-ion dopant profile, are presented. The results from these studies are also used to predict the characteristics of the buried channel guides.

5.2 Propagation characteristics

5.2.1 Background

The field-assisted ion-exchange process has been shown to have advantages over the thermal exchange owing to the drastic reduction in the diffusion time. It is also possible to obtain various refractive index profiles [1], including the step profile [2, 3]. in planar waveguides. Furthermore, this exchange has been used in a two-step process for the fabrication of deep, buried waveguides made by Ag^+-ion exchange [4] which are attractive in the design of passive devices optimized for efficient coupling with optical fibers. The field-assisted K^+-ion exchange was previously studied for chemical strengthening in commercial glass [5]. This process has led to low-loss planar and

channel buried waveguides in soda-lime and BK7 glass [6] and reproducible directional couplers [7]. Recently, this technique has also shown promise in the demonstration of integrated optic lasers on neodymium doped soda-lime glass [8].

However, a detailed characterization of the planar waveguide properties such as the effective field-dependent diffusion coefficient, guide depth and index change in soda-lime glass is lacking. Here, we report our experimental results of these characteristics for TE and TM modes and establish simple formulas for this coefficient and waveguide depth [9]. These relations would be useful in the design of passive devices which use field-assisted K^+-ion exchange waveguides as basic structures.

The characterizations of the purely thermal migration of Ag^+ ions [10] and K^+ ions [11] in glass yielded a square root dependence between the effective waveguide depth d and the diffusion time t, as given by

$$d = \sqrt{D_e\, t}\,, \tag{5.1}$$

where D_e is the effective diffusion coefficient dependent on the temperature T. For example at $T = 385^oC$, $D_e(TE) = 0.0649\,\mu m^2/\text{min.}$ and $D_e(TM) = 0.0637\,\mu m^2/\text{min.}$ for K^+ ions in soda-lime glass [11]. However, for the electromigration of silver [12, 13] and potassium ions [3, 6], several researchers have found a linear relationship between d and t. In particular, for low values of the total applied electric field E_a^T, the diffusion term can not be ignored. For Ag^+ ions, Ramaswamy *et al.* found that a linear combination of the diffusive and electromigrative terms [Eq. (12) of [12]] was more suitable for expressing the guide depth. Here, a similar approach can be adopted [9] and hence,

$$d = \sqrt{D_e\, t} + F_e t + K_o \tag{5.2}$$

where F_e is defined as the electromigrative coefficient and K_o is a constant. This coefficient is linearly proportional to the applied field E_a^T such that

$$F_e = \mu_K\, E_a^T \tag{5.3}$$

where μ_K is the K^+-ion mobility in glass. The importance of establishing relations (5.2) and (5.3) is that, given the fabrication conditions (E_a^T, t, T) for a waveguide, one can easily determine the guide depth without the need for further measurements.

5.2.2 Experimental observations

To fabricate the waveguides, the glass substrates were placed between symmetrical stainless steel half-cells isolated by Teflon seals in a container, as described in Chapter 3. Potassium nitrate crystals were placed in small steel containers suspended just over the half-cells. Once the furnace reached equilibrium at $T = 385°C$, the melt was then poured into the anode and cathode cells and a constant voltage was applied across the sample. Electric fields E_a and diffusion times ranged from 5.3 to 52.1 V/mm and 2 to 20 min, respectively. The samples made for $t < 2min$ will be presented later. To overcome the preliminary difficulties of substrate cracking, the samples remained in the furnace for an additional 10 min before cooling in air.

We observed that the ionic current decreased sharply to about one-half its initial value in the first minute of diffusion and then decayed exponentially with time, as shown in Fig. 5.1. This phenomenon was also reported by other researchers [5, 6] and can be explained based on ion-exchange theory. Since $\alpha \neq 0$ for soda-lime glass, a constant applied field will not result in a constant ionic flux. This can be deduced from (2.13). Since the concentration of K^+ ions increases with time and E_a is fixed, then the term $(1 - \alpha \hat{c}_K)$, which is proportional to the ionic current, decreases. Furthermore, when the applied voltage was removed and the two half-cells short-circuited through a voltage meter, an average value of 1.3 V was measured for all the samples. This voltage decayed to about 0.5 V by the end of the cooling process. This potential drop V_o (battery effect) was also observed by previous researchers [12, 14] and can be represented by a constant field E_o so that $E_a^T = E_a - E_o$, where E_a is the applied field. In terms of voltages, $E_a^T = (V_a - V_o)/d_{sub}$ where V_a the applied voltage and d_{sub} is the substrate thickness.

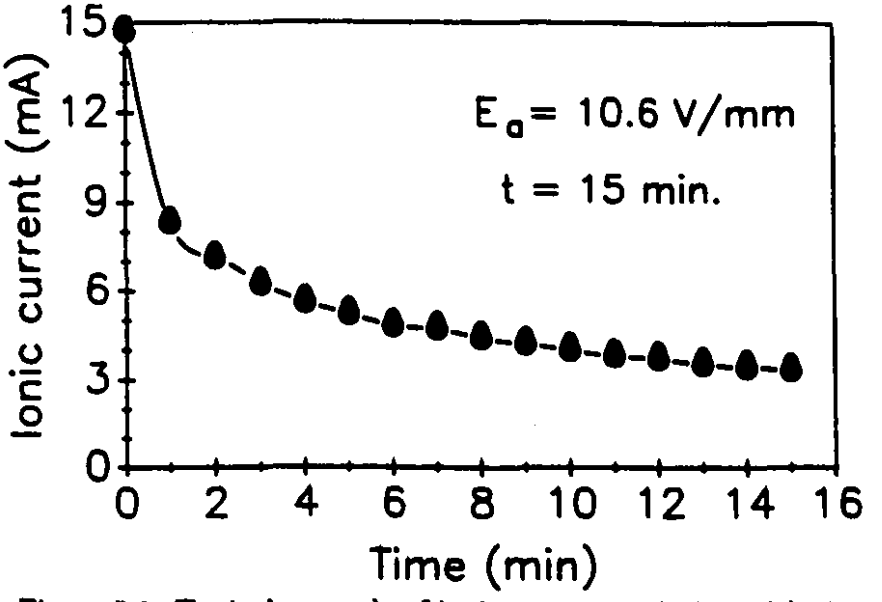

Figure 5.1: Typical example of ionic current variation with time

5.2.3 Data reduction and dispersion curves

From the measured effective mode indices, presented in Tables 5.1 and 5.2, the refractive index profile can be deduced. We have chosen a direct, statistical approach that involves *a priori* knowledge of this profile [10, 11]. The crux of the method lies in finding a suitable refractive index profile for which a solution to the WKB dispersion relations yields effective indices that fit as closely as possible to the measured ones. The choice of the profile is based on ion-exchange theory and is justified by the successful reproduction of the measured data in comparison to the theoretical curves. Another popular approach is an inverse method, known as the inverse WKB method [15], which involves reconstruction of the index profile from the mode index measurements. This method is only accurate when many modes are measurable.

	17	39	41	Wvg.# 37	14	38	29	22
TE_o	1.5196	1.5215	1.5217	1.5206	1.5223	1.5230	1.5204	1.5221
TE_1	1.5140	1.5169	1.5178	1.5156	1.5192	1.5210	1.5154	1.5190
TE_2		1.5125	1.5136		1.5155	1.5181		1.5153
TE_3						1.5148		

	15	21	8	Wvg.# 32	33	2	30	5
TE_o	1.5232	1.5235	1.5236	1.5222	1.5232	1.5235	1.5227	1.5235
TE_1	1.5219	1.5227	1.5229	1.5180	1.5214	1.5225	1.5204	1.5230
TE_2	1.5199	1.5213	1.5218	1.5137	1.5189	1.5212	1.5174	1.5224
TE_3	1.5176	1.5197	1.5207		1.5163	1.5194	1.5141	1.5214
TE_4	1.5149	1.5178	1.5190		1.5131	1.5175		1.5204
TE_5	1.5125	1.5156	1.5172			1.5145		1.5191
TE_6		1.5133	1.5154			1.5129		1.5176
TE_7			1.5133					1.5161
TE_8								1.5145
TE_9								1.5129

Table 5.1: Measured effective TE mode indices at $T = 385^oC$

	17	39	41	Wvg.# 37	14	38	29	22
TM_0	1.5214	1.5241	1.5243	1.5228	1.5247	1.5253	1.5224	1.5255
TM_1	1.5151	1.5191	1.5200	1.5173	1.5213	1.5229	1.5171	1.5224
TM_2		1.5137	1.5155		1.5173	1.5200		1.5183
TM_3					1.5132	1.5164		1.5141
TM_4						1.5128		

	15	21	8	Wvg.# 32	33	2	30	5
TM_0	1.5257	1.5257	1.5258	1.5242	1.5255	1.5260	1.5250	1.5260
TM_1	1.5243	1.5248	1.5252	1.5198	1.5240	1.5250	1.5226	1.5255
TM_2	1.5222	1.5235	1.5241	1.5150	1.5210	1.5236	1.5194	1.5249
TM_3	1.5197	1.5218	1.5228		1.5180	1.5217	1.5159	1.5238
TM_4	1.5170	1.5197	1.5212		1.5148	1.5196	1.5125	1.5227
TM_5	1.5139	1.5174	1.5195			1.5174		1.5213
TM_6		1.5149	1.5174			1.5148		1.5198
TM_7		1.5125	1.5152			1.5125		1.5182
TM_8			1.5130					1.5164
TM_9								1.5144
TM_{10}								1.5129

Table 5.2: Measured effective TM mode indices at $T = 385^oC$

The refractive index (concentration) profile of constant applied current [3] and constant applied electric [5, 6] field-assisted K^+-ion exchange planar waveguides was found to be step-like and in the former case, this step-index model was used to generate dispersion curves. Although this may be suitable for waveguides fabricated by either high current or electric field, it may not yield accurate results for the lower field strengths used in our experiments. For reasons discussed in Chapter 2, we used a modified Fermi index distribution [16] which was previously used to model glass waveguides made by Tl^+ ion exchange. The profile is modified to accommodate the fact that $f(0) = 1$ for surface guides. The index profile

$$n(x) = n_b + \Delta n_s \left[1 - \exp\left(-\frac{d}{a}\right) + \exp\left(\frac{x-d}{a}\right) \right]^{-1} . \tag{5.4}$$

where $\Delta n_s = n_s - n_b$, n_s is the surface index and a is a fitting parameter associated with the shape of the profile. The effective guide depth d is such that $n(d) = n_b + \Delta n_s/[2-\exp(-d/a)]$. For the mult-mode measurements, it was found that d/a ranged from about 4 to 23 and $\exp(-d/a) \ll 1$, so that the guide depth occurs close to the half-point of the profile.

The WKB dispersion relation for graded-index profiles (4.32) was used. Letting $\varepsilon = \exp(-d/a)$, so that $a = -d/\ln(\varepsilon)$, in (5.4), the profile becomes

$$n(x) = n_b + \Delta n_s \left[1 - \varepsilon + \varepsilon \exp\left(-\frac{x}{d}\ln(\varepsilon)\right) \right]^{-1} ,$$

which, upon defining the normalized variable $\xi = x/d$, it becomes

$$n(\xi) = n_b + \Delta n_s [\, 1 - \varepsilon + \varepsilon \exp(-\xi \ln(\varepsilon)) \,]^{-1}. \tag{5.5}$$

At the normalized turning point, $n(\xi_t) = N_{eff}$ and after some manipulations, we obtain

$$\xi_t = -\ln\left\{1 + \frac{n_s - N_{eff}}{\varepsilon(N_{eff} - n_b)}\right\} / \ln(\varepsilon).$$

Also, the depth d can now be expressed with the help of (4.32) as

$$d = \frac{m\pi + \phi_1 + \phi_2}{k_o \int_0^{\xi_t} \sqrt{n^2(\xi) - N_{eff}^2}\, d\xi}. \tag{5.6}$$

To find the unknowns n_s, d, and a, we started with multimode ($m > 2$) waveguides. This is necessary because this three parameter system needs at least three modes to be solved deterministically. Equation (5.6) involves the unknowns n_s and ε. Thus, given any pair of measured indices, one can eliminate d using (5.6) and, for a given value of ε, n_s can be determined by a root-searching technique. Then, n_s and ε can be substituted back into (5.6) to find d. Applying this procedure repeatedly to all the possible pairs of mode indices for a particular waveguide, one can determine the average values of n_s and d for that guide. The best value of ε that minimized the deviations of n_s and d from their average values was chosen for each guide. The profile parameter a is then determined from $a = -d/\ln(\varepsilon)$. For single and two mode waveguides, we used the average values of n_s and a from the multimode samples to determine the depth d using (5.6).

We have observed that the value of the surface index, n_s, is affected only by the temperature and applied field but is independent of the diffusion time. In addition, n_s was found to be higher in comparison to that of the purely thermal ion exchange [11]. This increase may be due to the stress-optic effect [3, 17]. However, any further investigation of this point is beyond the scope of this thesis.

For each chosen field, waveguides were prepared with various diffusion times and the average values of n_s and a for all the samples were then used to compute the theoretical dispersion curves from the WKB dispersion relation. In Fig. 5.2, these curves are presented together with the experimentally measured data for both polarizations in the samples prepared at $E_a = 21.1\,V/mm$, respectively. The values of n_s, d and a for each waveguide are listed in Tables 5.3 and 5.4. Furthermore, as mentioned previously, step-index approximations to the refractive index profile were made by other researchers. For comparison, we also used this model for the $E_a = 21.1\,V/mm$ TE case. Based on the step-index dispersion relation (4.29), the curves were generated and compared to those of Fig. 5.2 as shown in Fig. 5.3. Clearly, the modified Fermi profile gives better agreement to experimental data.

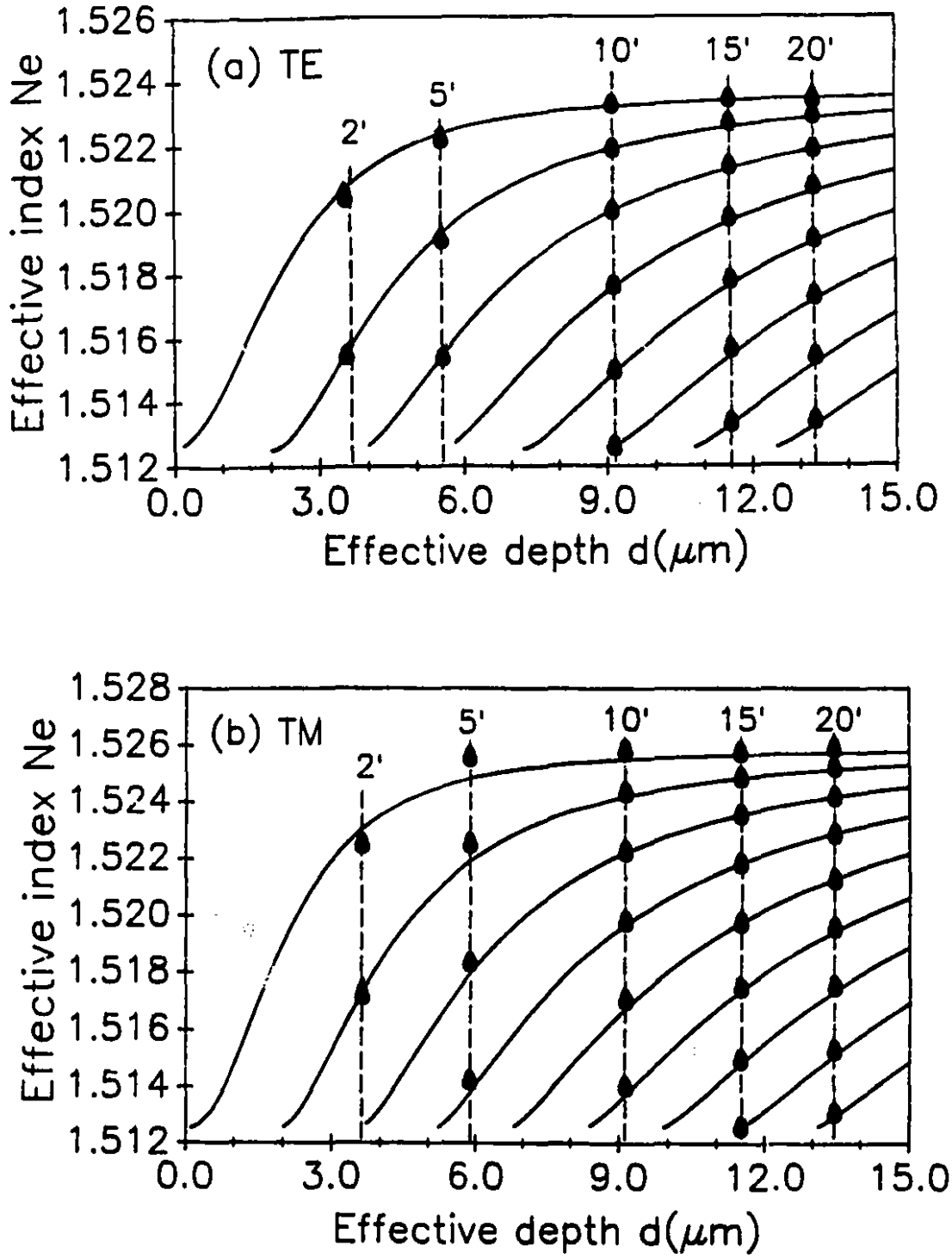

Figure 5.2: Theoretical dispersion curves (modified Fermi profile) compared with measured mode indices for waveguides prepared at $E_s = 21.1\,V/mm$ (diffusion time in minutes) (a) TE modes (b) TM modes

As we have seen, the relation between n_s, d, and a can be modeled accurately using the dispersion curves. However, a deterministic relation between the applied field and time duration (E_a^T, t) and the refractive index change, guide depth and profile parameter $(\Delta n_s, d, a)$ needs to be established so that necessary waveguide parameters can be predicted from arbitrary fabrication conditions. As described earlier, the effective depth d can be expressed by (5.6) for each applied field. The validity of this relation can be verified by plotting d against t for all the measured guides (TE and TM), as shown in Figs. 5.4 (a) and (b). The constant K_o and the coefficient F_e are obtained by using a least square fit for every E_a^T and extrapolating the fits for $t < 2min$ to intersect the ordinate. We note that the $10min$ cooling time contributes to K_o; further discussion will be presented in the next section. All the relevant parameters are tabulated in Tables 5.5 and 5.6. In Fig. 5.4(a) and (b), the F_e values are plotted against E_a^T with the help of linear regression yielding $\mu_K(TE) = 21.33\ \mu m^2/Vmin$ and $\mu_K(TM) = 20.52\ \mu m^2/Vmin$.

These values compare well with the results of other researchers that dealt with field-assisted K^+-ion exchange used for the chemical strengthening of glass. Using EPMA to determine the potassium concentration profiles in silicate glass, Urnes measured the depth of penetration of three exchanged samples (see Table II of [5]). From his results we deduce that μ_K varies from ≈ 21 to $23\ \mu m^2/Vmin$ for $E_a \approx 60V/mm$ and temperatures ranging from 350 to 365^oC. Ohta and Hara studied the same process, and from their rersults (see Fig. 3 of [18] we deduce that $\mu_K \approx 30\mu m^2/Vmin$ at 420^oC and $99\,V/cm$. Recently, Miliou *et al* reported a mobility value of $1.63\ \mu m^2/Vmin$ [6]. However, they used a much lower temperature of 330^oC, $E_a = 100V/mm$, and a diluted KNO_3 melt.

$Wvg.\#$	E_a (V/mm)	t (min)	d (μm)	n_s	a (μm)
17		10	3.03	1.5233	0.60
39	5.3	15	4.16	1.5233	0.43
41		20	4.72	1.5232	0.61
37		5	3.72	1.5238	0.66
14	10.6	10	5.56	1.5237	0.76
38		15	7.06	1.5238	0.69
29		2	3.55	1.5234	0.75
22		5	5.54	1.5235	0.76
15	21.1	10	9.15	1.5235	0.57
21		15	11.56	1.5237	0.63
8		20	13.31	1.5237	0.67
32		2	4.54	1.5240	0.64
33	32.1	5	8.00	1.5235	0.50
2		10	11.08	1.5237	0.66
30	52.1	2	6.74	1.5235	0.68
5		10	16.38	1.5236	0.79

Table 5.3: Calculated TE mode modified Fermi profile parameters at $T = 385^oC$

$Wvg.\#$	E_a (V/mm)	t (min)	d (μm)	n_s	a (μm)
17		10	2.97	1.5254	0.64
39	5.3	15	4.10	1.5265	0.58
41		20	4.74	1.5261	0.70
37		5	3.72	1.5255	0.57
14	10.6	10	5.61	1.5258	0.55
38		15	7.05	1.5258	0.51
29		2	3.62	1.5260	0.75
22		5	5.88	1.5263	0.48
15	21.1	10	9.14	1.5260	0.65
21		15	11.51	1.5258	0.50
8		20	13.45	1.5259	0.58
32		2	4.60	1.5261	0.66
33	32.1	5	7.90	1.5264	0.80
2		10	11.29	1.5260	0.53
30	52.1	2	6.87	1.5255	0.47
5		10	16.17	1.5261	0.85

Table 5.4: Calculated TM mode modified Fermi profile parameters at $T = 385^oC$

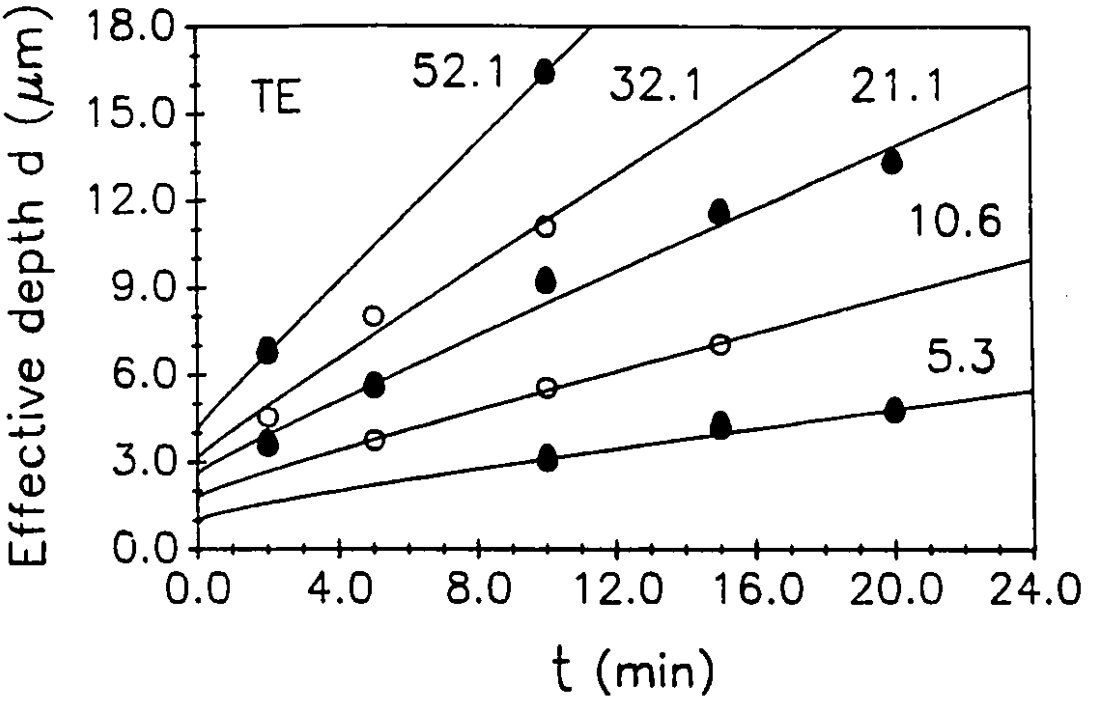

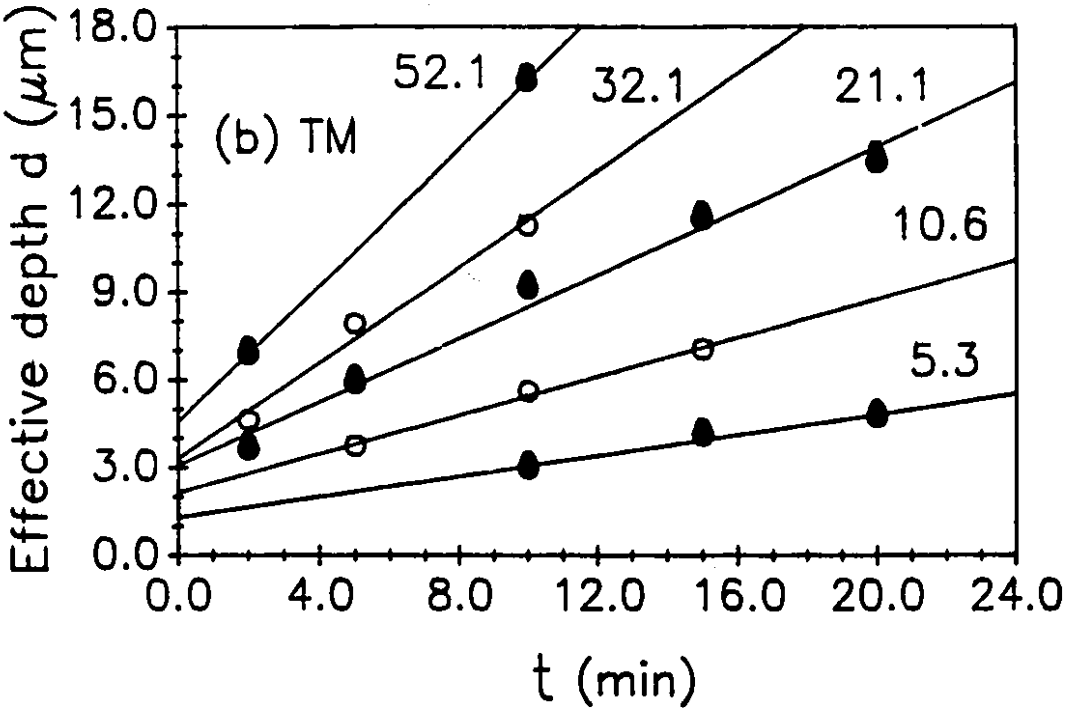

Figure 5.3: Effective guide depths vs. the diffusion time (applied field in V/mm) for (a) TE modes (b) TM modes

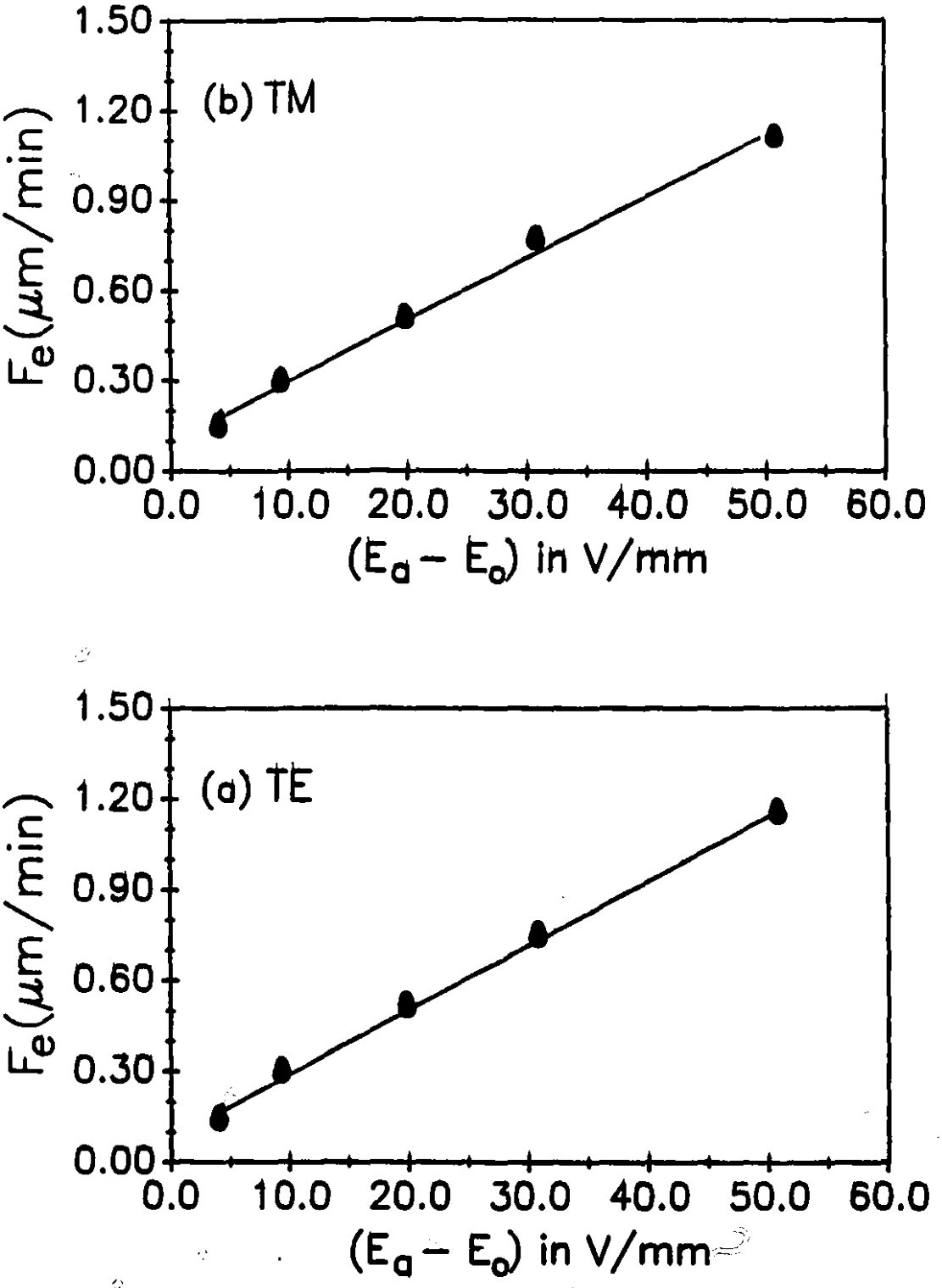

Figure 5.4: Variation of coefficient F_e with applied field E_a for (a) TE modes and (b) TM modes

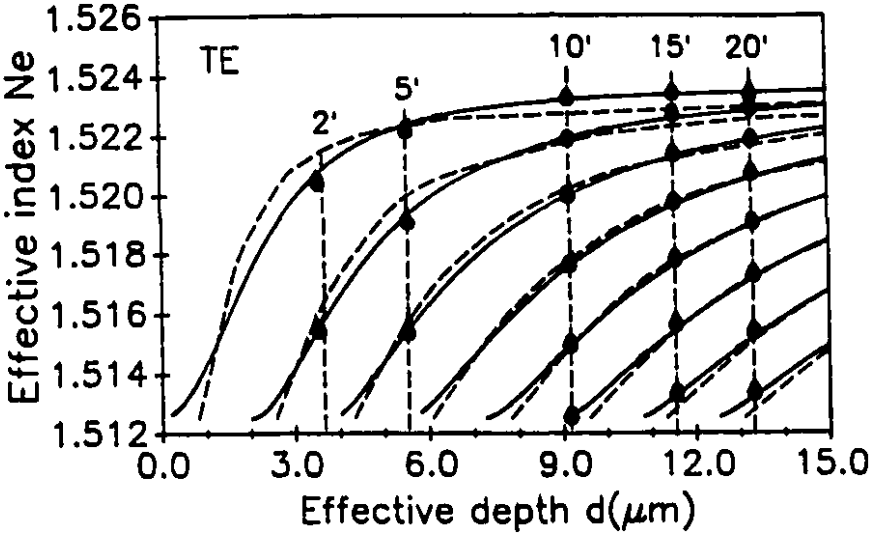

Figure 5.5: Comparison of the theoretical dispersion curves of a modified Fermi profile (solid curve) with the step profile (dashed curve) together with the experimental data of Fig. 5.2(a) at $T = 385°C$

E_a (V/mm)	$\Delta n_s(TE)$ $(\times 10^{-3})$	$\Delta n_s(TM)$ $(\times 10^{-3})$	$a(TE)$ (μm)	$a(TM)$ (μm)
5.3	10.8 ± 0.0	13.7 ± 0.3	0.53	0.64
10.6	11.2 ± 0.2	13.3 ± 0.1	0.69	0.52
21.1	11.1 ± 0.1	13.4 ± 0.2	0.65	0.57
32.1	11.2 ± 0.1	13.6 ± 0.2	0.61	0.60
52.1	11.1 ± 0.0	13.5 ± 0.2	0.78	0.79

Table 5.5: Measured Δn_s and profile parameters for various E_a at $T = 385°C$

E_a (V/mm)	$F_e(TE)$ $(\mu m/min)$	$F_e(TM)$ $(\mu m/min)$	$K_o(TE)$ (μm)	$K_o(TM)$ (μm)
5.3	0.136	0.144	0.96	0.81
10.6	0.292	0.291	1.74	1.76
21.1	0.509	0.503	2.56	2.72
32.1	0.742	0.765	3.09	3.01
52.1	1.149	1.107	4.08	4.30

Table 5.6: F_e and K_o values for various applied fields at $T = 385°C$

5.2.4 Discussion of errors

From the dispersion curves of Fig. 5.2. the agreement between the experimentally measured mode indices and the theoretical curves seems quite good. The discrepancies between theory and experiment were calculated for each of the 153 measured indices and the average of these was found to be:

$$| N_e(meas.) - N_e(theo.) | = (1.1 \pm 1.2) \times 10^{-4}$$

with the largest single deviation being 6×10^{-4}. Another key factor in this characterization involves the reproducibility of such waveguides under given fabrication conditions. To evaluate this property, two waveguides were fabricated one week apart under identical fabrication conditions. It was found that the differences in the measured mode indices were within the measurement error (see Table 5.7). Although short diffusion times were used, we were able to control the fabrication process quite accurately with the estimated error in the time measurements being $\pm 1\,s$.

$Wvg.\#15$	$Wvg.\#11$	$\delta\,(\times 10^{-4})$
1.5231	1.5233	2
1.5218	1.5219	1
1.5199	1.5200	1
1.5175	1.5177	2
1.5149	1.5150	1
1.5125	1.5125	0

Table 5.7: Comparison of the effective indices of two waveguides fabricated under identical conditions

5.2.5 Single-mode surface guides

The characterization of single-mode planar surface guides is also very important for device design. Here, the modified Fermi profile parameters (Δn, and a) are assumed to be the same as those for the multi-mode case. Two applied fields (20 and 50 V/mm) were investigated more closely so as to determine the range of diffusion times needed for single-mode operation. The effective depth d is determined using the measured N_{eff} in (5.6) with $m = 0$ and for the two-mode cases with $m = 1$. Fig. 5.6 shows the dispersion curves together with the experimentally measured data for $E_a = 50V/mm$. The effective depths d are compared to those obtained for the multi-mode waveguides in Fig. 5.7. Note that the multi-mode region begins when $t > 60\,s$ for 20 V/mm and $t > 15\,s$ for 50 V/mm. It seems that the depth varies linearly with time and then saturates to another level with a smaller gradient. This 'dual slope effect' was also observed by Chiba *et al* [19] in the fabrication of planar microlenses using K^+-ion electromigration in glass. The reason for this is due to the thermal diffusion effect ($\propto \sqrt{t}$) becoming more dominant when the diffusion time is small. Mathematically, this can be seen by differentiating (5.2) yielding

$$\frac{\partial}{\partial t}(d) = \frac{1}{2}\left(\frac{D_e}{t}\right)^{1/2} + F_e$$

At larger diffusion times, the first term is negligible and the slope is constant and equal to F_e. As t decreases, the first term gains importance causing the slope to become steeper, as shown in Fig. 5.8. This diffusion-dominant region has convinced some authors that (5.1) alone is needed to characterize field-assisted K^+-ion exchanged waveguides also [20].

Finally, the index profiles for the 20 and 50 V/mm single-mode samples are plotted in Fig. 5.8. Note how the profile shape changes as d increases; this is expected to occur when the profile parameter a and d become comparable. Here, d does not occur at the half-point of the profile as was assumed for the multi-mode cases.

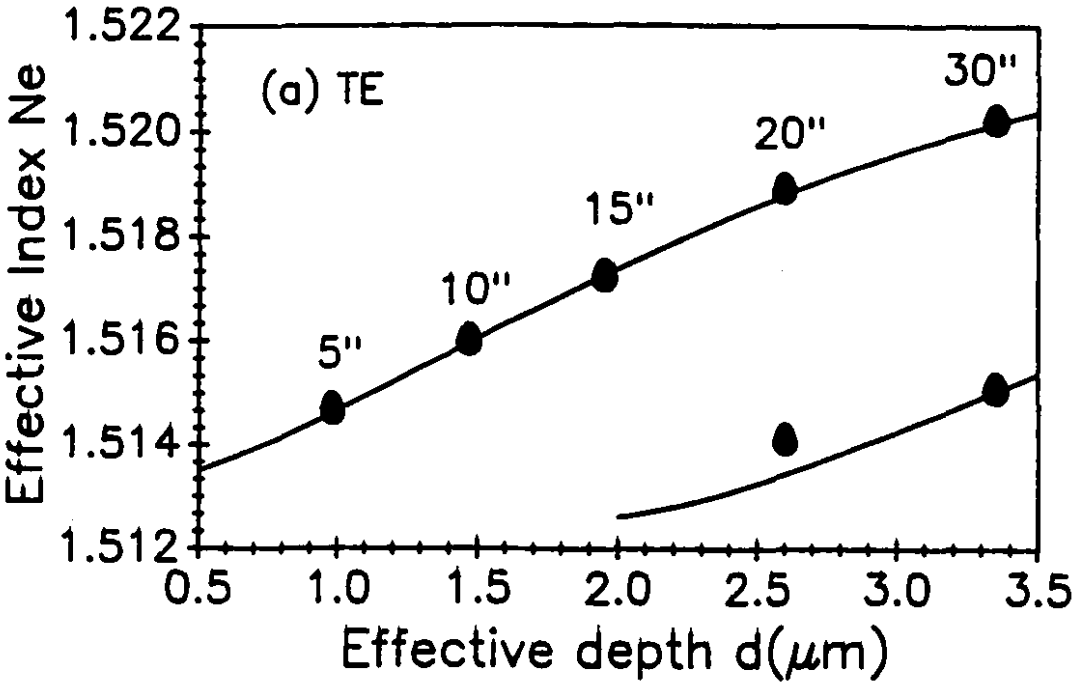

Figure 5.6: Theoretical dispersion curves of the guided TE modes compared with measured indices for guides prepared at $E_a = 50\,V/mm$ for a modified Fermi profile (time in seconds) at $T = 385°C$

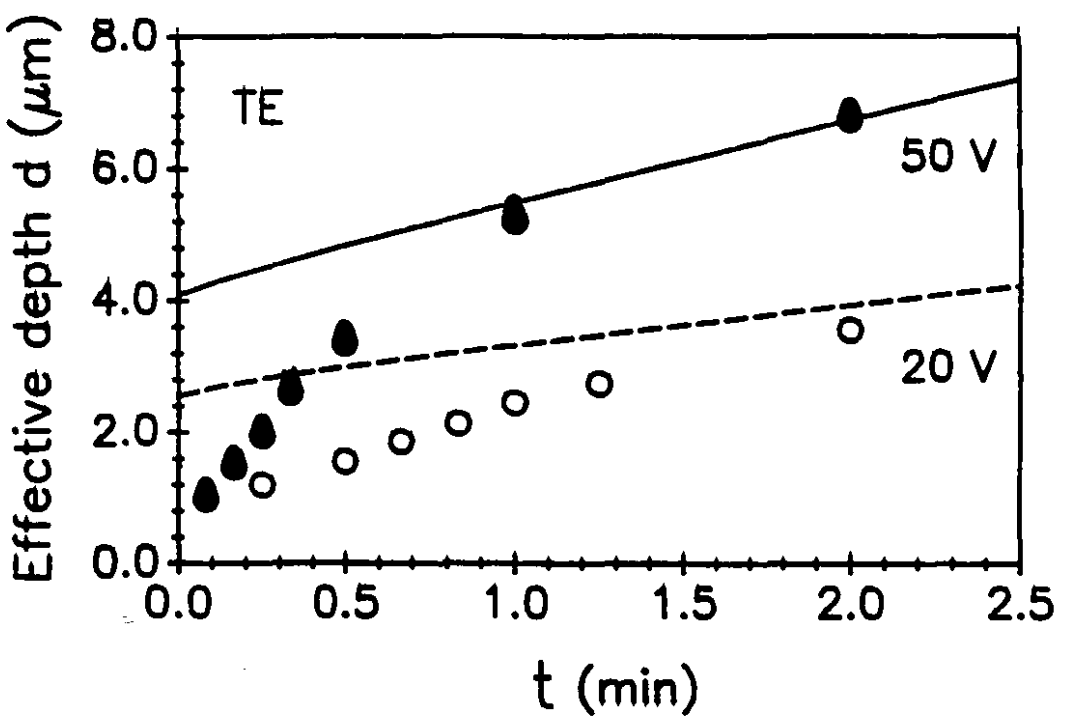

Figure 5.7: Comparison of the variation of guide depth with diffusion time for the lower- and higher-order TE modes at $T = 385°C$

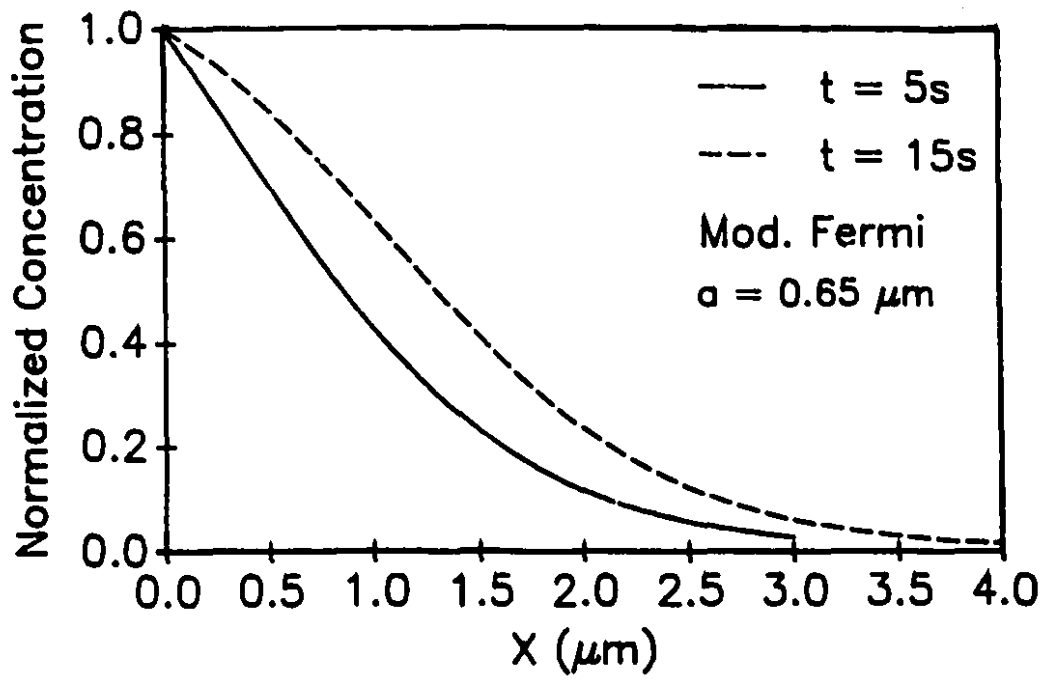

(a)

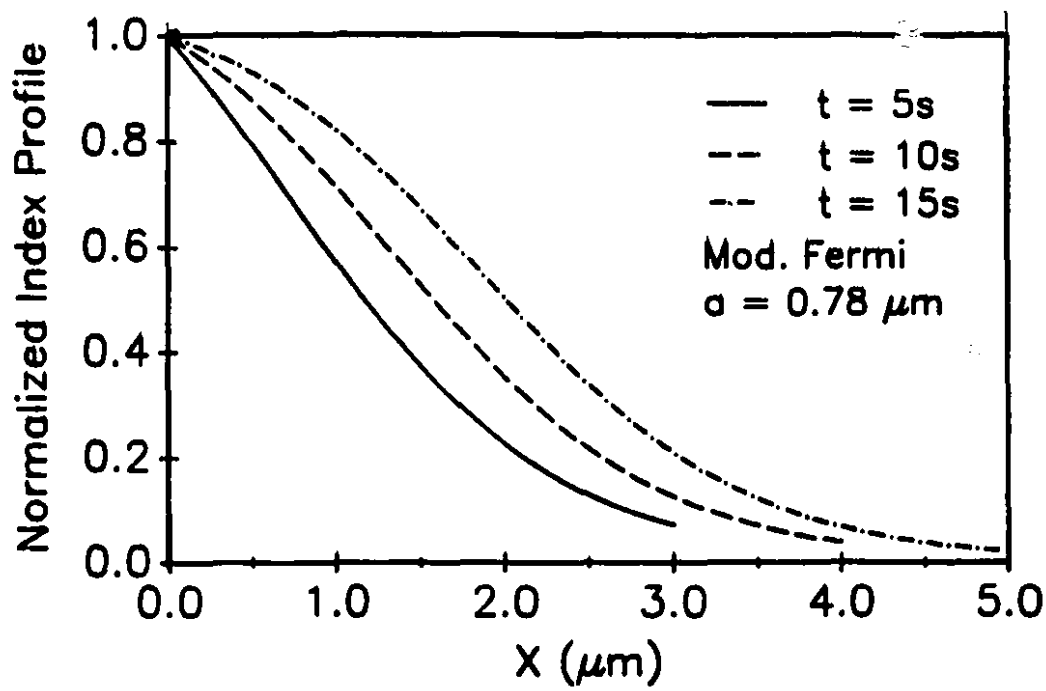

(b)

Figure 5.8: Modified Fermi profiles in the single-mode region for (a) 20 V/mm and (b) 50 V/mm at $T = 385°C$

5.2.6 Single-mode buried waveguides

The single-mode buried waveguide propagation characteristics were also of interest. For these guides, the characterization procedure was markedly different from that of the surface guides. We did not pursue a detailed multi-mode analysis to determine the profile. Instead, we relied on the concentration profile $c(x)$ calculated in Section 2.3 using the value of μ_K determined previously to construct the index profile $n(x)$. Further details of the diffusion characteristics are to be presented in the next section. Then, the Runge-Kutta method was used to calculate the effective indices for various t_2 and compared to measured data as shown in Table 5.8 for $E_{a1} = 20\,V/mm$, $t_1 = 5\,s$, and $E_{a2} = 100\,V/mm$. Here, the 20 V/mm surface guide data $\Delta n_s(TE) = 0.0111$ and $\Delta n_s(TM) = 0.0134$ (see Table 5.5) was used. Note that at $t_2 = 0$, the surface guide results are presented. The good agreement shows that the buried index model based on $c(x)$ is quite reliable.

t_2 (s)	$N_{eff}(TE)$ (theo.)	$N_{eff}(TE)$ (meas.)	$N_{eff}(TM)$ (theo.)	$N_{eff}(TM)$ (meas.)
0	1.5131712	1.5138	1.5135798	1.5145
30	1.5138598	N/A	1.5143349	N/A
60	1.5142305	N/A	1.5147429	N/A
90	1.5142997	N/A	1.5147995	N/A
100	1.5143023	1.5148	1.5147975	1.5152
120	1.5142963	1.5147	1.5147833	1.5149
140	1.5142835	1.5146	1.5147636	1.5148

Table 5.8: Comparison of calculated and measured buried guide effective indices at $T = 385^oC$

5.2.7 Propagation loss

The propagation losses of both surface and buried waveguides were measured as discussed in Chapter 3. One single-mode surface guide fabricated at $E_a = 50\,V/mm$ and $t = 5\,s$ was measured yielding a loss of $0.22 \pm 0.02 dB/cm$ for the TM mode. The $logP$ versus ΔL linear regression fit is shown in Fig. 5.9 (a) showing small deviations. In addition, one single-mode buried guide fabricated at $E_{a1} = 100\,V/mm$, $t_1 = 5\,s$, $E_{a2} = 100\,V/mm$, $t_2 = 120\,s$ yielded a lower loss of $0.1 \pm 0.04 dB/cm$ (see Fig. 5.9(b)). These two measurements show that the field-assisted K^+-ion exchange process yields low-loss guides that are suitable for integrated optics.

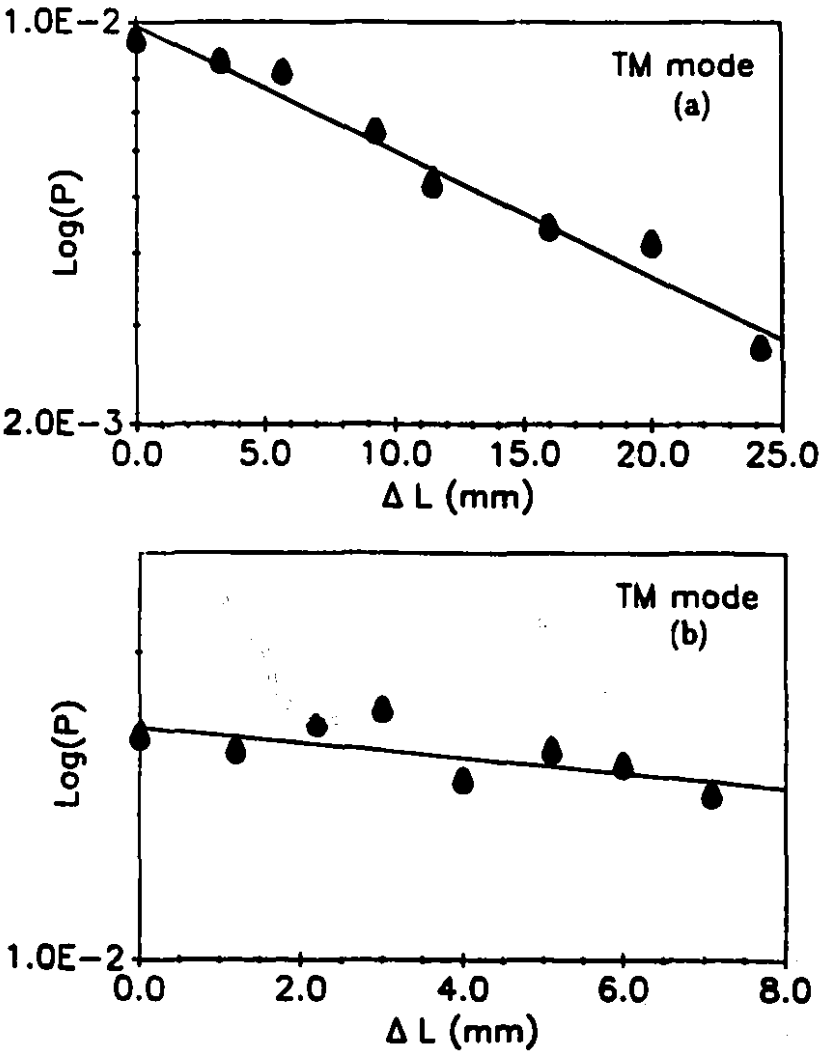

Figure 5.9: $LogP$ vs. ΔL variation yielding propagation loss for a single-mode (a) surface guide and (b) buried guide

5.2.8 Discussions

A few points for discussion should be brought forth. The first deals with prism coupling into the single-mode buried waveguides for the effective index measurements. We were able to couple the light into these guides because the index peaks occurred only at $2-6\,\mu m$ below the surface, thereby allowing for evanescent coupling. Also, it has been noted that using pure $NaNO_3$ in the backdiffusion process allows for ample out-diffusion of K^+ ions inducing tensile stresses that promote crack formation in the glass [21, 22]. This has been observed for purely thermal backdiffusion processes. However, for field-assisted cases, it has been shown that the electric field in the second step [23] prevents out-diffusion of K^+ ions and retards microcrack formation. This process yields good quality, low-loss waveguides without microcracks. Our own observations and loss measurements confirm this point.

Finally, it is worth noting that the diffusion depth d is slightly different for TE and TM modes due to the polarization dependence of F_e. This was observed by other researchers for the corresponding value of D_e, in the case of purely thermal K^+-ion exchange [6, 11]. Ideally, these depth values should be equal because the K^+-ion concentration is assumed to be the same as the index profile. In our study, we used D_K and μ_K in our ion-exchange model to be the respective average values for both TE and TM polarizations. The modeling of the index profile including polarizability and stress-optic effects [3, 21] is beyond the scope of this thesis.

5.3 Diffusion characteristics

5.3.1 Introduction

The diffusion characteristics of these optical waveguides refer to the dopant K^+-ion distribution in the glass that can be measured directly using the EPMA. In addition, these characteristics can be modelled using the ion-exchange equations developed in Chapter 2. As we are well aware, the knowledge of these dopant profiles is important since they are directly proportional to the refractive index. In this section, we present the results of the diffusion characteristics for both surface and buried waveguides.

5.3.2 Electron microprobe analysis

In the past, other researchers have used the probe for ion-exchanged profile measurements [6, 10]. Here, analyses for both flat and bevelled surfaces were carried out providing us with information that is relevant for modelling the diffusion characteristics to be presented in the next section.

The flat surface analysis is used to determine the fraction of exchanged K^+ ions close to the surface, h_K, leading to a knowledge of the boundary condition $\hat{c}_K(0,t)$. This value h_K was defined previously in (3.6). Various multi-mode and single-mode planar guides are studied with the results shown in Tables 5.9 and 5.10, for surface and buried guides, respectively. For the surface guide 8-92D, fabricated at $E_a^T = 19.8 V/mm$ for $t = 20 min$, h_K was found to be $90.5 \pm 1\%$, as mentioned in Chapter 3. However, for short exchange times (eg. $t = 5\,s$), h_K is quite far from the value of 0.9. This is to be expected since it takes a finite amount of time for the initial surface K^+ concentration ($\hat{c}_K(0,0) = 0$) in the glass to reach this value. The variation of h_K with t shows a rapid saturation to 0.9 with applied field. For $20\,V/mm$, saturation is reached within one minute of diffusion time, whereas for $50\,V/mm$, it is reached within $20s$. From this data, it is now evident that the boundary condition $\hat{c}_K(0,t) \neq 1$ even though c_K is normalized with respect to c_o. The renormalization

of (2.18) to fulfill the boundary condition $c(0,t) = \dot{c}_K(0,t)/h_K = 1$ yields a value of $\dot{\alpha} = \alpha \times h_K$. For the buried guides, the potassium surface concentration decreases dramatically as the applied field increases up to a maximum of $100V/mm$. The higher potential in the backdiffusion process in $NaNO_3$ allows more of the Na^+ ions to displace the K^+ ions of the initial surface guide, allowing the guide to achieve almost complete burial. Hence, the boundary condition for backdiffusion at $x = 0$ is equal to h_K of Table 5.10.

The analysis for the bevelled surface is performed along the samples' angle-polished surface, as described in Chapter 3, with $\theta = 1.01°$, to measure the waveguide concentration profile. Sample $8 - 92D$ was measured yielding the profile shown in Fig. 5.10, which is in good agreement to the optically measured Fermi index profile for the TE mode with $a = 0.65\,\mu m$ and $d = 13.3\,\mu m$.

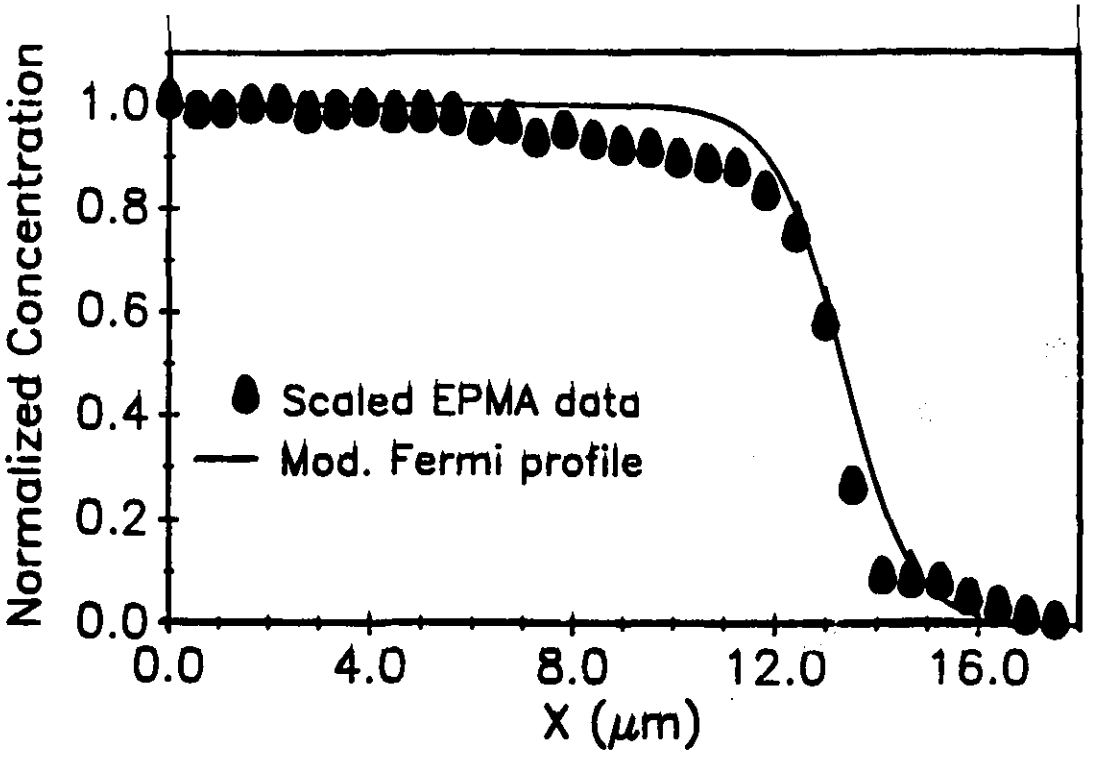

Figure 5.10: Comparison of the modified Fermi profile to the EPMA data

Table 5.9: Measured fractional exchange for various surface guides at $T = 385°C$

Sample	E_a^T (V/mm)	t $(s; min)$	h_K (%)
8-92D	19.8	$20\,min$	90.5 ± 1.0
50-20	50.8	$20\,s$	89.6 ± 1.0
20-60	19.3	$60\,s$	85.1 ± 1.0
20-5	19.3	$5\,s$	27.4 ± 1.0

Table 5.10: Measured fractional exchange for various buried guides at $T = 385°C$

Sample	E_{a1} (V/mm)	t_1 $(s; min)$	E_{a2} (V/mm)	t_2 $(s; min)$	h_K (%)
B20-20/10	21.1	$20\,min$	21.1	$10\,min$	28.3 ± 1.0
B50-20/20	50.4	$20\,s$	50.4	$20\,s$	21.8 ± 1.0
B75v5c	50.4	$15\,s$	75.2	$5\,min$	5.7 ± 1.0
B100v5c	50.4	$5\,s$	101.8	$2\,min$	3.0 ± 1.0

5.3.3 Modelled diffusion profiles

The field-assisted ion-exchange equation (2.23) was solved by the numerical scheme described in Chapter 2. Surface guide profiles were modelled using appropriate initial and boundary conditions. Initially at $t = 0$, there are no K^+-ions in the glass and hence, $c(x, 0) = 0$. For the exchange of K^+ and Na^+ ions in soda-lime glass at $T = 374°C$, it has been established that the much smaller Na^+ ions have a higher mobility than the K^+ ions yielding a ratio (D_K/D_{Na}) of 1/500, corresponding to $\alpha = 0.998$ [24]. The values D_K and μ_K were determined from the average of the TE and TM mode values to be $D_K = 0.06429\,\mu m^2/min$ and $\mu_K = 20.925 \mu m^2/V min$. For surface guides that have reached saturation ($h_K = 0.9$), we used $\dot{\alpha} = 0.898$ and the left boundary condition (LBC) $c(0, t) = 1$. The right boundary condition $c(\infty, t) = 0$ was assumed. Equation (2.23) was solved for time t and then followed by the ten minute cooling simulation. The solution for $E_a^T = 9.3\,V/mm$ and $t = 10 min$ is shown in Fig. 5.11 in comparison to the modified Fermi profile where good agreement is obtained. Here, the TE and TM mode values for a and d, shown in Tables 5.3 and

5.4 were used.

For samples that had not yet reached saturation (mostly in the single-mode region), we used the h_K values of Table 5.9 to find $\hat{a}$. Fig. 5.12 shows the diffusion profile for $E_a^T = 18.3\,V/mm$, $t = 5\,s$, $\hat{a} = 0.2994$ ($h_K = 0.3$, $LBC = 1$) including the cooling effect. This profile is compared to the Fermi profile for both TE and TM modes showing good agreement.

For single-mode surface and buried waveguides, no EPMA bevelled data is available. However, using the results of Table 5.10, the profiles were numerically simulated. In Chapter 2 (Fig. 2.6), the evolution of the buried waveguides was shown for $E_{a1}^T = 18.3\,V/mm$, $t_1 = 5\,s$, $E_{a2} = 94.7\,V/mm$, and t_2 ranging from 30 to 140 s using $\hat{a} = 0.2994$ and $LBC = 1$. These simulations include a $10min$ cooling process after both field-assisted processes. The location of the concentration peak, x_{peak}, and its maximum value, n_{peak} are plotted against t_2 in Fig. 5.13 (a) and (b), respectively. Note the flat behaviour of n_{peak} over a wide range range of t_2. Assuming that the refractive index profile is proportional to the concentration profile, these profiles were then used to determine the index profile $n(x) = n_b + \Delta n_s c(x)$ with the surface index values of Table 5.5.

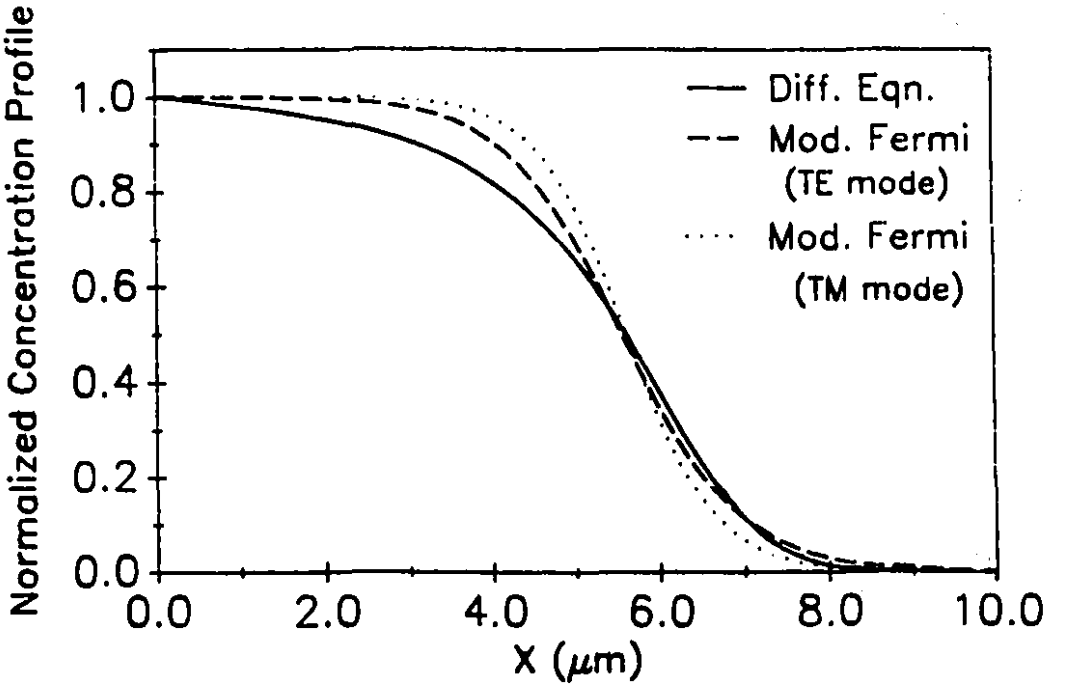

Figure 5.11: Comparison of the modified Fermi profile to the ion-exchange simulation for $E_a^T = 9.3\,V/mm$ and $t = 10\,min$

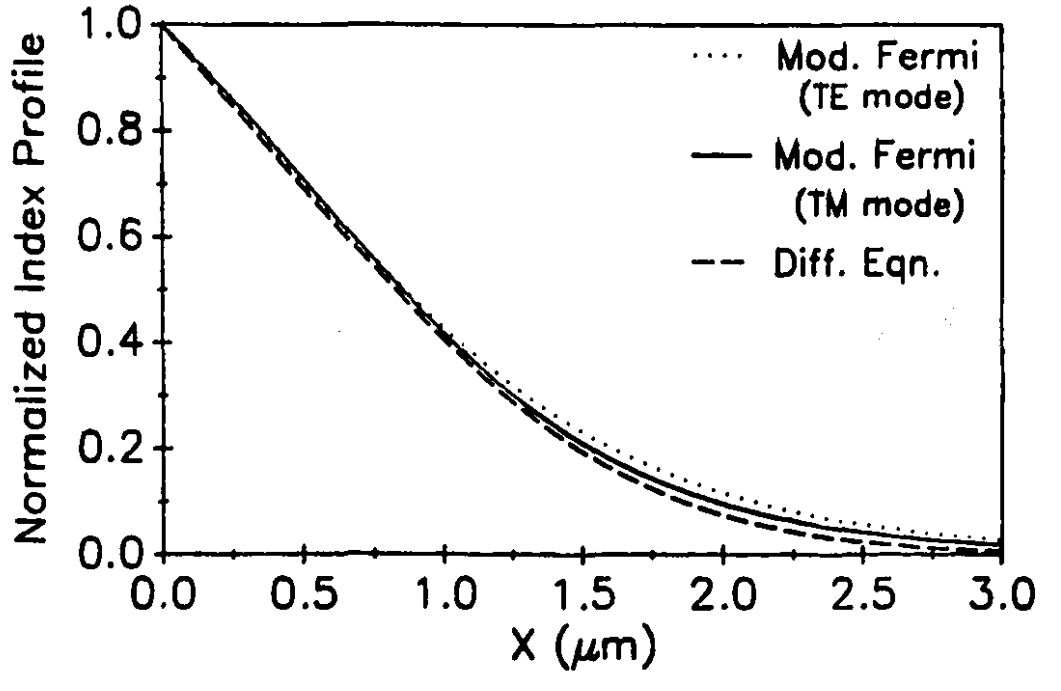

Figure 5.12: Comparison of the modified Fermi profile to the ion-exchange simulation for $E_a^T = 18.3\,V/mm$ and $t = 5\,s$

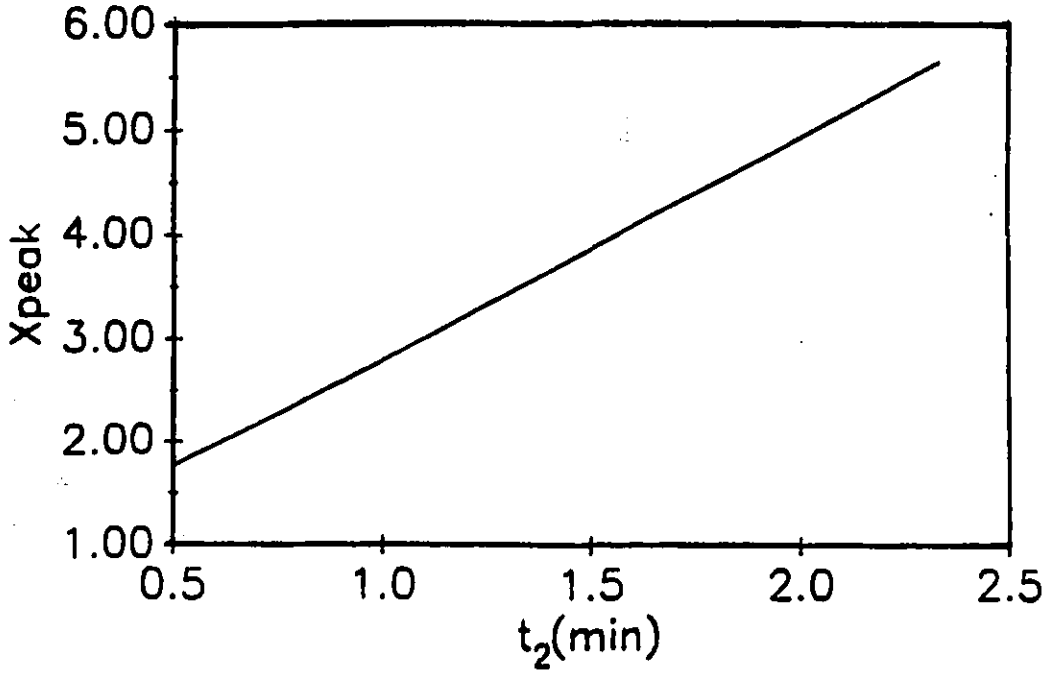

(a)

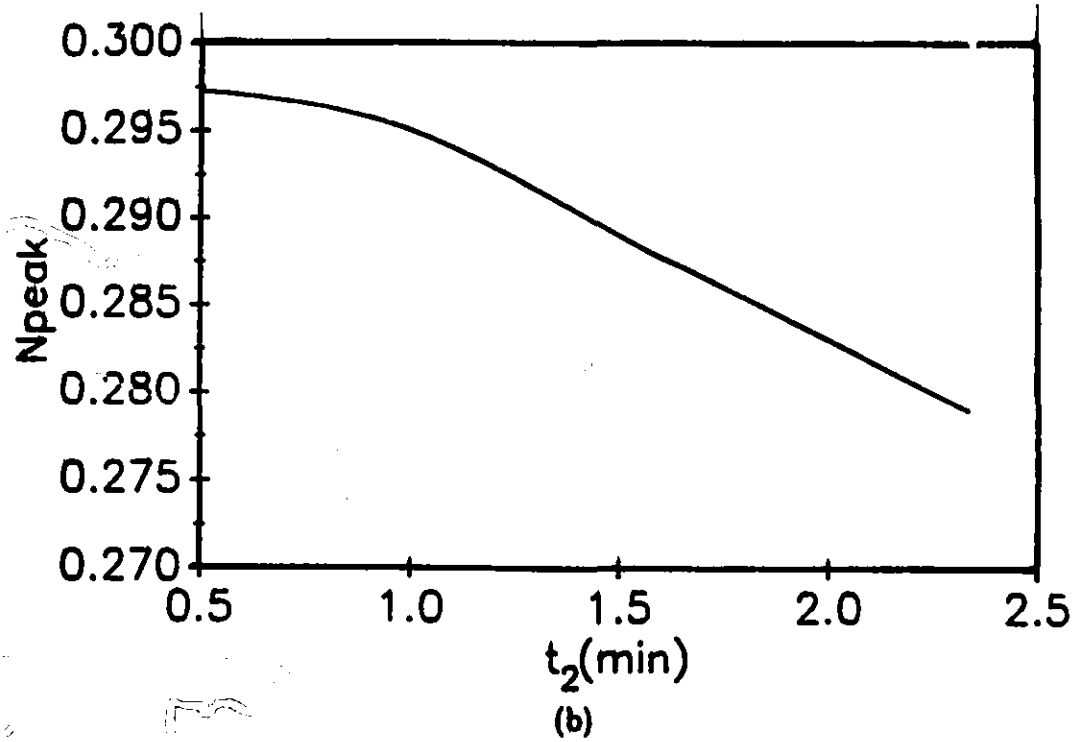

(b)

Figure 5.13: Variation of (a) x_{peak} and (b) n_{peak} with t_2

5.3.4 Discussions

Before leaving this section, some further discussion of the results is called for. From our measurements and numerical modeling, we observed two important effects of the field-assisted backdiffusion process at $E_a = 100\,V/mm$, as shown in Table 5.8:

1. An initial increase and very gradual decrease of N_{eff} with t_2
2. A decrease of the waveguide birefringence $(N_{eff}^{TM} - N_{eff}^{TE})$ with t_2

The first effect can be understood by realizing that the burying process acts to symmetrize the index profile which tends to increase the effective index. Fig. 2.8 of [25] shows clearly that as the asymmetry parameter a tends to zero (i.e. symmetry), the normalized guide index b (related to N_{eff}) increases. Even though this is shown for a step-index guide, the same trend is true for GRIN profiles [26]. This effect is different from that reported for purely thermal buried guides in which the n_{peak} decreased more dramatically with t_2 dominating the declining effect of N_{eff}. The second effect may again be attributed to this symmetry. The asymmetry parameter for the TM modes begins to approach that for the TE modes [25]. Table 5.8 shows that the measured birefringence begins at a value of 7×10^{-4} for the surface guides ($t_2 = 0$) and ends up at 1.5×10^{-4} at $t_2 = 140\,s$. This finding may be very useful to fabricate single-mode polarization insensitive waveguides which have attracted interest for improving the characteristics of $1 \times N$ branching devices in glass [27].

As for the numerical ion-exchange modeling in particular, we used $\hat{a} = a \times h_K$ throughout the simulation, assuming h_K to be the same for all t. This was done for convenience, but it may not be a true reflection of the actual process. In fact, for the surface guides, we saw how h_K increased from zero to the saturation value (Table 5.9) during the diffusion time. This approximation in the numerical model remains as a source of error.

Finally, we must address the reason as to why we used $D_K = 0.06492\,\mu m^2/min = D_e$ [11] in the field-assisted ion-exchange simulations. For the purely thermal simu-

lations, the self-diffusion coefficient $D_K = 0.01174\,\mu m^2/min$ has been used in (2.17) [22, 28] to model surface and buried waveguides. However, for field-assisted ion exchange, this D_K was not used. In the literature, other researchers have also used the effective diffusion coefficient [13, 29] since it is well known that D_K is different for electromigration [30]. We have compared the modelled profiles using $D_K = D_e$ in comparison with those using $D_K = D_e/4(1.17)^2$ and found that there is a comparable difference. Fig. 5.14 shows this discrepancy for the data shown in Fig. 5.12.

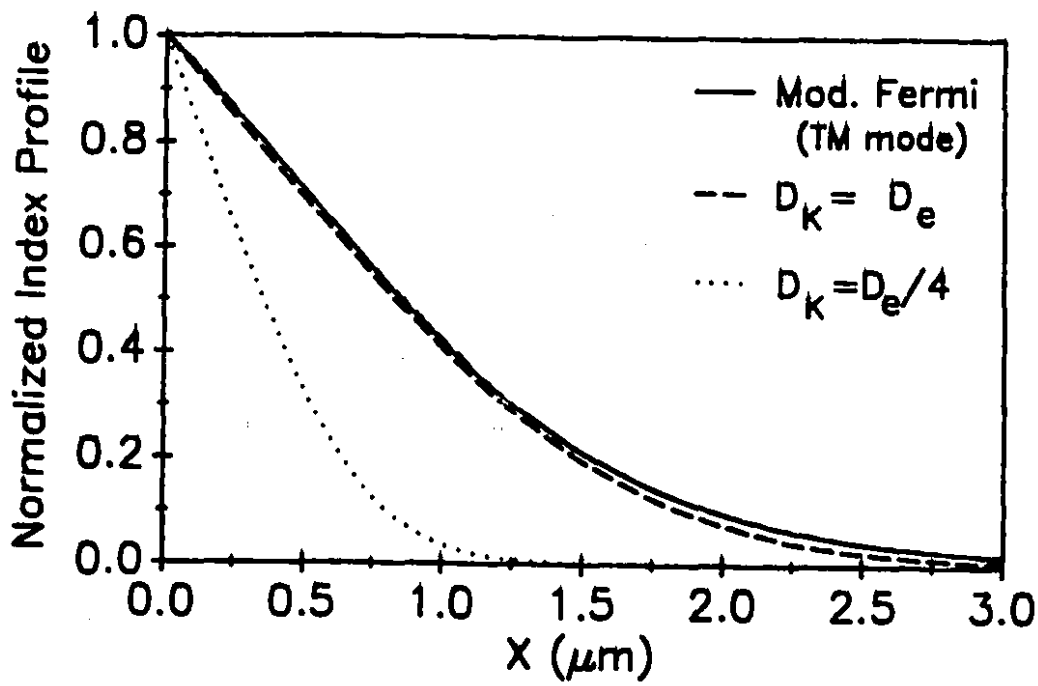

Figure 5.14: Comparison of ion-exchange profiles using different D_K values

5.4 Buried channel guides

5.4.1 Introduction

As mentioned earlier, the buried channel waveguides are key components in the vertical directional couplers. In this section, the ion-exchange model described in Chapter 2 was used to determine x_{peak} and n_{peak}. Also, the theoretical mode mismatch loss to an optical fiber was calculated so as to assess the compatability of the buried channel guide with a fiber. Finally, the measured near-field mode profile is compared to that calculated by the 3-D BPM scheme.

5.4.2 Modelled diffusion characteristics

The diffusion profiles were calculated for various fabrication conditions W, t_1, t_2, and E_a as described in 2.3.3. The chosen conditions were $W = 4.0, 4.4, 4.8, 5.2\,\mu m$, $t_1 = 15, 20, 25\,min$, $t_2 = 1.0, 1.5, 2.0\,min$ with $E_a = 100\,V/mm$. Fig. 5.15(a) and (b) show the variation of x_{peak} and n_{peak} with t_2, respectively, for various t_1 and $W = 4.4\,\mu m$. Similar behaviour occurs at other channel widths.

5.4.3 Calculated mode mismatch loss

The insertion loss is made up of two components, namely the Fresnel loss and the mode mismatch loss. The Fresnel loss arises from reflections of the field from the fiber to the buried guide. Since the refractive index of the fiber and buried guide are very similar, this loss is very small. In fact, it can be made negligible if the fiber-guide spacing is adjusted for maximum transmission [31] or if antireflection coatings are used. The mode mismatch loss arises due to the different field distributions of the single-mode fiber and the buried channel guide. This power loss is calculated by evaluating the normalized overlap integral [32]:

$$\eta_{fg} = \frac{\left(\int_{-\infty}^{\infty}\int_{-\infty}^{\infty} E_f(x,y)E_g(x,y)dxdy\right)^2}{\left(\int_{-\infty}^{\infty}\int_{-\infty}^{\infty} E_f^2 dxdy\right)\left(\int_{-\infty}^{\infty}\int_{-\infty}^{\infty} E_g^2 dxdy\right)} \tag{5.7}$$

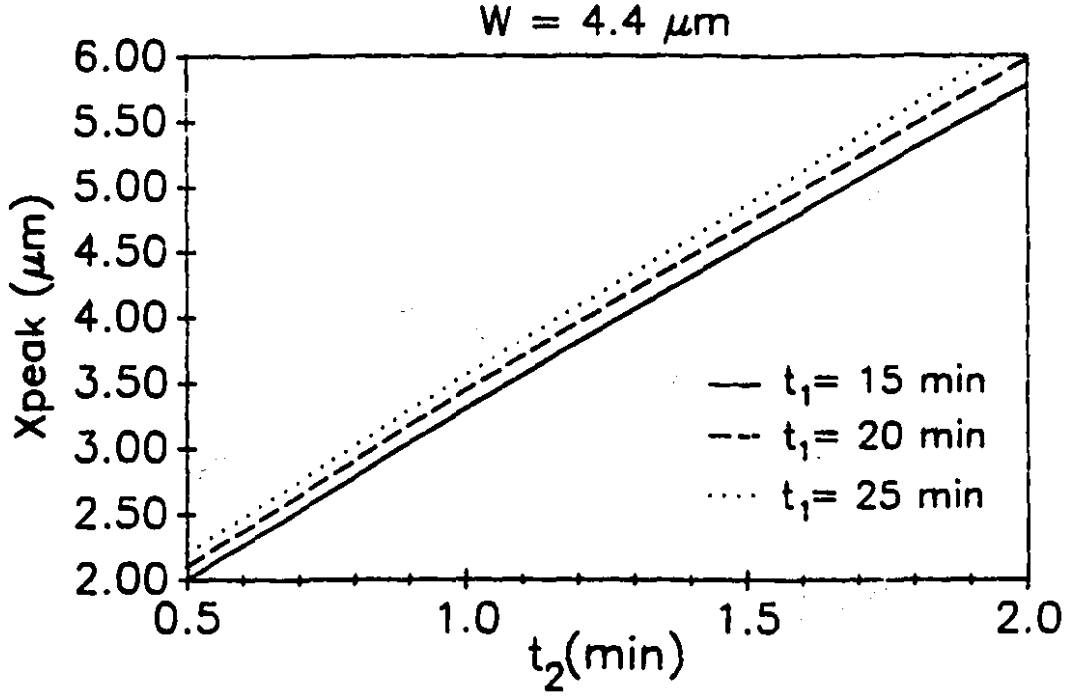

(a)

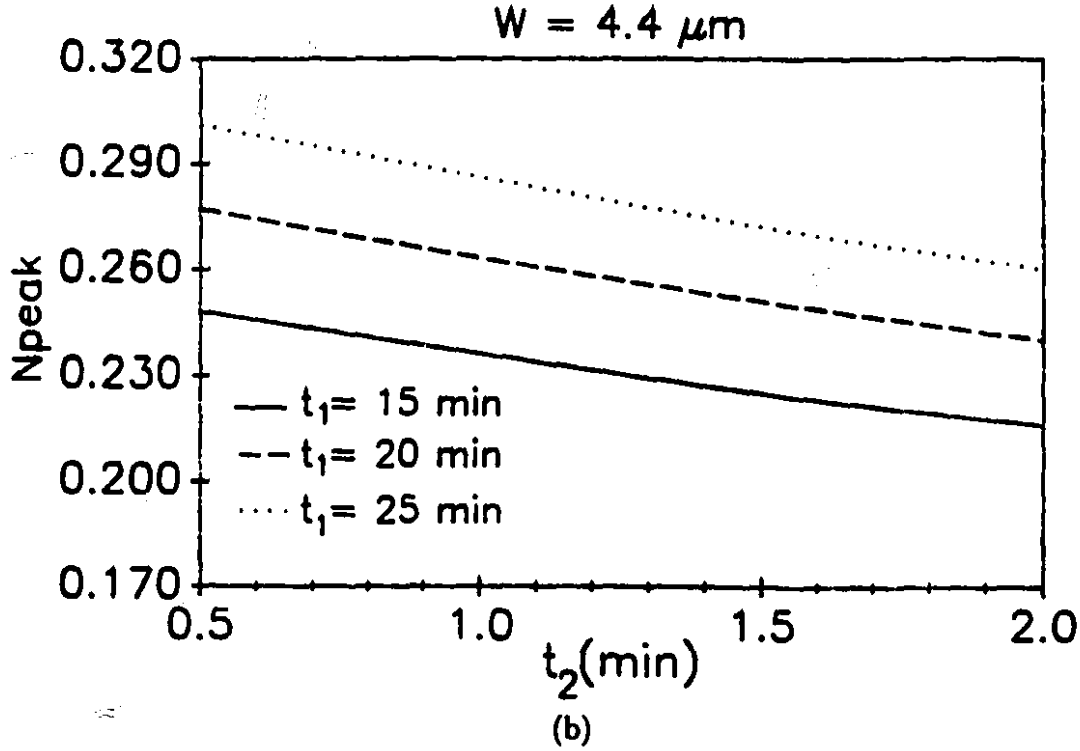

(b)

Figure 5.15: Buried channel guide variation of (a) x_{peak} and (b) n_{peak} with t_2

where E_f and E_g are the amplitudes of the single-mode field profiles of the fiber and buried guide, respectively. This loss can be expressed by $-10log_{10}\eta_{fg}$ in the decibel dB scale.

Here, η_{fg} is evaluated based on the calculation of $E_g(x,y) = F(x,y)G(x)$ from the EIM, as described in Chapter 4, and the Gaussian mode approximation for the symmetric fiber field profile. For the fiber mode, a step-index fiber with a core diameter of $4\,\mu m$ and a relative index change of $0.3\,\%$ is chosen with its mode size $w_f = 2.3\,\mu m$ [33, 34]:

$$E_f(x,y) = \exp\left(-\frac{x^2+y^2}{w_f^2}\right) \tag{5.8}$$

In the calculations, the spatial coordinates of the peaks in both E_f and E_g were made to coincide. Fig. 5.16(a) shows the variation of this loss with t_2 for various t_1 and $W = 4.4\,\mu m$. Similar behaviour occurs at other values of W. The lowest value ($0.47\,dB$) occurs for the narrowest width and deepest guide ($W = 4\,\mu m$, $t_1 = 25\,min$, $t_2 = 2.0\,min$) where the lateral diffusion is lowest and the buried guide profile is most symmetric (see Fig. 5.16(b)).

A related issue involves the improvement in the fiber-guide insertion loss of a buried channel guide over a surface channel guide. As mentioned earlier, the advantages of the buried guide consist of lower propagation and mode-matching loss yielding lower insertion loss. The improvement in insertion loss was studied theoretically for two different channel widths, as shown in Table 5.11. The surface channel guide was simulated with $t_1 = 20\,min$ and the buried guide with $t_2 = 2.0\,min$ using the surface guide as the initial condition. The improvement is about $1.7\,dB$. Experimentally, such measurements were not carried out in this work, however, others have published results for buried channel guides using fabrication conditions quite different from ours [6]. An improvement of $0.43\,dB$ was measured at $\lambda_o = 1.3\,\mu m$ and further improvement of at least $0.61\,dB$ can be achieved by a careful choice of the process parameters.

Table 5.11: Calculated insertion loss improvement

	$W = 4.0\mu m$	$W = 4.4\mu m$
Surface	$2.24dB$	$2.20dB$
Buried	$0.51dB$	$0.52dB$
Improvement	$1.73dB$	$1.67dB$

5.4.4 Modal field profiles

As described in Chapter 3, the near-field intensity distribution of a buried channel guide was studied for the purpose of examining its circularity and verifying the numerical models used in our design. The measured mode profile of a buried channel guide fabricated with the conditions $W = 5.4 \pm 0.2\mu m$, $t_1 = 25\,min$, $E_{a2}^T = 98.5\,V/mm$, and $t_2 = 1.0\,min$ is shown in Fig. 5.17(a). The vertical (x) and horizontal (y) intensity scans are shown in Fig. 5.17(b) and (c), respectively, together with those calculated by the 3-D ADI-BPM and including 2-D convolution for the microscope objective. Good agreement is obtained when the measured and calculated intensity peak locations are made to coincide. It was found that the calculated peak occurred at $x = 3.68\,\mu m$ whereas the measured peak was found at $x = 3.0\mu m$. This discrepancy may be attributable in part to the difficulty of determining experimentally the exact position of the waveguide edge because of the diffraction effect.

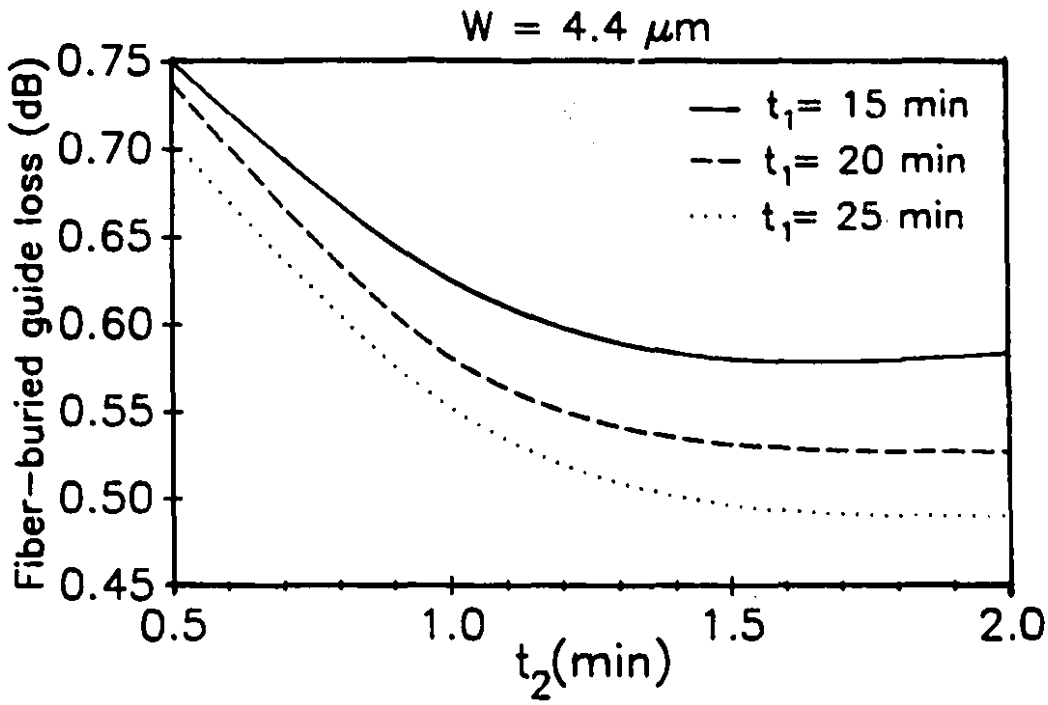

(a)

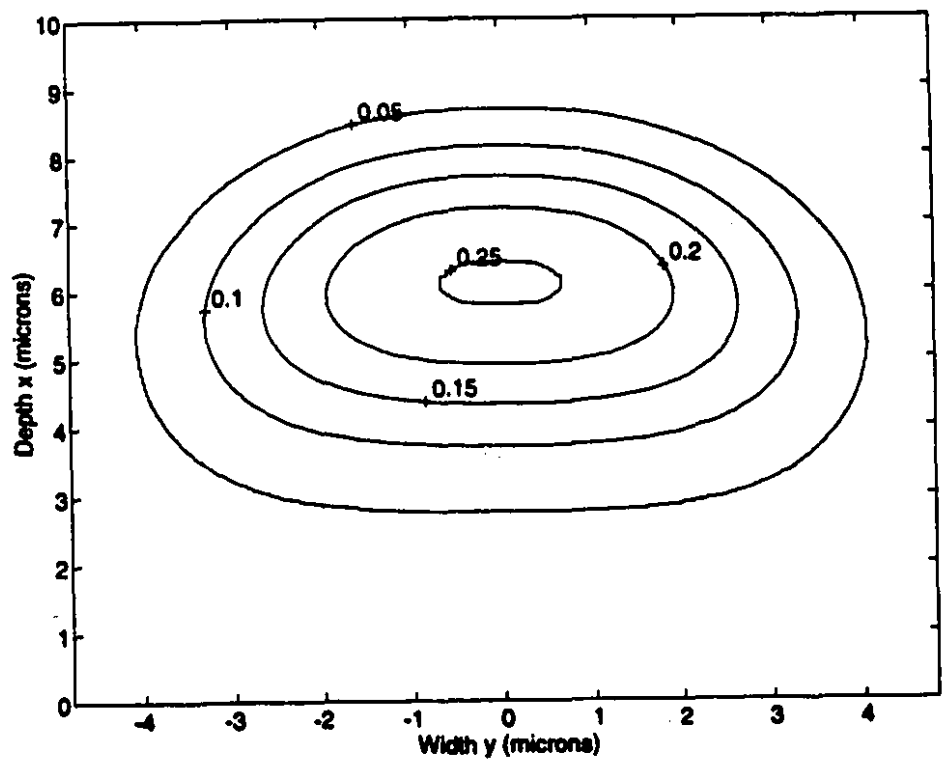

(b)

Figure 5.16: (a) Calculated mode mismatch loss vs. t_2 and (b) most symmetric buried guide concentration profile

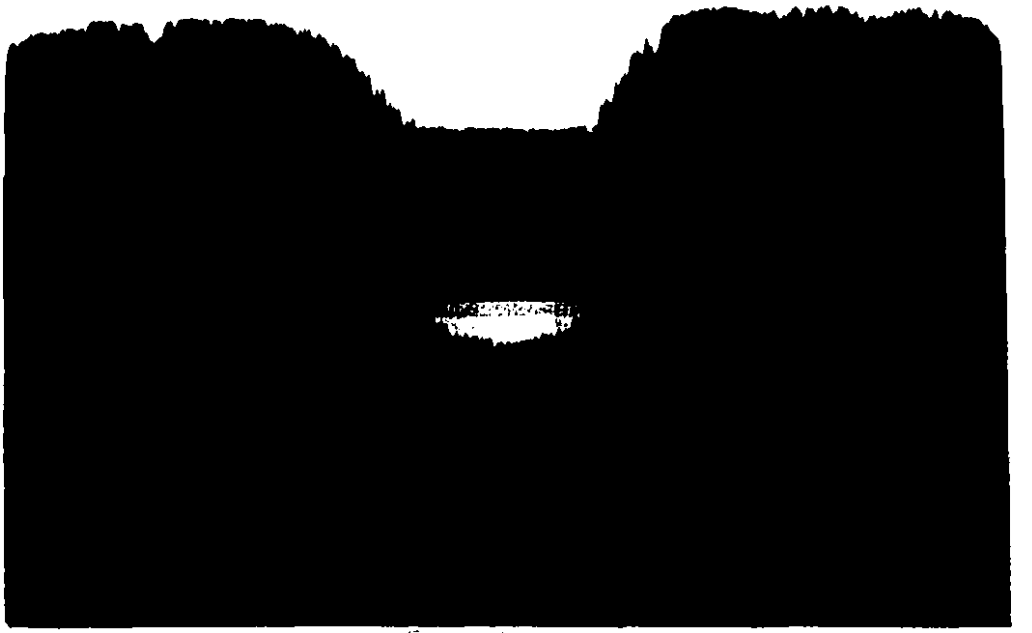

(a)

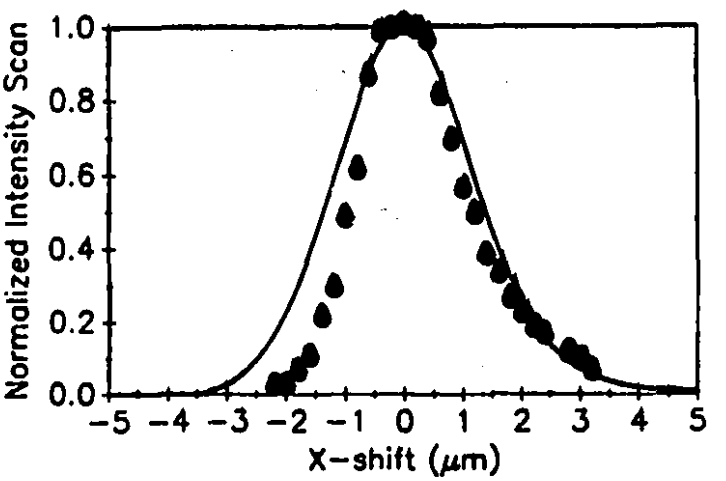

(b)

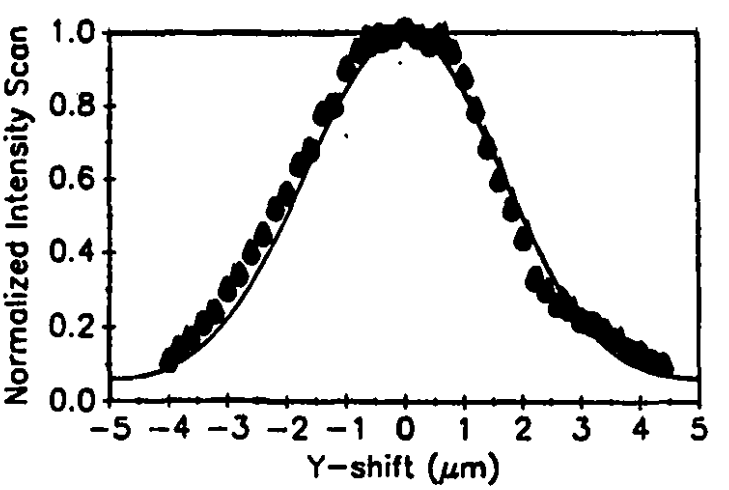

(c)

Figure 5.17: (a) Measured near-field intensity profile and comparison between measured (dots) and modeled (solid line) (b) vertical and (c) horizontal scans

5.5 Al_2O_3 planar guide characteristics

5.5.1 Introduction

The characterization of the Al_2O_3 sputtered thin film is important in the design of the improved vertical directional coupler. The waveguide properties such as the film index n_f and the sputtering rate r need to be determined. The experimental techniques and conditions for fabrication and measurement were presented in Chapter 3. Initially, high target voltage levels ($> 1kV$) were tried but this did not produce any waveguiding effect: prism coupling measurements showed no m-line output. It is believed that the high power caused the escaping Al_2O_3 atoms from the target to bombard the glass substrate with high energy causing microdefects and very lossy waveguides. In our study, two different target voltages, $0.5kV$ and $0.75kV$ were tried yielding better quality, low loss waveguides.

5.5.2 Dispersion curves

It is standard practice to characterize optical waveguides using multi-mode effective index measurements (see Chapter 3). For these thin film sputtered guides however, these multi-mode measurements can be replaced by single-mode measurements by taking advantage of two important characteristics of plasma sputtering of which we have *a priori* knowledge. The first one is that the sputtered index profile is a step and the second is that the film thickness varies linearly with time. These two known observations [36] were utilized in conjunction with the step-index dispersion relation (4.29) with $m = 0$. To determine the unknowns n_f and r, we begin with one pair of single-mode effective index measurements, say (N_{eff1}, N_{eff2}), for the two corresponding sputtering times, say (t_{s1}, t_{s2}). The two equations are set up, as in (4.29), with $d = rt_{s1}$, N_{eff1} for one and $d = rt_{s2}$, N_{eff2} for the other. Then, dividing one by the other leads to a nonlinear transcendental equation which is root-searched for n_f. This value is then substituted back into (4.29) to find d, which when divided by the

Table 5.12: Measured n_f and r for 0.5 and 0.75kV

Target voltage (kV)	$n_f(TM)$	$r(\mu m/h)$
0.50	1.576 ± 0.007	0.080 ± 0.015
0.75	1.617 ± 0.008	0.186 ± 0.013

appropriate t_{s1} or t_{s2} yields the sputtering rate, r. This shortened approach provides for an accurate characterization of the sputtered thin films based on single-mode measurements alone.

Single-mode measurements were made at 0.5kV for $t_s = 4.5, 5.5, 6.5h$ and at 0.75kV for $t_s = 1.5 - 3.5h$, in $0.5h$ intervals. The thin films produced by the latter conditions were performed on the new substrates with $n_b = 1.5208$. The TM mode dispersion curve for 0.75kV is shown in Fig. 5.18 in good agreement to experiment. Also, the thickness versus sputtering time graph (Fig. 5.19) shows a linear variation. The results for the TM mode are shown in Table 5.12. Note that the accuracy of n_f is only in the third decimal place.

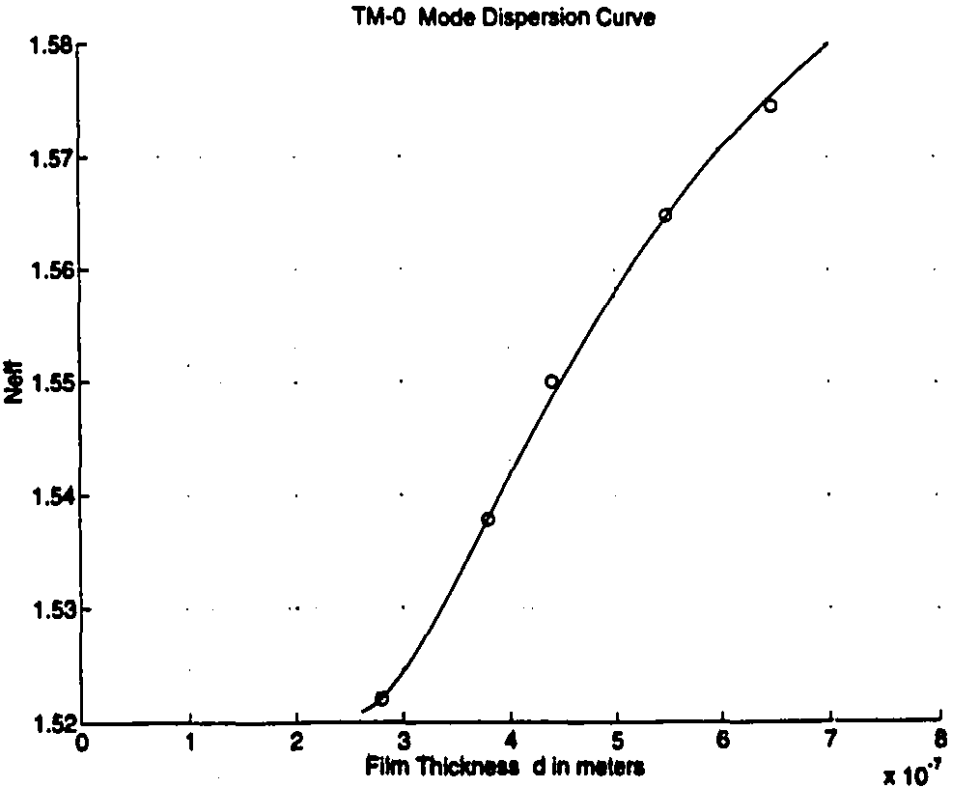

Figure 5.18: Single-mode theoretical dispersion curve (step profile) compared with measured mode indices for sputtered samples prepared at $0.75kV$ (TM mode)

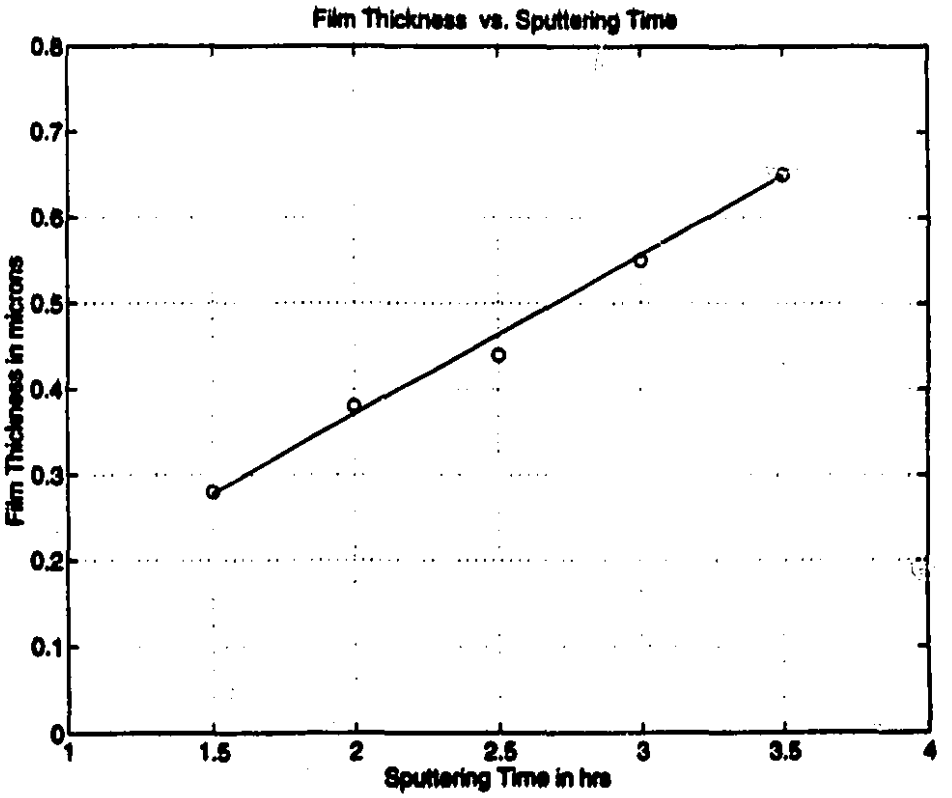

Figure 5.19: Thin-film guide thickness vs. sputtering time (TM mode)

5.5.3 Propagation loss

The propagation loss of the Al_2O_3 single-mode guide was measured using the two-prism sliding method described in Chapter 3. One sample fabricated at $0.75kV$, $t_s = 1.5h$ was measured for the TM mode yielding a propagation loss of $0.27 \pm 0.04 dB/cm$. This loss is comparable to that of the surface and buried single-mode waveguides.

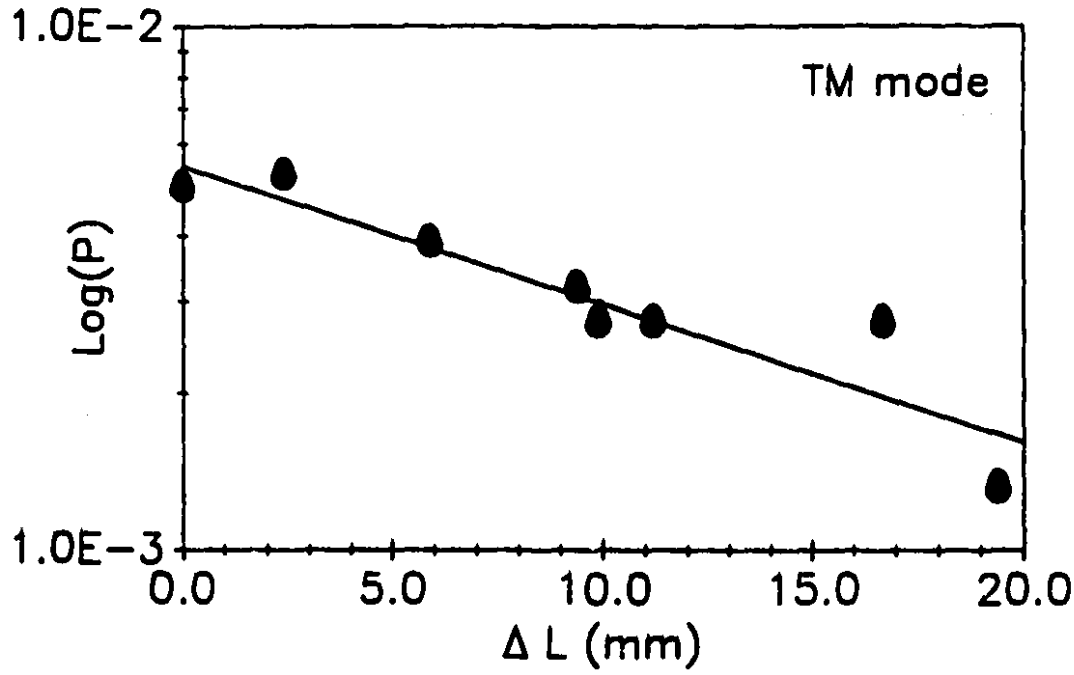

Figure 5.20: $LogP$ vs. ΔL variation yielding propagation loss for a single-mode sputtered Al_2O_3 guide

Bibliography

[1] G.H. Chartier, P. Jaussaud, A.D. De Oliveira, and O. Parriaux, 'Optical waveguides fabricated by electric field controlled ion-exchange in glass', Electron. Lett., 14 (5), pp. 132-134, 1978

[2] T. Izawa and H. Nakagome, 'Optical waveguide formed by electrically induced migration of ions in glass plates', Appl. Phys. Lett., 21 (12), pp. 584-586, 1972

[3] M. Abou-el-Liel and F. Leonberger, 'Model for ion-exchanged waveguides in glass', J. Amer. Cer. Soc. 71 (6), pp. 497-502, 1988

[4] B.G. Pantchev, 'One-step field-assisted ion exchange for fabrication of buried multimode optical strip waveguides', Electron. Lett., 23 (22), pp. 1188-1190, 1987

[5] S. Urnes, 'Na-K Exchange in Silicate Glasses', J. Amer. Cer. Soc., 56 (10), pp. 514-519, 1973

[6] A. Miliou, H. Zhenguang, H.C. Cheng, R. Srivastava, and R.V. Ramaswamy, 'Fiber-Compatible $K^+ - Na^+$ Ion-Exchanged Channel Waveguides: Fabrication and Characterization', J. Quantum Electron., 25 (8), pp. 1889-1897, 1989

[7] R. Klein, D. Jestel, H.J. Lilienhof and E. Voges, 'Reproducible fabrication of integrated optical components by charge controlled ion exchange in glass', in SPIE Proc. Integrated Optical Circuit Engineering VI, 993, pp. 7-12, 1988

[8] N.A. Sanford. K.J. Malone. and D.R. Larson. 'Integrated optic laser fabricated by field-assisted ion-exchange in neodymium-doped soda-lime silicate glass'. Opt. Lett.. 15 (7). pp. 366-368. 1990

[9] G.L. Yip. P.C. Noutsios. and K. Kishioka. 'Characteristics of optical waveguides made by electric-field-assisted K^+-ion exchange'. Opt. Lett.. 15 (14). pp. 789-791. 1990

[10] G. Stewart. C.A. Miller. P.J.R. Laybourn. C.D W. Wilkinson. and R.M. De LaRue. 'Planar optical waveguides formed by silver-ion migration in glass'. J. Quantum Electron.. 13 (4). pp. 192-200. 1977

[11] G.L. Yip and J.Albert, 'Characterization of planar optical waveguides by K^+-ion exchange in glass', Opt. Lett. 10 (3), pp. 151-153, 1985

[12] R.V. Ramaswamy and S.I. Najafi. 'Planar, buried. ion-exchanged glass waveguides: Diffusion characteristics', J. Quantum Electron.. 22 (6), pp. 883-891. 1986

[13] H.J. Lilienhof. E. Voges. D. Ritter. and B. Pantschew. 'Field-induced index profiles multimode ion-exchanged strip waveguides'. J. Quantum Electron., 18 (11), pp. 1877-1883, 1982

[14] S.N. Houde-Walter and D.T. Moore, 'Gradient-index profile control by field-assisted ion exchange in glass', Appl. Opt.. 24 (24), pp. 4326-4333, 1985

[15] J.M. White and P.F. Heidrich. 'Optical waveguide refractive index profiles determined from measurement of mode indices: a simple analysis', Appl. Opt.. 15. pp. 151-155. 1976

[16] T.R. Chen and Z.L. Yang, 'Modes of a planar waveguide with Fermi index profile', Appl. Opt., 24 (17). pp. 2809-2812, 1985

[17] J.Albert and G.L. Yip, 'Stress-induced index change for $K^+ - Na^+$ ion exchange in glass', Electron. Lett.. 23 (14), pp. 737-738, 1987

[18] H. Ohta and M. Hara, 'Ion Exchange in Sheet Glass by Electrolysis', Yogyo Kyokai, 78 (5), pp. 158-164, 1970

[19] T. Chiba, S. Misawa, K. Iga, and M. Oikawa, 'Distributed index formation of planar microlens (II)', Opt. Quantum Electron., 84-88, pp. 39-45, 1984 (in Japanese)

[20] B. Pantchev and Z. Nikolov, 'Method of refractive index profile reconstruction from effective index of planar optical monomode waveguides: application to potassium ion-exchanged waveguides', J. Quantum Electron., 29 (1), pp. 154-160, 1993

[21] A. Brandenburg, 'Stress in ion-exchanged glass waveguides', J. Lightwave Technol., 4 (2), pp. 1580-1593, 1986

[22] P.C. Noutsios and G.L. Yip, 'Shallow buried waveguides made by purely thermal migration of K^+ ions in glass', Opt. Lett., 15 (4), pp. 212-214, 1990

[23] A. Beguin, T. Dumas, M.J. Hackert, R. Jansen, and C. Nissim, 'Fabrication and performance of low loss optical components made by ion exchange in glass', J. Lightwave Technol., 6 (10), pp. 1483-1487, 1988

[24] R.H. Doremus, 'Ion exchange in glasses', in *Ion-Exchange*, vol. 2, J.A. Marinsky, Ed., Dekker, New York 1969

[25] H. Kogelnik, 'Theory of optical waveguides', in *Guided-Wave Optoelectronics*, T. Tamir, Ed., Springer-Verlag, Berlin, 1990

[26] A. Tervonen, 'Theoretical Analysis of Ion-Exchanged Glass Waveguides', in *Introduction to Glass Integrated Optics*, S.I. Najafi, Ed., Artech House, Boston, 1992

[27] H. Hashizume, M. Seki, and K. Nakama, 'Polarization-insensitive planar waveguides 1×4 branching device with good wavelength flattened characteristics', Proceedings of OFC'89, WM1, pp. 90, Houston, 1989

[28] J. Albert and G.L. Yip, 'Refractive index profiles of planar waveguides made by ion-exchange in glass', Appl. Opt., 24 (22), pp. 3692-3693, 1985

[29] S. Honkanen, A. Tervonen, H. von Bagh, and M. Leppihalme, 'Ion exchange process for fabrication of waveguide couplers for fiber optic sensor applications', J. Appl. Phys., 61 (1), pp. 52-56, 1987

[30] R. Terai and R. Hayami, 'Ionic diffusion in glasses', J. Noncryst. Solids, 18, pp. 217-230, 1975

[31] R.V. Ramaswamy and R. Srivastava, 'Ion-exchanged glass waveguides: A review', J. Lightwave Technol., 6 (6), pp. 984-1002, 1988

[32] W.K. Burns and G.B. Hocker, 'Endfire coupling between optical fibers and diffused channel waveguides', Appl. Opt., 16 (8), pp. 2048-2050, 1977

[33] D. Marcuse, *Light Transmission Optics*, Van Nostrand Reinhold, New York, 1982

[34] J. Albert and G.L. Yip, 'Insertion loss reduction between single-mode fibers and diffused channel waveguides', Appl. Opt., 27 (23), pp. 4837-4843, 1988

[35] M. Ramos, I. Verrier, M. Reglat, P. Sass, and J.P. Goure, 'Study of a butt-joint coupling between a single-mode optical fiber and a channel waveguide on glass at $1.3\,\mu m$', J. Opt. Comm., 15 (5), pp. 190-196, 1994

[36] C.W. Pitt, 'Sputtered-glass optical waveguides', Electron. Lett., 9 (17), pp. 401-403, 1973

Chapter 6

Planar Vertical Directional Coupler

6.1 Introduction

The field-assisted ion-exchange process described in Chapter 3 has been used in the fabrication of a novel vertical directional coupler [1] whose configuration is given in Fig. 6.1. As described in the first chapter, much attention has been attracted to hybrid active components made by combining ion-exchanged waveguides with overlayers of semiconductors.

In these waveguide-detector geometries, the single-mode glass waveguides are fabricated by ion exchange and must not be buried below the surface so as to increase the coupling efficiency of the light to the photodetector. However, these waveguides are not adequate when trying to couple light from an optical fiber with minimal insertion loss. Buried guides are desirable because, compared with surface guides, they exhibit less surface scattering and therefore lower propagation loss. In addition, their more symmetrical index profile provides better mode matching to an optical fiber. Consequently, a better solution is to couple the signal into a buried waveguide, which can transfer almost all the power throu[illegible]escent coupling from a passive vertical directional coupler (VDC) into a surface guide just beneath the detector.

The concept of vertical integration is well known in the area of semiconductor guided-wave optical devices. However, for passive components, most research efforts

have focused on lateral integration of adjacent channel guides. In particular for glass waveguides, only a handful of vertically integrated structures are available, as described in Chapter 1. The novelty of our structure is that it is composed of graded-index planar guides fabricated by field-assisted K^+-ion exchange [1].

The objective of this chapter is to present an in-depth study of the optimized VDC characteristics such as the refractive index profile, the coupling length and the power transfer ratio. Firstly, a diffusion model of the GRIN profile is developed based on the waveguide characterizations presented in Chapter 5. This profile is then used in the design of the coupler using the vector beam propagation method (see Chapter 4) within the framework of the normal mode analysis. The measured characteristics of the fabricated device are compared to those predicted by theory.

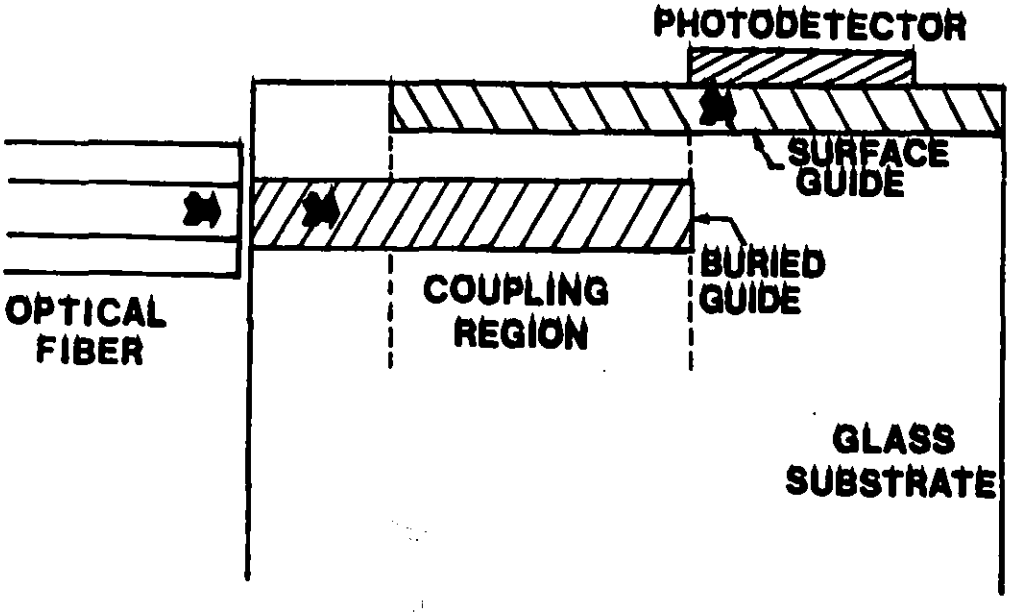

Figure 6.1: Vertical directional coupler used in waveguide-detector geometry

6.2 Determination of the index profile

From the optical characterizations, EMP studies and diffusion modelling presented in Chapter 5, we now have the confidence to decide upon the optimized fabrication conditions of the VDC. The main criteria that should be satisfied are:

1. both surface and buried guides must be single-moded
2. the buried guide should be as deep and as completely buried as possible to avoid significant overlapping of the surface guide

For the buried guide made by two-step backdiffusion, $V_a = 100\,V$ is chosen since it yields the most completely buried condition (lowest h_K). For the surface guide, the single-mode conditions $V_a = 20V$, $t = 5s$ provide for a shallow guide that does not overlap too much with the buried guide.

The modelling of the GRIN coupler is rather complex involving the sequential solution of (2.23) for the field-assisted and cooling processes with the appropriate initial and boundary conditions. Table 6.1 shows the fabrication parameters used in (2.23) for the six ion-exchange steps. Note that the values $\mu_K = 20.925\mu m^2/Vmin$, $D_K = 0.06429\mu m^2/min$, $\hat{\alpha} = 0.2994$ (with $h_K = 0.3$ from Table 5.9) and the measured substrate thickness $d_{sub} = 1.04\,mm$ are used throughout the simulations. Fig. 6.2 shows modelled profiles for two different times t_2. The EMP data for such a coupler with $t_2 = 60s$ is presented in Fig. 6.3 showing fairly good agreement. Note that there is significant overlap between the surface and buried index profiles which can be improved by driving the buried guide deeper into the substrate. Thus, couplers were designed and fabricated with longer t_2 ($60 < t_2 < 140s$) to provide for more isolation between the guides and as we shall see, higher power transfer. Once $c(x)$ is determined, the index profile is given by $n(x) = n_b + \Delta n_s c(x)$, where $n_b = 1.5125$, $\Delta n_s(TE) = 0.0111$ and $\Delta n_s(TM) = 0.0134$.

Table 6.1: VDC fabrication parameters

Process	t (s:min)	V_a (V)	V_o (V)	E_a^I (V/mm)	LBC
$K^+ - Na^+$	5 s	20.0	1.0	18.3	1.00
Cooling	10 min	0.0	0.0	0.0	1.00
$Na^+ - K^+$	60-140 s	100.0	1.5	94.7	0.03
Cooling	10 min	0.0	0.0	0.0	0.03
$K^+ - Na^+$	5 s	20.0	1.0	18.3	1.00
Cooling	10 min	0.0	0.0	0.0	1.00

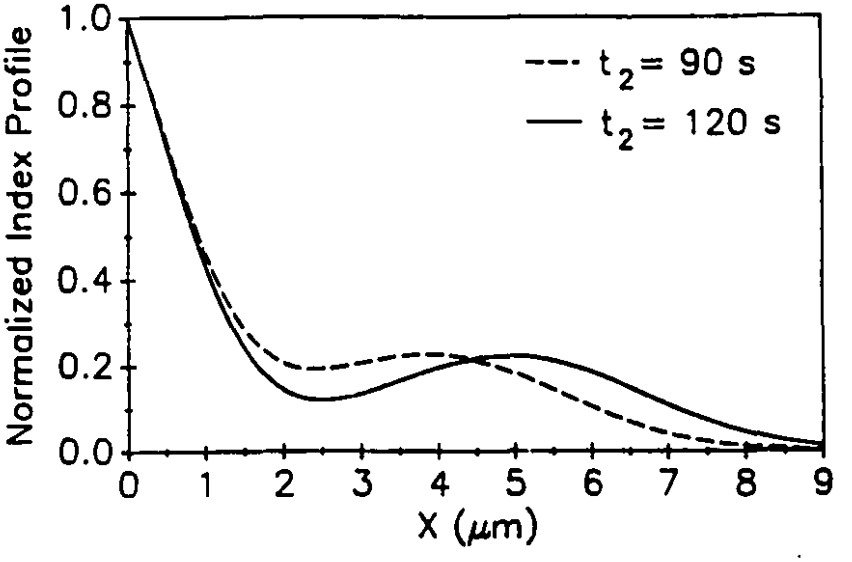

Figure 6.2: Numerical simulation of coupler GRIN profiles for $t_2 = 90s$ (solid line) and $t_2 = 120s$ (dashed line)

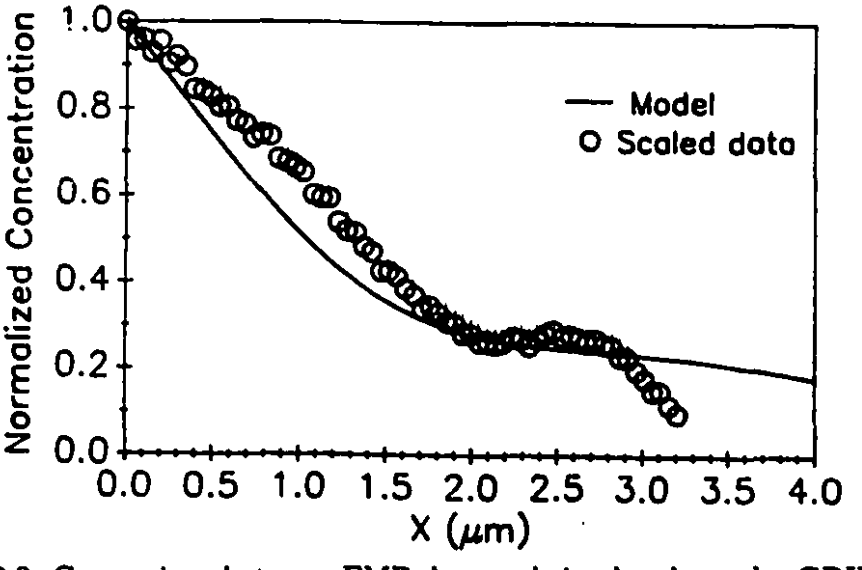

Figure 6.3: Comparison between EMP data and simulated coupler GRIN profile

6.3 Fabrication and measurement

The vertical directional coupler, comprising two parallel slab waveguides, is fabricated by a three-step field-assisted ion-exchange using pure KNO_3 and $NaNO_3$ melts in soda-lime glass. The fabrication conditions are chosen with the aid of (2.23) and the 2-D FD-VBPM design tool. The buried guide is made by a two-step exchange, using an applied voltage of 20 V and exchange time $t_1 = 5s$ in the first step, and 100 V in the second step with t_2 varying from 60 to 140 s. The single-mode surface guide is made by a one-step exchange with 20 V and $t_3 = 5s$ at a temperature of 385°C.

The TE and TM effective indices corresponding to the normal even (N_{even}) and odd (N_{odd}) mode m-lines (see Fig. 6.4(a)) were measured via prism-coupling techniques at $\lambda_o = 0.6328\,\mu m$. The coupling length L_c is given by [2]:

$$L_c = \frac{\pi}{\Delta\beta} = \frac{\lambda_o}{2\Delta N_e} \tag{6.1}$$

where $\Delta N_e = N_{even} - N_{odd}$, $\Delta\beta = k_o \Delta N_e$, and $k_o = 2\pi/\lambda_o$. To observe the two-mode interference, we used a lens to focus the light into the input prism to excite initially the fundamental mode of the surface guide. Subsequently, the even and odd normal modes of the coupler are excited simultaneously, yielding a streak of periodic dots on the glass surface as shown in Fig. 6.4(b). These dots represent the power transferred to the upper surface guide from the lower buried guide and their period is equal to twice the coupling length. This length was measured carefully for all the fabricated samples from the photograph of the coupling pattern using an accurate Vernier caliper. It was found to be in excellent agreement with the L_c deduced from the measured ΔN_e in accordance with (6.1).

In addition, the power transfer can be deduced by measuring the relative intensities (power ratios) of the normal mode m-lines [3] with an IR vidicon and an oscilloscope. These are measured at three different locations along the coupler by changing the position of the prism. The measured $R = A_o/A_e$, where A_o and A_e are the amplitudes of the odd and even modes, respectively, remains relatively constant.

The maximum power transfer η_{max} can be calculated from the following formula based on the normal mode analysis [4]:

$$\eta_{max} = \frac{1}{2} + \frac{R}{1 + R^2} \tag{6.2}$$

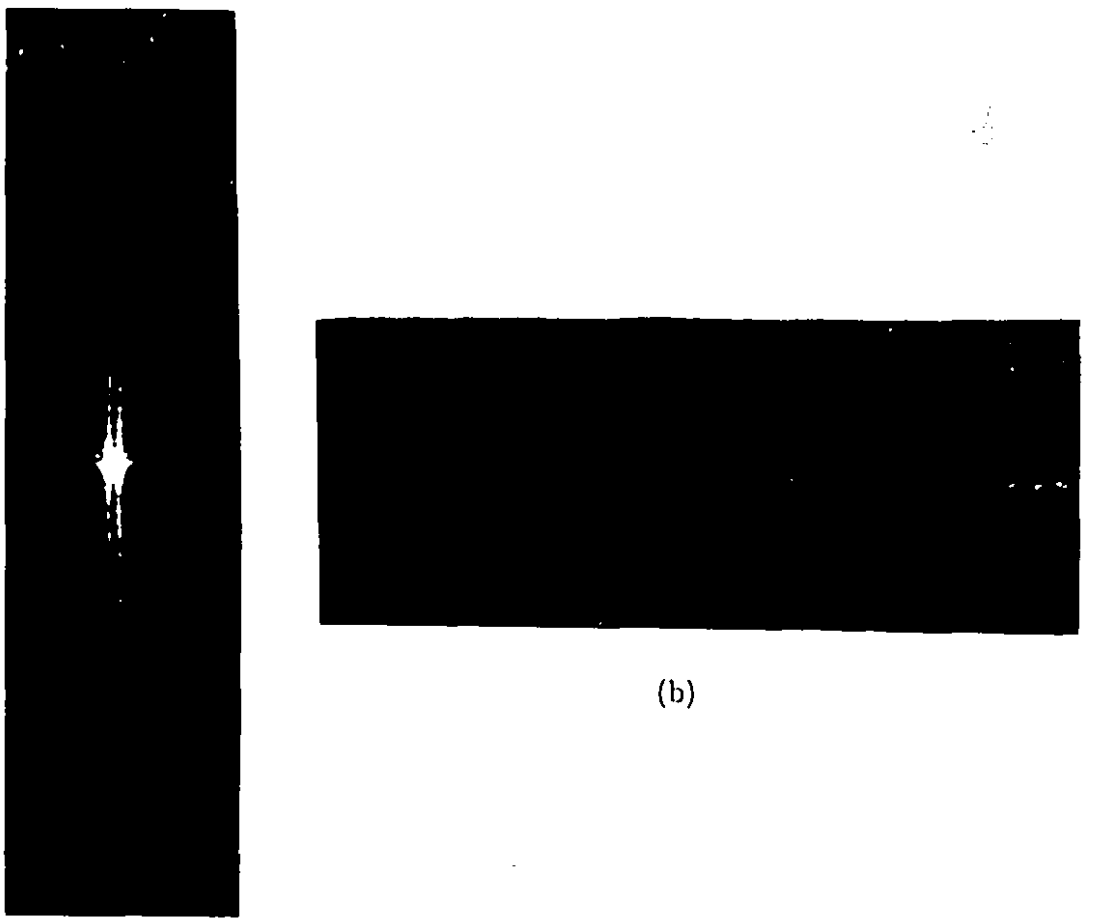

Figure 6.4: (a) Output m-lines of even and odd normal modes and (b) periodic variation of coupled power seen on glass surface

6.4 Coupler design and measured performance

The objective of the coupler design is to determine the optimum fabrication conditions that allows for high power transfer from the buried to the surface guide. The approach involves using the 2-D FD-VBPM and the modal power spectrum within the framework of the normal mode analysis. The index profile $n(x)$ is used in the BPM simulations to track the propagating wave. The chosen step size along z is $\Delta z = 0.02\,\mu m$ and along x is $\Delta x = 0.02\,\mu m$. The computational windows are $X_{max} = 20\,\mu m$, $Z_{max} = 3000\,\mu m$, the weight is $w = 0.53$ and the reference index is $n_r = n_b$ used for weakly guiding structures [5]. The incident field is that of a buried slab guide which is then coupled periodically between the slabs (see Fig. 6.5).

The coupling length L_c is determined by locating the z positions of the power transfer intervals of the BPM plots. Alternatively, N_{even} and N_{odd} are calculated using the modal power spectrum [6] and L_c is deduced via (6.1). In this case, a longer $Z_{max} = 10485.76\,\mu m$ is chosen to provide for a finer spectral resolution [6] of about 6×10^{-5} in the effective index. Both methods yield very similar results except that the computational times are very different. Due to the long Z_{max} needed, the spectrum method took eight hours to compute on a SunSparc whereas the BPM alone took about 1.5-3 h depending on L_c. Fig. 6.6 shows two distinct peaks identifying the effective indexes of the coupler's normal modes. The coupling lengths for the TE mode are shown in comparison to the measured ones in Fig. 6.7(a), showing very good agreement. Similar agreement is obtained for the TM mode when the improved FD-VBPM algorithm [7] is used. A comparison between both algorithms and the measured data is shown in Fig. 6.7(b). Tables 6.2 and 6.3 show the calculated and measured effective indices of the normal modes to be in good agreement. The behaviour of these indices as a function of t_2 (shown in Fig. 6.8) is very similar to that observed for conventional lateral couplers varying with interguide spacing [2] if it is remembered that t_2 is related to the depth of the buried guide.

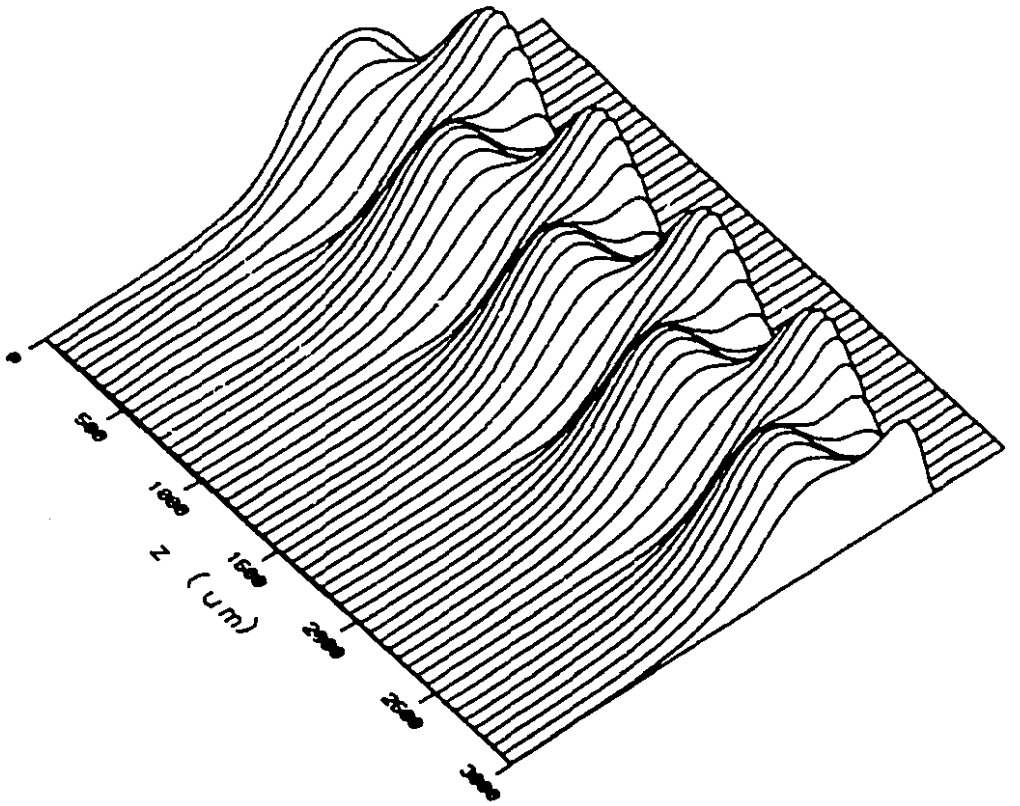

Figure 6.5: TE mode BPM simulation of power transfer for VDC calculated with $t_2 = 120s$

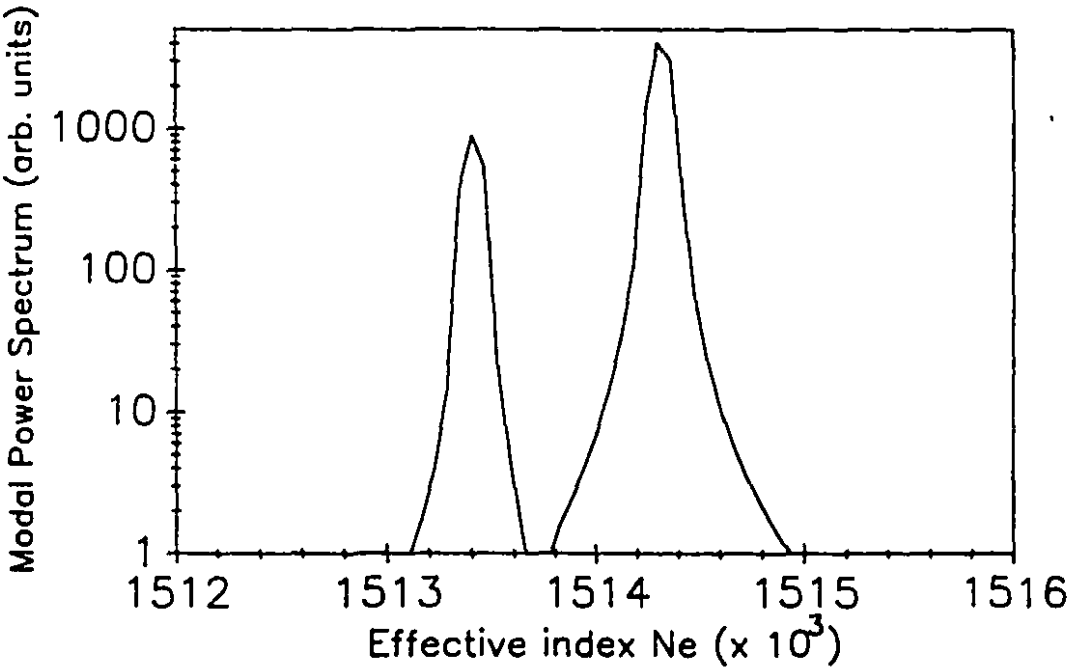

Figure 6.6: Peaks in the modal power spectrum identifying coupler's even and odd normal TE modes for $t_2 = 120s$

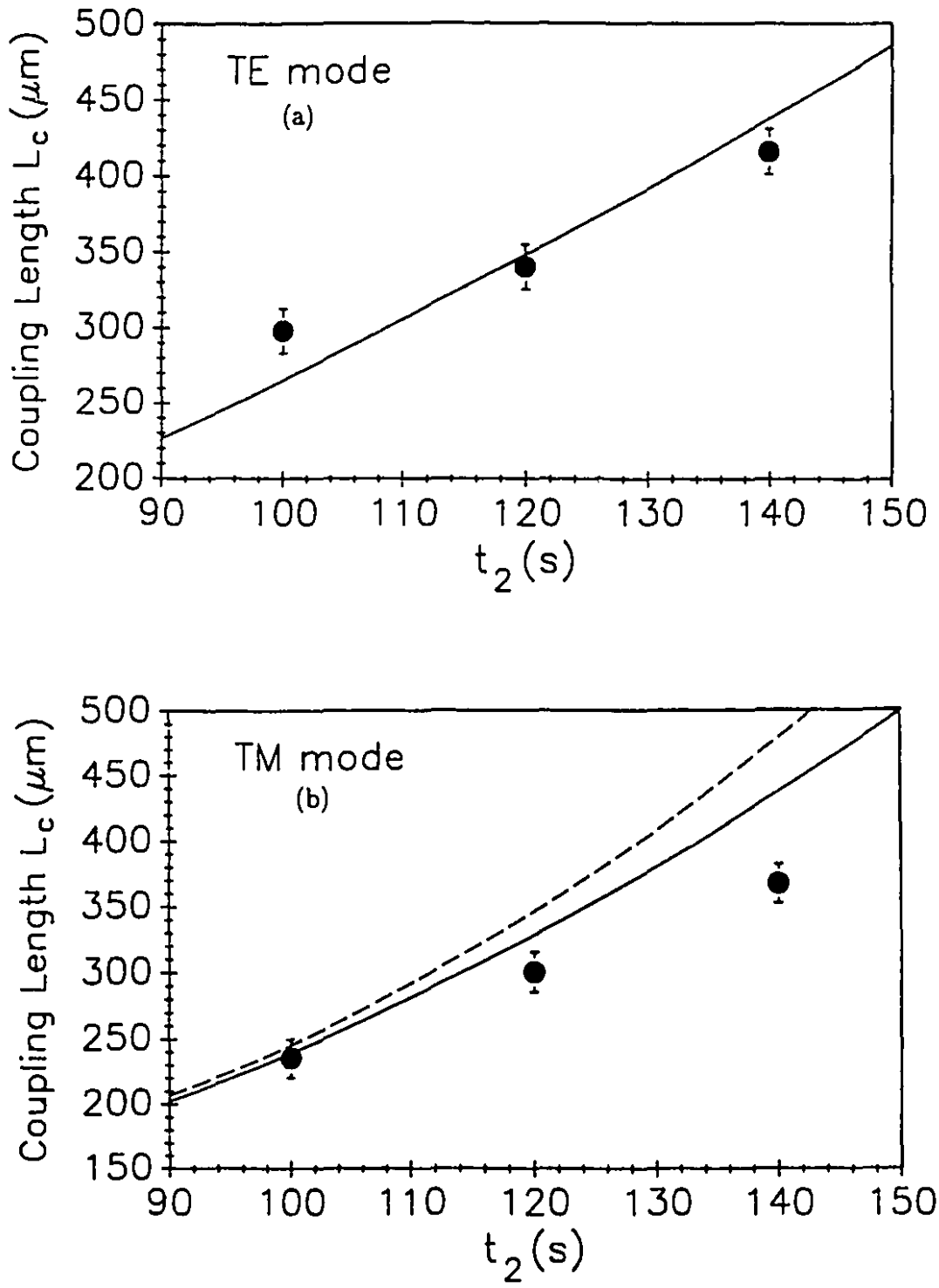

Figure 6.7: (a) Comparison between measured (dots) and calculated (solid line) TE mode coupling lengths (b) TM mode calculations based on existing (dashed) and improved (solid) FD-VBPM schemes

	Theory			Experiment		
t_2(s)	N_{odd}	N_{even}	$L_c(\mu m)$	N_{odd}	N_{even}	$L_c(\mu m)$
100	1.5132843	1.5144902	262	1.51389	1.51495	298 ± 10
120	1.5134049	1.5143094	350	1.51357	1.51450	340 ± 10
140	1.5134653	1.5141888	437	1.51392	1.51468	416 ± 12

Table 6.2: Calculated and measured TE effective indices of the VDC normal modes

$t_2(s)$	Theory			Experiment		
	N_{odd}	N_{even}	$L_c(\mu m)$	N_{odd}	N_{even}	$L_c(\mu m)$
100	1.5137065	1.5150325	239	1.51373	1.51507	236 ± 10
120	1.5138271	1.5147915	328	1.51387	1.51492	301 ± 10
140	1.5138874	1.5146107	437	1.51391	1.51477	368 ± 10

Table 6.3: Calculated and measured TM effective indices of the VDC normal modes

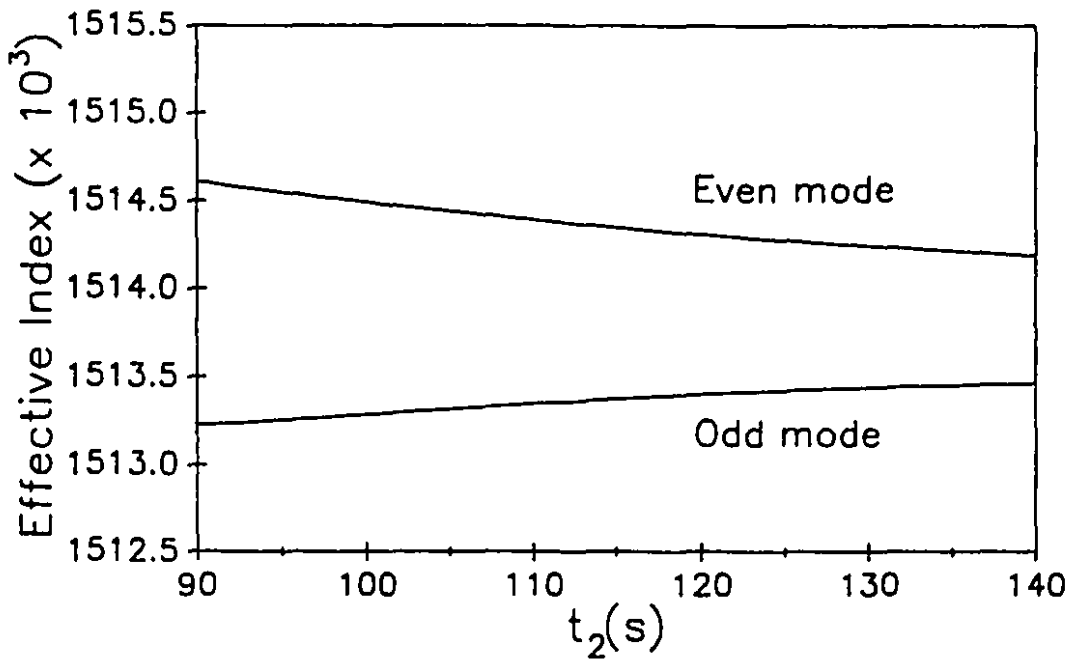

Figure 6.8: Variation of normal mode indices as a function of t_2 for TE mode

The calculation of the maximum power transfer requires the knowledge of the power that propagates in each slab. This normalized power can be expressed by the projection [8, 9] of the output field $E(x, z)$, calculated at the end of the interaction region $z = L_{int}$, onto the individual field (eigenfunction) of the surface guide $E_a(x)$, calculated using (4.60):

$$P_a = \frac{< E_a|E(L_{int}) >^2}{< E_a|E_a >< E(L_{int})|E(L_{int}) >} \tag{6.3}$$

with the inner product definition:

$$< f|g >= \int_{-\infty}^{\infty} f(x)g(x)dx$$

In our study of vertical couplers, light is ideally launched as a single mode of the buried guide 'b' that subsequently excites the normal modes, as shown in Fig. 6.9. The maximum power transfer into surface guide 'a' is defined as:

$$\eta_{max} = \frac{P_a}{P_T} \tag{6.4}$$

where P_T is the total power at $z = L_{int}$. Three different interaction lengths, $L_{int} = L_c$, $L_{int} = 2L_c$, and $L_{int} = 3L_c$ where P_a is a maximum, are chosen to calculate $E(L_{int})$ and determine the average η_{max}. The measured η_{max} values are in fair agreement to those calculated using (6.2), as shown in Fig. 6.10. The curve displays an optimum value of η_{max} for a given range of t_2.

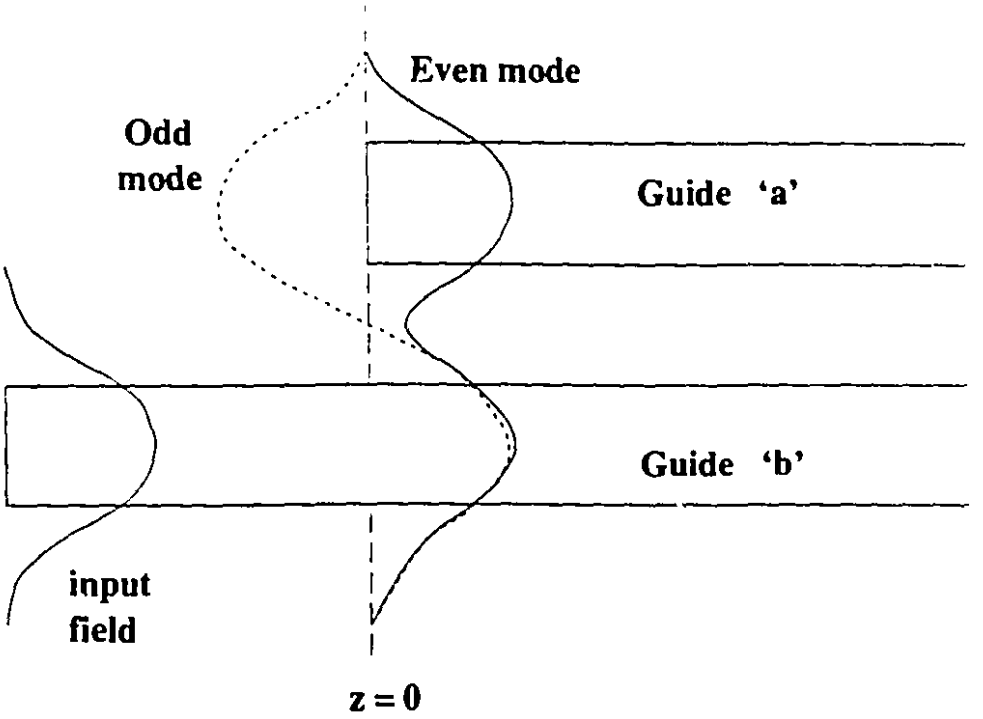

Figure 6.9: Schematic of the VDC structure in which the fundamental mode of the buried guide excites the coupler's normal modes

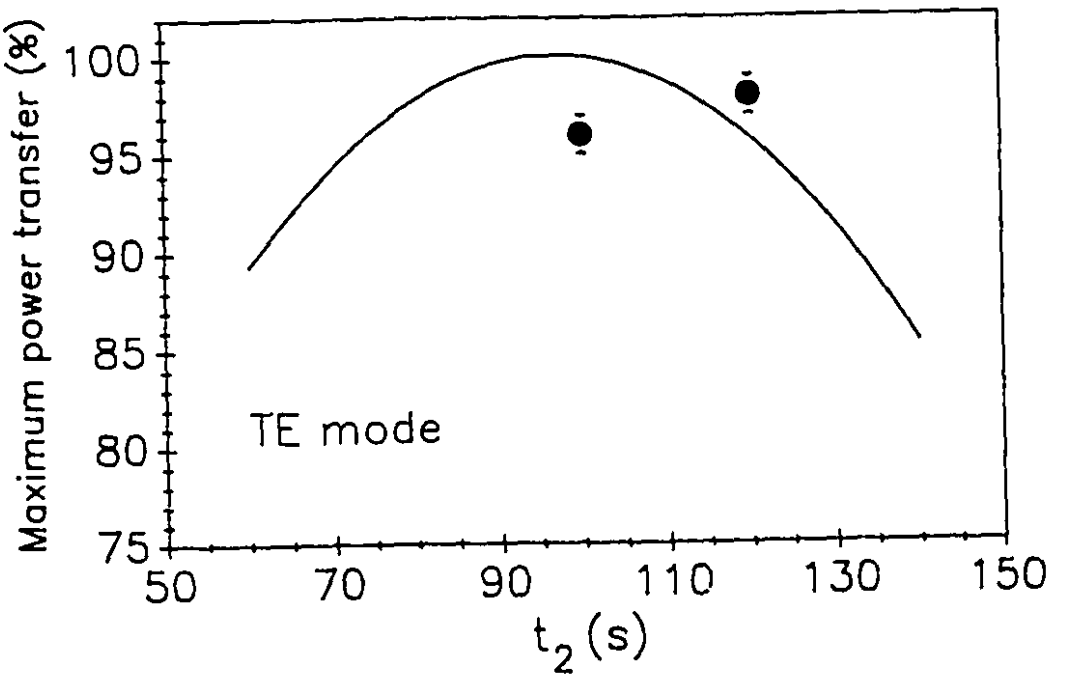

Figure 6.10: Calculated maximum power transfer as a function of t_2 for TE modes. Dots represent experimental data

Before concluding this chapter, it may be interesting to see what effect a small change in the complicated six-step ion-exchange model has on the coupler's characteristics. Since there are so many different parameters in this model, we decided to focus on one in particular: the left boundary condition (LBC) during backdiffusion. By changing it from 0.03 to zero, the calculated TE mode L_c values are compared (see Table 6.4) and shown to have a discrepancy of up to 7.6 %. Hence, we see that the model is quite sensitive to even modest changes.

Finally, we should also mention the results of our preliminary, unoptimized device [1] that was fabricated using different process conditions. The buried slab was made by a two-step process, using an applied field of $50\,V/mm$ and exchange time $t_1 = 15s$ in the first step, and $75\,V/mm$ in the second step (backdiffusion) with time t_2 varying from 4 to 10 min. The single-mode surface guide was formed by a one-step exchange with an applied field of $50\,V/mm$ and time $t_3 = 5\,s$. The calculated and measured results showing good power transfer are tabulated in Table 6.5.

t_2 (s)	$L_c(\mu m)$ ($LBC = 0.03$)	$L_c(\mu m)$ ($LBC = 0.00$)	*Change* (%)
100	262	276	5.3
120	350	350	0.0
140	437	404	-7.6

Table 6.4: Comparison between calculated L_c using different LBC values

Coupler	$L_c(\mu m)$ (BPM)	$L_c(\mu m)$ (meas)	$\eta_{max}(\%)$ (BPM)	$\eta_{max}(\%)$ (meas)
VDC1(TE)	239	234 ± 8	95.4	99.2 ± 1
VDC1(TM)	219	236 ± 9	93.7	98.8 ± 1
VDC2(TE)	276	288 ± 8	96.4	89.3 ± 4
VDC2(TM)	250	264 ± 8	93.2	95.1 ± 3

Table 6.5: Calculated and measured characteristics of preliminary VDC

6.5 Conclusion

In conclusion, the characteristics of this planar vertical coupling structure have been measured and compared to modelled results based on optical and micro-analytical waveguide characterizations. The combination of ion-exchange modelling and a vector beam propagation method provide for a computational design tool that yields good accuracy. Good agreement between calculated and experimental results was obtained within fabrication and measurement error for TE and TM polarizations. This passive coupling structure with high power transfer efficiency may prove to be a useful device in hybrid waveguide-detector geometries on glass. The following chapter will present another vertical coupler configuration that offers other advantages to waveguide-detector coupling.

Bibliography

[1] P.C. Noutsios, G.L. Yip, and J. Albert, 'Novel vertical directional coupler made by field-assisted ion-exchanged slab waveguides', Electron. Lett., 28 (14), pp. 1340-1342, 1992

[2] H. Nishihara, M. Haruna, T. Suhara, *Optical Integrated Circuits*, McGraw-Hill, New York, 1989

[3] E. Marom, O.G. Ramer, and S. Ruschin, 'Relation between normal-mode and coupled-mode analyses of parallel waveguides', J. Quantum Electron., 20 (12), pp. 1311-1319, 1984

[4] M.D. Feit, J.A. Fleck, Jr., and L. McCaughan, 'Comparison of calculated and measured performance of diffused channel-waveguide couplers', J. Opt. Soc. Amer., 73 (10), pp. 1296-1304, 1983

[5] W.P. Huang, C.L. Xu, S.T. Chu, and S.K. Chaudhuri, 'The finite difference vector beam propagation method: analysis and assessment', J. Lightwave Technol., 10 (3), pp. 295-305, 1992

[6] M.D. Feit and J.A. Fleck, Jr., 'Computation of mode properties in optical fiber waveguides by a propagating beam method', Appl. Opt., 19 (7), pp. 1154-1163, 1980

[7] G.L. Yip and P.C. Noutsios, 'An improved finite-difference vector beam propagation formulation for graded-index waveguides', IEEE Photon. Technol. Lett., 6 (4), pp. 543-545, 1994

[8] Y. Suematsu and K. Kishino, 'Coupling coefficient in strongly coupled dielectric waveguides', Radio Science, 12 (4), pp. 587-592, 1977

[9] J. Albert and G.L. Yip, 'Wide single-mode channels and directional coupler by two-step ion-exchange in glass', J. Lightwave Technol., 6 (4), pp. 552-563, 1988

Chapter 7

Improved Vertical Coupler

7.1 Introduction

In the previous chapter, we studied the characteristics of a directional coupler that allows for vertical coupling of light to the photodetector. However, this coupling efficiency has shown to be impaired by the presence of a thin layer of low index amorphous material at the semiconductor-guide bonding interface [1]. An effective way to avoid this problem is to use edge coupling to the detector which can be achieved by cladding the structure with a dielectric thin film having a refractive index higher than that of the waveguide [2]. Recently, we reported the realization of a new vertical coupling structure [3] composed of a planar buried guide in glass and a dielectric overlayer (see Fig. 7.1) that takes advantage of this edge-coupling scheme.

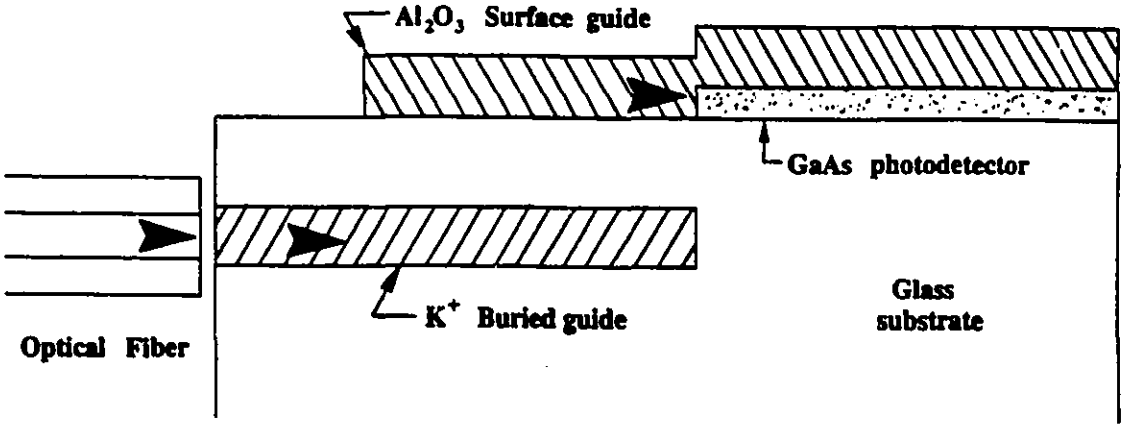

Figure 7.1: Improved vertical coupling structure for optimized edge coupling

In this chapter, the design, fabrication and measurement of such a device, in both planar and channel-guide form, for optimum edge coupling to a modelled $GaAs$ photodetector is described.

7.2 Fabrication and measurement

The improved planar vertical coupler is comprised of two parallel slab waveguides. The lower buried guide is fabricated by a two-step field-assisted K^+-ion exchange. An applied voltage of 20 V and exchange time $t_1 = 5s$ is used in the first step, and 100 V in the second step (backdiffusion) with exchange time $t_2 = 120s$. The single-mode dielectric surface guide of thickness D_2 and refractive index n_f is made by rf plasma sputtering with an Al_2O_3 target under the conditions of 2×10^{-2} Torr Ar/O_2 (4:1 mixture) gas pressure and target voltage of $0.5\,kV$, as described in Chapter 3. The sputtering time t_s ranges from 280 to 320 min.

The channel-guide VDC is composed of a buried channel guide and a planar dielectric thin film. The buried guide is fabricated by a two-step K^+-ion exchange. The first purely thermal exchange in KNO_3 at $T = 385^oC$ is carried out for times t_1 ranging from $15 - 25\,min$ through various mask openings between 4.0 and $5.2\,\mu m$ to achieve single-mode operation. The masking material is then etched away and a field-assisted exchange in $NaNO_3$ is performed over the whole surface with applied field strengths of $100\,V/mm$ and times t_2 ranging from $1 - 2\,min$ at $T = 385^oC$. As mentioned in Chapter 2, the purely thermal exchange in the first step was preferred over the field-assisted exchange to minimize lateral spreading of the concentration profile, resulting in channel guides with better circular symmetry. The Al_2O_3 planar surface guide is fabricated with a higher target voltage of $0.75\,kV$ for a fixed $t_s = 1.5h$ to obtain $0.26 < D_2 < 0.30\,\mu m$ using the measured sputtering rate $r = 0.186 \pm 0.013\,\mu/h$ (see Table 5.11). This higher voltage is chosen to achieve a larger $n_f = 1.617$ for reasons to be discussed later. The planar structure is needed to embed the photodetector since the width of the $GaAs$ layer, typically $15\,\mu m$ [2] is greater than

that of the buried channel guide.

For the planar structure, the two-mode interference effect is observed via prism coupling techniques. The output m-lines and the periodic variation of coupled power are shown in Fig. 7.2(a) and (b), respectively. For the channel-guide device, a single-mode fiber is butt-coupled to the buried channel guide to excite initially the fundamental mode. Subsequently, the even and odd normal modes of the coupler are excited simultaneously, yielding the periodic coupling pattern representing power transfer (see Fig. 7.3). The coupling length L_c is deduced as half of the period of the striped coupling pattern. The maximum power transfer ratio η_{max} is determined by measuring the relative intensities (power ratios) of the normal mode m-lines for both the planar and channel structures, as described in Chapter 6.

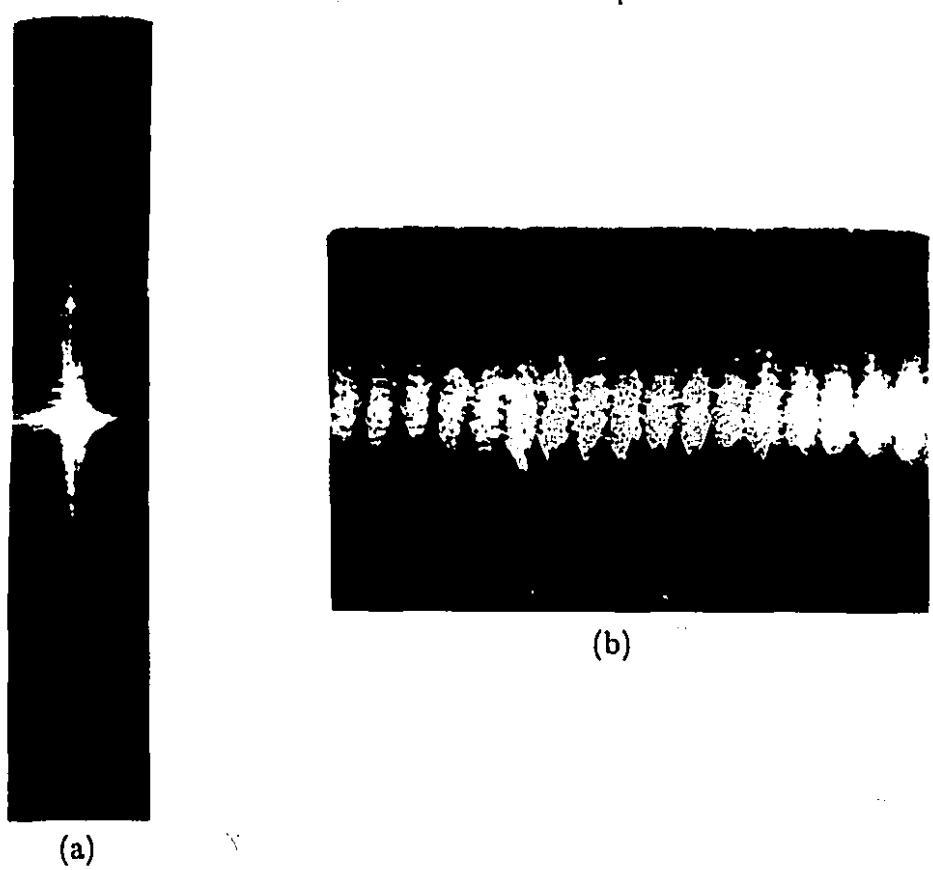

Figure 7.2: (a) Output normal mode m-lines and (b) periodic variation of coupled power seen on the glass surface

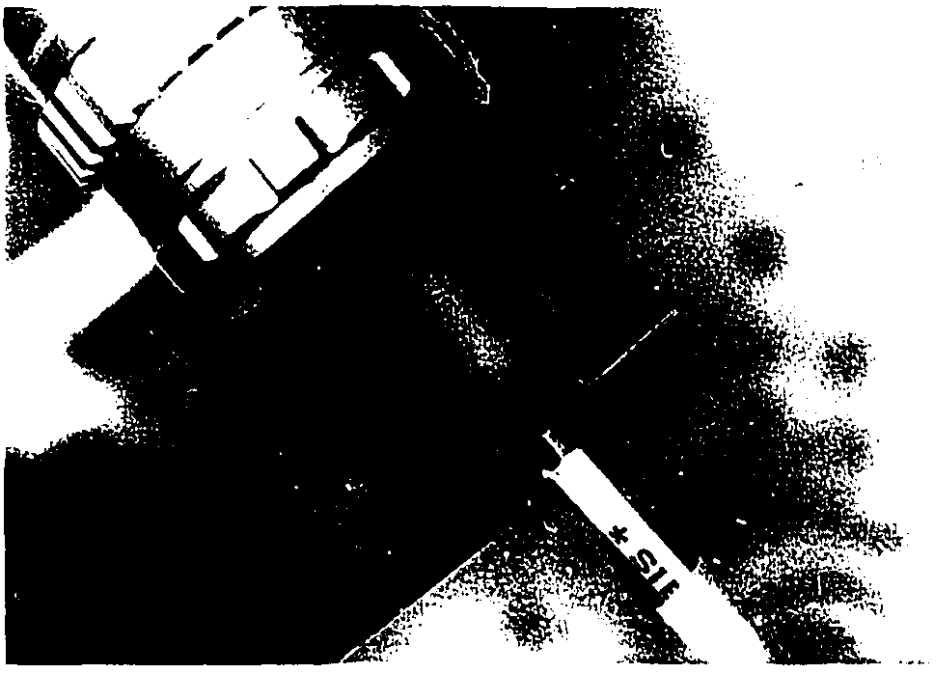

(a)

(b)

Figure 7.3: (a) Top-view photograph of fiber butt coupling into buried channel guide (b) periodic coupling pattern

7.3 Modeling of the photodetector

With the buried-to-surface guide coupling accounted for, the following aspect of the work involves directing the light from the upper surface guide into the embedded $GaAs$ detector. Although the detector is not included experimentally here, its important characteristics such as the attenuation coefficient and the end-fire coupling efficiency have been modelled numerically.

The power attenuation coefficient can be deduced from the complex propagation constant ($\beta^c = \beta' - j\beta''$, $\beta'' > 0$) of a guiding structure containing the absorbing layer. It is well known that the guided field follows an exponential $\exp(-j\beta^c z)$ dependence along the direction of propagation. Thus,

$$\exp(-j\beta^c z) = \exp(-j(\beta' - j\beta'')z) = \exp(-\beta'' z)\exp(-j\beta' z)$$

where β'' accounts for the light absorption along z. The power, $P_d(z)$, proportional to the square of the field, yields

$$P_d(z) = P_o \exp(-2\beta'' z) = P_o \exp(-\alpha_c z)$$

where α_c is the power attenuation coefficient. If the effective index is used instead then

$$N^c_{eff} = \beta^c/k_o = \beta'/k_o - j\beta''/k_o = N^r_e - jN^i_e$$

whence we obtain

$$\alpha_c = 2k_o N^i_e = 4\pi N^i_e/\lambda_o \tag{7.1}$$

The optimum design of the detector is based on calculating the TM mode α_c of a four-layer complex index waveguide structure using the TRT described in Chapter 4. We focused our study only on the TM polarization because α_c yields a larger value than that for the TE mode [2, 4]. The imaginary part of the complex effective index ($N^c_{eff} = N^r_e - j\alpha_c\lambda_o/4\pi$) is used to calculate α_c for the four-layer model shown as an inset in Fig. 7.4(a). The detector's index n_3 is based on [2], and the other indices

have been measured in our laboratory. α_c is calculated for various D_2 presented in Fig. 7.4(a) for $n_f = 1.576$ and $n_b = 1.5125$. Care must be taken to ensure single-mode operation of the surface guide without the detector. Step-index dispersion calculations show that this region occurs for $0.32\,\mu m < D_2 < 1.04\,\mu m$. Note that the maximum α_c of $1220cm^{-1}$ occurs at $D_2 = 0.47\,\mu m$. For the channel-guide version fabricated on the new substrates with $n_b = 1.5208$ and $n_f = 1.617$, α_c shows a similar behavior with D_2 (see Fig. 7.4(b)). The maximum α_c of $1530cm^{-1}$ occurs at $D_2 = 0.40\,\mu m$ with the single-mode region of the surface guide (without detector) being $0.26\,\mu m < D_2 < 0.83\,\mu m$.

The physical reason for these high α_c values is due to an improvement in the geometry of edge coupling. Previously, the five-layer structure provided for edge coupling by cladding the K^+ guide with a higher index of Al_2O_3 film that lifted the guided wave closer to the interface [2]. The largest reported value $\alpha_c = 200cm^{-1}$ may be improved by optimizing the thickness of the $GaAs$ layer D_3 [2]. However, in our four-layer structure, the cladding acts as the waveguide confining the guided wave well above the interface and thus providing a better 'head-on collision' with the detector.

We can determine the end-fire coupling efficiency, η_o, from the three-layer dielectric surface guide into the four-layer detector by calculating the overlap integral [5] of the mode field profiles presented in Chapter 4:

$$\eta_o = \frac{(\int_{-\infty}^{+\infty} E_{x3}(x) E_{x4} dx)^2}{(\int_{-\infty}^{+\infty} E_{x3}^2 dx)(\int_{-\infty}^{+\infty} E_{x4}^2 dx)} \tag{7.2}$$

where E_{x3} is the three-layer planar field profile obtained from the H_y of (4.31) and E_{x4} is the four-layer planar field obtained from (4.33). For $n_f(TM) = 1.576$ and $n_b = 1.5125$, the $GaAs$ thickness $D_3 = 89.5\,nm$ is chosen to yield the largest $\eta_o = 86\,\%$. For $n_f(TM) = 1.617$ and $n_b = 1.5208$, the $GaAs$ thickness $D_3 = 88.0\,nm$ is chosen to yield the largest $\eta_o = 89\,\%$.

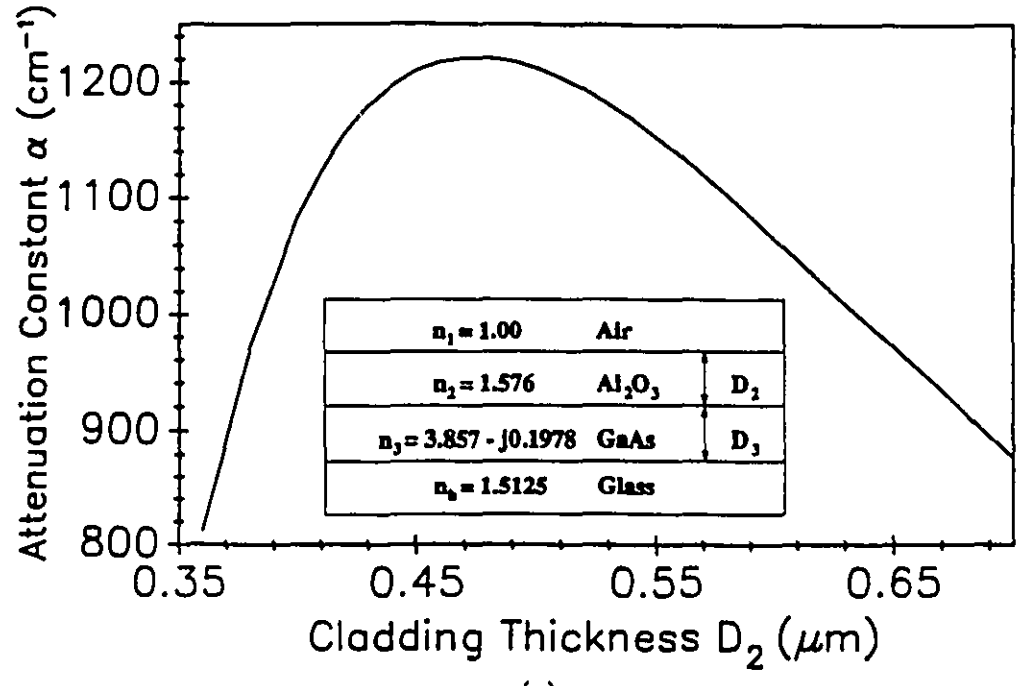

(a)

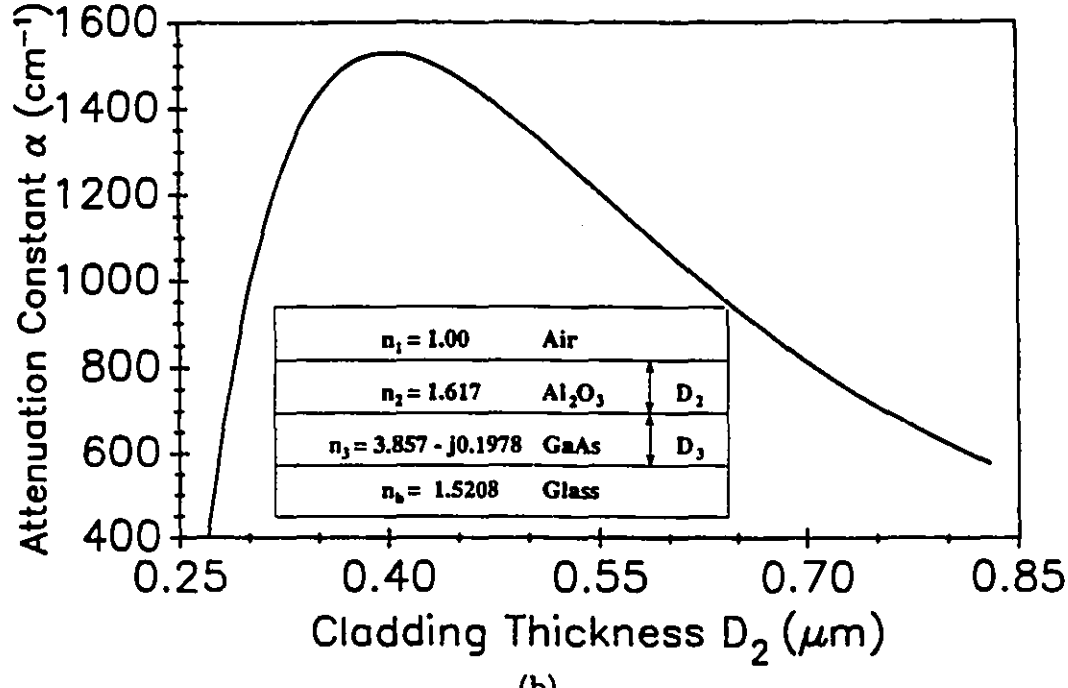

(b)

Figure 7.4: Theoretical absorption coefficient versus dielectric thickness for the four-layer model as indicated in the insets for (a) $n_f = 1.576$, $n_b = 1.5125$ and (b) $n_f = 1.617$, $n_b = 1.5208$

7.4 Coupler design and performance

7.4.1 Planar structure

The device performance can be simulated numerically for comparison to the experimental data. The GRIN profile of the buried waveguide is determined directly from the dopant concentration profile $c(x)$, as described in Chapter 5. With $c(x)$ determined, the buried index profile is given by $n(x) = n_b + \Delta n_s\, c(x)$ with $n_b = 1.5125$ and $\Delta n_s = 0.0134$ for the TM mode. This index profile is then used in an improved 2-D vector BPM (Chapter 4) to determine the device characteristics. Fig. 7.5 shows a typical BPM simulation of the guided wave being coupled vertically from the buried guide to the surface guide over one L_c. As shown, the dielectric guide confines the field well above the interface, providing an efficient edge coupling. In the BPM calculations, the input light excites the fundamental mode of the buried slab waveguide. The coupling length is determined by locating the z positions of the maximum power transfer from the buried to the surface guide. This power transfer is calculated by projecting the coupler's output field onto the individual field of the three-layer surface guide, as described in Chapter 6.

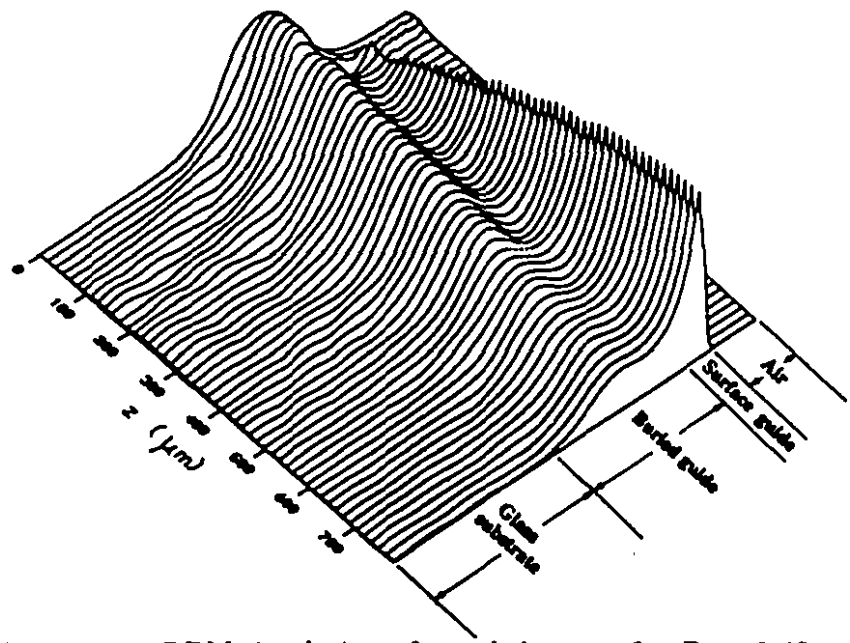

Figure 7.5: BPM simulation of coupled power for $D_2 = 0.40\,\mu m$

The behavior of the calculated and measured coupling lengths with thickness D_2 is shown in Fig. 7.6 where fair agreement is obtained, except at $D_2 = 0.40\,\mu m$ where the largest $L_c = 750\,\mu m$ is obtained. This discrepancy occurs due to the sensitivity of the sputtering process that provides only three decimal accuracy in n_f and an error of $0.015\,\mu/h$ in the sputtering rate r. In addition, the variation of η_{max} with D_2 is shown in Fig. 7.7, where a maximum in the power transfer is also observed at $D_2 = 0.40\,\mu m$. This η_{max} was measured to be $89\pm2\%$ with $R = 0.48\pm0.04$. Ideally, it would be desirable to have $D_2 = 0.47\,\mu m$ to match that of the maximum absorption (see Fig. 7.4(a)). Nevertheless, the calculated $\alpha = 1082\,cm^{-1}$ at $D_2 = 0.40\,\mu m$ is still quite high.

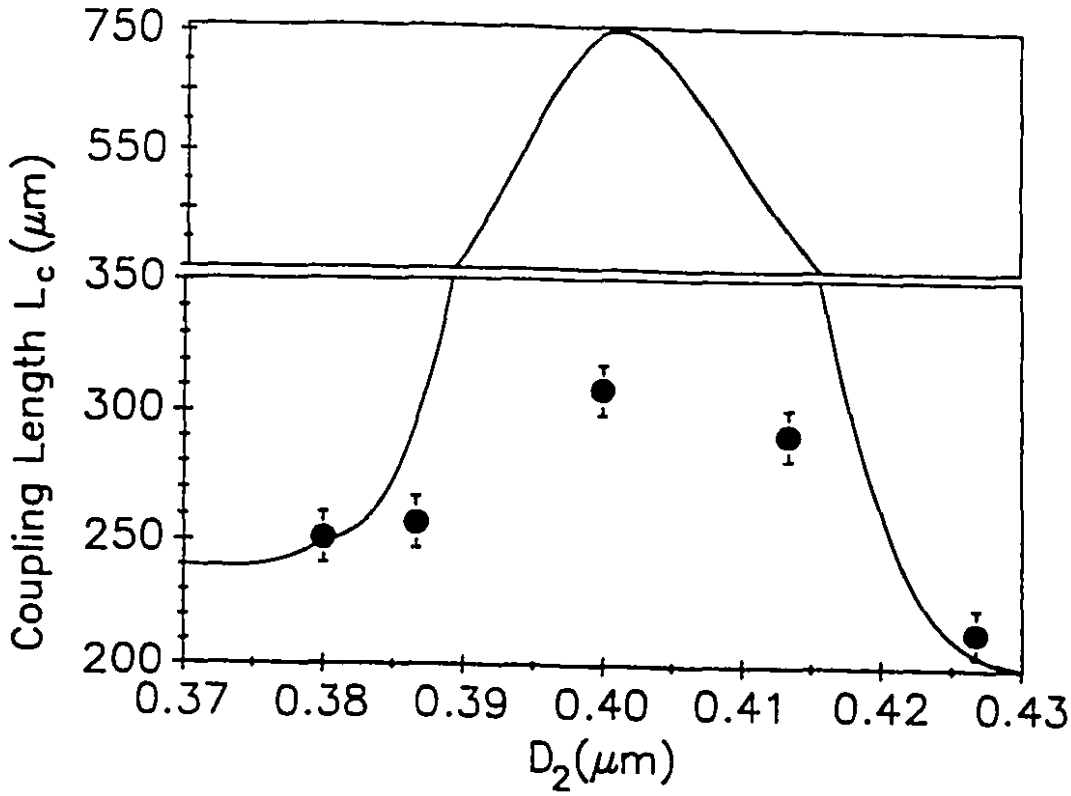

Figure 7.6: Comparison between measured (dots) and calculated (solid curve) coupling lengths for various D_2

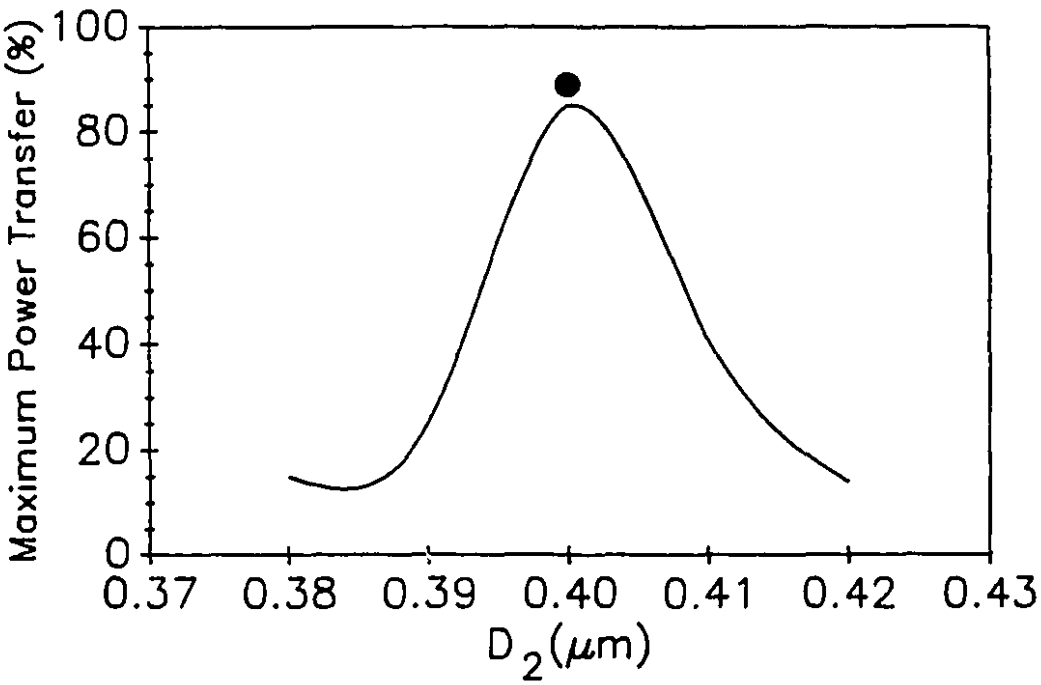

Figure 7.7: Variation of calculated maximum power transfer with D_2 including the measured value (dot) at $D_2 = 0.40\,\mu m$.

7.4.2 Channel-guide structure

For the channel-guide structure, the improved 3-D FD-VBPM based on the ADI method (Chapter 4) was used to model the device characteristics. Both the full-vector (FV-ADI) and the quasi-vectorial (QV-ADI) schemes were tried and compared. The GRIN channel buried guide $c(x,y)$ was obtained as described in 2.3.3 with $E_a^T = 98.5\,V/mm$ and $\alpha = 0.898$. With $c(x,y)$ determined, the refractive index profile $n(x,y) = n_b + \Delta n_s c(x,y)$ with $n_b = 1.5208$ and $\Delta n_s = 0.0108$. The planar Al_2O_3 guide with $n_f = 1.617$ and $D_2 = 0.30\,\mu m$ is chosen based on the BPM design that yields the best power transfer. Since $n_f = 1.576$ did not yield a high enough power transfer, the next available target voltage of $0.75\,kV$ was used. Fig. 7.8 shows typical contour plots of the 3D field profiles at $z = 0$, $z = L_c/2$ and $z = L_c$. Note how the field evolves from a channel to a planar profile over one L_c. These fields were calculated using the QV-ADI scheme. Since the structure consists of a weakly-guiding buried guide and a stongly-guiding planar guide, it was thought initially that the FV-ADI scheme would be necessary. However, the QV-ADI scheme was tested and found to give identical results with the advantage of being twice as fast computationally. Table 7.1 shows the results comparing these two schemes for a channel-guide VDC simulated with parameters $W = 4.8\,\mu m$, $t_1 = 20\,min$, and $t_2 = 1.5\,min$. Excellent agreement is obtained.

Scheme	$L_c(\mu m)$	$\eta_{max}(\%)$
FV-ADI	501	88.9
QV-ADI	501	88.9

Table 7.1: Comparison of calculated channel VDC characteristics using the FV-ADI and the QV-ADI schemes

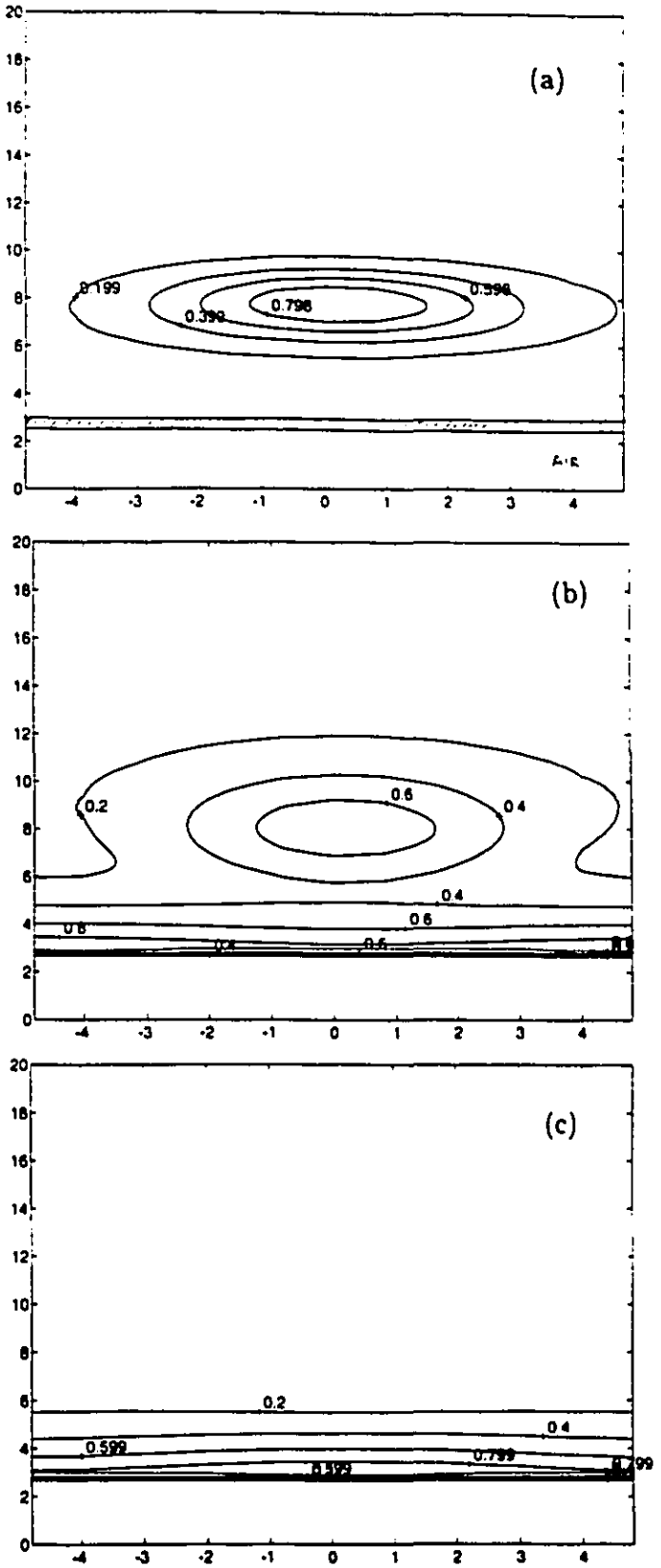

Figure 7.8: Contour plots of 3D BPM fields at (a) $z = 0$ (b) $z = L_c/2$ and (c) $z = L_c$

Using the QV-ADI scheme, the VDC characteristics were calculated for the TM mode. The coupling lengths show an increase with t_2, as shown in Fig. 7.9, for $W = 4.0\,\mu m$; similar behavior is obtained for the other channel widths. We see that the values of L_c, ranging from about $200 - 900\,\mu m$, are larger than those obtained for the planar VDC described in Chapter 6. This is to be expected because the Al_2O_3 planar surface guide's field is confined above the substrate surface yielding better isolation from the buried guide and hence, larger L_c values. The maximum power transfer shows an optimum value for a given range of t_2 (see Fig. 7.10).

For the experimental part, we decided to choose conditions that would yield a high η_{max} with a fairly large L_c. A larger L_c would allow for easier alignment of the photodetector. Thus, guided by the BPM design values, we chose to fabricate four devices on the same substrate with various W, $t_1 = 20\,min$ and $t_2 = 2.0\,min$. Considering the tradeoff between L_c and η_{max} shown in Figs. 7.9 and 7.10, the chosen conditions provide a good compromise for a large L_c ($\approx 900\,\mu m$) and a reasonable η_{max} of about 85 %. A simple photomask was used with various channel apertures ranging from 4.0 to 5.0 μm. After photolithography, the channel guide widths were measured using the far-field technique described in Chapter 3. They are presented in Table 7.2 in comparison to the photomask apertures for two samples. The discrepancies are due to the fluctuations in the development and wet etching processes that do not always yield repeatable aperture widths. The entries marked 'N/A' indicate that the processed channel was not acceptable due to the many defects that were observed under the microscope. The last column shows the values of W chosen in the BPM design calculations that are closest to the measured values.

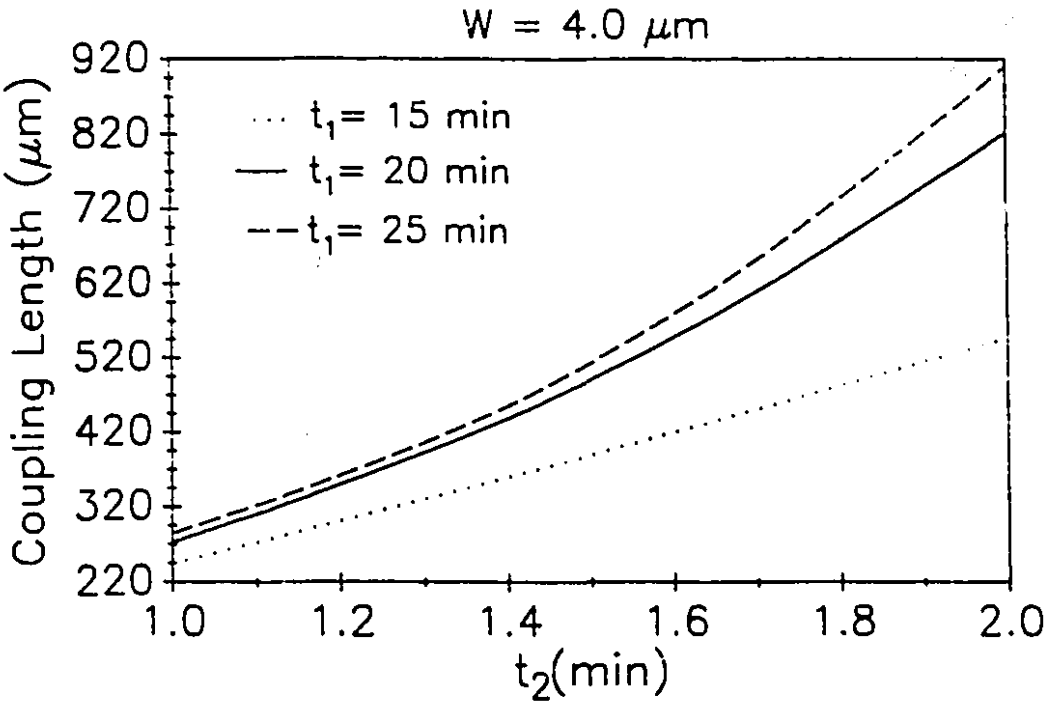

Figure 7.9: Calculated coupling length vs. t_2 for $W = 4.0\,\mu m$

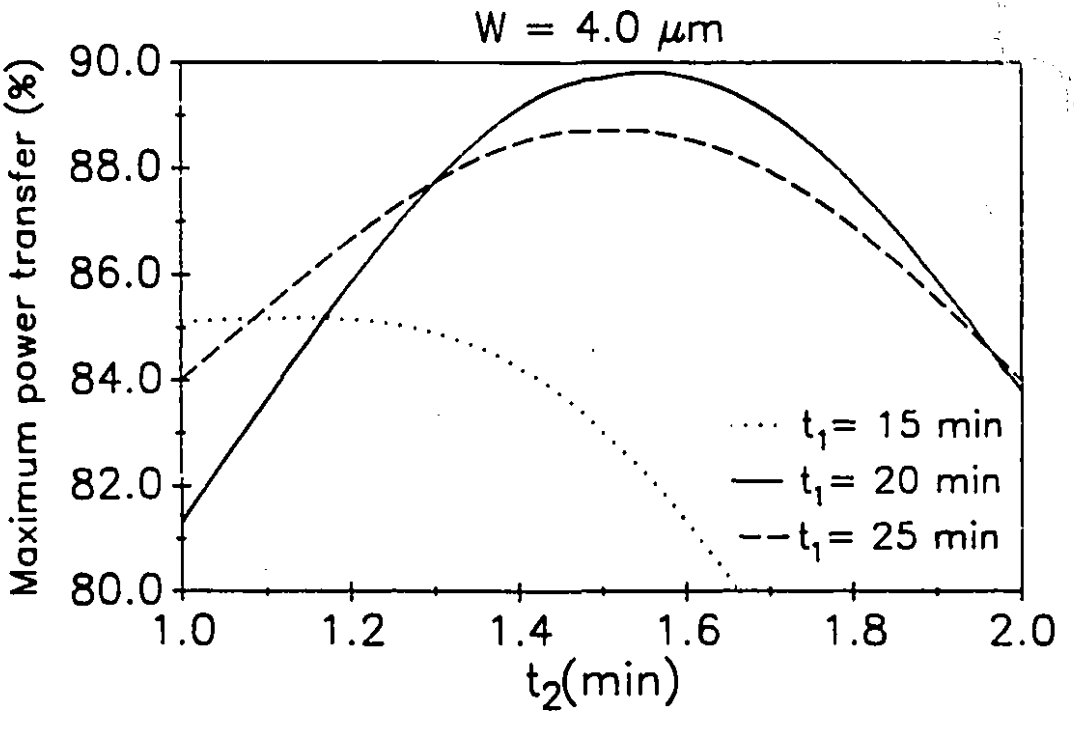

Figure 7.10: Calculated maximum power transfer vs. t_2 for $W = 4.0\,\mu m$

Two samples A2 and A3, each consisting of four channels, were fabricated as channel-guide VDC's. From A2, three devices (channels 1,3 and 4) were measured and from A3, only one device (channel 1) was considered. The comparisons to the BPM design calculations are shown in Fig. 7.11 and Table 7.3 for the coupling length and maximum power transfer, respectively. Fairly good agreement is obtained.

On a final note, it is worthwhile to determine if the vertical coupler actually gives better performance than the channel guide structure [2]. To determine this quantitatively, the calculated maximum power transfer ratio (89.8% or a loss of $0.47\,dB$) and the improvement in insertion loss ($1.7\,dB$, see Chapter 5) are needed. For our vertical coupler to be deemed better than the channel-guide structure of [2], the improvement in the insertion loss must be large enough to offset the loss involved in the buried to surface guide power transfer. As shown, the $1.7\,dB$ improvement is larger than the $0.47\,dB$ of power transfer loss, hence justifying the need for the vertical coupler. Experimentally, the improvement in insertion loss may not be as high as that predicted by theory. Since we did not pursue any such insertion loss measurements in this thesis, the only comparison we can make is with the results published by Milion *et al* for buried K^+-ion exchanged channel guides [6] made under very different fabrication conditions. An improvement of at least $0.43\,dB$ has been measured at $\lambda_o = 1.3\,\mu m$ which can be further improved to at least $0.61\,dB$ by a careful choice of the process parameters. Similar results are expected at $\lambda_o = 0.6328\,\mu m$. This measured value is not as large as we would like when compared to the vertical coupling loss. However, we must be optimistic and keep in mind that $0.6dB$ is a lower limit that can be improved by proper optimization.

Sample	Channel	Mask aperture (μm)	Measured W (μm)	Modeled W (μm)
A2	1	4.0	3.98	4.0
	2	4.0	N/A	-
	3	4.5	4.48	4.4
	4	5.0	4.95	4.8
A3	1	4.0	5.51	5.2
	2	4.0	5.59	-
	3	4.5	6.26	-
	4	5.0	6.77	-

Table 7.2: VDC channel width measurements

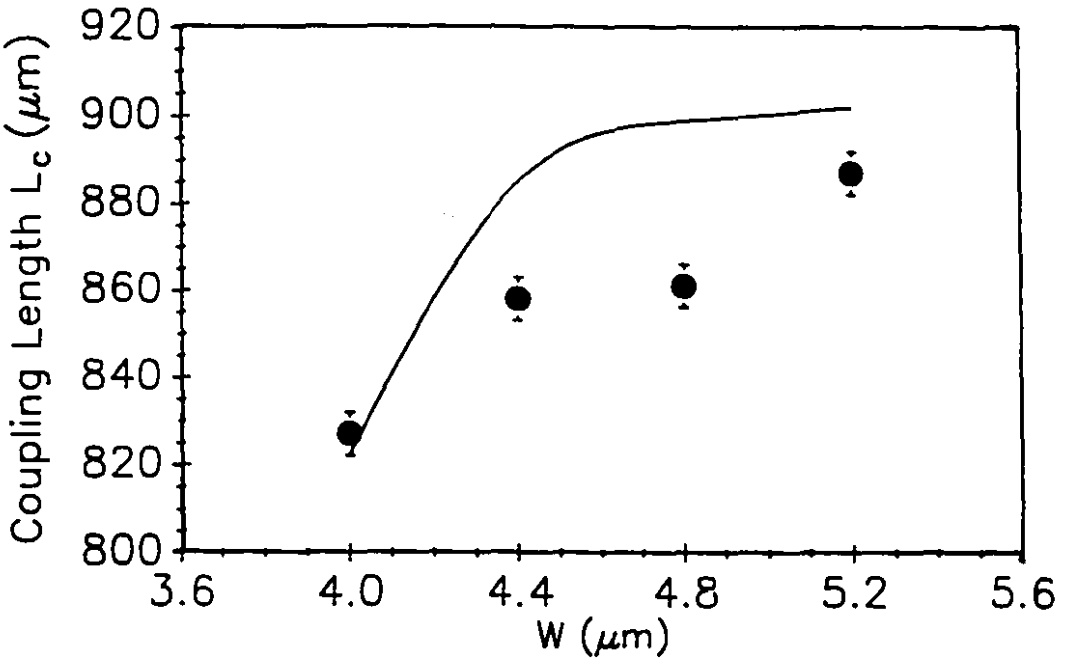

Figure 7.11: Comparison between measured (dots) and modeled (solid line) coupling lengths

W (μm)	η_{max} (BPM) (%)	η_{max} (meas.) (%)
4.0	83.8	87.2 ± 0.9
4.4	84.8	82.6 ± 1.1
4.8	83.2	81.6 ± 0.6

Table 7.3: Comparison between measured and modeled power transfer ratio η_{max}

7.5 Conclusion

In summary, the characteristics of an improved vertical directional coupler comprising a buried waveguide in glass and a dielectric surface guide are reported. Both a planar and a channel-guide version of the device have been investigated. This new structure takes advantage of edge coupling instead of vertical coupling of light to the photodetector. The measured coupling lengths and power transfer ratio are shown to be in good agreement within experimental error in comparison to those computed by the beam propagation method using the graded-index profile model. Calculations of the attenuation coefficient and the coupling efficiency of the modelled detector show an optimum absorption behavior.

Bibliography

[1] W.K. Chan, A. Yi-Yan, T.J. Gmitter, L.T. Florez, J.L. Jackel, D.M. Hwang, E. Yablonovitch, R. Bhat, and J.P. Harbison, 'Optical coupling of $GaAs$ photodetectors integrated with lithium niobate waveguides', IEEE Photon. Technol. Lett., 2 (3), pp. 194-196, 1990

[2] W.K. Chan, A. Yi-Yan, T.J. Gmitter, L.T. Florez, N. Andreadakis, and C.K. Nguyen, 'Channel glass waveguide detectors with grafted $GaAs$ film in embedded configuration', Electron. Lett., 27 (5), pp. 410-412, 1991

[3] P.C. Noutsios and G.L. Yip, 'Improved vertical directional coupler for optimum edge coupling to an embedded photodetector', Opt. Lett., 20 (21), pp. 2198-2200, 1995

[4] A. Yi-Yan, W.K. Chan, C.K. Nguyen, T.J. Gmitter, R. Bhat, and J.L. Jackel, '$GaInAs/InP$ photodetectors integrated with glass waveguide', Electron. Lett., 27 (1), pp. 87-89, 1991

[5] W.K. Burns and G.B. Hocker, 'Endfire coupling between optical fibers and diffused channel waveguides', Appl. Opt., 16 (8), pp. 2048-2051, 1977

[6] A. Miliou, H. Zhenguang, H.C. Cheng, R. Srivastava, and R.V. Ramaswamy, 'Fiber-compatible $K^+ - Na^+$ Ion-Exchanged Channel Waveguides: Fabrication and Characterization', J. Quantum Electron., 25 (8), pp. 1889-1897, 1989

Chapter 8

Conclusion

8.1 Thesis contents

The main goal of this thesis has been to study the design, fabrication and measurement of novel vertical directional couplers made by field-assisted K^+-ion exchange in soda-lime silicate glass. The characteristics of two vertical coupling structures have been modeled from fabrication conditions based on both optical and micro-analytical characterizations. The combination of ion-exchange concentration profile simulations and a vector beam propagation method provided for a fully numerical design tool that yielded very good accuracy. Good agreement between calculated and experimental results was obtained within the fabrication and measurement errors. This potentially useful device can be applied directly for optimized coupling from an optical fiber to a hybrid waveguide-detector structure.

Besides the device characterizations presented in the last two chapters, a fair amount of work has been devoted to the understanding of the field-assisted ion-exchange process for the purposes of optical waveguide formation. The ion-exchange physics and the modeling procedures used to obtain the solution of the differential equations, presented in Chapter 2, laid the foundation for predicting the dopant concentration profile. The micro-analytical study of the waveguides using the electron microprobe yielded direct measurement of this profile. In addition, it provided us with information on the surface concentration (h_K) for both buried and surface guides.

The results, especially in the single-mode region, shed new light of the pre-saturation behavior of h_K, that were needed for design purposes.

Parallel to the study of the concentration profile, an exhaustive optical characterization of the planar surface guides for a given set of fabrication conditions has been performed to determine the refractive index profile. Standard mode-index measurements were carried out to determine the maximum index change Δn_s, the profile shape (modified Fermi) and the mobility μ_K. In addition, these measurements were performed on single-mode waveguides to determine the effective index values and results showed how the thermal effect became more prevalent in this region.

Finally, the channel-guide profile characteristics were modeled solely from two-dimensional ion-exchange simulations. One channel-guide sample was measured for its near-field mode profile showing good agreement to that predicted by theory. This provided us with an indirect verification that our 2-D profile was fairly accurate, however, it does not go far enough. Further characterization work needs to be performed, especially for buried guides. Recently, the characterization of channel surface guides made by purely thermal K^+-ion exchange were reported showing an unexpected saturation behavior for long difusion times [1]. Future characterization of our field-assisted buried channel guides needs to be performed to see if this similar behavior is observed.

The experimental data derived using both optical and micro-analytical characterizations allowed us to numerically model the refractive index profile quite accurately without the need for any analytical functions. This fully numerical approach proved to be quite useful in the modeling of the complex diffusion and cooling processes used for the vertical coupling structures.

The numerical methods of Chapter 4, including the vector BPM, provided us with accurate computational design tools for the device characteristics. Here, the main contribution of our work has been to account for the graded-index nature of the index profiles in the finite-difference formulation that was not attempted previously.

Although this provided some minor improvements for our weakly-guiding structures, it is believed that this scheme is needed for strongly-guiding structures.

8.2 Future directions

Finally, the novel vertical couplers presented in Chapters 6 and 7 were demonstrated only at one wavelength, $\lambda_o = 0.6328\,\mu m$, to accommodate the $GaAs$ detector whose wavelength absorption region includes λ_o. However, nothing prevents us from studying this structure at other wavelength regions that are more applicable to fiber-optic communications, namely $\lambda_o = 1.3\,\mu m$ and $1.55\,\mu m$. In these latter cases, the VDC needs to be re-designed to accommodate the $GaInAs/InP$ grafted detectors [2] in the $\lambda_o = 1.3\,\mu m$ range. Another possibility is to have wavelength-flattened performance over both wavelength ranges by taking advantage of the vertical coupler's strong asymmetric structure. Previous work on lateral asymmetric couplers using SiO_2/Si have demonstrated this type of performance [3]. If this can be realized, the potential of the VDC may become attractive for hybrid detector applications in WDM systems where many wavelengths are used.

As for other applications, the improved VDC structure may prove to be a good candidate as an optical wavelength filter [4]. In fact, there is some recent work showing how a buried waveguide cladded by a thick film of photoresist can act as a notch filter with the best resolution being $11\,nm$ in the $1.22\,\mu m$ window. Future work with a high index Al_2O_3 cladding may offer similar filtering behavior. In addition, our VDC can become quite useful in the arena for integrated optic sensors. For example, the VDC may be used as an evanescent field sensor for any type of refractive index change that may occur on the device's surface. These index perturbations would change the VDC's power transfer ratio and coupling length. When properly calibrated, the VDC can monitor any changes in its environment such as detecting a gas leak or a water flow level.

Bibliography

[1] M.N. Weiss and R. Srivastava. 'Determination of ion-exchanged channel waveguide profile parameters by mode-index measurements'. Appl. Opt., 34 (3), pp. 455-458. 1995

[2] A. Yi-Yan, W.K. Chan, C.K. Nguyen, T.J. Gmitter, R. Bhat, and J.L. Jackel. '$GaInAs/InP$ *pin* photodetectors integrated with glass waveguide'. Electron. Lett., 27 (1), pp. 87-89, 1991

[3] H. Yanagawa, S. Nakamura, I. Ohyama and K. Ueki, 'Broad-band high silica optical waveguide star coupler with asymmetric directional couplers'. J. Lightwave Technol., 8 (9), pp. 1292-1297. 1990

[4] I.S. Mauchline and G. Stewart. 'Fabrication of buried channel waveguides in $K^+ - Na^+$ ion-exchanged glass and their application to notch filters'. Opt. Lett., 18 (21), pp. 1801-1803. 1993